



GDAŃSK UNIVERSITY  
OF TECHNOLOGY

INSTITUTE  
OF  
NAVAL ARCHITECTURE  
AND  
OCEAN ENGINEERING



# Polish Maritime Research

No 2 (110) 2021  
Vol. 28

ADDRESS OF PUBLISHER  
& EDITOR'S OFFICE:

GDAŃSK UNIVERSITY  
OF TECHNOLOGY

Institute  
of Naval Architecture  
and Ocean Engineering  
G. Narutowicza 11/12  
80-233 Gdańsk, POLAND

EDITORIAL STAFF:

Wiesław Tarełko  
| Editor in Chief  
Janusz Kozak  
| Deputy Editors-in-Chief  
Wojciech Litwin  
| Deputy Editors-in-Chief

Price:  
single issue: 25 PLN

Prices for abroad  
single issue:  
- in Europe EURO 15  
- overseas USD 20

WEB:  
[pg.edu.pl/pmr](http://pg.edu.pl/pmr)

e-mail : [pmr@pg.edu.pl](mailto:pmr@pg.edu.pl)

ISSN 1233-2585

## CONTENS

- 4 **Xiangcheng Wu, Pengyao Yu, Guangzhao Li, Fengkun Li**  
*NUMERICAL STUDY OF THE EFFECT OF WING POSITION ON THE DYNAMIC MOTION CHARACTERISTICS OF AN UNDERWATER GLIDER*
- 18 **Ligang Li, Zhiyuan Pei, Jiucui Jin, Yongshou Dai**  
*CONTROL OF UNMANNED SURFACE VEHICLE ALONG THE DESIRED TRAJECTORY USING IMPROVED LINE OF SIGHT AND ESTIMATED SIDESLIP ANGLE*
- 27 **Remigiusz Iwańkiewicz**  
*A MULTI-CASE-BASED ASSEMBLY MANAGEMENT METHOD FOR THE SHIPBUILDING INDUSTRY*
- 36 **Tomasz Cepowski, Paweł Chorab, Dorota Łozowicka**  
*APPLICATION OF AN ARTIFICIAL NEURAL NETWORK AND MULTIPLE NONLINEAR REGRESSION TO ESTIMATE CONTAINER SHIP LENGTH BETWEEN PERPENDICULARS*
- 46 **Radosław Kołodziej, Paweł Hoffmann**  
*NUMERICAL ESTIMATION OF HULL HYDRODYNAMIC DERIVATIVES IN SHIP MANEUVERING PREDICTION*
- 54 **M. Burak Samsul**  
*BLADE CUP METHOD FOR CAVITATION REDUCTION IN MARINE PROPELLERS*
- 63 **Nenad Vulić, Karlo Bratić, Branko Lalić, Ladislav Stazić**  
*IMPLEMENTING SIMULATIONX IN THE MODELLING OF MARINE SHAFTING STEADY STATE TORSIONAL VIBRATIONS*
- 72 **Zbigniew Korczewski, Konrad Marszałkowski**  
*ENERGY ANALYSIS OF THE PROPULSION SHAFT FATIGUE PROCESS IN A ROTATING MECHANICAL SYSTEM PART III DIMENSIONAL ANALYSIS*
- 78 **Andrzej Młynarczak, Krzysztof Rudzki**  
*OPTIMISATION OF THE TOPPING-UP PROCESS OF LUBRICATING OIL IN MEDIUM-SPEED MARINE ENGINES*
- 85 **Serhiy Serbin, Badri Diasamidze, Viktor Gorbov, Jerzy Kowalski**  
*INVESTIGATIONS OF THE EMISSION CHARACTERISTICS OF A DUAL-FUEL GAS TURBINE COMBUSTION CHAMBER OPERATING SIMULTANEOUSLY ON LIQUID AND GASEOUS FUELS*
- 96 **Zygfryd Domachowski**  
*MINIMIZING GREENHOUSE GAS EMISSIONS FROM SHIPS USING A PARETO MULTI-OBJECTIVE OPTIMIZATION APPROACH*

**ADDRESS OF PUBLISHER  
& EDITOR'S OFFICE:**

**GDAŃSK UNIVERSITY  
OF TECHNOLOGY**

**Institute  
of Naval Architecture  
and Ocean Engineering  
G. Narutowicza 11/12  
80-233 Gdańsk, POLAND**

- 102 Xiaowei Yan, Hao Song, Zilong Peng, Huimin Kong, Yipeng Cheng,  
Linjiang Han**  
*REVIEW OF RESEARCH RESULTS CONCERNING THE MODELLING OF  
SHIPPING NOISE*
- 116 Arturo Silva-Campillo, Juan Carlos Suárez-Bermejo, Miguel Ángel  
Herrerros-Sierra**  
*DESIGN CRITERIA FOR SCANTLING OF LONGITUDINAL AND TRANSVERSE  
CONNECTIONS IN THE TORSION BOX UNDER FATIGUE LOADING*
- 128 Janusz Kozak**  
*JOINTS OF STEEL SANDWICH STRUCTURES*

---

## Editorial

POLISH MARITIME RESEARCH is the scientific journal with a worldwide circulation. This journal is published quarterly (four times a year) by Gdansk University of Technology (GUT). On September, 1994, the first issue of POLISH MARITIME RESEARCH was published. The main objective of this journal is to present original research, innovative scientific ideas, and significant findings and application in the field of :

### **Naval Architecture, Ocean Engineering and Underwater Technology,**

The scope of the journal covers selected issues related to all phases of product lifecycle and corresponding technologies for offshore floating and fixed structures and their components.

All researchers are invited to submit their original papers for peer review and publications related to methods of the design; production and manufacturing; maintenance and operational processes of such technical items as:

- all types of vessels and their equipment,
- fixed and floating offshore units and their components,
- autonomous underwater vehicle (AUV) and remotely operated vehicle (ROV).

We welcome submissions from these fields in the following technical topics:

- ship hydrodynamics: buoyancy and stability; ship resistance and propulsion, etc.,
  - structural integrity of ship and offshore unit structures: materials; welding; fatigue and fracture, etc.,
  - marine equipment: ship and offshore unit power plants: overboarding equipment; etc.
- 

### Scientific Board

**Chairman : Prof. JERZY GIRTLEK - Gdańsk University of Technology, Poland**

**Vice-chairman : Prof. CARLOS GUEDES SOARES, Universidade de Lisboa, Lisbon, Portugal**

**Vice-chairman : Prof. MIROSLAW L. WYSZYŃSKI - University of Birmingham, United Kingdom**

<b>Prof. POUL ANDERSEN</b> Technical University of Denmark Kongens Lyngby Denmark	<b>Prof. STOJCE DIMOV ILCEV</b> Durban University of Technology Durban South Africa	<b>Prof. JERZY MERKISZ</b> Poznan University of Technology Poznan Poland
<b>Prof. JIAHN-HORNG CHEN</b> National Taiwan Ocean University Keelung Taiwan	<b>Prof. YORDAN GARBATOV</b> Universidade de Lisboa, Lisbon Portugal	<b>Prof. VALERI NIEKRASOV</b> Admiral Makarov National University of Shipbuilding Mikolaiv Ukraine
<b>Prof. VINCENZO CRUPI</b> University of Messina Messina Italy	<b>Prof. STANISLAW GUCMA</b> Maritime University of Szczecin Szczecin Poland	<b>Prof. SERHIY SERBIN</b> Admiral Makarov National University of Shipbuilding Mikolaiv Ukraine
<b>Prof. MAREK DZIDA</b> Gdansk University of Technology Gdansk Poland	<b>Prof. ANTONI ISKRA</b> Poznan University of Technology Poznan Poland	<b>Prof. JOZEF SZALA</b> UTP University of Science and Technology Bydgoszcz Poland
<b>Dr. KATRIEN ELOOT,</b> Flanders Hydraulics Research, Antwerpen Belgium	<b>Prof. JAN KICINSKI</b> Institute of Fluid-Flow Machinery - Polish Academy of Sciences Gdansk Poland	<b>Prof. HOANG ANH TUAN</b> Ho Chi Minh City University of Technology (HUTECH) Ho Chi Minh Vietnam
<b>Prof. ODD MAGNUS FALTINSEN</b> Norwegian University of Science and Technology Trondheim Norway	<b>Prof. ZBIGNIEW KORCZEWSKI</b> Gdansk University of Technology Gdansk Poland	<b>Prof. TADEUSZ SZELANGIEWICZ</b> Maritime University of Szczecin Szczecin Poland
<b>Prof. MASSIMO FIGARI</b> University of Genova Genova Italy	<b>Prof. JOZEF LISOWSKI</b> Gdynia Maritime University Gdynia Poland	<b>Prof. DRACOS VASSALOS</b> University of Strathclyde Glasgow United Kingdom
<b>Prof. HASSAN GHASSEMI</b> Amirkabir University of Technology Tehran Iran	<b>Prof. JERZY EDWARD MATUSIAK</b> Aalto University Espoo Finland	

# NUMERICAL STUDY OF THE EFFECT OF WING POSITION ON THE DYNAMIC MOTION CHARACTERISTICS OF AN UNDERWATER GLIDER

Xiangcheng Wu

Pengyao Yu\*

Guangzhao Li

Fengkun Li

Dalian Maritime University, China

\* Corresponding author: [yupengyao@dlmu.edu.cn](mailto:yupengyao@dlmu.edu.cn) (P. Yu)

## ABSTRACT

*Underwater gliders are winged, autonomous underwater vehicles that are broadly applied in physical and biological oceanography. The position of the wing has an important effect on the movement performance of the underwater glider. In this paper, the dynamic motion of a series of underwater glider models with different longitudinal wing positions are simulated, which provides guidance for the design of underwater gliders. The results show that when the net buoyancy is constant, the wing position affects the gliding angle, but does not affect the relationship between the gliding angle and the gliding speed. In addition, the farther the wing position of the glider is from the buoyancy centre, the longer it takes for the attitude of a glider to change, whether the wing is in front of, or behind, the buoyancy centre.*

**Keywords:** underwater glider, motion simulation, wing position

## INTRODUCTION

An underwater glider is a special type of autonomous underwater vehicle which is controlled by adjusting its buoyancy. Since the idea for an underwater glider was put forward by Stommel [1] in 1989, it has attracted wide attention. For the characteristics of low energy consumption, low cost and long range, several typical underwater gliders have been developed and broadly applied in physical and biological oceanography, such as Slocum [2], Spray [3], Seaglider [4], Petrel [5] and Seawing [6].

Underwater gliders can change direction by controlling their centre of gravity and moving in the horizontal plane by the hydrodynamic force exerted on the wings. As a result, underwater gliders follow a saw tooth motion in the vertical plane [7]. Therefore, the wings greatly affect the dynamic motion characteristics of underwater gliders by influencing the hydrodynamic characteristics. Shankar [8] studied the impact of the variation of wing position on the hydrodynamic characteristics of an underwater glider with NACA0012 wings by computational fluid dynamics (CFD) methodology.

The study brings out that the wing position at the farther aft improves the lift-drag ratio and stability in the longitudinal motion of the glider but the increase of the lift-drag ratio is small across all angles of attack, with a slight increase at higher angles ( $\pm 8^\circ$ ). Javaid [9] studied the effect of wing form on the hydrodynamic characteristics of an underwater glider by experimental and numerical methods. The results show that a rectangular winged glider has higher lift force and drag force than the tapered wing glider due to a larger wetted area. The author also studied the effect on the dynamic stability by numerical methods. The results show that the tapered wing glider has higher linear velocity while the rectangular wing glider has a smaller spiral turning radius [10]. Zhang [11] developed a prototype of a gliding robotic fish with two types of wings. The wings had the same wingspan but different aspect ratios. By analysing the motion performance of the gliding robotic fish with different wings during steady gliding, the author came to the conclusion that the larger wings result in shallower gliding paths, but a slower gliding speed compared to the smaller wings. Liu [12] designed an orthogonal test to study the impact of wing parameters on the movement efficiency and

stability of a hybrid underwater glider. The results show that the chord length has the most remarkable effect on the movement efficacy while the axial position has a negligible effect on the movement efficacy. The sweep angle has the most significant impact on the stability of the underwater glider. Fan [13] studied the impact of geometric parameters on the steady wings-level flight of a generic glider shape. The conclusions included the fact that higher speeds can be attained using smaller wingspans and higher wing aspect ratios for a glider with fixed mass and buoyancy capacity. A higher lift-drag ratio can be attained by increasing the wingspan ratio at a given gliding angle speed and, the farther aft the wing is located, the more stable the glider's longitudinal dynamics becomes, which is due, in part, to the increased pitch damping.

In Graver [14] and Bhatta [15], dynamic models of underwater gliders were established and corresponding motion simulation analysis was conducted. In Leonard [16] and Bhatta [17], the nonlinear gliding stability was analysed and stabilising control methods for gliders were discussed. In Isa [18, 19] and Noh [20], a kinetic model for the underwater glider designed by the University of Science, Malaysia, was established. Fan [21] presented a multibody dynamic model for an underwater glider which was operating in an unsteady non-uniform flow field.

The effect of wing position on the hydrodynamic characteristics of underwater gliders has been studied by the CFD method but these studies do not directly show the effect of wing position on motion characteristics. In this paper, the effect of wing position on the dynamic motion characteristics of an underwater glider is studied by simulating three typical motion states: the motion of steady gliding, the motion after receiving a small disturbance, and the motion after adjusting the position of the movable block.

The paper is organised as follows. Section 2 derives the dynamic model for underwater gliders. Section 3 describes the models constructed in this paper and calculates the hydrodynamic parameters needed by the dynamic model. Section 4 simulates several motion states of different models and analyses the effect of wing position. Section 5 summarises the main conclusions.

## DYNAMIC MODEL

### REFERENCE FRAMES

In this paper, the inertial frame  $E-\xi\eta\zeta$ , the body frame  $O-XYZ$  and the flow frame  $V-V_1V_2V_3$  are adopted to describe the motion of the glider and are shown in Fig. 1 [22].

The inertial frame  $E-\xi\eta\zeta$  is fixed in the inertial space and the coordinate axis  $E-\zeta$  points to the direction of gravity. The origin of body frame  $O-XYZ$  is fixed at the buoyancy centre of the glider. The  $O-Y$  axis coincides with the longitudinal axis of the glider and the  $O-X$  axis lies in the wing plane, pointing to the right. The position  $\mathbf{b}$  and the attitude  $\mathbf{\Omega}$  of the underwater glider in the inertial frame and the linear velocity  $\mathbf{v}$  and angular velocity  $\mathbf{\omega}$  of the glider in the body frame are defined as:

$$\mathbf{b} = \begin{Bmatrix} \xi_B \\ \eta_B \\ \zeta_B \end{Bmatrix}, \mathbf{\Omega} = \begin{Bmatrix} \varphi \\ \theta \\ \psi \end{Bmatrix}, \mathbf{v} = \begin{Bmatrix} u \\ v \\ w \end{Bmatrix}, \mathbf{\omega} = \begin{Bmatrix} p \\ q \\ r \end{Bmatrix}, \quad (1)$$

The flow frame is defined relative to the body frame. First, the attack angle  $\alpha$  and the slip angle  $\beta$  are defined as:

$$\alpha = \tan^{-1}\left(\frac{w}{u}\right), \quad \beta = \tan^{-1}\left(\frac{v}{\sqrt{u^2 + w^2}}\right) \quad (2)$$

The body frame is then rotated around the  $O-Y$  axis by the angle  $-\alpha$  and around the new  $O-Z$  axis by the angle  $\beta$ . As a result, the body frame is rotated to a new position which is defined as the flow frame  $V-V_1V_2V_3$ , as shown in Fig. 1.

The underwater glider is regarded as a system of mass blocks in this paper. The components of the system are shown in Table 1. It should be noted that all the positions are given by the vectors from the buoyancy centre to the respective masses in the body frame. As shown in Fig. 2, the centre of the movable block is located at position  $r_{px}$  along the  $O-X$  axis with eccentric offset  $R_p$ , and is rotated with an angle  $\gamma$  around the  $O-X$  axis.

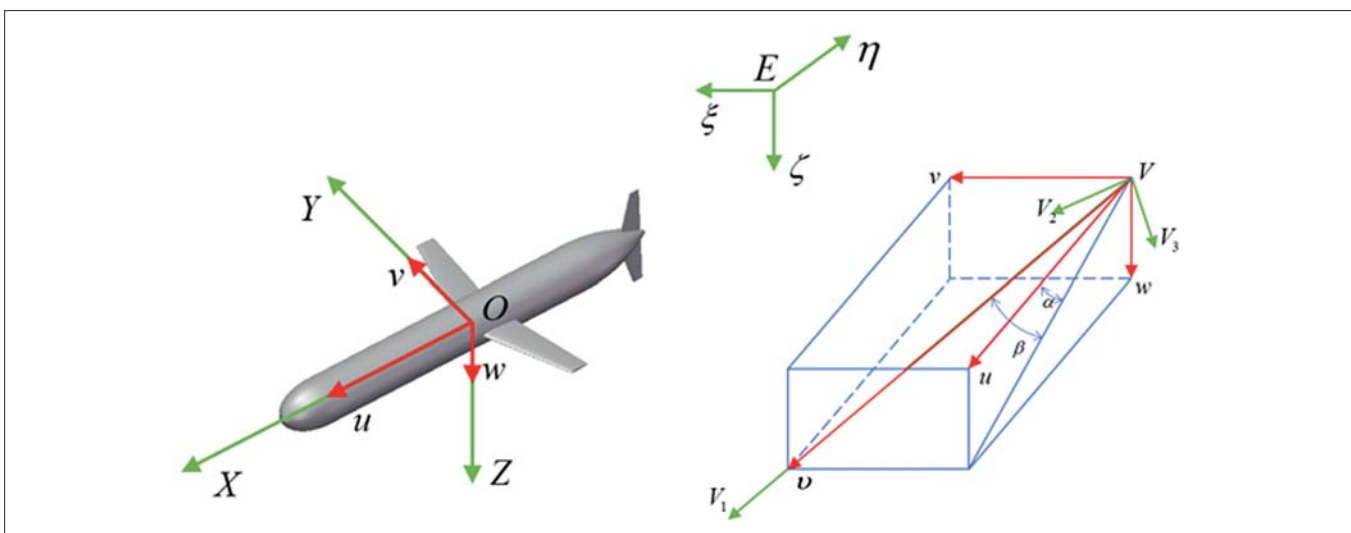


Fig. 1. Reference frames

Tab. 1. The components of the underwater glider system

	Mass	Position
Movable block	Stationary mass $m_p$	Variable position $r_p$
Net buoyancy	Adjustable mass $m_b$	Constant position $r_b$
All other fixed structures	Stationary mass $m_h$	Constant position $r_h$

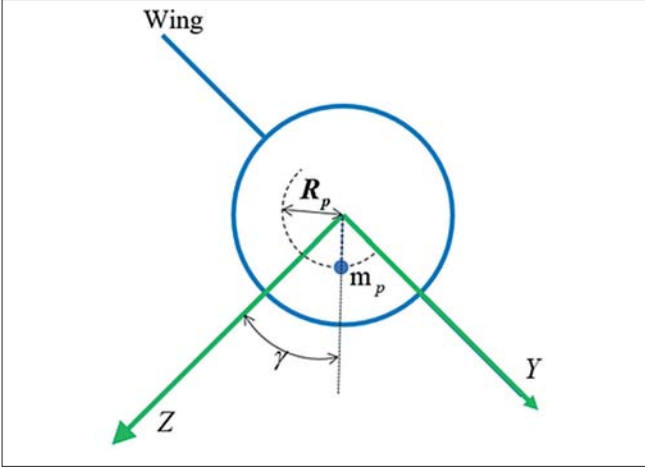


Fig. 2. Mechanisms of turning spiralling motion

## KINEMATICS

According to the reference frames, the inertial velocity and the attitude kinematics of the glider system are defined in [23].

$$\begin{aligned}\dot{\mathbf{b}} &= \mathbf{R}_{EB} \mathbf{v} \\ \dot{\mathbf{R}}_{EB} &= \mathbf{R}_{EB} \hat{\boldsymbol{\omega}}\end{aligned}\quad (3)$$

$\mathbf{R}_{EB}$  is a rotational transformed matrix from the body frame to the inertial frame. The operator ‘ $\hat{\cdot}$ ’ maps a vector to a  $3 \times 3$  skew-symmetric matrix, which satisfies  $\hat{\mathbf{a}}\mathbf{c} = \mathbf{a} \times \mathbf{c}$  for vectors  $\mathbf{a}$  and  $\mathbf{c}$ .

The attitude of the glider in the inertial frame can be described by the Euler angle  $\boldsymbol{\Omega}$ , including the roll angle  $\varphi$ , the pitch angle  $\theta$ , and the yaw angle  $\psi$ . The relationship between the Euler angle rates and the angular velocity of the glider, with respect to the body frame, can be expressed as:

$$\dot{\boldsymbol{\Omega}}_{EB} = \mathbf{R}_{\Omega B} \boldsymbol{\omega}\quad (4)$$

Transform matrices  $\mathbf{R}_{EB}$  and  $\mathbf{R}_{\Omega B}$  have similar properties to  $\mathbf{R}_{EB}^{-1} = \mathbf{R}_{EB}^T$  and  $\mathbf{R}_{\Omega B}^{-1} = \mathbf{R}_{\Omega B}^T$ . Using the simplified notation  $c = \cos(\cdot)$ ,  $s = \sin(\cdot)$ ,  $t = \tan(\cdot)$ ,  $\mathbf{R}_{EB}$  and  $\mathbf{R}_{\Omega B}$  are expressed in the form given in [24].

$$\begin{aligned}\mathbf{R}_{EB} &= \begin{Bmatrix} c\theta c\psi & s\varphi s\theta c\psi - c\varphi s\psi & c\varphi s\theta c\psi - s\varphi s\psi \\ c\theta s\psi & s\varphi s\theta s\psi - c\varphi c\psi & c\varphi s\theta s\psi - s\varphi c\psi \\ -s\theta & s\varphi c\theta & c\varphi c\theta \end{Bmatrix}, \\ \mathbf{R}_{\Omega B} &= \begin{Bmatrix} 1 & s\varphi t\theta & c\varphi t\theta \\ 0 & c\varphi & -s\varphi \\ 0 & s\varphi/c\theta & c\varphi/c\theta \end{Bmatrix}\end{aligned}\quad (5)$$

## DYNAMICS

The gravity of the glider  $\mathbf{G}$  and the buoyancy of the glider  $\mathbf{B}$  can be expressed as:

$$\begin{aligned}\mathbf{G} &= (m_p + m_h + m_b)g\mathbf{k} \\ \mathbf{B} &= -(m_p + m_h)g\mathbf{k}\end{aligned}\quad (6)$$

where  $\mathbf{k}$  is the unit vector of the  $E$ - $\zeta$  axis. The net weight of the glider system can be described as:

$$\mathbf{W} = \mathbf{G} + \mathbf{B} = m_b g \mathbf{k}\quad (7)$$

$m_b = 0$  when the glider is suspended, therefore the glider would tend to sink when  $m_b$  is greater than zero but rise when  $m_b$  is less than zero.

If  $\mathbf{p}$  represents the translational momentum of the glider system then  $\boldsymbol{\pi}$  represents the angular momentum of the glider system about the inertial frame. According to the momentum theorem, we know that

$$\begin{aligned}\dot{\mathbf{p}} &= \mathbf{G} + \mathbf{B} + \mathbf{f}_{ext} \\ \dot{\boldsymbol{\pi}} &= \mathbf{b}_G \times \mathbf{G} + \mathbf{b} \times \mathbf{B} + \mathbf{b} \times \mathbf{f}_{ext} + \boldsymbol{\tau}_{ext}\end{aligned}\quad (8)$$

where  $\mathbf{b}_G$  is the position vectors of the centre of gravity in the inertial frame.  $\mathbf{f}_{ext}$  and  $\boldsymbol{\tau}_{ext}$  represent the external force and external moment of the glider system in the inertial frame, respectively. In this paper, only viscous hydrodynamic components are expressed as external forces and moments in the momentum equations.

$\mathbf{P}$  and  $\boldsymbol{\Pi}$  are defined as the expression of  $\mathbf{p}$  and  $\boldsymbol{\pi}$  in the body frame, so the transformation equations are:

$$\begin{aligned}\mathbf{p} &= \mathbf{R}_{EB} \mathbf{P} \\ \boldsymbol{\pi} &= \mathbf{R}_{EB} \boldsymbol{\Pi} + \mathbf{b} \times \mathbf{p}\end{aligned}\quad (9)$$

By differentiating Eq. (9) with respect to time, we get the following equations:

$$\begin{aligned}\dot{\mathbf{p}} &= \mathbf{R}_{EB} (\dot{\mathbf{P}} + \hat{\boldsymbol{\omega}} \mathbf{P}) \\ \dot{\boldsymbol{\pi}} &= \mathbf{R}_{EB} (\dot{\boldsymbol{\Pi}} + \hat{\boldsymbol{\omega}} \boldsymbol{\Pi}) + \mathbf{R}_{EB} \mathbf{v} \times \mathbf{p} + \mathbf{b} \times \dot{\mathbf{p}}\end{aligned}\quad (10)$$

Substituting Eq. (8) into Eq. (10) will give

$$\begin{aligned}\dot{\mathbf{P}} &= \mathbf{P} \times \boldsymbol{\omega} + \mathbf{R}_{EB}^T (\mathbf{G} + \mathbf{B}) + \mathbf{F} \\ \dot{\boldsymbol{\Pi}} &= \boldsymbol{\Pi} \times \boldsymbol{\omega} + \mathbf{P} \times \mathbf{v} + \mathbf{r}_G \times \mathbf{R}_{EB}^T \mathbf{G} + \mathbf{T}\end{aligned}\quad (11)$$

where  $\mathbf{r}_G$  is the position vector of the gravity centre in the body frame,  $\mathbf{F} = \mathbf{R}_{EB}^T \mathbf{f}_{ext}$  represents viscous hydrodynamic force in the body frame, and  $\mathbf{T} = \mathbf{R}_{EB}^T \boldsymbol{\tau}_{ext}$  represents viscous hydrodynamic moment in the body frame.

The momentum of the glider system in the body frame can be expressed in the following equations:

$$\begin{Bmatrix} \mathbf{P} \\ \mathbf{\Pi} \end{Bmatrix} = \mathbf{M} \begin{Bmatrix} \mathbf{v} \\ \boldsymbol{\omega} \end{Bmatrix} \quad (12)$$

where  $\mathbf{M}$  is the generalised inertia matrix of the glider system.

To find the equations for  $\mathbf{M}$ , we need to derive the total kinetic energy of the glider-fluid system. The kinetic energy of the movable block is

$$\mathbf{T}_p = \frac{1}{2} \begin{bmatrix} \mathbf{v} \\ \boldsymbol{\omega} \end{bmatrix}^T \begin{bmatrix} m_p \mathbf{I} & -m_p \hat{\mathbf{r}}_p \\ m_p \hat{\mathbf{r}}_p^T \mathbf{R}_x^T(\gamma) \mathbf{I}_p^0 \mathbf{R}_x(\gamma) & -m_p \hat{\mathbf{r}}_p \hat{\mathbf{r}}_p^T \end{bmatrix} \begin{bmatrix} \mathbf{v} \\ \boldsymbol{\omega} \end{bmatrix} \quad (13)$$

$\mathbf{I}$  is the 3×3 identity matrix.  $\mathbf{I}_p^0$  represents the principal inertia matrix of the movable block, computed in the stationary state with  $\gamma = 0$ .  $\mathbf{R}_x(\gamma)$  is a rotation matrix for the inertia matrix of the movable block and its expression is:

$$\mathbf{R}_x(\gamma) = \begin{Bmatrix} 1 & 0 & 0 \\ 0 & \cos \gamma & -\sin \gamma \\ 0 & \sin \gamma & \cos \gamma \end{Bmatrix} \quad (14)$$

The kinetic energy of the net buoyancy and the fixed structure of the glider are

$$\begin{aligned} \mathbf{T}_b &= \frac{1}{2} \begin{bmatrix} \mathbf{v} \\ \boldsymbol{\omega} \end{bmatrix}^T \begin{bmatrix} m_b \mathbf{I} & -m_b \hat{\mathbf{r}}_b \\ m_b \hat{\mathbf{r}}_b^T & -m_b \hat{\mathbf{r}}_b \hat{\mathbf{r}}_b^T \end{bmatrix} \begin{bmatrix} \mathbf{v} \\ \boldsymbol{\omega} \end{bmatrix} \\ \mathbf{T}_h &= \frac{1}{2} \begin{bmatrix} \mathbf{v} \\ \boldsymbol{\omega} \end{bmatrix}^T \begin{bmatrix} m_h \mathbf{I} & -m_h \hat{\mathbf{r}}_h \\ m_h \hat{\mathbf{r}}_h^T & -m_h \hat{\mathbf{r}}_h \hat{\mathbf{r}}_h^T \end{bmatrix} \begin{bmatrix} \mathbf{v} \\ \boldsymbol{\omega} \end{bmatrix} \end{aligned} \quad (15)$$

When the glider accelerates in the flow, the surrounding fluid would be affected and accelerated. The kinetic energy of the fluid is

$$\mathbf{T}_f = \frac{1}{2} \begin{bmatrix} \mathbf{v} \\ \boldsymbol{\omega} \end{bmatrix}^T \begin{bmatrix} \mathbf{M}_f & \mathbf{C}_f \\ \mathbf{C}_f^T & \mathbf{J}_f \end{bmatrix} \begin{bmatrix} \mathbf{v} \\ \boldsymbol{\omega} \end{bmatrix} \quad (16)$$

where,  $\mathbf{M}_f$ ,  $\mathbf{J}_f$  and  $\mathbf{C}_f$  are added mass terms, added inertia terms and added coupling terms, respectively.

The total kinetic energy of the glider-fluid system is then

$$\mathbf{T} = \mathbf{T}_p + \mathbf{T}_b + \mathbf{T}_h + \mathbf{T}_f = \frac{1}{2} \begin{bmatrix} \mathbf{v} \\ \boldsymbol{\omega} \end{bmatrix}^T \mathbf{M} \begin{bmatrix} \mathbf{v} \\ \boldsymbol{\omega} \end{bmatrix} \quad (17)$$

The generalised inertia matrix is

$$\mathbf{M} = \begin{Bmatrix} \mathbf{M}_f + (m_p + m_b + m_h) \mathbf{I} \\ \mathbf{C}_f^T + m_p \hat{\mathbf{r}}_p^T + m_b \hat{\mathbf{r}}_b^T + m_h \hat{\mathbf{r}}_h^T \\ \mathbf{C}_f - m_p \hat{\mathbf{r}}_p - m_b \hat{\mathbf{r}}_b - m_h \hat{\mathbf{r}}_h \\ \mathbf{J}_f + \mathbf{I}_h + \mathbf{R}_x^T(\gamma) \mathbf{I}_p^0 \mathbf{R}_x(\gamma) - m_p \hat{\mathbf{r}}_p \hat{\mathbf{r}}_p^T - m_b \hat{\mathbf{r}}_b \hat{\mathbf{r}}_b^T - m_h \hat{\mathbf{r}}_h \hat{\mathbf{r}}_h^T \end{Bmatrix} \quad (18)$$

Finally, by differentiating Eq. (12) with respect to time, we get the dynamic model to be:

$$\begin{Bmatrix} \dot{\mathbf{v}} \\ \dot{\boldsymbol{\omega}} \end{Bmatrix} = \mathbf{M}^{-1} \left\{ \begin{bmatrix} \dot{\mathbf{P}} \\ \dot{\mathbf{\Pi}} \end{bmatrix} - \dot{\mathbf{M}} \begin{bmatrix} \mathbf{v} \\ \boldsymbol{\omega} \end{bmatrix} \right\} \quad (19)$$

## MODELS AND HYDRODYNAMIC COEFFICIENTS

### MODELS

Six underwater glider models were designed with different wing positions. The standard NACA0012 section was adopted for the wings, and carbon fibre material, with a density of 2000 kg/m<sup>3</sup>, was selected. Some geometric dimensions of gliders are shown in Fig. 3. The distance between the wing root and the nose of the models is listed in Table 2. In addition, as the position of the wing changes, the position of the buoyancy centre also changes. Therefore, the internal structure is adjusted to ensure that the gravity centre of the glider system is directly below the buoyancy centre in the body frame  $O$ -XYZ when the movable block is in its central position. This means that  $r_p$ ,  $r_b$  and  $r_h$  have the same values when the movable block is in its central position in the six models. The distance between the buoyancy centre and the nose of the models is also listed in Table 2. In Model 1 and Model 2, the wings are in front of the buoyancy centre. In Model 3, the leading edge of the wing root is in front of the buoyancy centre, but the trailing edge of the wing root is after the buoyancy centre. In Model 4, Model 5 and Model 6, the wings are behind the buoyancy centre. The parameters of Model 4 are shown in Table 3.

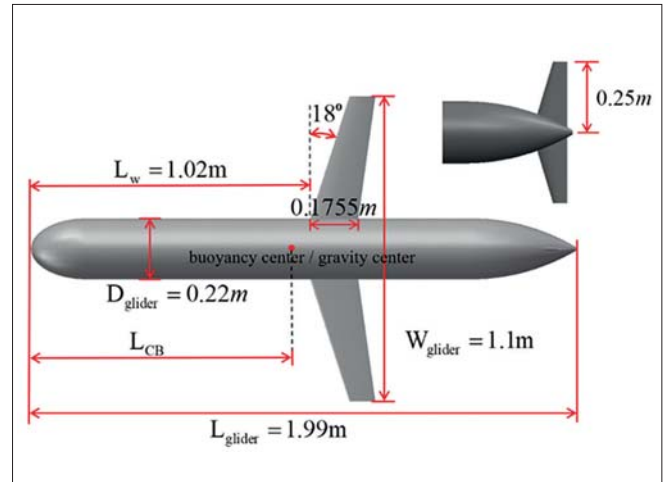


Fig. 3. Some geometric dimensions of gliders (the wing position of Model 4)

Tab. 2. Wing position in glider models

Models	Models 1	Models 2	Models 3	Models 4	Models 5	Models 6
$L_w$ (m)	0.42	0.62	0.82	1.02	1.22	1.42
$L_{CB}$ (m)	0.942	0.946	0.950	0.954	0.958	0.962

Tab. 3. Parameters of Model 4

Fixed structure mass $m_h$	58.92 kg
Position of the fixed structure $r_h$	[-0.075 0 0.0033] m
Inertia of the fixed structure $I_h$	diag ([0.59 15.14 15.4]) kg · m <sup>2</sup>
Movable block mass $m_p$	11 kg
Position of the movable block $r_p$	$R_p = 0.014\text{m}; 0.3516 \text{ m} < r_{p_x} < 0.4516 \text{ m}$ $-90 \text{ deg} < \gamma < 90 \text{ deg}$
Inertia of the movable block $I_p^0$	diag ([0.02 1.82 1.82]) kg · m <sup>2</sup>
Net buoyancy mass $m_b$	$-0.5 \text{ kg} < m_b < 0.5 \text{ kg}$
Position of the net buoyancy $r_b$	[0 0 0] m
Displaced fluid mass $m$	59.92 kg

### ADDED MASS, ADDED INERTIA, AND COUPLING TERMS

In this paper, inertial hydrodynamic components are expressed by the added mass, added inertia, and coupling terms [25]. Since the glider has two symmetry planes (O–XY and O–XZ), the added mass  $M_f$  and added inertia matrix  $J_f$  are approximately diagonal and have the form:

$$M_f = \begin{bmatrix} X_{\dot{u}} & 0 & 0 \\ 0 & Y_{\dot{v}} & 0 \\ 0 & 0 & Z_{\dot{w}} \end{bmatrix}, J_f = \begin{bmatrix} K_{\dot{\beta}} & 0 & 0 \\ 0 & M_{\dot{q}} & 0 \\ 0 & 0 & N_{\dot{r}} \end{bmatrix} \quad (20)$$

$X_{\dot{u}}$ ,  $Y_{\dot{v}}$  and  $Z_{\dot{w}}$  are the acceleration fluid mass terms generated from the force along the O–X, O–Y and O–Z axes, respectively.  $K_{\dot{\beta}}$ ,  $M_{\dot{q}}$  and  $N_{\dot{r}}$  are the acceleration fluid inertia terms generated from the moments around the O–X, O–Y and O–Z axes, respectively.

Because of the symmetry of the glider, the coupling term  $C_f$  has the form:

$$C_f = \begin{bmatrix} 0 & 0 & 0 \\ 0 & 0 & M_{\dot{w}} \\ 0 & N_{\dot{v}} & 0 \end{bmatrix} \quad (21)$$

where  $M_{\dot{w}}$  is the pitch moment with respect to the acceleration in the O–Z axis and  $N_{\dot{v}}$  is the yaw moment with respect to the acceleration in the O–Y axis.

The added hydrodynamic terms for each model are computed by potential flow theory and the results are shown

Tab. 4. Added hydrodynamic terms

	$M_f$ (kg)			$J_f$ (kg · m <sup>2</sup> )			$C_f$ (kg · m)	
	$X_{\dot{u}}$	$Y_{\dot{v}}$	$Z_{\dot{w}}$	$K_{\dot{\beta}}$	$M_{\dot{q}}$	$N_{\dot{r}}$	$N_{\dot{v}}$	$M_{\dot{w}}$
Model 1	2.92	69.95	87.38	1.29	18.43	18.63	-4.76	-7.31
Model 2	2.91	69.90	87.51	1.29	16.10	18.69	-4.34	-3.69
Model 3	2.90	69.91	87.66	1.29	15.29	18.70	-3.95	0.10
Model 4	2.90	69.91	87.57	1.29	16.01	18.66	-3.55	3.89
Model 5	2.91	69.93	87.43	1.29	18.27	18.57	-3.15	7.58
Model 6	2.93	69.95	86.79	1.29	21.82	18.43	-2.73	10.90

in Table. 4 [26]. The results show that the added mass of the six models are similar. The wing position mainly affects the moment around the O–Y axis and its related parameters, such as  $M_{\dot{q}}$  and  $M_{\dot{w}}$ .

### VISCOUS HYDRODYNAMIC COEFFICIENTS

In the flow frame, the components of the hydrodynamic force  $F_h = [-D \ SF \ -L]^T$  and the hydrodynamic moment  $T_h = [T_{DL1} \ T_{DL2} \ T_{DL3}]^T$  are usually modelled as [22]:

$$\begin{aligned} D &= (K_{D0} + K_D \alpha^2) V^2 \\ SF &= K_{\beta} \beta V^2 \\ L &= (K_{L0} + K_L \alpha) V^2 \\ T_{DL1} &= (K_{MR} \beta + K_p p) V^2 \\ T_{DL2} &= (K_{M0} + K_M \alpha + K_q q) V^2 \\ T_{DL3} &= (K_{MY} \beta + K_r r) V^2 \end{aligned} \quad (22)$$

The rotation matrix is then used to map the hydrodynamic force and moment from the flow frame to the body frame:

$$\begin{aligned} F &= R_{BC} F_h \\ T &= R_{BC} T_h \end{aligned} \quad (23)$$

$R_{BC}$  is expressed in the form:

$$R_{BC} = \begin{bmatrix} c\alpha c\beta & -c\alpha s\beta & -s\alpha \\ s\beta & c\beta & 0 \\ s\alpha c\beta & -s\alpha s\beta & c\alpha \end{bmatrix} \quad (24)$$

The commercial CFD software STAR-CCM+ is based on the incompressible Reynolds Averaged Navier Stokes equation and is used to compute the hydrodynamic force and moment in this paper. Because no experimental data of NACA0012 are found, the published experimental results of Zarruk [27] are taken as an example to verify the accuracy of the CFD calculation. The standard NACA0009 aerofoil used in this experiment has a chord length of 0.12 m at the root, 0.06 m at the tip and 0.30 m at the wingspan. As shown in Fig. 4, the lift

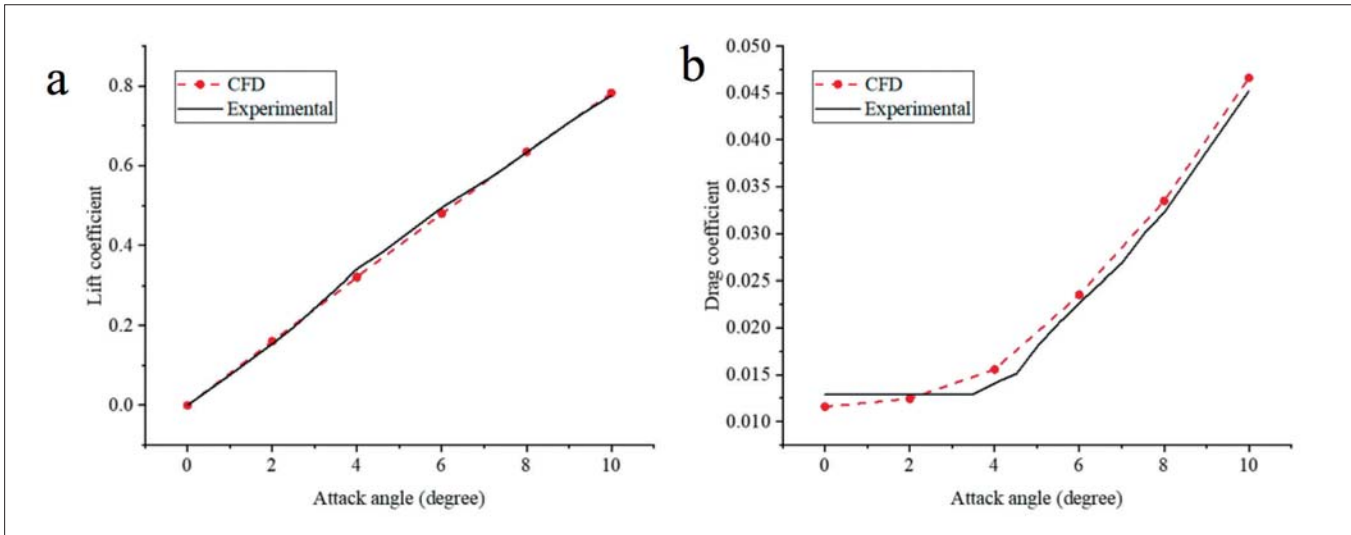


Fig. 4. Comparison of experimental and CFD results. (a) Lift coefficient. (b) Drag coefficient

coefficient and drag coefficient calculated by CFD show good agreement with the experimental results.

As shown in Fig. 5, only half of the domain is meshed as the body is axisymmetric. In this paper, the inlet position is 1.5 times  $L_{\text{glider}}$  away from the glider and the outlet is 3.5 times  $L_{\text{glider}}$  away from the glider. The top, bottom and side boundaries are 9 times  $D_{\text{glider}}$  away from the glider and the assigned velocity inlet condition. The SST (Menter)  $k-\omega$  turbulence model is selected to simulate the surrounding flow with a grid point for the first cell at  $y^+ < 1$  [28]. Based on the grid independence study shown in Fig. 6, the number of the mesh is set to 3.3 million.

The results of the viscous hydrodynamic forces of six models are shown in Fig. 7. Only the positive attack angle is calculated because of the symmetry of the models. The results show that the lift forces, drag forces and lift-drag ratios of the six models are similar but the pitch moments are quite different, which is consistent with the previous conclusions [9]. This may be because the wing-hull interaction is similar at small attack angles, so they have similar lift and drag. However, the arm force is quite different, so the pitch moment is also quite

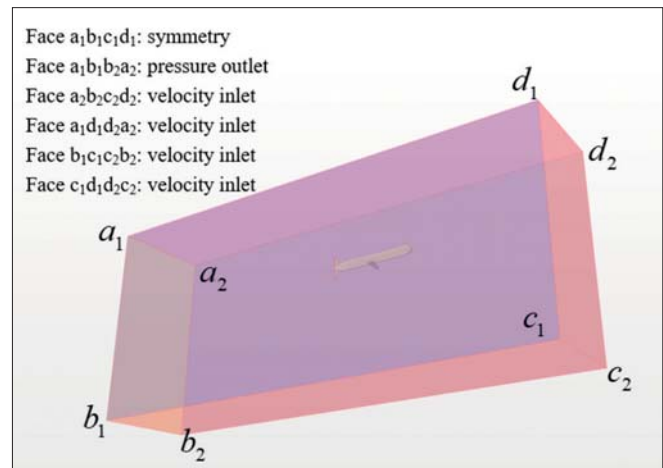


Fig. 5. Domain and boundary conditions

different. Furthermore, the difference of wing position leads to the opposite direction of pitching moment. This will further impression the performance of the underwater glider in motion,

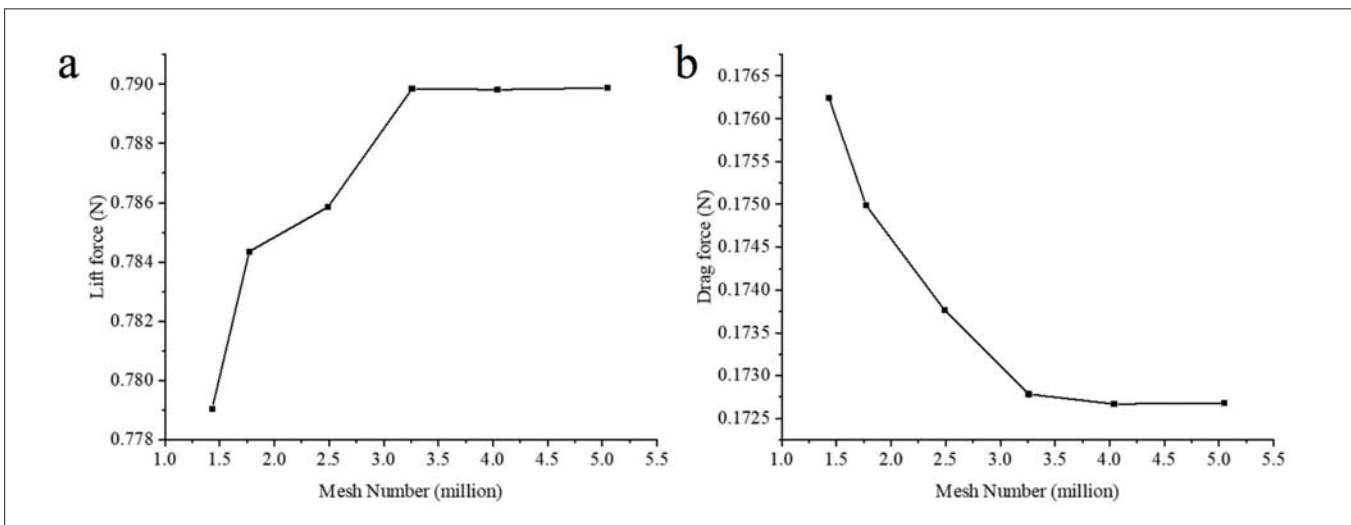


Fig. 6. Grid independency study. (a) Lift force. (b) Drag force

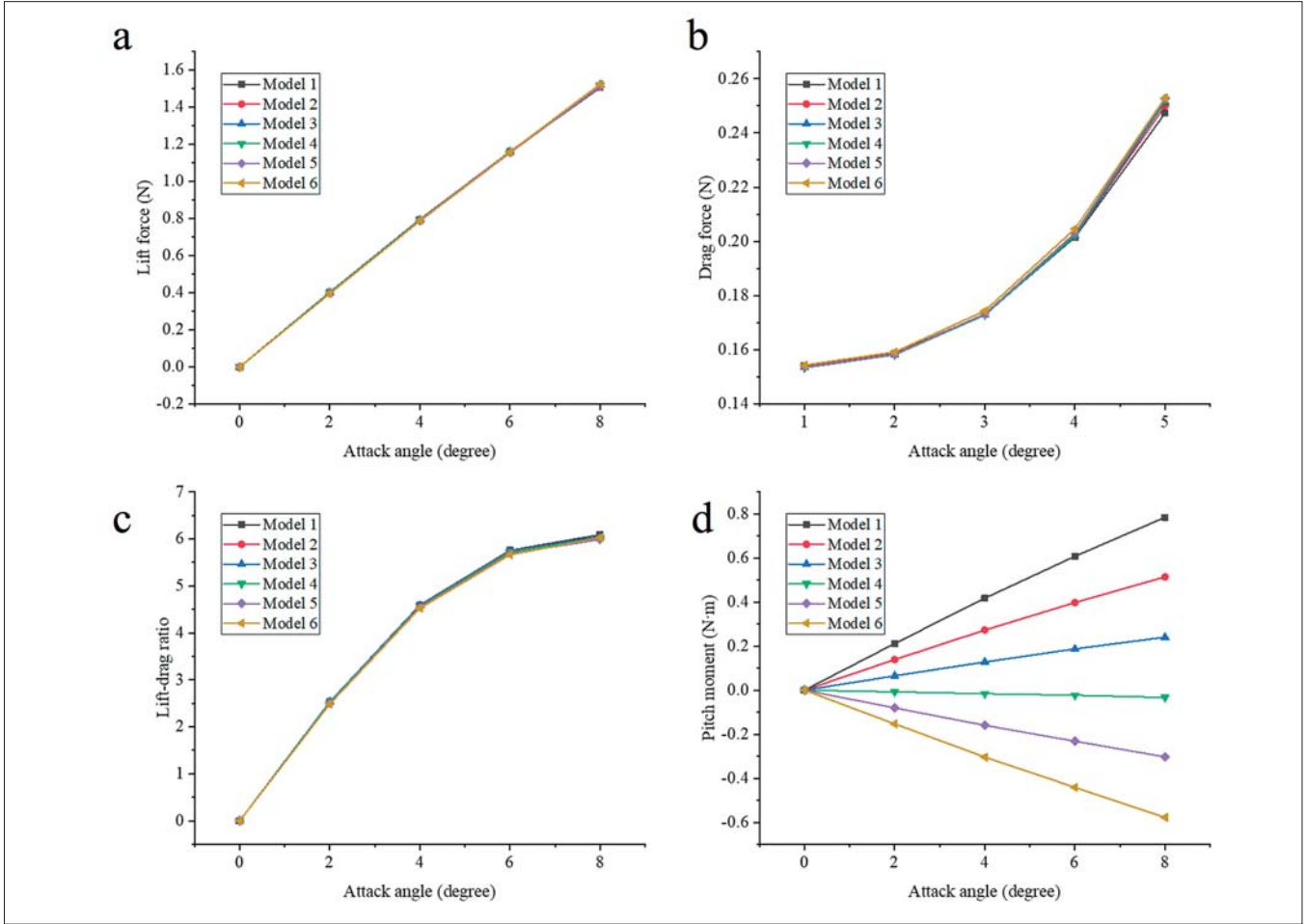


Fig. 7. Variation of hydrodynamic forces with attack angle. (a) Lift force. (b) Drag force. (c) Lift-drag ratio. (d) Pitch moment

By entering the results into Eq. (22), we get the viscous hydrodynamic coefficients of the models, as shown in Table 5. They have similar lift coefficients and drag coefficients but quite different pitch moment coefficients.

## MOTION SIMULATION AND DISCUSSION

### VALIDATION OF THE MOTION SIMULATION

In this paper, the published results in [22] are compared to validate the results of motion simulation. All the parameters needed for motion simulation are listed in Table 6. And in

the motion simulation, the influence of dynamic pressure on buoyancy centre and the change of gravity centre caused by the change of  $m_b$  are ignored. Because the offset is very small, it almost does not affect the results.

When the control parameters  $[m_b, r_{px}, \gamma]$  are set as  $[0.3 \text{ kg}, 0.4216 \text{ m}, 45^\circ]$ , the downward spiral motion is simulated based on the dynamic model in this paper and shown in Fig. 8. When the control parameters  $[m_b, r_{px}]$  are set as  $[0.3 \text{ kg}, 0.4216 \text{ m}]$  and  $\gamma$  varies from  $30^\circ$  to  $60^\circ$ , the change of glider turning radius with the moveable block position and the comparison with the results in [22] are shown in Fig. 9. There is little difference due to the introduction of some simplifications in [22]. In general, the dynamic model in this paper is proved to be reasonable and feasible.

Tab. 5. The viscous hydrodynamic coefficients

	$K_{D0}$ (kg/m)	$K_D$ (kg/m/rad)	$K_{L0}$ (kg/m)	$K_L$ (kg/m/rad)	$K_{M0}$ (kg/m)	$K_M$ (kg/rad)
Model 1	4.85	153.65	0	351.17	0	183.44
Model 2	4.82	159.39	0	351.78	0	120.21
Model 3	4.80	161.55	0	352.85	0	56.41
Model 4	4.80	163.15	0	352.27	0	-7.36
Model 5	4.81	164.57	0	350.89	0	-70.53
Model 6	4.84	163.94	0	352.76	0	-134.21

Tab. 6. Parameters of Seawing in [22]

Fixed structure mass $m_h$	54.28 kg
Position of the fixed structure $r_h$	$[-0.0814 \ 0 \ 0.0032]$ m
Inertia of the fixed structure $I_h$	diag $([0.60 \ 15.27 \ 15.32])$ kg · m <sup>2</sup>
Movable block mass $m_p$	11 kg
Position of the movable block $r_p$	$R_p = 0.014$ m; $0.3516$ m < $r_{px}$ < $0.4516$ m -90 deg < $\gamma$ < 90 deg
Inertia of the movable block $I_p^0$	diag $([0.02 \ 10.16 \ 0.17])$ kg · m <sup>2</sup>
Net buoyancy mass $m_b$	-0.5 kg < $m_b$ < 0.5 kg
Position of the net buoyancy $r_b$	$[0 \ 0 \ 0]$ m
Added mass $M_f$	diag $([1.48 \ 49.58 \ 65.92])$ kg
Added inertia matrix $J_f$	diag $([0.53 \ 7.88 \ 10.18])$ kg · m <sup>2</sup>
Added coupling terms $C_f$	$N_v = 2.57$ kg · m, $M_w = 3.61$ kg · m
Coefficients of drag force $D$	$K_{D0} = 7.19$ kg/m, $K_D = 386.29$ kg/m/rad <sup>2</sup>
Coefficients of side force $SF$	$K_p = -115.65$ kg/m/rad
Coefficients of lift force $L$	$K_{L0} = -0.36$ kg/m, $K_L = 440.99$ kg/m/rad
Coefficients of $T_{DL1}$	$K_{MR} = -58.27$ kg/rad, $K_M = -19.83$ kg · s/rad
Coefficients of $T_{DL2}$	$K_{M0} = 0.28$ kg, $K_M = -65.84$ kg/rad, $K_q = -205.64$ kg · s/rad <sup>2</sup>
Coefficients of $T_{DL3}$	$K_{MY} = 34.10$ kg/rad, $K_r = -389.30$ kg · s/rad <sup>2</sup>

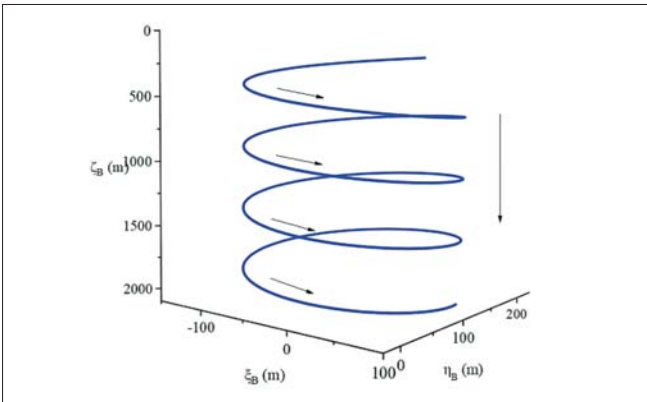


Fig. 8. Downward spiral motion

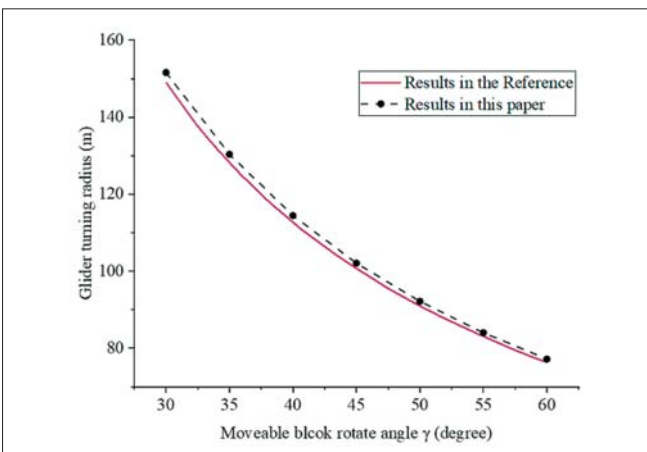


Fig. 9. Validation of the motion simulation

## MOTION OF STEADY GLIDING

In this section, the influence of the wing position on the motion of steady gliding is studied. Gliding speed and gliding angle were calculated with different positions of the movable block. The net buoyancy  $m_b$  is set to 0.5 kg during the descent process and -0.5 kg during the ascent process. The movable block is limited to only moving along the  $O-X$  axis and not rotating around the  $O-X$  axis, which means that  $\gamma$  is equal to zero. Because of the calculation of viscous hydrodynamic forces, only the data with an attack angle between -8 degrees and 8 degrees are retained. The simulation results are shown in Fig. 10.

The results show that, for a given net buoyancy, gliders with different wing position have the same gliding velocity and the same attack angle at the same gliding angle. Model 1, which has the minimum wing position parameter  $L_w$ , needed to move the movable block further to get the same gliding angle as the other models. This is because, at the same gliding angle, Model 1 has a larger overturning moment due to the forward position of the wing. As a result, it needs to move the movable block further to balance the pitch moment during equilibrium gliding. Model 6, which has the maximum wing position parameter  $L_w$ , can achieve the greatest gliding angle with the greatest gliding speed. When the movable block moves in the same range, the model with wings in the rear can realise a larger gliding angle than the model with wings in the front. Therefore, the range of glider motion attitude can be increased by moving the wing position backward, especially when the movable block has limited room to move. In addition, it should be noted that Model 6 needs to move the movable block back to have a smaller gliding angle during its dive.

## MOTION AFTER RECEIVING A SMALL DISTURBANCE

Vehicle geometry affects stability as well as performance. Fan [29] studied the effect of the wing position on stability by frequency analysis. In this paper, the influence of wing position on the longitudinal stability of an underwater glider is studied as a time-domain response. In this way, it can intuitively show the motion state of an underwater glider after receiving disturbance.

Previous analysis shows that three models can show the effect of wing position on the dynamic motion characteristics of an underwater glider. Therefore, in this section, Model 2, Model 4 and Model 6 are selected to study the influence of wing position on the motion of an underwater glider after receiving a small disturbance. In Model 2, the wings are in front of the buoyancy centre. In Model 4 and Model 6, the wings are behind the buoyancy centre. It is assumed that the underwater glider receives a small environmental disturbance during steady gliding. In the motion simulation analysis, the small disturbance is reflected by the suddenly changed attitude angle. To simulate the change process of attitude angle, the rotational hydrodynamic coefficient  $K_q$  in the vertical plane is calculated by the method described in [22]. The results are shown in Table 7.

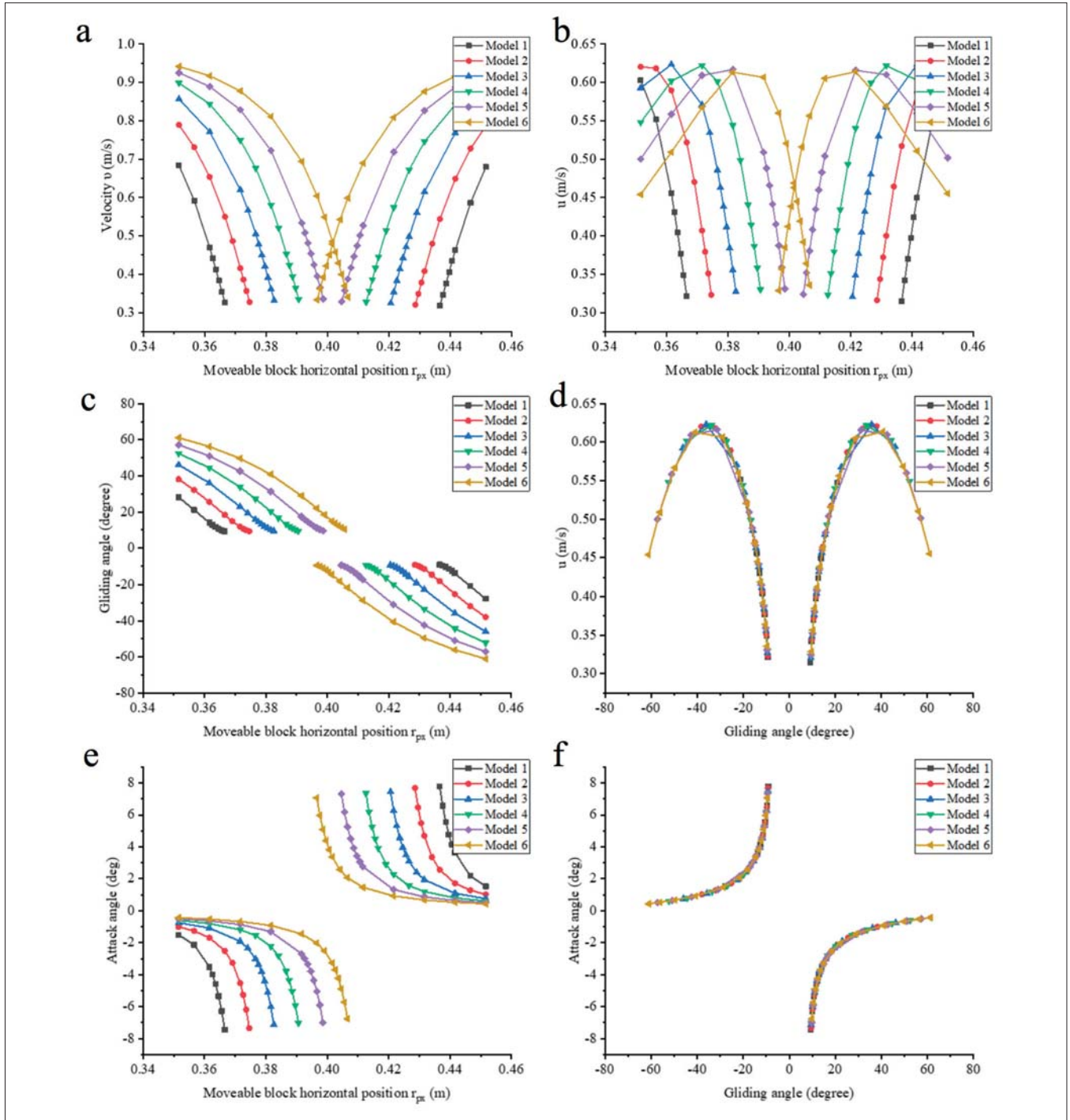


Fig. 10. Motion simulation results. (a) Velocity  $v$  vs  $r_{px}$ . (b) Horizontal velocity  $u$  vs  $r_{px}$ . (c) Gliding angle vs  $r_{px}$ . (d) Relationship between horizontal velocity  $u$  and gliding angle. (e) Attack angle vs  $r_{px}$ . (f) Relationship between attack angle and gliding angle

Tab. 7. Rotational hydrodynamic coefficient  $K_q$

	Model 2	Model 4	Model 6
$K_q$ (kg · s/rad <sup>2</sup> )	-220.02	-49.92	-250.88

The initial state of the motion simulation is set as steady gliding at a gliding angle of about  $-35^\circ$ . At the 5th second, the underwater glider receives environmental disturbance and produces a deflection angle of  $-5^\circ$ . As a result, the gliding angle

of the underwater glider changes to  $-40^\circ$ . The net buoyancy is set as 0.5 kg and the moveable block remains constant throughout the simulation. The results are shown in Fig. 11.

The results show that all three models can return to the initial state, whether the wing is in front of or behind the buoyancy centre. Model 4 has a larger angular velocity and can recover to the equilibrium state faster but it oscillates slightly, around the steady state. Model 2 and Model 6 have smaller angular velocities and take longer to recover to their initial

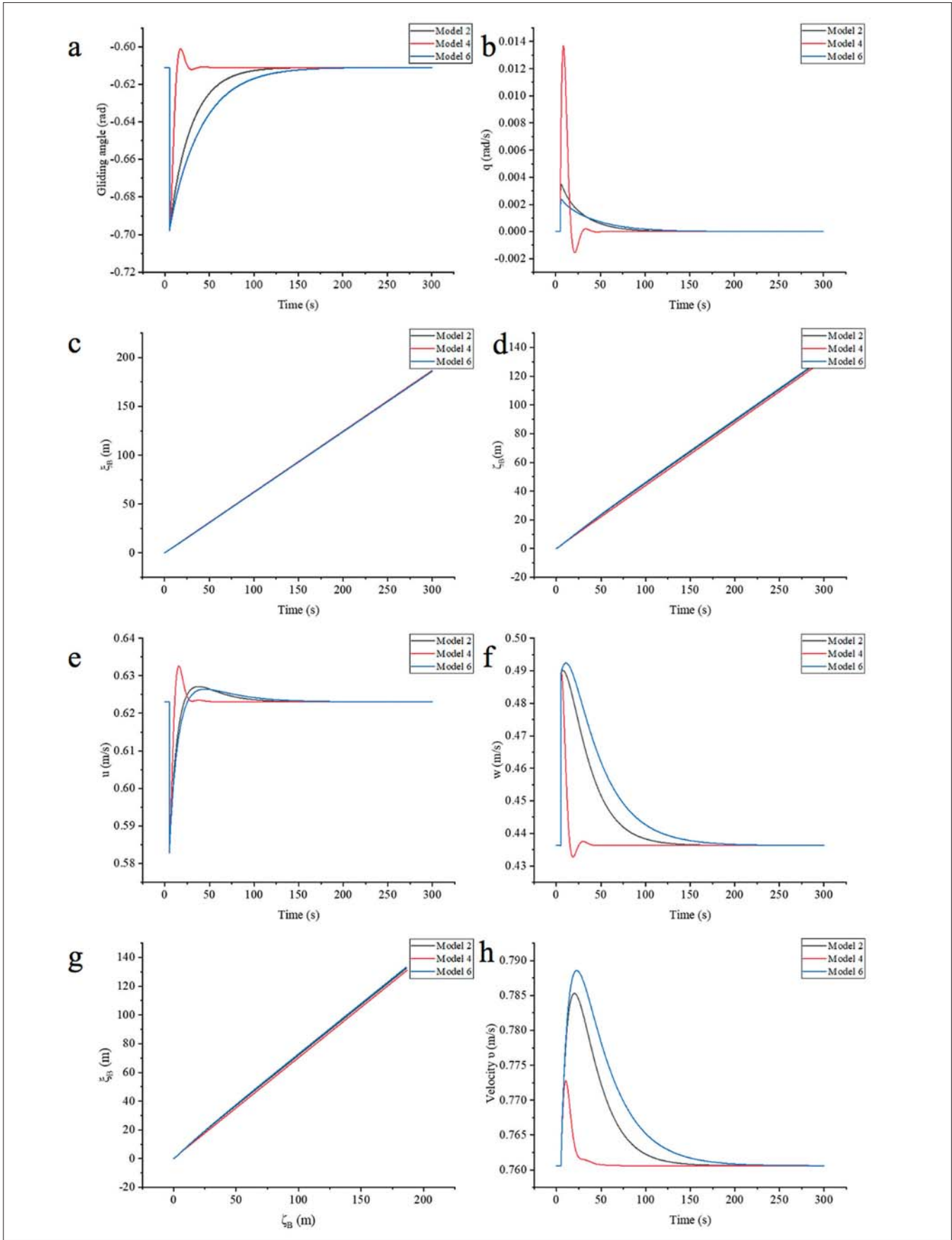


Fig. 11. Motion states of the glider after disturbance. (a) Gliding angle vs Time. (b) Angle velocity  $q$  vs Time. (c) Horizontal position  $\xi_B$  vs Time. (d) Vertical position  $\zeta_B$  vs Time. (e) Horizontal velocity  $u$  vs Time. (f) Vertical velocity  $w$  vs Time. (g) Simulated trajectory. (h) Velocity  $v$  vs Time

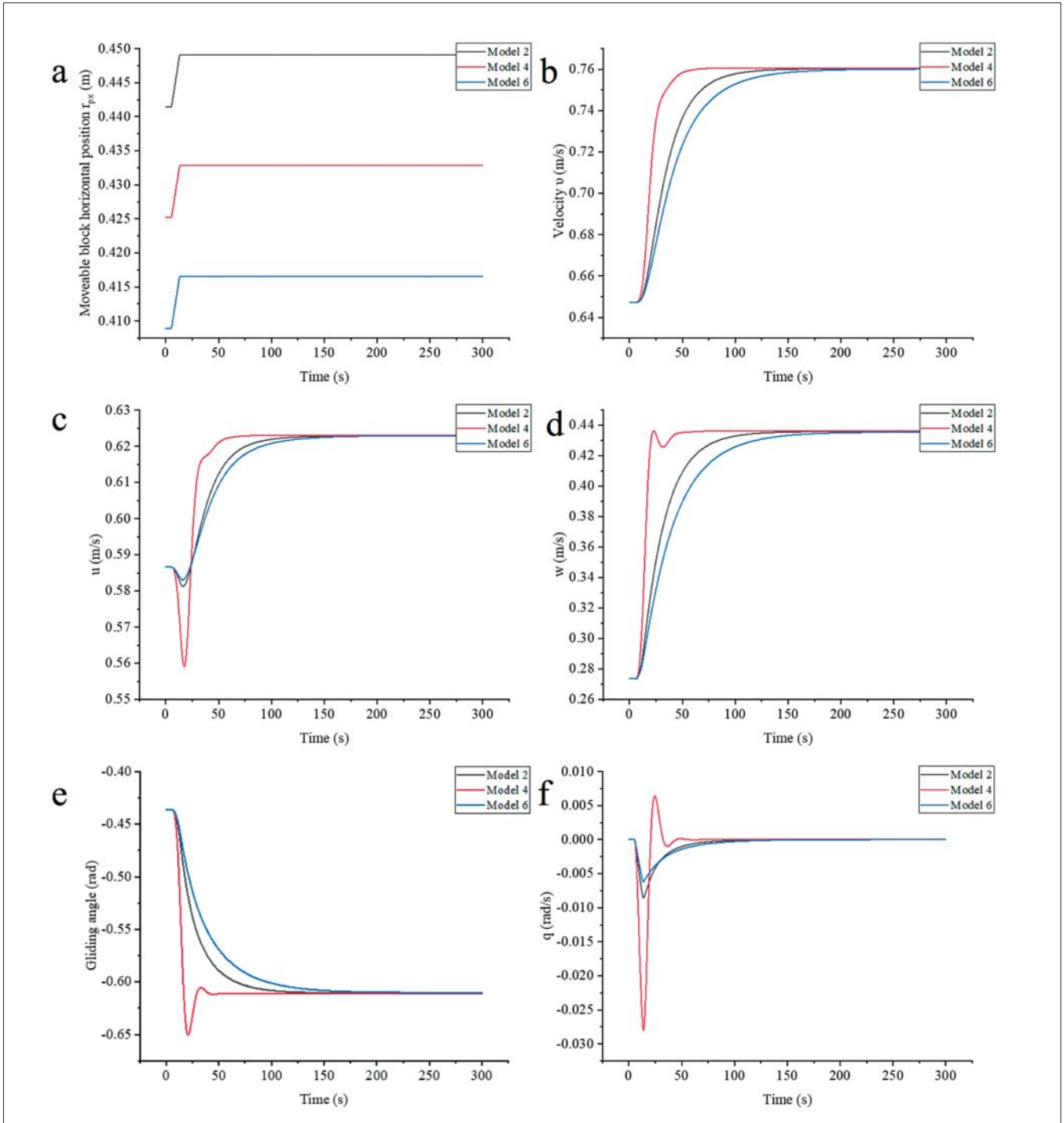


Fig. 12. Motion states of the glider after adjusting gliding angle. (a) Moveable block horizontal position  $r_{px}$  vs Time. (b) Velocity  $v$  vs Time. (c) Horizontal velocity  $u$  vs Time. (d) Vertical velocity  $w$  vs Time. (e) Gliding angle vs Time. (f) Angle velocity  $q$  vs Time

state. The reason for this difference is that the wings of Model 2 and Model 6 are far away from the buoyancy centre, which makes Model 2 and Model 6 have greater pitch moments in the process of rotation. Because Model 4 returns to the initial state faster, its trajectory deviation is smaller. In addition, the velocity of Model 6 changes the most and horizontal velocity approaches the stable value faster than vertical velocity. This means that if we want the glider to have a smaller trajectory offset after being disturbed, the wings should be installed near

the buoyancy centre. If we want the glider to have a more stable attitude after being disturbed, we should install the wing away from the buoyancy centre.

#### MOTION AFTER ADJUSTING GLIDING ANGLE

In this section, Model 2, Model 4 and Model 6 are selected to study the influence of wing position on the motion after adjusting the gliding angle of an underwater glider. The initial

state of the motion simulation is set as the steady gliding of the underwater glider at a gliding angle of  $-25^\circ$ . At the 5th second, the moveable block is moved to adjust the gliding angle. The target gliding angle is  $-35^\circ$ . The net buoyancy is set as 0.5 kg throughout the simulation. The change in the position of the movable block with time and the simulation results are shown in Fig. 12.

The results show that all three models need to move the moveable block the same distance to produce the same change of gliding angle. Model 4 has a larger angular velocity and can recover to its equilibrium state faster. The change of the gliding angle of Model 6 is more stable and it hardly vibrates near the target angle. This means that if we want the glider to respond faster to attitude adjustment, the wings should be installed near the buoyancy centre. If we want to have a higher stability, we should install the wing away from the buoyancy centre.

## CONCLUSIONS

In this paper, the effect of wing position on the dynamic motion characteristics of an underwater glider is analysed by motion simulation. These results could be helpful when choosing wing position, according to different performance requirements, when designing an underwater glider. By studying the motion of steady gliding, the motion after receiving a small disturbance, and the motion after adjusting the gliding angle of underwater gliders with different wing positions, we arrive at the following conclusions:

1. The wing position of the underwater glider has a great influence on the gliding angle but does not affect the relationship between gliding angle and gliding speed. The range of the gliding angle of the glider can be increased by moving the wing position backward when the adjustment ability of the movable block is limited.
  2. The closer the wing position is to the buoyancy centre, the faster it can recover to its previous state after receiving a disturbance, and the smaller the trajectory deviation is.
  3. The farther the wing position is from the buoyancy centre, the slower the state of change of the underwater glider. This can reduce drastic changes in underwater glider attitude.
- The results presented here are based on numerical studies and should be validated by prototype experiments in the laboratory and the field.

## ACKNOWLEDGEMENTS

This work was supported by the Natural Science Foundation of Liaoning Province in 2020 (Grant No. 2020-MS-125); the State Key Laboratory of Ocean Engineering, Shanghai Jiao Tong University (Grant No. 1904); the Fundamental Research Funds for the Central Universities (Grant No. 3132021120); and the National Key Research and Development Program of China (Grant No. 2016YFC0301500).

## REFERENCES

1. H. Stommel, "The Slocum Mission", *Oceanography*. 1989. Vol. 2(1), 22-25, doi: 10.5670/oceanog.1989.26.
2. D.C. Webb, P.J. Simonetti, and C.P. Jones, "SLOCUM: An underwater glider propelled by environmental energy", *IEEE Journal of Oceanic Engineering*. 2001. Vol. 26(4), 447-452, doi: 10.1109/48.972077.
3. J. Sherman, R.E. Davis, W.B. Owens, et al., "The autonomous underwater glider "spray"", *IEEE Journal of Oceanic Engineering*. 2001. Vol. 26(4), 437-446, doi: 10.1109/48.972076.
4. C.C. Eriksen, T.J. Osse, R.D. Light, et al., "Seaglider: A long-range autonomous underwater vehicle for oceanographic research", *IEEE Journal of Oceanic Engineering*. 2001. Vol. 26(4), 424-436, doi: 10.1109/48.972073.
5. S. Wang, X. Sun, Y. Wang, et al., "Dynamic Modeling and Motion Simulation for A Winged Hybrid-Driven Underwater Glider", *China Ocean Engineering*. 2011. Vol. 25(1), 97-112, doi: 10.1007/s13344-011-0008-7.
6. J. Yu, A. Zhang, W. Jin, et al., "Development and experiments of the Sea-Wing underwater glider", *China Ocean Engineering*. 2011. Vol. 25(4), 721-736, doi: 10.1007/s13344-011-0058-x.
7. D.L. Rudnick, R.E. Davis, C.C. Eriksen, et al., "Underwater Gliders for Ocean Research", *Marine Technology Society Journal*. 2004. Vol. 38(2), 73-84, doi: 10.4031/002533204787522703.
8. R.V.S. Shankar and R. Vijayakumar, "Numerical Study of the Effect of Wing Position on Autonomous Underwater Glider", *Defence Science Journal*. 2020. Vol. 70(2), 214-220, doi: 10.14429/dsj.70.14742.
9. M.Y. Javaid, M. Ovinis, F.B.M. Hashim, et al., "Effect of wing form on the hydrodynamic characteristics and dynamic stability of an underwater glider", *International Journal of Naval Architecture and Ocean Engineering*. 2017. Vol. 9(4), 382-389, doi: 10.1016/j.ijnaoe.2016.09.010.
10. M.Y. Javaid, M. Ovinis, N. Thirumalaiswamy, et al., "Dynamic Motion Analysis of a Newly Developed Autonomous Underwater Glider with Rectangular and Tapered Wing", *Indian Journal of Geo-Marine Sciences*. 2015. Vol. 44(12), 1928-1936.
11. F. Zhang, J. Thon, C. Thon, et al., "Miniature Underwater Glider: Design and Experimental Results", *IEEE-Asme Transactions on Mechatronics*. 2014. Vol. 19(1), 394-399, doi: 10.1109/tmech.2013.2279033.

12. F. Liu, Y. Wang, W. Niu, et al., "Hydrodynamic Performance Analysis and Experiments of A Hybrid Underwater Glider with Different Layout of Wings". OCEANS 2014 - TAIPEI, 2014, doi: 10.1109/OCEANS-TAIPEI.2014.6964512.
13. S. Fan and C. Woolsey, "Elements of Underwater Glider Performance and Stability", Marine Technology Society Journal. 2013. Vol. 47(3), 81-98, doi: 10.4031/mts.j.47.3.4.
14. J.G. Graver and N.E. Leonard, "Underwater glider dynamics and control". 12th international symposium on unmanned untethered submersible technology, 2001.
15. P. Bhatta and N.E. Leonard, "Stabilization and coordination of underwater gliders". Proceedings of the 41st IEEE Conference on Decision and Control, 2002, 2002, doi: 10.1109/CDC.2002.1184836.
16. N.E. Leonard and J.G. Graver, "Model-based feedback control of autonomous underwater gliders", IEEE Journal of Oceanic Engineering. 2001. Vol. 26(4), 633-645, doi: 10.1109/48.972106.
17. P. Bhatta and N.E. Leonard, "Nonlinear gliding stability and control for vehicles with hydrodynamic forcing", Automatica. 2008. Vol. 44(5), 1240-1250, doi: 10.1016/j.automatica.2007.10.006.
18. K. Isa and M. Rizal Arshad, "Motion simulation for propeller-driven USM underwater glider with controllable wings and rudder". 2011 2nd International Conference on Instrumentation Control and Automation, 2011.
19. K. Isa and M.R. Arshad, "Dynamic modeling and characteristics estimation for USM underwater glider". 2011 IEEE Control and System Graduate Research Colloquium, 2011, doi: 10.1109/ICSGRC.2011.5991821.
20. M.M. Noh, M.R. Arshad, and R.M. Mokhtar, "Modeling of USM underwater glider (USMUG)". International Conference on Electrical, Control and Computer Engineering 2011 (InECCE), 2011.
21. S. Fan and C.A. Woolsey, "Dynamics of underwater gliders in currents", Ocean Engineering. 2014. Vol. 84(JUL.1), 249-258, doi: 10.1016/j.oceaneng.2014.03.024.
22. S. Zhang, J. Yu, A. Zhang, et al., "Spiraling motion of underwater gliders: Modeling, analysis, and experimental results", Ocean Engineering. 2013. Vol. 60, 1-13, doi: 10.1016/j.oceaneng.2012.12.023.
23. H. Zhou, T. Wang, L. Sun, et al., "Disc-type Underwater Glider Modeling and Analysis for Omnidirectional and Steering Motion Characteristics", International Journal of Control Automation and Systems. 2020. Vol. 19(1), 532-547, doi: 10.1007/s12555-019-0432-7.
24. J.G. Graver, "Underwater gliders: dynamics, control and design". Princeton University, 2005.
25. P. Yu, Y. Zhao, T. Wang, et al., "Steady-state Spiral Motion Simulation and Turning Speed Analysis of an Underwater Glider". 2017 4th International Conference on Information, Cybernetics and Computational Social Systems (ICCSS), 2017, doi: 10.1109/ICCSS.2017.8091442.
26. C.W. Chen and N.M. Yan, "Prediction of Added Mass for an Autonomous Underwater Vehicle Moving Near Sea Bottom Using Panel Method". 2017 4th International Conference on Information Science and Control Engineering (ICISCE), 2017.
27. G.A. Zarruk, P.A. Brandner, B.W. Pearce, et al., "Experimental study of the steady fluid-structure interaction of flexible hydrofoils", Journal of Fluids and Structures. 2014. Vol. 51, 326-343, doi: 10.1016/j.jfluidstructs.2014.09.009.
28. Y. Singh, S.K. Bhattacharyya, and V.G. Idichandy, "CFD approach to modelling, hydrodynamic analysis and motion characteristics of a laboratory underwater glider with experimental results", Journal of Ocean Engineering and Science. 2017. Vol. 2(2), 90-119, doi: 10.1016/j.joes.2017.03.003.
29. S. Fan, A. Wolek, and C.A. Woolsey, "Stability and performance of underwater gliders". 2012 Oceans, 2012, doi: 10.1109/OCEANS.2012.6404993.

## CONTACT WITH THE AUTHORS

**Xiangcheng Wu**

*e-mail: wuxiangcheng@dlmu.edu.cn*

Dalian Maritime University  
No.1 Ganjingzi District  
0086 116026 Dalian  
**CHINA**

**Pengyao Yu**

*e-mail: yupengyao@dlmu.edu.cn*

Dalian Maritime University  
No.1 Ganjingzi District  
0086 116026 Dalian  
**CHINA**

**Guangzhao Li**

*e-mail: liguangzhao@dlmu.edu.cn*

Dalian Maritime University  
No.1 Ganjingzi District  
0086 116026 Dalian  
**CHINA**

**Fengkun Li**

*e-mail: fengkun\_li@dlmu.edu.cn*

Dalian Maritime University  
No.1 Ganjingzi District  
0086 116026 Dalian  
**CHINA**

# CONTROL OF UNMANNED SURFACE VEHICLE ALONG THE DESIRED TRAJECTORY USING IMPROVED LINE OF SIGHT AND ESTIMATED SIDESLIP ANGLE

Ligang Li <sup>1</sup>

Zhiyuan Pei\*<sup>1</sup>

Jiucui Jin <sup>2</sup>

Yongshou Dai <sup>1</sup>

<sup>1</sup> China University of Petroleum, Qingdao, China

<sup>2</sup> First Institute of Oceanography, Ministry of Natural Resources, Qingdao, China

\* Corresponding author: 577232138@qq.com (Z. Pei)

## ABSTRACT

*In order to improve the accuracy and robustness of path following control for an Unmanned Surface Vehicle (USV) suffering from unknown and complex disturbances, a variable speed curve path following a control method based on an extended state observer was proposed. Firstly, the effect of the environmental disturbances on the USV is equivalent to an unknown and time-varying sideslip angle, and the sideslip angle is estimated by using the extended state observer (ESO) and compensated in the Line of Sight (LOS) guidance law. Secondly, based on the traditional LOS guidance law, the design of the surge velocity guidance law is added to enable the USV to self-adjust the surge velocity according to the curvature of the curve path, thus further improving the tracking accuracy. Finally, the heading and speed controller of the USV is designed by using a sliding mode control to track the desired heading and speed accurately, and then the path following control of the USV's curve path is realised. Simulation results verify the effectiveness of the proposed method.*

**Keywords:** USV; curve path following control; surge velocity guidance law; extended state observer; sliding mode control

## INTRODUCTION

Unmanned Surface Vehicles (USV), as unmanned intelligent marine platforms, can undertake long-term, large-scale and low-cost marine scientific research and engineering tasks in the ocean, and have a broad application prospect. However, in the course of path following, a USV is bound to be affected by wind, waves, currents and other environmental factors. After the environmental disturbance acts on the USV, it will generate sway velocity, thus forming an included angle between the actual movement direction of the USV and the heading of the USV, that is, a sideslip angle. Due to the limitation of the USV's detection means, the actual movement direction of the USV cannot be directly measured, so the sideslip angle cannot be eliminated by feedback control. Therefore, many research works have been carried out on the estimation and compensation of the sideslip angle.

In order to eliminate the sideslip angle, Børhaug [1] and Caharija [2] propose an integrated Line of Sight (LOS)

guidance law. An integral term is added into the traditional LOS guidance law to compensate the sideslip angle caused by environmental disturbance. In order to make the selection of the parameters of the integral LOS guidance law more standardised, Lekkas [3] proposed an ILOS guidance law based on speed. This method requires the selection of parameters to satisfy the stability analysis. Qu [4] made improvements on the basis of ILOS guidance law, so that the integral effect could be adaptively adjusted according to the cross-path following errors, and further improved the flexibility of ILOS guidance law. Mu [5] applied the idea of a variable lookahead distance to ILOS guidance law, and improved the convergence rate and stability of the ILOS guidance law. Based on [4] and [5], Chen [6] proposed that the improved ILOS guidance law could simultaneously adjust the strength of the integral and increase the lookahead distance. The above methods are based on the assumption that the sideslip angle is small (3-5 degrees) and constant, but this is difficult to satisfy in practice. Therefore, Fan [7] directly calculated the value of the sideslip angle by

using the surge velocity and the total speed of the USV, thus relaxing the assumptions on the sideslip angle. Moe [8] also uses the surge velocity and sway velocity of the USV to directly calculate the sideslip angle. However, this method has a high requirement for the measurement precision of the sensor, and the measurement noise may be amplified during the calculation. Under the assumption that the sideslip angle is small and constant, Gu [9] applies the low-frequency learning method to estimation of the sideslip angle to realise the formation control of USVs. Wang [10] realised the estimation of the sideslip angle in finite time by introducing auxiliary variables and designing a finite time disturbance observer. Aiming at the cooperative formation control of underactuated USVs, several intermediate state variables and virtual control laws are designed based on nonlinear backstepping, and actual control algorithms for the follower USVs to control the surge force and yaw moment are presented by Dong [11]. Wang [12] by modelling the switching of network topologies with the use of a Markov process and considering the effect of wave-induced disturbance, a new sampled-data consensus control protocol is proposed.

Inspired by the above method and based on the research idea of [10], the extended state observer is applied to estimate the sideslip angle, which allows the sideslip angle to be unknown, time-varying and arbitrary, and relaxes the finite time disturbance observer for the smoothness of the sideslip angle, making it more applicable and closer to practical application. At the same time, the LOS guidance law is improved, and the relationship between the curvature of the expected path and the USV surge velocity is established, so that the USV can automatically adjust the surge velocity in the process of following the expected curve path, so as to improve the tracking accuracy. Finally, the heading and speed controller of the USV is designed by using sliding mode control, and the effectiveness and superiority of the algorithm are demonstrated by simulation and comparison experiments.

## PROBLEM DESCRIPTION

Firstly, a three-degrees-of-freedom mathematical model of the USV is given, and the assumptions in the model building process are explained. Secondly, the target of the path following control of the USV and the principle of the variable speed curve path following control method based on an extended state observer are described, which lays a foundation for the simulation experiment of the path following control method.

### USV MATHEMATICAL MODEL

The USV actually moves with 6 DOF, but in order to simplify the design of the path following controller, when the USV meets the following assumptions, the USV model can be simplified from 6 DOF to 3 DOF.

- 1) Ignore the motion of the USV in the direction of heave, pitch and roll, and only consider the three-degrees-of-freedom motion of the plane;

- 2) The USV is a homogeneous mass and is symmetrical about the plane with respect to the x, z coordinate axis;
- 3) The z axis is the coordinate axis where the center of buoyancy and the center of gravity of the USV are located.

The 3DOF mathematical model of the USV can be described as Eq. (1).

$$\begin{cases} \dot{\boldsymbol{\eta}} = \mathbf{J}(\boldsymbol{\psi})\boldsymbol{v} \\ \mathbf{M}\dot{\boldsymbol{v}} = -\mathbf{C}(\boldsymbol{v})\boldsymbol{v} - \mathbf{D}(\boldsymbol{v})\boldsymbol{v} + \boldsymbol{\tau} + \boldsymbol{b} \end{cases} \quad (1)$$

where  $\boldsymbol{\eta}$  is the position and heading vector of the USV in the earth-fixed frame;  $\mathbf{J}(\boldsymbol{\psi})$  is the rotation matrix between the earth-fixed frame and the body-fixed frame;  $\boldsymbol{v}$  is the velocity vector;  $\mathbf{M}$  is the inertial matrix;  $\mathbf{C}$  is the Coriolis centripetal force matrix;  $\mathbf{D}$  is the damping coefficient matrix;  $\boldsymbol{\tau}$  is the control input vector;  $\boldsymbol{b}$  is the external interference vector.

$$\boldsymbol{\eta} = \begin{bmatrix} x \\ y \\ \psi \end{bmatrix} \boldsymbol{v} = \begin{bmatrix} u \\ v \\ r \end{bmatrix} \boldsymbol{\tau} = \begin{bmatrix} \tau_u \\ 0 \\ \tau_r \end{bmatrix} \boldsymbol{b} = \begin{bmatrix} b_1 \\ b_2 \\ b_3 \end{bmatrix}$$

$$\mathbf{M} = \begin{bmatrix} m_{11} & 0 & 0 \\ 0 & m_{22} & 0 \\ 0 & 0 & m_{33} \end{bmatrix} \mathbf{D} = \begin{bmatrix} d_{11} & 0 & 0 \\ 0 & d_{22} & 0 \\ 0 & 0 & d_{33} \end{bmatrix}$$

$$\mathbf{J}(\boldsymbol{\psi}) = \begin{bmatrix} \cos \psi & -\sin \psi & 0 \\ \sin \psi & \cos \psi & 0 \\ 0 & 0 & 1 \end{bmatrix}$$

$$\mathbf{C}(\boldsymbol{v}) = \begin{bmatrix} 0 & 0 & -m_{22}v \\ 0 & 0 & m_{11}u \\ m_{22}v & -m_{11}u & 1 \end{bmatrix}$$

where  $(x, y, \psi)$  are the longitudinal and lateral positions and heading angle in the geodetic coordinate system;  $(u, v, r)$  describes the surge velocity, the sway velocity, and yaw rate of the USV in the body-fixed frame;  $\tau_u, \tau_r$  are the surge force and yaw moment;  $b_1, b_2, b_3$  represent the external disturbances caused by waves, wind, and ocean currents;  $m_{11}, m_{22}, m_{33}$  denote the USV inertia coefficients;  $d_{11}, d_{22}$  and  $d_{33}$  are hydrodynamic damping in surge, sway, and yaw respectively.

### DESCRIPTION OF THE CURVE PATH FOLLOWING PROBLEM

The schematic diagram of the curve path following strategy for the USV is shown in Fig. 1. It is considered that the expected path  $P(\theta)$  of the USV is composed of a series of continuous points  $(x_p, y_p)$ , wherein  $\theta$  is the time-dependent path variable with dynamics given by:

$$\dot{\theta} = \frac{U}{\sqrt{x_p'^2(\theta) + y_p'^2(\theta)}} \quad (2)$$

where  $y_p'(\theta) = dy_p(\theta)/d\theta$ ,  $x_p'(\theta) = dx_p(\theta)/d\theta$ ,  $U = \sqrt{u^2 + v^2} > 0$  is the total speed in the coordinate system.

$\gamma_p$  is the included angle between the tangent direction and due north in the earth-fixed frame at any point  $(x_p, y_p)$  on the parametric path, and its calculation formula is as follows:

$$\gamma_p(\theta) = \arctan\left(\frac{y'_p(\theta)}{x'_p(\theta)}\right), \gamma_p(\theta) \in (-\pi, \pi) \quad (3)$$

The Serret-Frenet coordinate system was established to better describe the tracking error of the USV curve. The coordinate system takes the free point on the expected path  $P(\theta)$  as the origin, and the horizontal axis  $X_p$  along the tangent direction of  $P(\theta)$ , and the vertical axis  $Y_p$  along the normal direction of  $P(\theta)$ , and points to the right.  $x_e$  represents the along-path following errors;  $P_{los}$  is the line-of-sight guidance vector, and its direction is the expected heading  $\psi_d$  of the USV;  $\Delta$  is the lookahead distance of the USV;  $\beta$  is the sideslip angle generated by the ocean disturbance of the USV.

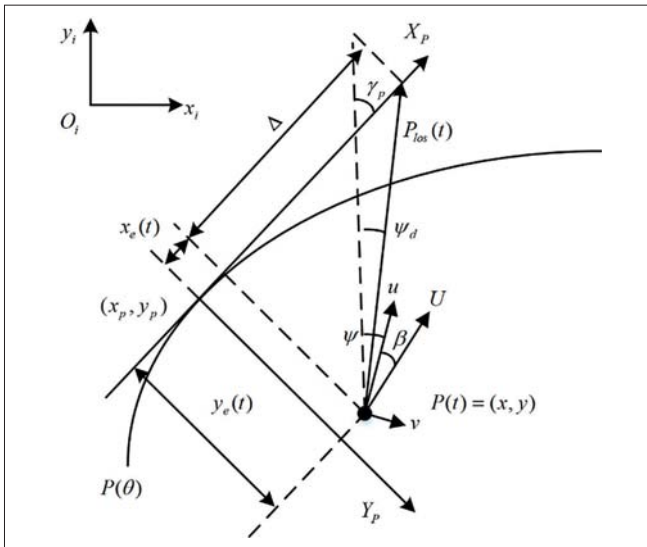


Fig. 1. Schematic diagram of USV curve path following strategy

In the geodetic coordinate system, the actual current position of the USV is  $(x, y)$ . According to the geometric relationship in Fig. 1, the cross-path following error  $y_e$  is as follows:

$$y_e = -(x - x_p(\theta)) \sin(\gamma_p(\theta)) + (y - y_p(\theta)) \cos(\gamma_p(\theta)) \quad (4)$$

When the cross-path following error  $\lim_{t \rightarrow \infty} y_e = 0$ , this means that the USV is already tracking the path of the curve.

Therefore, the curve path following problem of the USV can be described as follows: under the condition of the existence of the sideslip angle, the improved LOS guidance law is adopted to make the cross-path following error  $y_e$  converge to 0 by controlling the heading and surge velocity of the USV. Thus, the USV path following control strategy is formulated, and its overall control principle is shown in Fig. 2.

## CONTROLLER DESIGN

The curve path following control algorithm designed in this paper includes three parts: improved LOS guidance law, extended state observer and sliding mode heading/speed controller. Firstly, the surge velocity guidance law is added on the basis of the traditional LOS guidance law, so that the LSO guidance law provides both the desired heading and the desired surge velocity. Secondly, an extended state observer is designed to estimate the sideslip angle and compensate it in LOS guidance law to eliminate the influence of environmental disturbance on path following. Finally, a sliding mode controller is designed to drive the USV to track the desired heading and desired surge velocity given by LOS guidance law, so as to realise accurate path following.

### IMPROVED CURVE LOS GUIDANCE LAW

The traditional LOS (line-of-sight) guidance law can calculate the desired heading of the USV based on the USV's position and desired path, which has been widely used in the field of USV path following. When there is a sideslip angle, the traditional LOS guidance law calculates the desired heading as follows:

$$\psi_d = \gamma_p(\theta) - \beta - \arctan\left(\frac{y_e}{\Delta}\right) \quad (5)$$

where  $\Delta$  is the lookahead distance;  $\beta$  is a time-varying and unknown sideslip angle.

The traditional LOS guidance law only focuses on the calculation of the desired heading, and the surge velocity is generally a user-defined constant value. However, when the curve path following is carried out at a fixed surge velocity, the

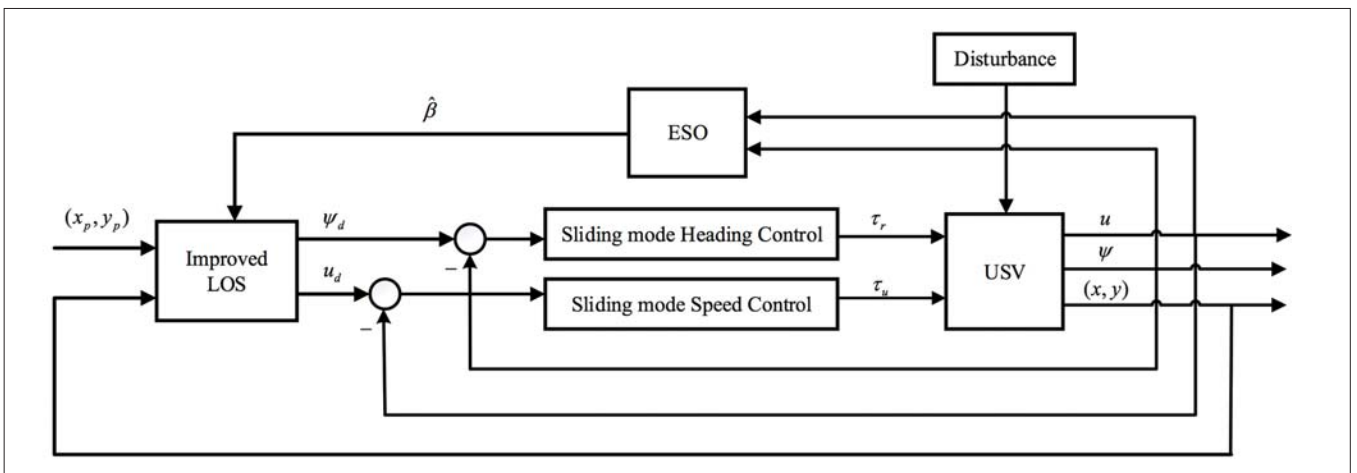


Fig. 2. Schematic diagram of path following control of USV

expected curve path curvature will affect the tracking effect. The greater the curvature, the greater the tracking error. Moreover, the oscillation increases during the path following convergence, and the stability of the system decreases. Therefore, based on the traditional LOS guidance law, the surge velocity guidance law is designed and added in this paper, so that the improved LOS guidance law can provide both the desired heading and desired surge velocity, thus further improving the tracking accuracy of the curve path.

The surge velocity guidance law of the USV is designed by establishing the relationship between the surge velocity and the curvature of the desired path, so that the surge velocity of the USV can be adaptively adjusted according to the curvature. The surge velocity guidance law is designed as follows:

$$u_d = u_1 + u_2 \frac{1}{1 + e^{(hK+\delta)}} \quad (6)$$

where  $u_d$  represents the desired surge velocity of the USV, and  $u_1$  represents the minimum surge velocity.  $u_2$  represents the maximum increment of the variable surge velocity part;  $h$ ,  $\delta$  are the user-defined constant parameters;  $K$  is the curvature of the expected curve path, and its calculation formula is as follows:

$$K = \frac{|x'(\theta)y''(\theta) - x''(\theta)y'(\theta)|}{[x'^2(\theta) + y'^2(\theta)]^{3/2}} \quad (7)$$

The USV path following process, under the effect of the variable surge velocity guidance law according to the curvature of the curve path, independently regulates the USV speed: the greater the curvature,  $\lim_{K \rightarrow \infty} \frac{1}{1 + e^{(hK+\delta)}} \approx 0$ , the closer it gets to the minimum speed; the smaller the curvature,  $\lim_{K \rightarrow 0} \frac{1}{1 + e^{(hK+\delta)}} \approx \frac{1}{1 + e^\delta}$ . By setting parameter  $\delta$  appropriately,  $u_d$  can be close to the maximum speed.

In conclusion, the improved LOS guidance law can provide both the desired surge velocity and the desired heading for the USV. Under the desired heading shown in Eq. (5), the USV can converge steadily to the expected path. The design of the surge velocity guidance law enables the USV to adjust the desired surge velocity in real time according to the curvature of the curve path during the heading of track tracking, thus effectively reducing the error of path following and improving the accuracy.

## DESIGN OF AN ESO TO ESTIMATE THE SIDESLIP ANGLE

The Extended State Observer (ESO) is the core part of the active disturbance rejection controller [13]. It adopts a discontinuous smooth structure design and can perform real-time estimation and compensation for disturbances. In this paper, the estimation of the sideslip angle by means of an extended state observer is divided into two steps: firstly, an auxiliary variable is introduced to construct a second-order extended state system about the sideslip angle to satisfy the application conditions of the extended state observer; then a second-order extended state observer is designed to estimate the sideslip angle.

## Introduction of auxiliary variables

In order to apply the extended state observer to the estimation of the sideslip angle, a second-order system is constructed by using the cross-path following errors  $y_e$ , and the sideslip angle is independent of the extended state, so as to facilitate the subsequent observer design.

In [6] Eq. (4) is differentiated, and together with Eq. (1) and Eq. (3), we can obtain the cross-path following error dynamics as follows:

$$\dot{y}_e = u \cdot \sin(\psi - \gamma_p(\theta)) + u \cdot \tan\beta \cdot \cos(\psi - \gamma_p(\theta)) \quad (8)$$

An auxiliary variable is first defined as follows:

$$\vartheta = \frac{y_e}{\cos(\psi - \gamma_p(\theta))} \quad (9)$$

where it is theoretically possible that  $\cos(\psi - \gamma_p(\theta))$ . Therefore, it is assumed that  $\psi - \gamma_p(\theta) \in (-\frac{\pi}{2}, \frac{\pi}{2})$  which is easy to satisfy in practice.

Combining with Eq. (9) yields the following dynamics:

$$\dot{\vartheta} = u \cdot \tan(\psi - \gamma_p(\theta)) + u \cdot \tan\beta - \frac{y_e \cdot \sin(\psi - \gamma_p(\theta))}{\cos^2(\psi - \gamma_p(\theta))} \dot{\gamma}_p(\theta) \quad (10)$$

Rewriting  $\vartheta = x_1$ ;  $u \cdot \tan\beta = x_2$ ;  $u \cdot \tan(\psi - \gamma_p(\theta)) - \frac{y_e \cdot \sin(\psi - \gamma_p(\theta))}{\cos^2(\psi - \gamma_p(\theta))} \dot{\gamma}_p(\theta) = h$ , the above system can be extended to of a second-order system as shown in Eq. (11):

$$\begin{cases} \dot{x}_1 = x_2 + h \\ \dot{x}_2 = w(t) \end{cases} \quad (11)$$

So far, with the introduction of auxiliary variable  $\vartheta$  a second-order system is constructed, and the function term with an unknown sideslip angle is independent of the extended state  $x_2$ , laying the groundwork for our subsequent extended state observer design.

## Design of extended state observer

Next, an extended state observer is designed to estimate the sideslip angle. Eq. (11) is rewritten as Eq. (12):

$$\begin{cases} \dot{x}_1 = x_2 + h \\ \dot{x}_2 = w(t) \\ y = x_1 \end{cases} \quad (12)$$

The extended state observer is designed as shown in Eq. (13):

$$\begin{cases} e = z_1 - y \\ \dot{z}_1 = z_2 - \beta_1 e + h \\ \dot{z}_2 = -\beta_1 \text{fal}(e, \alpha_1, \sigma) \end{cases} \quad (13)$$

where  $\text{fal}(e, \alpha_1, \sigma)$  is a nonlinear continuous function, shown in the following formula:

$$\text{fal}(e, \alpha_1, \sigma) = \begin{cases} |e|^{\alpha_1} \text{sign}(e), & |e| > \sigma \\ \frac{e}{\sigma^{\alpha_1}}, & |e| \leq \sigma \end{cases} \quad (14)$$

The parameters  $\beta_1, \beta_2, \alpha_1$  and  $\sigma$  are determined according to the empirical formula provided in [14], and the estimation of  $x_1, x_2$  by  $z_1, z_2$  can be realised. Since  $x_2 = utan\beta$ , and  $u$  is the surge velocity of the USV, which can be obtained by the sensor, the calculation formula of the final sideslip angle is as follows:

$$\hat{\beta} = \arctan\left(\frac{z_2}{u}\right) \quad (15)$$

By designing an extended state observer, the sideslip angle  $\beta$  has been estimated and substituted into Eq. (6) to obtain the compensated desired heading of the USV:

$$\psi_d = \gamma_p(\theta) - \hat{\beta} - \arctan\left(\frac{\gamma_c}{\Delta}\right) \quad (16)$$

With the introduction of auxiliary variables and the design of the extended state observer, the estimation of the sideslip angle has been realised. The desired heading  $\psi_d$  given by the LOS guidance law is corrected by using the estimated sideslip angle to compensate the environmental disturbances. The desired heading given in Eq. (16) can ensure that the USV converges to the desired curve path in the presence of a sideslip angle.

## DESIGN OF SLIDING MODE CONTROLLER

In order to ensure that the USV can track the desired heading and desired surge velocity given by the improved LOS guidance law in real time, it is necessary to design the heading and speed controller. However, the complex and changeable environmental disturbance requires greater robustness of the controller. Sliding mode control is a special class of nonlinear control [15], which can switch the structure of the controller according to the degree of system state deviation from the sliding mode, and has strong robustness. In addition, sliding mode control is insensitive to model error and parameter perturbation of the controlled object. Therefore, based on the sliding mode control theory, the heading and speed controllers of the USV are designed respectively in this paper.

### Sliding mode heading controller

The improved LOS guidance law provides the desired heading  $\psi_d$  for the USV, and the actual heading  $\psi$  of the USV can be obtained by sensors. Therefore, the heading tracking error is defined as:

$$e_\psi = \psi_d - \psi \quad (17)$$

The sliding surface of heading tracking is designed as:

$$s_1 = \dot{e}_\psi + c_1 e_\psi, \quad c_1 > 0 \quad (18)$$

Taking the derivative along Eq. (18) and combining it with Eq. (1) obtains:

$$\dot{s}_1 = \dot{r}_d + c_1(r_d - r) - \frac{1}{m_{33}}((m_{11} - m_{22})uv - (1 + d_{33})r + \tau_r) \quad (19)$$

The control input  $\tau_{req}$  is originally designed as:

$$\tau_{req} = (m_{22} - m_{11})uv + (1 + d_{33})r - m_{33}(\dot{r}_d + c_1(r_d - r)) \quad (20)$$

In order to overcome possible chattering, the saturation function  $sat(s_1)$  is adopted in the controller instead of the switching function  $sgn(s_1)$ . The expression of the saturation function is as follows:

$$sat(s_1) = \begin{cases} 1 & s_1 > \omega_1 \\ s_1/\omega_1 & |s_1| \leq \omega_1 \\ -1 & s_1 < -\omega_1 \end{cases} \quad (21)$$

where  $\omega_1 > 0$  is called the boundary layer. Switching control is used outside the boundary layer, and linearised feedback control is used inside the boundary layer, which can effectively reduce chattering [16].

The approach law determines the speed at which the system reaches the sliding mode surface. In order to make the system converge faster without increasing chattering, the exponential approach law is selected:

$$\dot{s}_1 = -k_1 s_1 - \varepsilon_1 sat(s_1) \quad (22)$$

Combining with Eq. (20) and Eq. (23) yields the final control input  $\tau_r$  of the USV as:

$$\tau_r = m_{33}\dot{r}_d + (m_{22} - m_{11})uv + (d_{33} - 1)r + m_{33}[k_1 s_1 + \varepsilon_1 sat(s_1) + c_1(r_d - r)] \quad (23)$$

### Sliding mode speed controller

The design process of the sliding mode speed controller is the same as the heading controller. The surge velocity tracking error is defined as:

$$e_u = u_d - u \quad (24)$$

The sliding surface of the first-order exponential surge velocity tracking of the integrated type is designed as follows:

$$s_2 = e_u + c_2 \int e_u, \quad c_2 > 0 \quad (25)$$

Taking the derivative along Eq. (25) and combining it with Eq. (1) obtains:

$$\dot{s}_2 = \dot{u}_d + c_2(u_d - u) - \frac{1}{m_{11}}(m_{22}vr - d_{11}u + \tau_u) \quad (26)$$

The control input  $\tau_{ueq}$  is originally designed as:

$$\tau_{ueq} = -m_{22}vr + d_{11}u + m_{11}(\dot{u}_d + c_2(u_d - u)) \quad (27)$$

We select the law of exponential approach:

$$\dot{s}_2 = -k_2 s_2 - \varepsilon_2 sat(s_2) \quad (28)$$

Combining with Eq. (27) and Eq. (29) yields the final control input  $\tau_u$  of the USV as:

$$\tau_u = m_{11}\dot{u}_d - m_{22}vr + d_{11}u + m_{11}[k_2 s_2 + \varepsilon_2 sat(s_2) + c_2(u_d - u)] \quad (29)$$

Through the design of the sliding mode heading/speed controller, the USV can track the desired heading and surge velocity under the control law shown in Eq. (23) and Eq. (29). Moreover, due to the robustness of sliding mode control, the influence of environmental disturbance and model uncertainty on path following control is further restrained and the control performance is improved.

## SIMULATION EXPERIMENTS

In order to verify the effectiveness and superiority of the proposed method, MATLAB is used for simulation tests. The mathematical model of the USV in [17] is selected for simulation verification. The specific model parameters are as follows:  $\hat{m}_{11} = 200 \text{ kg}$ ,  $\hat{m}_{22} = 250 \text{ kg}$ ,  $\hat{m}_{33} = 80 \text{ kg} \cdot \text{m}^2$ ,  $\hat{d}_{11} = 70 \text{ kg/s}$ ,  $\hat{d}_{22} = 100 \text{ kg/s}$ ,  $\hat{d}_{33} = 50 \text{ kg/s} \cdot \text{m}^2$ ,  $\tau_{umax} = 200 \text{ N}$ ,  $\tau_{rmax} = 50 \text{ N} \cdot \text{m}$ .

### Simulation experiment 1

First of all, the simulation experiment of undisturbed path following control for the USV is carried out respectively based on the traditional LOS guidance law and improved LOS guidance law proposed in this paper.

The initial statuses of the USV are as follows:

$$\begin{aligned} \boldsymbol{\eta}(0) &= [0 \quad 0 \quad 0]^T \\ \boldsymbol{v}(0) &= [0 \quad 0 \quad 0]^T \end{aligned}$$

The design expectation curve path is as follows:

$$\begin{cases} x_p(\theta) = \theta \\ y_p(\theta) = 20\sin(0.1\theta) \end{cases}$$

where  $\theta$  is a parameter that satisfies Eq. (2).

On the basis of the improved LOS guidance law, the desired heading  $\psi_d$  and desired surge velocity  $u_d$  respectively are as follows:

$$\begin{cases} u_d = u_1 + u_2 \frac{1}{1 + e^{(hK + \delta)}} \\ \psi_d = \gamma_p(\theta) - \beta - \arctan\left(\frac{\gamma_p}{\Delta}\right) \end{cases}$$

The parameters are chosen as  $u_1 = 0.8$ ,  $u_2 = 0.7$ ,  $h = 40$ ,  $\delta = -2$ ,  $\Delta = 1$ .

In addition, the parameter design of the sliding mode heading controller is  $c_1 = 3$ ,  $k_1 = 3$ ,  $\varepsilon_1 = 1$ ,  $\omega_1 = 1$ . The parameters of the sliding mode speed controller are designed as  $c_2 = 0.1$ ,  $k_2 = 2$ ,  $\varepsilon_2 = 0.01$ ,  $\omega_2 = 1$ . Based on the above simulation conditions, the experimental results are shown in Fig. 1.

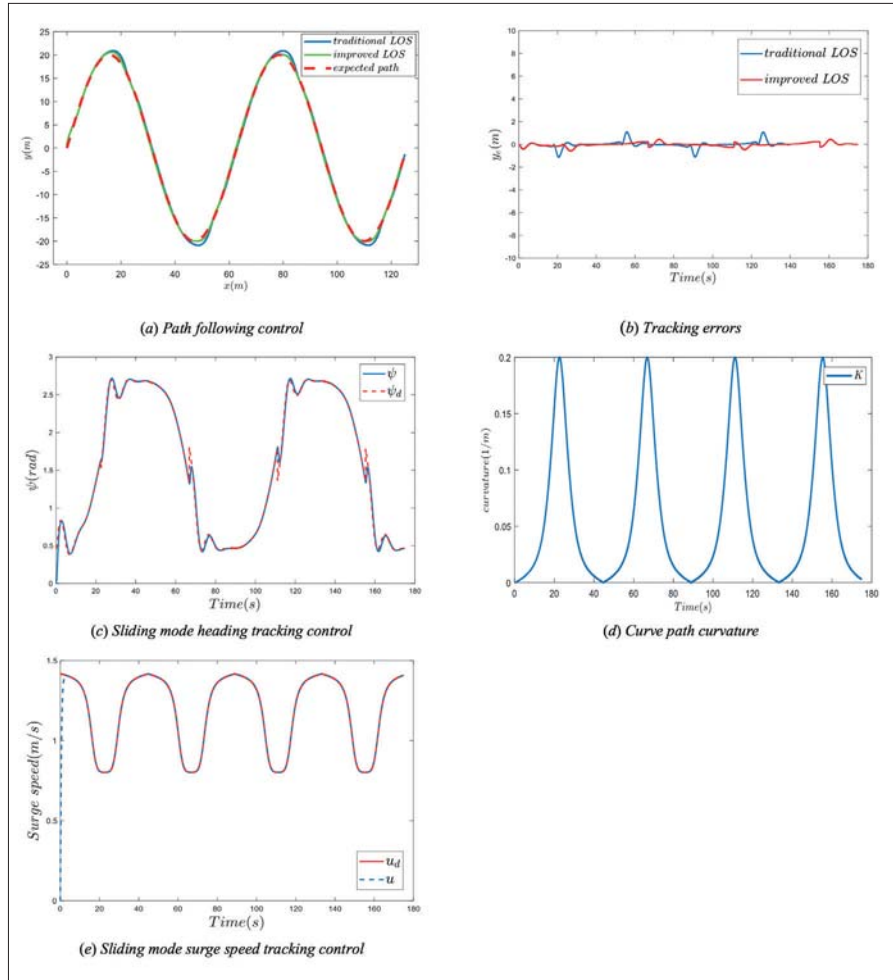


Fig. 3. In the absence of disturbance, contrast between traditional LOS and improved LOS

Fig. 3 (a) and (b) mainly compare the effect of path following control between the traditional LOS and the improved LOS. From the analysis of Fig. 3 (a), it can be seen that due to the improved LOS guidance law and the design of the surge velocity guidance law, there is a smaller tracking error in the position where the curvature of the curve path is larger. By analysing and comparing the tracking errors before and after the improvement of the LOS guidance law in Fig. 3 (b), it can be calculated that the average tracking error based on the improved LOS guidance law is 0.13 m, and the average tracking error of the traditional LOS guidance law is 0.157 m. The improved LOS guidance law improves the tracking accuracy of USVs by 28%. Thus, Fig. 3 (a) and (b) illustrate the advantages of improving the law of LOS guidance.

Fig. 3 (c) is the heading tracking control based on the sliding mode controller. It can be seen that the USV can track the desired heading well under the action of the sliding mode controller, which verifies the effectiveness of the sliding mode controller. Fig. 3 (d) shows the curvature change of the curve path; Fig. 3 (e) first reflects the effectiveness of the rate of change of surge velocity. The USV can adjust the desired surge velocity according to the path curvature during the path following process. Secondly, it verifies that the USV sliding mode speed

controller can track the desired surge velocity in timely fashion and accurately.

### Simulation experiment 2

The following is the simulation experiment of the USV curve path following control under oceanic environmental disturbance. Based on the simulation environment given in experiment 1, the design of the extended state observer is added. The parameters are as follows:  $\beta_1=100, \beta_2=300, \alpha_1=0.5, \delta=0.01$ .

In order to make the simulation effect reflect the USV navigation situation more realistically, the disturbance is assumed as follows:

$$\mathbf{b} = \begin{bmatrix} 0.1 * \sin(0.03 * t) \\ 0.3 * \sin(0.03 * t) \\ 0.2 * \sin(0.03 * t) \end{bmatrix}$$

Based on the above simulation conditions, the experimental results are shown in Fig. 2.

Fig. 4 is the simulation result for the validity verification of the sideslip angle estimation by the extended state observer. Fig. 4 (a) is the simulation result of the ESO's estimation of the unknown term  $x_2$  with the sideslip angle. It can be clearly seen that the ESO can accurately track a time-varying and unknown extended state, which proves the effectiveness of the proposed method. Fig. 4 (b) shows the simulation results of the USV speed control. The speed guidance law can adjust the surge velocity of the USV in real time. Fig. 4 (c) is the change curve of the estimated sideslip angle  $\hat{\beta}$  calculated by (15). After obtaining  $\hat{\beta}$ , the expected heading is compensated, and the change curve of the expected heading before and after the compensation is shown in Fig. 4 (d). Fig. 4 (e) shows the curve path following control of the USV, and compares the path following effect with that without the extended state observer. By analysing and comparing the curve path following error in Fig. 4 (f), it can be calculated that the average tracking error after adding sideslip angle compensation is 0.75 m, and the

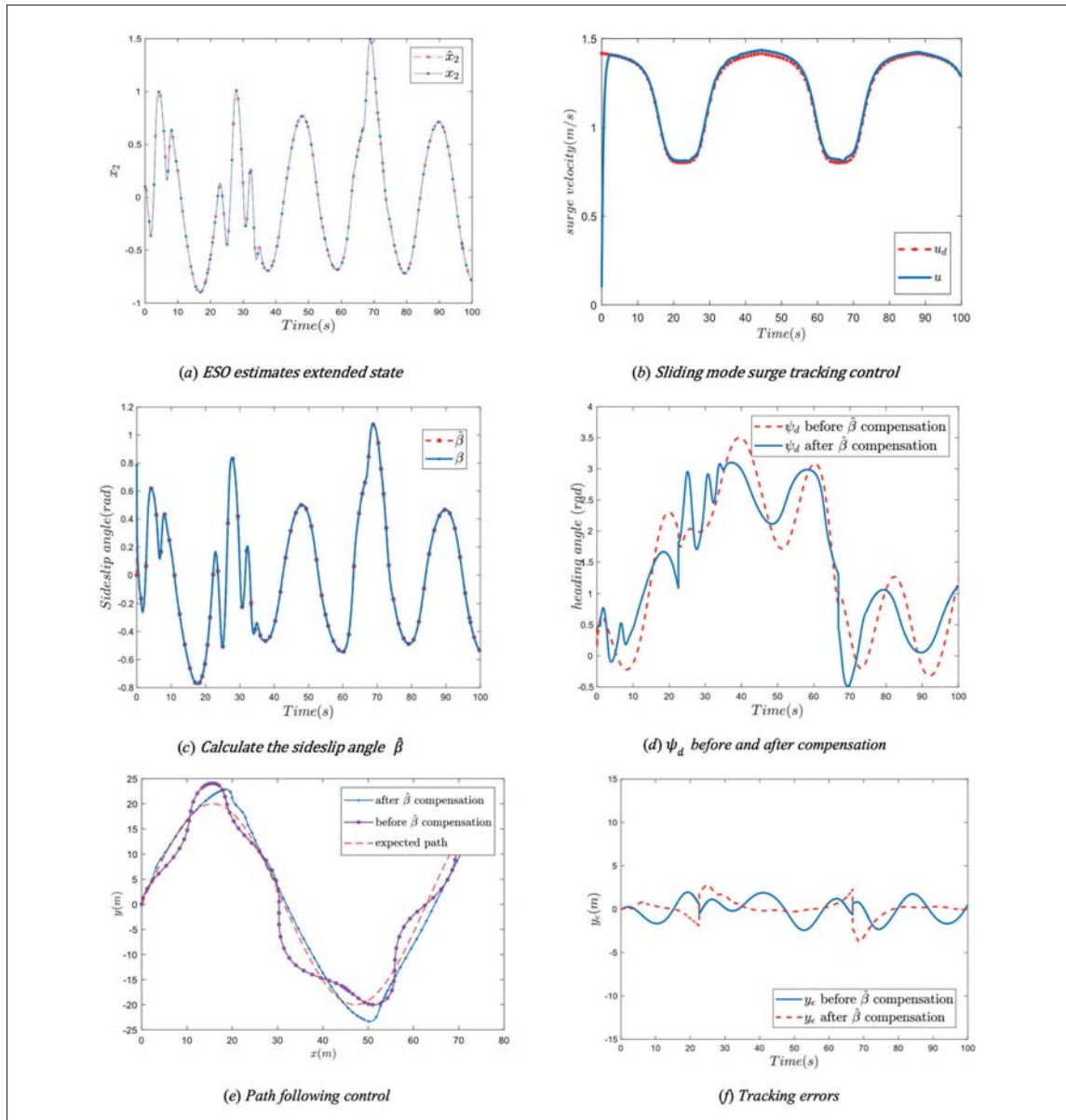


Fig. 4. In the presence of disturbance, ESO estimates the effectiveness of sideslip angle

average tracking error before sideslip angle compensation is 1.01 m. The design of the extended state observer estimation improves the curve path following accuracy of an unmanned ship under ocean disturbance by 26%.

## CONCLUSIONS

In this paper, the sideslip angle problem caused by environmental disturbance is studied in depth and a path following control method for a variable surge velocity curve based on an extended state observer is proposed. The extended state observer is designed to accurately estimate the unknown, time-varying and arbitrary sideslip angle, and then the desired heading given by LOS guidance law is compensated and corrected by using its estimated value, which ensures the stability of the trajectory tracking control of USV curves. Secondly, by analysing the relationship between the surge velocity of the USV and the curvature of the curved path, the design of the surge velocity guidance law is added on the basis of the traditional LOS guidance law, so that the USV can self-adjust the surge velocity according to the curvature of the path and further improve the tracking accuracy of the path. Finally, the sliding mode heading and speed controller is designed to track the desired heading and speed accurately. The effectiveness and superiority of the proposed method are verified by simulation experiments

## ACKNOWLEDGEMENTS

This work was supported by the National Key Research and Development Program of China (No.2017YFC1405203) and the Fundamental Research for the Central Universities (No.19CX05003A-1)

## REFERENCES

1. E. Børhaug, A. Pavlov and K.Y. Pettersen, "Integral LOS control for path following of underactuated marine surface vessels in the presence of constant ocean currents," in *47th IEEE Conference on Decision and Control, Cancun, Mexico, December 9–11, 2008*, pp. 4984–4991.
2. W. Caharija, M. Candeloro, K.Y. Pettersen, et al., "Relative Velocity Control and Integral LOS for Path Following of Underactuated Surface Vessels," *IFAC Proceedings*, vol. 45, pp. 380–385, September 2012.
3. A.M. Lekkas, *Guidance and path-planning systems for autonomous vehicles*, Norway: Norwegian University of Science and Technology, 2014.
4. Y. Qu, H. Xu, W. Yu, et al., "Integral Line-of-sight Guidance for Path Following of Underactuated Marine Surface Vessels," *Journal of Wuhan University of Technology (Transportation Science & Engineering)*, vol. 40, pp. 834–838, October 2016.
5. D. Mu, G. Wang, Y. Fan, et al., "Adaptive LOS Path Following for a Podded Propulsion Unmanned Surface Vehicle with Uncertainty of Model and Actuator Saturation," *Applied Sciences*, vol. 7, pp. 1232–1251, November 2017.
6. X. Chen, Z. Liu, J. Zhang, et al., "Path following of underactuated USV based on modified integral line-of-sight guidance strategies," *Journal of Beijing University of Aeronautics and Astronautics*, vol. 44, pp. 489–499, September 2018.
7. Y. Fan, C. Guo, Y. Zhao, G. Wang, W. Shi, "Design and verification of straight-line path following controller for USV with time-varying drift angle," *Chinese Journal of Scientific Instrument*, vol. 37, pp. 2514–2520, November 2016.
8. S. Moe, K.Y. Pettersen, T.I. Fossen, et al., "Line-of-Sight Curved Path Following for Underactuated USVs and AUVs in the Horizontal Plane under the Influence of Ocean Currents," in *2016 24th Mediterranean Conference on Control and Automation (MED), Athens, Greece, June 21–24, 2016*, pp. 38–45.
9. N. Gu, D. Wang, L. Liu, B. Zhang, Z. Peng, "Adaptive line-of-sight guidance law for synchronized path-following of under-actuated unmanned surface vehicles based on low-frequency learning," in *36th Chinese Control Conference, Dalian, China, July 26–28, 2017*, pp. 6632–6637.
10. N. Wang, X. Pan, "Path Following of Autonomous Underactuated Ships: A Translation–Rotation Cascade Control Approach," *IEEE/ASME Transactions on Mechatronics*, vol. 24, pp. 2583–2593, June 2020.
11. Z. Dong, Y. Liu, H. Wang, T. Qin, "Method of Cooperative Formation Control for Underactuated USVs Based on Nonlinear Backstepping and Cascade System Theory," *Polish Maritime Research*, vol. 28, no. 1, pp. 149–162, March 2021.
12. L. Wang, W. Yue, R. Zhang, "Consensus for Multiple Unmanned Surface Vehicle (Musv) Systems with Markov Switching Topologies," *Polish Maritime Research*, vol. 26, no. 1, pp. 145–152, March 2019.
13. H. Huang, Y. Fan, "Sliding mode based ADRC for curved path following of unmanned surface vessels," in *2017 Chinese Automation Congress (CAC), Jinan, China, October 20–22, 2017*, pp. 4198–4202.
14. Y. Zhou, W. Pan, H. Xiao, "Design of ship course controller based on fuzzy adaptive active disturbance rejection technique," In *International Conference on Automation and Logistics (ICAL), Hong Kong and Macau, China, August 16–20, 2010*, pp. 232–236.
15. Z. Qin, Z. Lin, H. Sun, D. Yang, "Sliding-mode control of path following for underactuated ships based on high

gain observer,” *Journal of Central South University*, vol. 23, pp. 3356–3364, January 2016.

16. J. Liu, F. Sun, “Research and development on theory and algorithms of sliding mode control,” *Control Theory & Applications*, vol. 24, pp. 407–418, June 2007.
17. S. Gao, Q. Zhu, L. Li, “Fuzzy NN control of high-speed unmanned surface vehicle,” *Journal of System Simulation*, vol. 19, pp. 776–779, February 2007.

## CONTACT WITH THE AUTHORS

**Ligang Li**

*e-mail: upcllg@163.com*

China University of Petroleum  
66 Changjiang West Road  
266580 Qingdao  
**CHINA**

**Zhiyuan Pei**

*e-mail: 577232138@qq.com*

China University of Petroleum  
66 Changjiang West Road  
266580 Qingdao  
**CHINA**

**Jiucui Jin**

*e-mail: jinjiucui@fio.org.cn*

First Institute of Oceanography  
Ministry of Natural Resources  
No. 6 Xianxialing Road  
266061 Qingdao  
**CHINA**

**Yongshou Dai**

*e-mail: daiys@upc.edu.cn*

China University of Petroleum  
66 Changjiang West Road  
266580 Qingdao  
**CHINA**

# A MULTI-CASE-BASED ASSEMBLY MANAGEMENT METHOD FOR THE SHIPBUILDING INDUSTRY

Remigiusz Iwańkiewicz

Maritime University of Szczecin, Poland

\* Corresponding author: [r.iwankowicz@am.szczecin.pl](mailto:r.iwankowicz@am.szczecin.pl) (R. Iwańkiewicz)

## ABSTRACT

*This article describes a method for planning the assembly of ship hulls that focuses on a welding sequence, takes into account subassembly processes and makes use of a previously built database of structures. Different degrees of similarity between structures are taken into account. The described research led to the development of an intelligent hybrid sequencing method for structure assembly that uses fuzzy clustering, case-based reasoning and evolutionary optimization. The method is called 'Multi-case-Based Assembly Planning (MBAP)'. The method is developed to provide satisfactory solutions with low user effort. The analyses carried out show that the calculations are highly time-efficient. The developed evolutionary algorithm converges on sub-optimal solutions. The MBAP method can be directly implemented by any shipbuilder that assembles hulls. Apart from this, fuzzy clustering integrated with case-based reasoning can be applied in practice. The integration of fuzzy clustering and case-based reasoning has been taken to a level higher than previously described in the literature.*

**Keywords:** assembly management, shipbuilding, case-based reasoning, fuzzy classification

## INTRODUCTION

The introduction of welded joints in ship hulls a century ago brought about technological changes in shipyards around the world. Thanks to the thermal joining of steel, the modular hull building method was developed. These modules are called sections and blocks – the largest structures that a dockyard can move (Fig. 1). These subassemblies are also built from modules, so-called lower-stage subassemblies.

The shipbuilding industry is following the global trend toward the Fourth Industrial Revolution (Industry 4.0), which poses three main challenges:

- improvement of production efficiency,
- ensuring ship safety, and
- balancing economic efficiency with economic responsibility.

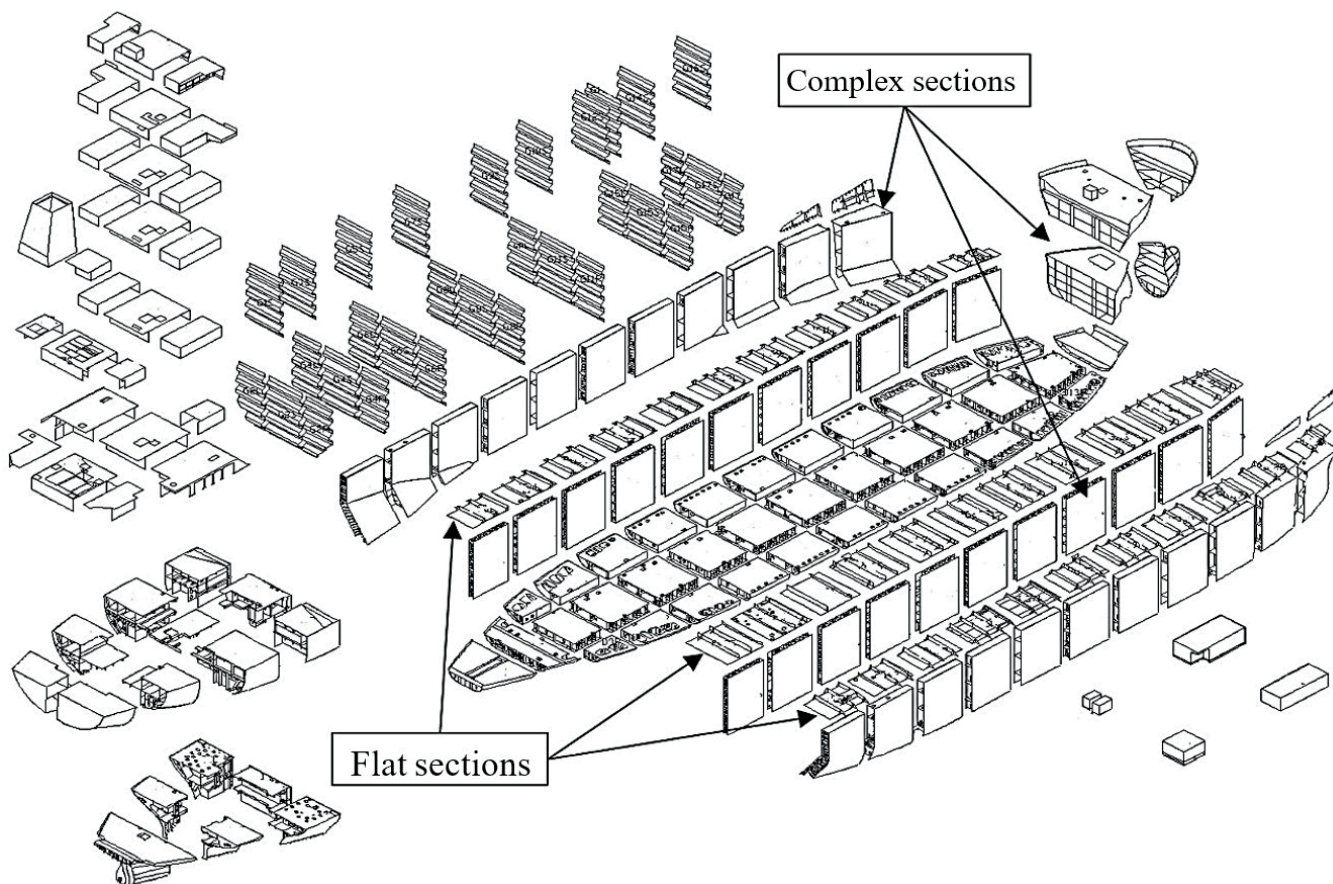


Fig. 1. Division of a chemical carrier hull into flat sections (open, single-shell structures) and complex sections (spatial, double-shell structures)

A shipyard in the age of Industry 4.0 should be a company that wisely adapts to changes in the environment, efficiently manages resources, is ergonomic and works closely with a ship owner and their suppliers. However, complete development toward automated shipbuilding requires balanced development of knowledge in key areas. There are several tasks that Computer Integrated Manufacturing (CIM) tools intended for this industry do not perform due to gaps in global knowledge such as in areas concerning the predictability of weld deformations, optimization of sheet metal cutting or modelling of the assembly of structures with complexity at least near to that of small vessels' hulls. This is mainly due to the size and complexity of the assembled structures. Individual shipyards are trying to solve these problems independently, but a comprehensive approach is needed to develop methods to control the processes of building large ship structures.

An important resource for each dockyard is the experience and knowledge being collected in production documents over decades. This knowledge is often stored in file cabinets, while experience passes away with retired employees. For a shipyard to become a knowledge-based company, it is necessary to seek solutions that will use databases for the management of key processes, including hull assembly. This article is intended to address this issue.

## LITERATURE REVIEW

The methods of planning the assembly of mechanisms have been developed for decades [1]. In building a hull, unlike mechanisms, the assembly cannot be planned by focusing solely on structural elements. Adding successive elements is conditional upon having previously completed certain welding operations to reinforce the structure and provide access for welders and equipment. In addition, this work may affect the structure geometry, which requires permanent verification of key dimensions [2]. Except for welding processes, the shipbuilding industry employs a very extensive collection of various subtractive and additive technologies. Each of them may have an unpredictable influence on the geometry of the assembled structure [3][4].

Hull assembly planning with a focus on welded joints is described in [5]. It addresses the issues of sequencing and scheduling for joints to be completed. The described models are based on a so-called sequence matrix, which is a binary record of the workflow. The assembly sequence serves to draw up a schedule, which takes into account additional aspects related to balancing the production capacity. Other authors [6] took into account the issue of hull welding. They combined the element of assembly sequencing with the prediction of welding deformation. A major problem with this model is the time taken to analyse temperature, elasticity and plasticity, which increases exponentially with the complexity of the structure. The serial nature of the generated sequences is a significant limitation of the method.

A way to simplify the planning of the assembly of large structures is to use a framework called subassembly-based division. The hull assembly process is completed at special workstations equipped with automatic welding machines, horizontal and vertical means of transport, structure turntables, beds with extendible supports etc. The planning of the hull structure assembly is related to the organization of the entire production system. However, these two issues are considered separately in the literature. The models for optimizing the shipyard's assembly lines are based on a pre-established assembly plan [7][8].

Bonneville, et al. were the first to propose the use of genetic algorithms (GA) as a tool for finding optimal and semi-optimal assembly plans [9]. The idea of using GA in assembly planning processes was developed further in [10]. The authors distinguish two types of limitations, that is, physical limitations and structure geometry limitations. It was noted that, for the proposed assembly plan to be considered acceptable, it must comply with all geometrical limitations. The physical limitations concerning the available equipment, assembly difficulty and cost were used as optimization criteria for the proposed algorithm.

In addition to evolutionary methods, so-called case-based reasoning (CBR) is included among computational intelligence methods. CBR methods have been developed since the early 1980s and are based on considerations given to the possibilities of digitally storing, analysing and gaining knowledge useful in predicting future events from past experience [11]. The first formal CBR system, CYRUS, was developed at Yale University in 1983 [12].

The main elements of CBR systems were described in [13]. The authors point out that the cyclical procedure consists of four stages (the so-called 4R cycle): analysis of the degree to which the database cases are similar to the case under consideration (retrieve), generation of a solution modelled on similar cases (reuse), verification of the generated solution (revise) and addition of the new case to the database (retain). Attempts have been made to adapt CBR methods to hull assembly planning since the 1990s, but difficulties are faced due to the complexity of the problem and the need for labour-intensive input by experts to control the calculations.

Shipeng et al. proposed use of the CBR method to generate assembly sequences for small sections of the hull [14]. It is worth noting the two-level classification of joints, which is the basis for analysing similarities between structures. However, CBR is only a supporting module in the proposed method. Serial sequences of elements are being determined.

The search for similarities between structures based on the classification of joints and structural elements is also proposed in other papers [15]–[18]. Authors dealing with the assembly of hulls introduce the classification of welded joints by their geometry. There are butt joints, fillet joints and cruciform joints. This is a simplification of the hull's geometric complexity. This approach limits the application of the methods to selected areas of hulls with a typical, repeatable structure, for example, in the area of a middle body.

In hull structures, there is a considerable variety of solutions, and many structures contain very similar parts. In that situation, it is difficult to clearly distinguish a subset of similar structures. This problem can be solved by using an intelligent hybrid system with fuzzy clustering [19]. The fuzzy c-means (FCM) algorithm allows the inclusion of different degrees of similarity between structures and thereby improves the effectiveness of case-based reasoning. Khan and Khan described the method of fuzzy clustering of a database in order to reduce a set of potentially similar cases [20]. However, the method does not use the information about the fuzzy cluster membership in the reasoning phase.

## THE CONCEPT OF ASSEMBLY PLANNING

The method described in this article involves the use of a database that stores the characteristics of multiple hull structures or their parts. In addition, every structure is linked to an assembly plan that has been previously implemented and verified for performance. The general scheme of the procedure in this method is modelled on the CBR method. However, it is necessary to adapt its basic components to solve the issues of hull assembly planning. A *case* is defined as any reference structure in a database. The architecture of the structure is the so-called *case problem*, and the assembly plan is *the solution to the case (problem)*. A progressively extended database is used as a *case library* (Fig. 2).

The proposed method will be referred to as 'Multi-case Based Assembly Planning' (MBAP). This method is distinctive due to the inclusion in the classic 4R cycle of fuzzy data clustering and the evolutionary search for the optimal solution. In addition, the author has described the unique architecture of the structure and its assembly plan.

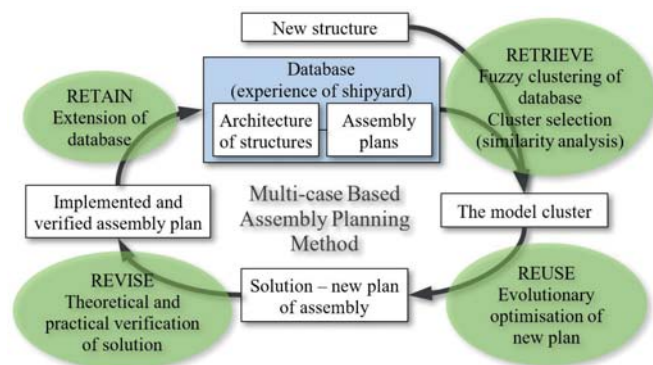


Fig. 2. The general MBAP scheme – the link between the 4R cycle, fuzzy clustering and evolutionary optimisation

The cyclical operation of the MBAP method allows the dockyard to perform the important role of learning from experience. To this end, the shipyard has to fulfil a number of additional functions associated with designing and manufacturing, namely to monitor the assembly of new structures in order to verify the planned subassembly-based

divisions and the order in which the elements are added, and to record all completed and corrected cases in the database.

## FORMAL DESCRIPTION OF THE STRUCTURE'S ARCHITECTURE

The structure under analysis is composed of  $E$  elements and  $J$  welded joints. Each joint is located between two structural elements. Every element can be connected to multiple others.

For example, consider sample structure no. 1, consisting of eight elements and 13 welded joints. The architecture of the structure is presented in Fig. 3, with squares representing the elements and the lines between them representing the joints. Joint numbers are circled, for example, joint 1 is between elements 1 and 2, joint 5 is between elements 2 and 3, etc.

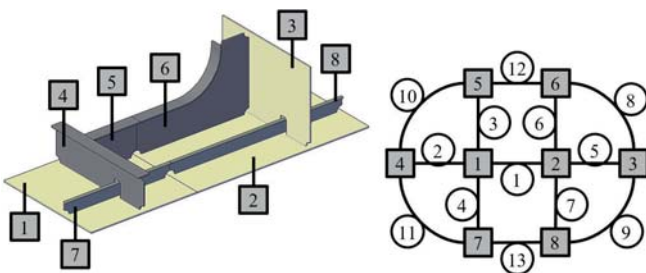


Fig. 3. Sample structure no. 1 and its architecture graph

The architecture of a structure can be described with a square matrix:  $\mathbf{A} = (a_{e_1, e_2})_{E \times E}$ , where, for each pair of elements indexed with  $e_1$  and  $e_2$  ( $e_1, e_2 = 1, 2, \dots, E$ ):

$a_{e_1, e_2}$  is the number of a joint between the elements,

$a_{e_1, e_2} = 0$  indicates that there is no welded joint between the elements,

$a_{e_1, e_2} = a_{e_2, e_1}$ .

For the structure shown in Fig. 3, we have an architecture matrix (zero values are skipped beyond the diagonal):

$$\mathbf{A}^1 = \begin{pmatrix} 0 & 1 & 2 & 3 & 4 \\ 1 & 0 & 5 & & 6 & 7 \\ & 5 & 0 & & 8 & 9 \\ 2 & & 0 & 10 & & 11 \\ 3 & & 10 & 0 & 12 & \\ & 6 & 8 & 12 & 0 & \\ 4 & & 11 & & 0 & 13 \\ & 7 & 9 & & 13 & 0 \end{pmatrix} \quad (1)$$

One can determine the number of joints as follows:

$$J = \max(\mathbf{A}) \quad (2)$$

Another important feature of the structure is the classification of its welded joints. They can be divided into butt joints (no. 1), fillet joints (no. 2) and cross joints (no. 3), classes typically distinguished in shipbuilding. It is also worth considering the types of elements to be joined. It is easiest to

divide the elements into plates (no. 1), frames (no. 2), stiffeners (no. 3) and brackets (no. 4). As a result, each joint can be described with a three-digit class code:  $abc$ , where  $a$  and  $c$  are the types of elements being joined, while  $b$  is the joint type. For example, a joint classified as 221 is a fillet joint between a frame and a plate.

Not all joint classes can be found in real structures; for example, brackets are never joined, and there are no cross joints between stiffeners. For further analysis, 10 classes of welded joints are considered in Table 1.

Tab. 1. Classes of welds

Class number	Class code	Joined elements	Weld
1	111	plate + plate	butt
2	212	frame + frame	butt
3	313	stiffener + stiffener	butt
4	121	plate + plate	fillet
5	122	plate + frame	fillet
6	123	plate + stiffener	fillet
7	222	frame + frame	fillet
8	324	stiffener + bracket	fillet
9	133	plate + stiffener	cross
10	233	frame + stiffener	cross

It should be noted that this model does not impose a specific classification system. That system should be adapted to the individual needs of a user. A set of joint classes should not be so large as to make the analysis too complex. It is important to be able to clearly identify which joints are considered to be members of the same class and which joints are treated as essentially different.

Considering  $K$  joint classes, the classification using a binary matrix is defined:  $\mathbf{C} = (c_{j,k})_{J \times K}$ , where  $c_{j,k} = 1$  if and only if the  $j$ -th joint is assigned to the  $k$ -th class. A classification matrix for sample structure no. 1 (Fig. 3) is presented in Table 2.

Tab. 2. Classification of welds of sample structure no. 1

$C_1$		Classes											
		1	2	3	4	5	6	7	8	9	10		
Welds	1	1											
	2					1							
	3					1							
	4						1						
	5				1								
	6					1							
	7						1						
	8					1							
	9										1		
	10								1				
	11												1
	12		1										
	13			1									

The matrix  $C_i$  indicates that class 8 is not represented in the structure. Fillet joints between plates and frames (class 5) are the most frequent.

### CLUSTER ANALYSIS OF A DATABASE OF STRUCTURES

There is a very wide variety of structures in shipyard practice. In order to analyse the similarities between them, one needs to build a database of all structures described under a common classification system. Therefore, a universal set of joints can often go beyond a description of a single structure.

The considered database includes structure number 1 and five other structures shown in Fig. 4.

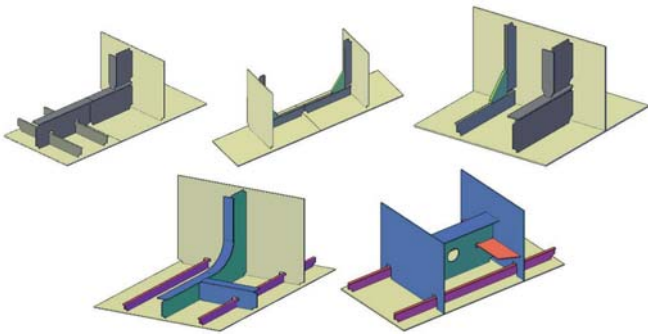


Fig. 4. Sample structure nos. 2-6

For each structure in the database, the cumulative classification vector is determined:

$$\chi = (\chi_1, \chi_2, \dots, \chi_K), \quad \forall k = 1, 2, \dots, K: \chi_k = \sum_{j=1}^J c_{j,k} \quad (3)$$

where  $\chi_k$  is the number of the class  $k$  joints that are present in the structure.

Each structure is therefore represented by a point in  $K$ -dimensional space.

The database is a set of  $B$  elements  $\{\chi_1, \chi_2, \dots, \chi_B\}$  and is subject to cluster analysis in order to evaluate all structures for similarities and differences. Clustering is completed by the FCM method. This method determines the degree of each structure's membership in each of the  $N$  clusters, and the result is the following matrix:  $U = (u_{n,b})_{N \times B}$ , where  $u_{n,b} \in [0,1]$  is a measure of the membership of structure  $b$  in cluster  $n$ .

In the FCM method, the solution depends on a control parameter  $m > 1$ . This parameter provides control over the degree of cluster overlap. Values close to 1 result in a sharp division. Increasing the parameter value results in equalisation of the structure's membership in different clusters. The calculation is performed according to the following algorithm:

1. filling in the initial membership matrix  $U$  by a draw,
2. determining cluster centres:

$$\alpha_n = \frac{\sum_{b=1}^B u_{n,b}^m \chi_b}{\sum_{b=1}^B u_{n,b}^m} \quad (4)$$

3. updating the structure's membership in clusters:

$$u_{n,b} = \frac{1}{\sum_{\eta=1}^N \left( \frac{\|\chi_b - \alpha_n\|}{\|\chi_b - \alpha_\eta\|} \right)^{\frac{2}{m-1}}} \quad (5)$$

4. calculation of the target function:

$$Q = \sum_{b=1}^B \sum_{n=1}^N u_{n,b}^m \|\chi_b - \alpha_n\|^2 \quad (6)$$

5. repeat steps 2-4 until the target function improvement is not less than a set level or until the iteration limit is reached.

Fuzzy membership of each structure in three clusters is shown in Table 3. For example, structure no. 1 is assigned to the third cluster more than to the first or second. However, the parameters of membership in all clusters do not differ by much. In turn, structure no. 3 was definitely assigned to cluster 2.

Tab. 3. Clustering for 3 groups with parameter  $m = 4$

$U_4$		Structure					
		1	2	3	4	5	6
Cluster	1	0.2614	0.3012	0.0461	0.3584	0.7552	0.4447
	2	0.1301	0.1727	0.9085	0.2719	0.0801	0.2311
	3	0.6085	0.5261	0.0454	0.3697	0.1647	0.3242

Based on the membership matrix  $U$ , a structure importance matrix is determined in clusters:

$$\forall n = 1, \dots, N, b = 1, \dots, B: w_{n,b} = \frac{u_{n,b}}{\sum_{\beta=1}^B u_{n,\beta}} \quad (7)$$

The results of the calculations are presented in Table 4. As a result of the transformation of matrix  $U$  into matrix  $W$ , the sum of the values in each row is equal to 1.

Tab. 4. Importance of structures in clusters for parameter  $m = 4$

$W_4$		Structure					
		1	2	3	4	5	6
Cluster	1	0.1206	0.139	0.0213	0.1654	0.3485	0.2052
	2	0.0725	0.0962	0.5063	0.1515	0.0446	0.1288
	3	0.2985	0.2581	0.0223	0.1813	0.0808	0.159

Matrix  $W$  characterizes each cluster by means of weights assigned to individual structures. The higher the weight of the structure in the cluster, the greater its impact on the characteristics of the cluster. The method of determining this characteristic is described below.

### ASSEMBLY PROCESS MODELLING

The assembly process will be described into a sequence of stages. Each stage is a period on the process timeline. In other words, we divide the process timeline into successive intervals of some indefinite length. Welding of one or more joints starts in every stage. Welding of any joint may take more than one stage, but the welding start time must be at the beginning of one of the stages. The stages do not have to be of equal duration. A structure assembly plan is a vector:

$$\mathbf{p} = (p_1, p_2, \dots, p_J) \quad (8)$$

where  $p_j$  is the number of the stage in which welding of the  $j$ -th joint starts.

For the database-stored structures shown in Fig. 3 and Fig. 4, assembly plans, which have been tested in practice and subjected to critical assessment, are defined. It is assumed that a plan stored in the database is a preferred solution for the given structure.

### ASSEMBLY SEQUENCE KNOWLEDGE

Based on the assembly plan  $\mathbf{p}$ , one can define a sequence relationship between joints with a square matrix:

$$\mathbf{SW} = (sw_{j_1, j_2})_{J \times J}, \quad \forall j_1, j_2 = 1, 2, \dots, J : sw_{j_1, j_2} = \frac{p_{j_2} - p_{j_1}}{S - 1} \quad (9)$$

where  $S$  equals the maximum value in vector  $\mathbf{p}$ .

The sequence  $\mathbf{SW}$  is determined for each structure stored in the database. For example, for structure no. 1, the matrix shown in Table 5 is obtained.

Tab. 5. Sequence of welding of example structure no. 1

SW <sub>1</sub>	Welds												
	1	2	3	4	5	6	7	8	9	10	11	12	13
1	0	-0.7	-0.3	-1	-0.7	-1	-1	-0.3	-0.3	-0.3			
2	0.7	0	0.3	-0.3		-0.3	-0.3	0.3	0.3	0.3	0.3	0.7	0.7
3	0.3	-0.3	0	-0.7	-0.3	-0.7	-0.7					0.3	0.3
4	1	0.3	0.7	0	0.3			0.7	0.7	0.7	0.7	1	1
5	0.7		0.3	-0.3	0	-0.3	-0.3	0.3	0.3	0.3	0.3	0.7	0.7
6	1	0.3	0.7		0.3	0		0.7	0.7	0.7	0.7	1	1
7	1	0.3	0.7		0.3		0	0.7	0.7	0.7	0.7	1	1
8	0.3	-0.3		-0.7	-0.3	-0.7	-0.7	0				0.3	0.3
9	0.3	-0.3		-0.7	-0.3	-0.7	-0.7		0			0.3	0.3
10	0.3	-0.3		-0.7	-0.3	-0.7	-0.7			0		0.3	0.3
11	0.3	-0.3		-0.7	-0.3	-0.7	-0.7				0	0.3	0.3
12		-0.7	-0.3	-1	-0.7	-1	-1	-0.3	-0.3	-0.3	-0.3	0	
13		-0.7	-0.3	-1	-0.7	-1	-1	-0.3	-0.3	-0.3	-0.3		0

The value of the component  $sw_{j_1, j_2} < 0$  (negative) indicates that joint  $j_1$  is completed at a later stage than joint  $j_2$ . The extreme value  $-1$  means that joint  $j_1$  is completed in the last stage of the process and joint  $j_2$  in the first stage. The positive values of the component  $sw_{j_1, j_2}$  indicate the opposite case. Of course, this equality holds:  $sw_{j_1, j_2} = -sw_{j_2, j_1}$ .

We generalize our knowledge of the assembly processes of individual structures by using the classification of their joints. The joint class sequence matrix is found with the formula:

$$\mathbf{SC}^{um} = \mathbf{C}^T \cdot \mathbf{SW} \cdot \mathbf{C} \quad (10)$$

$$\mathbf{SC} = \frac{\mathbf{SC}^{um}}{\max(\mathbf{SC}^{um})}$$

As with the matrix  $\mathbf{SW}$ , the class sequence also shows the direction and strength of the precedence relationship, but it applies to classes of joints. For structure number 1 discussed above, we obtain the matrix in Table 6.

Tab. 6. Sequence of welds classes for structure 1

SC <sub>1</sub>	Classes										
	1	2	3	4	5	6	7	8	9	10	
Classes	1	0			-0.2	-0.7	-0.6	-0.1		-0.1	-0.1
	2		0		-0.2	-0.7	-0.6	-0.1		-0.1	-0.1
	3			0	-0.2	-0.7	-0.6	-0.1		-0.1	-0.1
	4	0.2	0.2	0.2	0	0.1	-0.2	0.1		0.1	0.1
	5	0.7	0.7	0.7	-0.1	0	-1	0.3		0.3	0.3
	6	0.6	0.6	0.6	0.2	1	0	0.4		0.4	0.4
	7	0.1	0.1	0.1	-0.1	-0.3	-0.4	0			
	8								0		
	9	0.1	0.1	0.1	-0.1	-0.3	-0.4			0	
	10	0.1	0.1	0.1	-0.1	-0.3	-0.4				0

Class 5 is quite strongly indicated to precede classes 1, 2 and 3. Class 6 has a smaller tendency to precede classes 1, 2 and 3 but a greater tendency to precede classes 4, 7, 9 and 10. Class 8 welds (comprising a stiffener and a bracket), do not have a specific relationship with any class. This is understandable because this class is not represented in structure 1.

The class sequences are calculated for all structures in the database in order to obtain aggregate knowledge of preferred solutions within the previously determined clusters. In practice, we determine each cluster's sequence matrix as a weighted average:

$$\forall n = 1, 2, \dots, N : \mathbf{SCC}_n = \sum_{b=1}^B w_{n,b} \cdot \mathbf{SC}_b \quad (11)$$

Of course, there is still the parameter  $m$ , which controls the importance of structure in clusters. For example, with the value of  $m = 4$  and for the division of the described database into three clusters, three sequence matrices are obtained.

A sample matrix for cluster number 3 is shown in Table 7. Values significantly different from zero are in bold type.

Tab. 7. Sequence for cluster 3 and parameter  $m = 4$

SCC <sub>4,2</sub>		Classes									
		1	2	3	4	5	6	7	8	9	10
Classes	1	0			-0.09	-0.34	-0.32	-0.03	-0.01	-0.03	-0.03
	2		0		-0.09	-0.34	-0.31	-0.03		-0.03	-0.03
	3			0	-0.06	-0.21	-0.19	-0.03	-0.01	-0.03	-0.03
	4	0.09	0.09	0.06	0	-0.07	-0.35	0.06		0.03	0.09
	5	<b>0.34</b>	<b>0.34</b>	0.21	0.07	0	-0.87	<b>0.33</b>	0.18	0.10	<b>0.36</b>
	6	<b>0.32</b>	<b>0.31</b>	0.19	<b>0.35</b>	<b>0.87</b>	0	<b>0.38</b>	0.20	<b>0.36</b>	<b>0.46</b>
	7	0.03	0.03	0.03	-0.06	-0.33	-0.38	0			
	8	0.01		0.01		-0.18	-0.20		0		
	9	0.03	0.03	0.03	-0.03	-0.10	<b>-0.36</b>			0	
	10	0.03	0.03	0.03	-0.09	<b>-0.36</b>	<b>-0.46</b>				0

The selection of the cluster and the related matrix  $\mathbf{SCC}$  depends on the architecture of the new structure under analysis and for which we are planning the assembly. We select the cluster with a centroid  $\mathbf{a}$  (see formula 4) that is closest to the new structure's aggregate classification vector.

## OPTIMISATION OF THE NEW STRUCTURE'S ASSEMBLY

In order to use the developed mathematical models in shipbuilding, it is necessary to supplement the method with a module for generating new assembly plans. The computational algorithm expanded to include the optimisation of the new plan can be summarised in the following steps:

- setting the control parameter  $m$ , for which the database is clustered,
- determining the number of stages of the assembly process being planned  $S_{\text{new}}^{\text{max}}$ ,
- determining an aggregate classification vector  $\chi_{\text{new}}$ ,
- selecting the cluster with its centroid at the smallest Euclidean distance from the vector  $\chi_{\text{new}}$ ,
- determining the sequence matrix  $\mathbf{SCC}_{m,n}$  for the selected  $n$ -th cluster,
- searching for the plan vector  $\mathbf{p}_n$ , which corresponds to a sequence of joint classes  $\mathbf{SC}_{\text{new}}$  that minimizes the function:

$$f = \sum_{k1=1}^{K-1} \sum_{k2=k1+1}^K \chi_{\text{new},k1} \cdot \chi_{\text{new},k2} \cdot \alpha_{n,k1} \cdot \alpha_{n,k2} \cdot |s_{\text{new},k1,k2} - s_{\text{CC},m,n,k1,k2}| \rightarrow \min \quad (12)$$

The plan can be optimised by an evolutionary method, using classic crossover and mutation operators. The draw of the first generation produces the assumed number of plan vectors. Each vector is a sequence of random numbers from the interval  $[1, S_{\text{new}}^{\text{max}}]$ . The crossover of plans contained in the population is relatively simple, as it is performed by exchanging some vectors  $\mathbf{p}$  assigned to two parents. The intersection of the vectors is selected randomly. The crossover may cause a change in the number of assembly stages,

which is desirable as it increases the diversity of plans being analysed. The mutating operator is used with a predetermined probability. This operator replaces one of the components of the plan vector  $\mathbf{p}$  with another random value from the range  $[1, S_{\text{new}}^{\text{max}}]$ . Fig. 5 shows the procedure for planning the assembly of a new structure.

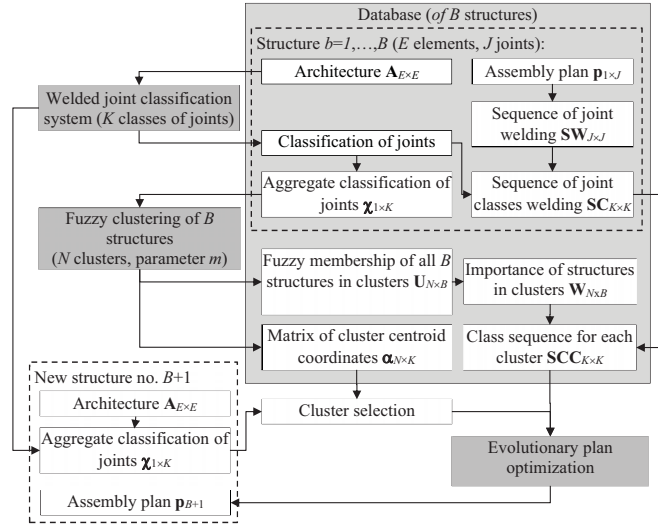


Fig. 5. Algorithm of the procedure for implementing the RETRIEVE and REUSE stages of the proposed MBAP method

## EXAMPLE OF APPLICATION

Sample calculations were performed for the structure shown in Fig. 6. It consists of five plates (elements 1–5), two frames (elements 6 and 7), two stiffeners (elements 8 and 9) and a bracket (element 10). The complexity of structure no. 7 has been matched to the relatively non-complex structures in the database.

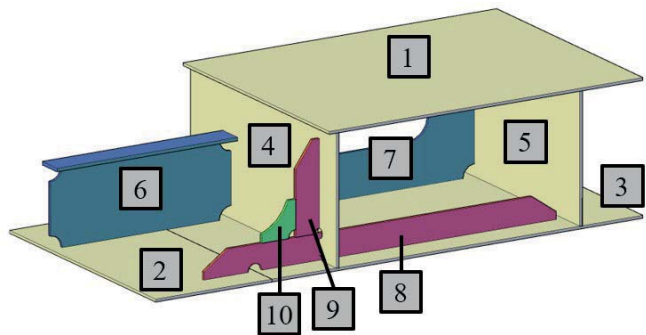


Fig. 6. Sample structure no. 7

The architecture of structure no. 7 is a simplified two-shell structure. There were 19 welded joints identified between the elements.

The analysis is aimed to verify whether the MBAP method can generate an assembly plan that is feasible and meets the sequence rules included in reference structure plans.

For 10 classes and the structure consisting of 19 joints, the optimization calculations were performed by a mid-range computer in 1 second. The evolutionary algorithm has reached a suboptimal solution after 200 cycles when there were 20 specimens in the population.

The calculation resulted in the following assembly plan:

$$\mathbf{p}_7 = (1, 1, 2, 1, 2, 2, 3, 3, 2, 4, 2, 4, 2, 4, 4, 2, 5, 5, 5) \quad (13)$$

The plan  $\mathbf{p}^7$  is implemented in five stages (Fig. 7). In the first stage, plates no. 2 and 3 are butt-welded, and plate no. 1 is joined with plates no. 4 and 5. In this way, two subassembled units are created, which are further expanded in the next step. Subassemblies are joined in stage 3. In stage 4, stiffener no. 9 is added, and structure reinforcement welds are completed. The last element, or bracket no. 10, is added in stage 5.

The result of optimisation calculations can be considered satisfactory. The advantage of this solution is that most welds can be completed from underneath. One of the subassembled units in its final position is shown in Fig. 7, but in practice, it will be completed in the inverted position. It should be considered whether frame no. 6 should be added before the two subassemblies are joined. Adding this element in stage no. 3 or later will enable better control of the welding deformation and easier relative positioning of subassemblies.

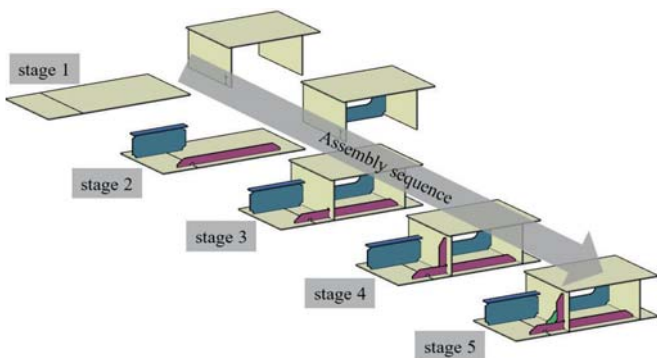


Fig. 7. Assembly sequence for structure no. 7 generated by the MBAP method

The major disadvantage of this solution is the addition of stiffener no. 9 only in stage no. 4. This operation requires welding vertically or rotating the entire structure when welding. It would be better to join this stiffener with plate no. 4 in the first stage of assembly and join plate no. 4 with plate no. 1 only in the next stage.

However, the obtained assembly plan confirms the ability of the MBAP to generate interesting solutions that can be a valuable support for production engineers.

## CONCLUSIONS

This article has highlighted the complexity of planning problems in ship hull assembly. There are relatively few papers dealing with these issues, and they present a simplified

approach with a strong focus on experts' involvement in the decision-making process. As a result, the published methods have a limited practical value. In this article, attempts have been made to develop a method for managing the shipyard database and generating assembly plans for structures of any size. The focus was on welding processes, as they are crucial to shipbuilding, which distinguishes this sector from the machinery industry.

The presented example of the application of the MBAP method shows that the general concept is correct. Successful reasoning based on the cases stored in the database can be traced. It has also been shown that the obtained results require independent evaluation. Like any method based on computational intelligence, MBAP also requires a large amount of data to function properly. The initial stages of its implementation require a learning process and the supervision of production engineers. During the implementation process, the values of the control parameters should be set.

The MBAP method requires a shipyard to archive and analyse the data on the processes completed in order to acquire knowledge useful for assembly planning. The article proposes a system that allows for flexible definition of element and weld classes. As a result, the method can be adapted to a specific production profile. The article proposes a two-step approach to classification. In the first step, structural elements are classified by their geometry and, at the same time, welded joints are classified by their geometry and the functions they perform. In the second stage, both element and weld classes are considered. As a result, a so-called class code is assigned to each weld. The classification is the basis for analysing the similarities between structures and clustering the database. The proposed method uses fuzzy clustering, but it is also possible to develop hierarchical links between structures. As a result, the shipyard is able to extend the CIM system to include further modules, for example, to assist in the planning of plate cutting during processing, planning of supplies, etc.

It is worth noting that the proposed approach to assembly planning is versatile and can be adapted to planning various processes, particularly, very complex, long-term and high capacity-intensive projects. The system should be further developed toward greater automation in data exchange between the computing module and the CAD software used in a shipyard's design office. Manual input of geometric data is too labour-intensive for hulls containing thousands of elements. Modern design software systems include functions for exporting necessary information, but the standardisation of data between different systems is currently being investigated. It is also important to stress the need to expand the capabilities of MBAP to include new optimization criteria. An important direction for development is, for example, to address the problem of job queuing at workstations. From a strategic planning point of view, it is important to examine more closely the links between production system performance and the assembly plans being implemented.

## REFERENCES

1. M. Suszyński, M. Rogalewicz, 'Selection of an Industrial Robot for Assembly Jobs Using Multi-Criteria Decision Making Methods', *Management and Production Engineering Review*. 2020, doi: 10.24425/mper.2020.
2. R. Iwańkiewicz and R. Rutkowski, 'Assembly Management in the Shipyard Using a Welding Database', in: *Application of Computational Methods in Engineering Science*. Wydawnictwo Politechniki Lubelskiej, Lublin 2019.
3. M. Deja, M. S. Siemiatkowski, and D. Zielinski, 'Multi-criteria comparative analysis of the use of subtractive and additive technologies in the manufacturing of offshore machinery components', *Polish Maritime Research*. 2020, doi: 10.2478/pomr-2020-0048.
4. X. Li, Z. Zhu, Y. Li, and Z. Hu, 'Design and Mechanical Analysis of a Composite T-Type Connection Structure for Marine Structures', *Polish Maritime Research*. 2020, doi: 10.2478/pomr-2020-0036.
5. R. Iwańkiewicz, 'An efficient evolutionary method of assembly sequence planning for shipbuilding industry', *Assembly Automation*. 2016, doi: 10.1108/AA-02-2015-013.
6. M. Kang, J. Seo, and H. Chung, 'Ship block assembly sequence planning considering productivity and welding deformation', *International Journal of Naval Architecture and Ocean Engineering*. 2017, doi: 10.1016/j.ijnaoe.2017.09.005.
7. D. Kolich, R. L. Storch, and N. Fafandjel, 'Lean built-up panel assembly in a newbuilding shipyard', *Journal of Ship Production and Design*. 2018, doi: 10.5957/JSPD.170007.
8. A. Oliveira, and J. M. Gordo, 'Lean tools applied to a shipbuilding panel line assembling process', *Brodogradnja: Teorija i praksa brodogradnje i pomorske tehnike*. 2018, doi: 10.21278/brod69404.
9. F. Bonneville, C. Perrard, and J. M. Henrioud, 'A genetic algorithm to generate and evaluate assembly plans', *IEEE Symposium on Emerging Technology and Factory Automation*. 1995, doi: 10.1109/ETFA.1995.496663.
10. S.F. Chen and Y.J. Liu, 'An adaptive genetic assembly-sequence planner', *International Journal of Computer Integrated Manufacturing*. 2001, doi: 10.1080/09511920110034987.
11. R. Schank, *Dynamic memory: A theory of reminding and learning in computers and people*. Cambridge University Press, 1982.
12. J. Kolodner, 'Reconstructive memory, a computer model'. *Cognitive Science*. 1983, doi: 10.1016/S0364-0213(83)80002-0.
13. A. Aamodt and E. Plaza, 'Case-based reasoning: Foundational issues, methodological variations, and aystem approaches', *AI Communications*. IOS Press. 1994, doi: 10.3233/AIC-1994-7104.
14. Q. Shipeng, J. Zuhua, and T. Ningrong, 'An integrated method for block assembly sequence planning in shipbuilding', *The International Journal of Advanced Manufacturing Technology*. 2013, doi: 10.1007/s00170-013-5087-6.
15. K.K. Cho, S.H. Lee, and D.S. Chung, 'An automatic process-planning system for block assembly in shipbuilding', *Annals of the CIRP*. 1996, doi: 10.1016/S0007-8506(07)63013-3.
16. K.K. Cho, J.G. Sun, and J.S. Oh, 'An automated welding operation planning system for block assembly in shipbuilding', *International Journal of Production Economics*. 1999, doi: 10.1016/S0925-5273(98)00151-0.
17. S. Qu, Z. Jiang, and N. Tao, 'An integrated method for block assembly sequence planning in shipbuilding', *The International Journal of Advanced Manufacturing Technology*. 2013, doi: 10.1007/s00170-013-5087-6.
18. Y. Seo, D. Sheen, and T. Kim, 'Block assembly planning in shipbuilding using case-based reasoning', *Expert Systems with Applications*. 2007, doi: 10.1016/j.eswa.2005.11.013
19. J.C. Bezdek, 'Pattern recognition with fuzzy objective function algorithms', *Plenum Press, New York*. 1981, doi:10.1007/978-1-4757-0450-1.
20. M.J. Khan and C. Khan, 'Performance evaluation of fuzzy clustered case-based reasoning', *Journal of Experimental & Theoretical Artificial Intelligence*. 2020, doi: 10.1080/0952813X.2020.1744194.

## CONTACT WITH THE AUTHOR

**Remigiusz Iwańkiewicz**

*e-mail: r.iwankowicz@am.szczecin.pl*

Maritime University of Szczecin,  
ul. Wały Chrobrego 1-2, 70-500 Szczecin,  
**POLAND**

# APPLICATION OF AN ARTIFICIAL NEURAL NETWORK AND MULTIPLE NONLINEAR REGRESSION TO ESTIMATE CONTAINER SHIP LENGTH BETWEEN PERPENDICULARS

Tomasz Cepowski\*

Paweł Chorab

Dorota Łozowicka

Akademia Morska w Szczecinie, W. Chrobrego 1-2, 70-500 Szczecin, Polska

\* Corresponding author: [t.cepowski@am.szczecin.pl](mailto:t.cepowski@am.szczecin.pl) (T. Cepowski)

## ABSTRACT

*Container ship length was estimated using artificial neural networks (ANN), as well as a random search based on Multiple Nonlinear Regression (MNL). Two alternative equations were developed to estimate the length between perpendiculars based on container number and ship velocity using the aforementioned methods and an up-to-date container ship database. These equations could have practical applications during the preliminary design stage of a container ship. The application of heuristic techniques for the development of a MNL model by variable and function randomisation leads to the automatic discovery of equation sets. It has been shown that an equation elaborated using this method, based on a random search, is more accurate and has a simpler mathematical form than an equation derived using ANN.*

**Keywords:** ship design, ANN, regression, container ship, length

## INTRODUCTION

The ship design process consists of three main stages: the preliminary, contract, and detailed design steps. The key characteristics of ship design are based on the main requirements of a shipowner during the preliminary design stage. A parametric and geometric design stage are the main phases of preliminary design. Watson [1], Rawson and Tupper [2], and Papanikolaou [3] have argued that the selection of a ship's main dimensions such as length, breadth, and draught are the main parametric design objectives. However, there is no detailed information about technical characteristics of a ship during the parametric design stage to accurately estimate these parameters. The ship designer

should resolve this problem and select these characteristics based on the requirements of the shipowner, the character of the ship's mission, and various formal maritime rules and regulations [1-3].

Ship design is a loop iterate process which goes through a design spiral, originally introduced in 1959 by Evans [4] and modified in 1985 by Andrews [5]. The inaccurate estimation of ship dimensions during the parametric design stage increases the number of design spiral loops, and the design time and project cost. As noted by Papanikolaou [3] and Chądzyński [6] for a standard ship type, various statistical, empirical, or regression methods based on similar ship builds may be used to solve this problem.

Chądzyński [6] and Papanikolaou [3] argued that initially, the length of a cargo ship is estimated based on cargo capacity, such as its deadweight, hold, or TEU capacity. Other ship dimensions are usually estimated based on this length at later stages.

Various linear or nonlinear equations developed using a container ship database have often been used for the initial estimation of a ship's length. Piko [7], Kristensen [8], and Papanikolaou [3] prepared a set of equations for estimating a container ship's main dimensions. Piko's equations were based on the statistical data of container ships that were being built up to 1980. Papanikolaou used the data of container ships built prior to 2005 and Kristensen used a database of container ships built before 2013. Linear and nonlinear regression methods were used in these studies.

Over the past 20 years, container ship design trends have been influenced by market and trade demands. The financial crisis of 2007-2008, together with fuel price changes and strict emission requirements have all had an influence on these trends. Container ships are usually categorised as volume carriers in common design procedures. Container number and velocity are the main requirements of any container ship owner. Economic and environmental factors could have an influence on changing these requirements and later, the design process in the future. Figure 1 shows container ship age profiles which are dependent on size and mean speed values. The Sea-web Ships database [9] of all container ships built from 2000-2020 was used in this analysis. Figure 1 shows that container ship capacity and speed have fluctuated to a large degree throughout the last 6-7 years. Moreover, the latest container ships usually have a higher TEU capacity and a lower Froude number.

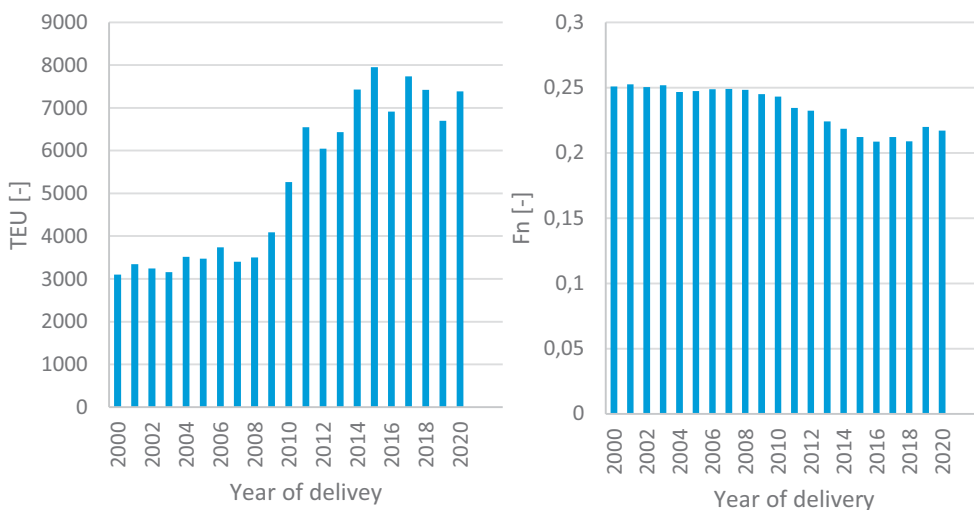


Fig. 1. Age profiles of the container ships: mean number of containers' TEU capacity and Froude number ( $F_n$ ) vs delivery year

Old regression formulas developed before 2014 are inadequate for considering the design trend changes of modern container ships.

A literature review showed that key container ship characteristic equations were developed based on deadweight or container number capacity. While Piko [7] and Papanikolaou [3] used deadweight capacity, Kristensen [8] used a TEU container number for a ship's characteristic estimation. Deadweight capacity includes the mass of the cargo, ballast, and ship stores. To calculate the cargo mass, the number and mass of containers must be known. Container mass is based on the number of containers. However, a design characteristic estimation based on the number of TEU containers does not include ballast and store mass. However, a deadweight calculation using the number of containers required is unnecessary in this case.

A literature review did not show which parameter led to the smallest estimation error of a design characteristic, i.e., the deadweight or container number capacity. Piko, Papanikolaou, and Kristensen's formulas for a container ship length's estimate did not consider velocity, despite it being a main ship owner's requirement. These formulas were developed using regression methods. Initially, Piko implemented nonlinear approximation methods such as power and 2<sup>nd</sup> degree polynomial regression models. Deadweight was used as an independent variable in these equations. Piko compared the results and considered that the functions developed using the power regression model provided reliable estimates of the parameters over a wider range of deadweights.

Papanikolaou [3] presented a theory and a detailed compendium of knowledge on practical methods for the preliminary design of a ship. This book also provides an equation for estimating the length between perpendiculars of a container ship using the deadweight developed using

a power regression model. In Piko and Papanikolaou's studies, the exponent values of non-linear regression functions were similar and almost 0.4. The Kristensen approximations were based only on TEU capacity and were developed using linear, 2<sup>nd</sup> degree polynomial and power regression models. In this study, the exponents of the power regression models were 0.38, 0.55, and 0.34 for Small, Panamax, and Post-Panamax container ships, respectively.

There have been no publications in the scientific literature on the use of artificial neural networks (ANN) to determine the length of a container vessel. Only Gurgun et al. [10] applied an ANN to predict the main dimensions of chemical tankers using deadweight capacity and speed. An ANN based on a multi-layer perceptron structure with 13 neurons in a hidden layer was used in this research. Gurgun et al. [10] argued that

neural networks may create more accurate models for complex systems than standard statistical methods.

Therefore, the aim of this study was to develop an empirical equation to estimate the length between perpendiculars for container ships built since 2014, considering the container number and velocity.

## MATERIALS AND METHODS

The container ship characteristics used in this study are defined as follows:

Length between perpendiculars (LBP) – the horizontal distance measured parallel to the baseline from the aft to forward perpendicular.

Ship velocity (V) – service speed in knots, which is less than the maximum ahead service speed.

TEU – the maximum number of 20-foot standard containers below and above the deck.

Deadweight (DWT) – the maximum deadweight of the ship immersed at the summer load line in water with a 1.025 t/m<sup>3</sup> density.

Froude number (Fn) – a dimensional number calculated as shown in Eq.(1).

$$Fn = \frac{V}{\sqrt{g \times L}} \quad (1)$$

where

V – ship velocity in m/s,

g – standard gravity.

L – length of the ship (it was here assumed that L = LBP)

The data of the 120 latest new build container ships from 2014 to 2020 was used in this study. The source of the data was Sea-web Ships [9]. Sister ships with identical or similar characteristics were removed from the data set. The range and mean values of ship samples that remained after verification are shown in Table 1.

Tab. 1. The mean, minimal, and maximal values of container ships, where: LBP = length between perpendiculars, B – breadth, D – side depth, T – draft, V – velocity, TEU – the number of containers, DWT – deadweight, and Fn – Froude number

	LBP [m]	LBP/B [-]	B/D [-]	T [m]	V [kts]	TEU [-]	DWT [t]	Fn [-]
Min	69.20	3.95	1.61	3.50	9.0	100	1780	0.15
Mean	214.59	6.12	1.96	10.94	19.0	5265	60675	0.22
Max	386.23	7.26	3.67	16.50	25.0	21000	202036	0.30

In this study, ANNs and a random search method based on nonlinear regression and heuristics techniques were used to estimate the container ship's length. The second aim of the research was to compare the accuracy of these methods for estimating the container ship's length.

## ARTIFICIAL NEURAL NETWORKS (ANN)

In recent years, ANNs have been used in several scientific ship design theory publications. For example, Alkan et al. [11] calculated the initial stability parameters of a fishing vessel using neural networks. Artificial neural networks were developed using sample ship data to estimate the vertical centre of gravity, the transverse metacentre height above the keel, and the vertical centre of buoyancy of the ship. Gurgun et al. [10] created an ANN to estimate chemical tanker dimensions. In this paper, the main ship parameters, such as, overall length, length between perpendiculars, breadth, draught, and freeboard were estimated based on deadweight and vessel speed. Gurgun et al. [10] argued that the initial main particulars of chemical tankers could be determined using ANNs, offering results which were much more accurate than those obtained with sample ship data. Ekinci et al. [12] used 18 computational intelligence methods (including neural network methods) to estimate the main design parameters of oil/chemical tankers. Abramowski [13] developed a model for determining the effective power of a ship using neural networks. In this publication, a mathematical model was developed using neural networks to determine the effective power of a ship. Cepowski [14] applied ANNs to estimate added resistance in regular head waves while using ship design parameters, such as length, breadth, draught, and Froude number. To create a reliable model, only experimental data determined through model test measurements was used to train the neural network. Song et al. [15] used the radial base function ANN to predict a ship's rolling motion. Based on this method, the disturbing moment and roll time series were estimated. Sahin et al. [16] used the ANN model linked to the main ship parameters to estimate the dilution factors in the preliminary design. Gross and deadweight ton, passenger number, freeboard, engine power, propeller number, and block coefficient values were used to estimate the likely dilution factors. Luan et al. [17] used ANNs to

estimate the fuel consumption of container vessels. Cheng et al. [18] presented a comparative study of the sensitivity analysis and simplification of the ANN for a ship's motion prediction. Indeed, the use of ANNs has provided excellent results in several research experiments.

An ANN was created based on the functioning of the biological nervous system. The nervous system is a structure consisting of neurons and connections linking them. A numerical model of the neural network was developed based on this structure and the signal transmission method. The neural network was built from an input, output, and one or more hidden layers that consist of neurons [19]. Values from previous layers were passed through neurons which were connected with weights. These weights determined the relationships between input and output data [20]. The main

problem in developing an artificial network is selecting an optimal network structure and calculating the neuron weight values. Therefore, different types of neural networks and methods of learning can be used. Multilayer nonlinear neural networks and a learning backpropagation algorithm are often applied to predict technical parameters.

Overfitting phenomena are an additional problem in the development of neural networks. This phenomenon occurs when a statistical model has too many parameters in relation to the data sample size used in the creation of the model. A test set method is usually used to detect this phenomenon. Unfortunately, about 25-30% of randomly selected data is wasted to test the model in this method. Additionally, about 25-30% of data are used to validate the neural network during the learning process. This means that about half of the dataset is wasted throughout the neural network development process.

In this study, the search process for the best neural network included the following steps:

- creating a neural network topology,
- training a network,
- testing a network,
- making an accuracy assessment of a network's model based on the test results.

The statistical method of mean absolute error (MAE) value was used for an accuracy assessment Eq (2).

$$MAE = \frac{\sum |LBP - LBP_e|}{n} \quad (2)$$

where:

- LBP – length between perpendiculars from the data set,
- LBP<sub>e</sub> – estimated length between perpendiculars using a neural network,
- n – number of ships in the data set.

The following neural network types were tested for container ship length prediction:

- generalised regression neural network (GRNN),
- multilayer perceptron (MLP),
- radial basis function network (RBF),
- linear network.

To develop these neural networks the following assumptions were made:

- sum of squares as an error function,
- backpropagation as demonstrated by [19,21,22], the conjugate gradient descent [19], and Levenberga-Marquardt [23,24] as a training algorithm,
- logistic sigmoid function as activation,
- validation and test sets included 30 cases each (60 cases in total).

## RANDOM SEARCH METHOD

A random search method based on a Multiple Nonlinear Regression (MNL) and heuristic algorithm was applied to estimate the alternative length between perpendiculars. A general MNL model is given by the relations in Eq. (3) [25,26].

$$Y = \alpha + \beta_1 X_1 + \beta_2 X_j + \beta_3 X_1^2 + \beta_4 X_j^2 + \dots + \beta_k X_i X_j \quad (3)$$

where:

- Y – dependent variable,
- X – independent variables,
- i, j – number of independent variables,
- α – intercept,
- β – coefficient,
- k – observation number.

The authors defined the following general model Eq. (4) to develop the relationship between the length between perpendiculars (LBP), velocity (V), and the number of containers (TEU) based on the model Eq. (3):

$$LBP = \alpha + \beta_1 f_1(V) + \dots + \beta_n f_n(V) + \beta_{n+1} f_{n+1}(TEU) + \dots + \beta_{n+m} f_{n+m}(TEU) + \beta_{n+m+1} f_{n+m+1}(V) f_{n+m+2}(TEU) + \dots + \beta_{n+m+z} f_{n+m+k-1}(V) f_{n+m+k}(TEU) \quad (4)$$

where:

- α – intercept,
- β – coefficient,
- f – base function, such as power, logarithmic, or exponential function,
- n, m, k, z – the number of functions or β coefficient.

A set of 400 power, logarithmic, or exponential functions was used in this study. Finding the best TEU and V combinations in this model and selecting the best-fitting functions from the function set led to a large number of possible variants. For example, if we assume the simplest model Eq. (5):

$$LBP = \alpha + \beta_1 f_1(V) + \beta_2 f_2(TEU) + \beta_3 f_3(V) f_4(TEU) \quad (5)$$

which consists of four function combinations (f1, ..., f4) selected from a collection of 400 base functions, we get the total combination number (n):

$$n = 400^4 = 2,65E+10 \quad (6)$$

Searching through all these possible variants using an exact algorithm is computationally expensive and time-consuming, and thus, a heuristic approach was applied to solve this problem. The disadvantage of this method is that the solution is not as optimal as the exact approach. However, multiple searches allow the user to find a solution which is almost optimal.

An algorithm can be developed in which variables and base function combinations are randomised during the first step. Then, the model's fit to data is checked, and statistical errors are calculated. Finally, the best functions and variable combinations are selected through looped searching.

The authors implemented selected parts of this algorithm in the ndCurveMaster computer program [27] which was used to support equation searching.

Increasing model elements improves accuracy but may lead to overfitting with this method. Therefore, the next problem was to detect and prevent overfitting.

A test set was randomly selected from the data set to detect overfitting. The following two data sets were selected:

- data set A contained 75% of all data (90 cases) used for model development,
- test data set B contained 25% of all data (30 cases) used for overfitting detection.

For data sets A and B, the root mean squared errors RMSE(A) and RMSE(B) were calculated using the following formula:

$$RMSE(A \text{ or } B) = \sqrt{\frac{\sum(LBP - LBP_e)^2}{n}} \quad (7)$$

where:

- LBP – length between perpendiculars from the data set,
- $LBP_e$  – estimated length between perpendiculars,
- n – number of ships in set A or B.

In this study it was assumed that overfitting occurs when the root mean squared error related to test set B is 20% higher than the root mean squared error related to set A. To estimate the overfitting, the ratio of the error RMSE(B) to RMSE(A) was calculated.

The algorithm schemes are shown in Figures 2 and 3. As shown in Figure 2, during the first step, data for sets A and B were randomly selected, and the simplest model (5) was initially defined. Next, the best functions  $f_1$ – $f_4$  and regression coefficient values were discovered through random searching, based on the algorithm shown in Figure 3. Better functions were selected based on a higher correlation coefficient R value.

As shown in Fig 2, after the initial development of the model (5), a standard error (SE) value was checked. The research assumed that the SE value limit was 7.7 m (ship length).

If the SE was greater than this limit value, the model was randomly expanded in the next step. After this expansion, the occurrence of overfitting phenomena was checked by computing the ratio RMSE(B)/RMSE(A). If this ratio value was greater than 1.2, the least statistically significant component was removed from the model. This procedure was looped until these two conditions were met.

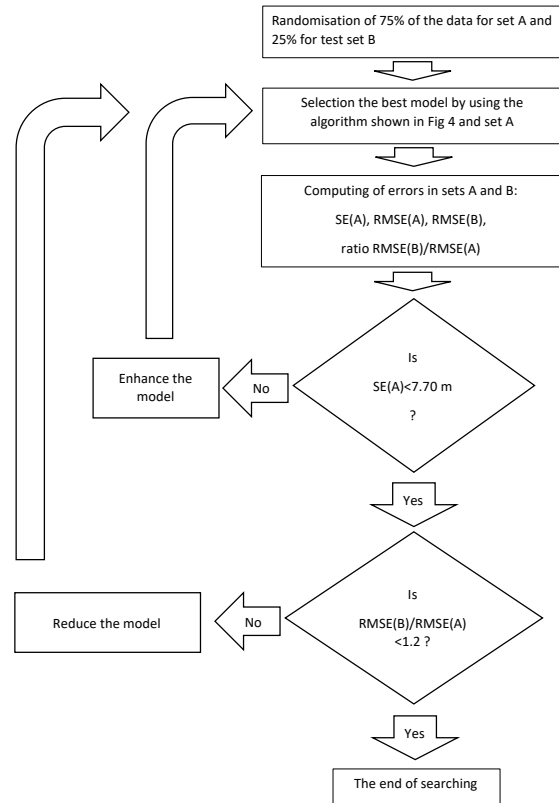


Fig. 2. The general algorithm scheme, where: A – data set, B – test data set, SE(A) – standard error related to set A, RMSE(A) – root mean squared error related to set A, RMSE(B) – root mean squared error related to test set B

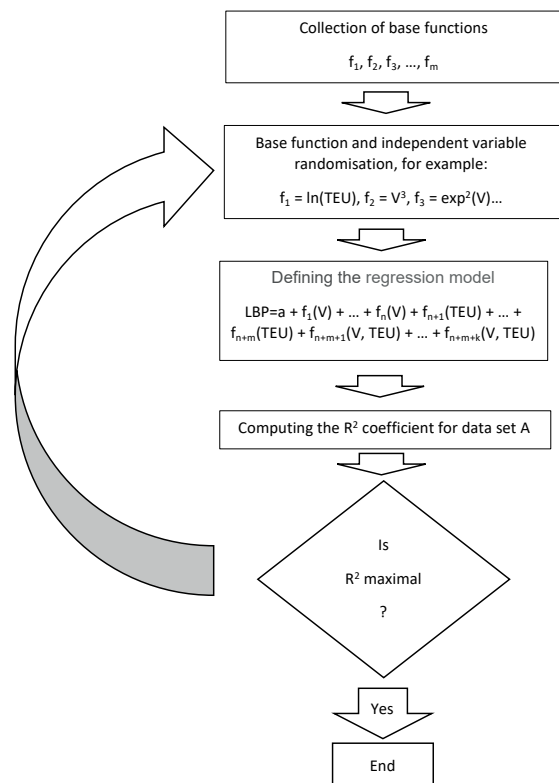


Fig. 3. The general algorithm scheme for searching the model for the maximum R-squared value, where f – base function, n, m, k – the number of functions

## RESULTS

### ARTIFICIAL NEURAL NETWORKS

Among all the neural network types, the multiple perceptron (MLP), which has two neurons in the input layer, 11 neurons in the hidden layer, and one neuron in the output layer, was the most accurate. Table 2 shows the statistical data of this neural network broken down by teaching, validation, and testing sets. The mathematical form of this network is given by the formulas in Eqs. (8), (9), (10), (11), (12), and (13).

$$\text{LBP} = \frac{c}{0.00318} + 0.22 \quad (2)$$

where:

c – the variable, calculated as follows:

$$c = [0.098, 0.297, -1.485, -0.032, -0.176, -1.325, -0.529, -0.702, -0.727, -0.494, 4.206] \times A + 1.386 \quad (3)$$

where

A – column matrix:

$$A = \begin{bmatrix} 1 \\ \frac{1}{1+e^{-a_1}} \\ 1 \\ \frac{1}{1+e^{-a_2}} \\ \frac{1}{1+e^{-a_3}} \\ \vdots \\ 1 \\ \frac{1}{1+e^{-a_{11}}} \end{bmatrix}$$

where:

$$\begin{bmatrix} a_1 \\ a_2 \\ a_3 \\ a_4 \\ a_5 \\ a_6 \\ a_7 \\ a_8 \\ a_9 \\ a_{10} \\ a_{11} \end{bmatrix} = \begin{bmatrix} 0.899 & -0.219 \\ 0.416 & -0.965 \\ -0.993 & -0.426 \\ -0.036 & -0.159 \\ 0.486 & -0.604 \\ -0.739 & 0.330 \\ 0.704 & 0.001 \\ -0.575 & 0.053 \\ 0.438 & -0.448 \\ -0.672 & 0.541 \\ 7.409 & 0.280 \end{bmatrix} \times \begin{bmatrix} b_1 \\ b_2 \end{bmatrix} - \begin{bmatrix} 0.007 \\ 0.509 \\ -0.032 \\ 0.822 \\ 0.764 \\ 0.320 \\ 0.675 \\ 0.735 \\ -0.003 \\ -1.239 \\ -2.186 \end{bmatrix} \quad (5)$$

where:

$$b_1 = \text{TEU} \cdot 4.89 \cdot 10^{-5} + 0.00489 \quad (6)$$

$$b_2 = V \cdot 0.0654 + 0.5882 \quad (7)$$

Tab. 2. Statistical parameters of an ANN

	Training set	Validation set	Testing set
Mean absolute error (MAE)	8.49	8.12	7.88
Correlation	0.99	0.99	0.99

### RANDOM SEARCH METHOD

Figures 4 and 5 show the process of discovering an equation for estimating the length between perpendiculars using the random search method. The SE value related to set A, the ratio RMSE(B)/RMSE(A), and the number of model elements are shown through the model evolution. In the first phase, the model was inaccurate and the SE value was high. Therefore, the model was expanded to seven elements in the next phase. This model extension reduced the SE error but increased the RMSE(B)/RMSE(A) ratio which overfitted the model. In the next phase, the model was reduced to four elements to avoid overfitting. However, the model accuracy was reduced after this procedure. Finally, increasing the model element number to five and finding the most accurate functions allowed the successful completion of this search. Eq. (14) was discovered:

$$\text{LBP} = 54.296 + 2.656 \cdot \text{TEU}^{1/2} + 1.4\text{E-}06 \cdot V^{5.6} - 2.821\text{E-}21 \cdot \text{TEU}^{5.6} \cdot V^{-1.8} - 1.116\text{E+}08 \cdot \text{TEU}^{-1.3} \cdot V^{-4} - 1.007\text{E-}04 \cdot \text{TEU}^{0.4} \cdot V^{3.1} \quad (8)$$

Eq. (14) is characterised by high accuracy for set A, i.e.:

- R-squared = 0.993,
- Standard error SE = 7.69 m.

The error difference between set A and test set B is less than 20%, i.e.:

- Root mean squared error related to set A RMSE(A) = 7.43 m,
- Root mean squared error related to set test B RMSE(B) = 8.69 m,
- the ratio of RMSE(B) to RMSE(A) = 1.17.

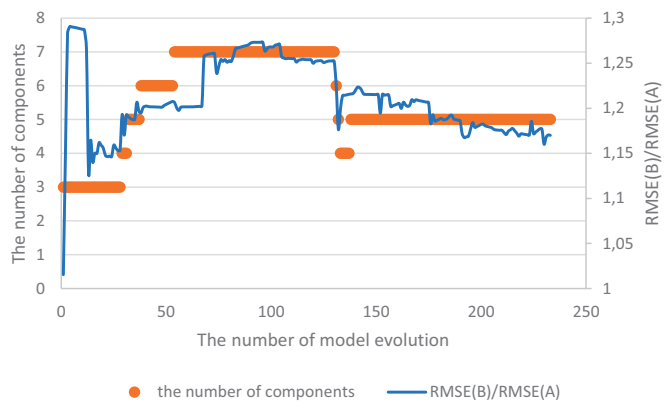


Fig. 2. The ratio of the root mean squared error in test set RMSE(B) to data set RMSE(A), and the number of model elements through the model evolution

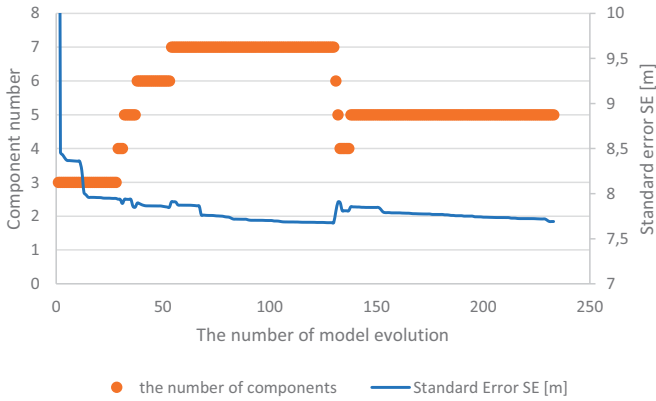


Fig. 5. Standard error (SE) value in set A, and the number of model elements through the model evolution

## DISCUSSION

### EVALUATION OF MODELS IN TERMS OF ESTIMATION ACCURACY

Figures 6 and 7 show the estimated length (LBP) values in the full range of TEU capacity and ship velocity calculated using Eqs. (8) and (14). The surfaces presented on these figures look similar, though for the extreme values of velocity and TEU capacity, the length calculated using an ANN was slightly larger than the one obtained using the random search method.

Figure 8 compares the length calculations using both methods for ship sample data for selected speeds. As shown in Figure 8 both methods gave similar results; Eq. (14) provided slightly more accurate results in relation to sample ship data at a speed of 11 kts.

Figure 9 illustrates the estimates obtained using both methods compared to test sample ship data. The test data was in the range of full ship length. This figure shows that the length values calculated using both methods were close to the perfect fit line.

Table 3 shows the root mean squared error (RMSE) and Pearson R-squared coefficient values relating to regression Eq. (14) and the developed neural network referenced for the entire data set (including the training, validation, and test sets). This table shows that Eq. (14) is characterised by a RMSE estimation error 2 metres smaller than Eq. (8).

Tab. 2. The values of the root mean squared RMSE error and Pearson R-squared coefficients relating to regression (14) and the developed neural network referenced for the entire data set

Equation	RMSE [t]	R-Pearson [-]
equation (14)	7.77	0.996
equation (8)	9.86	0.994

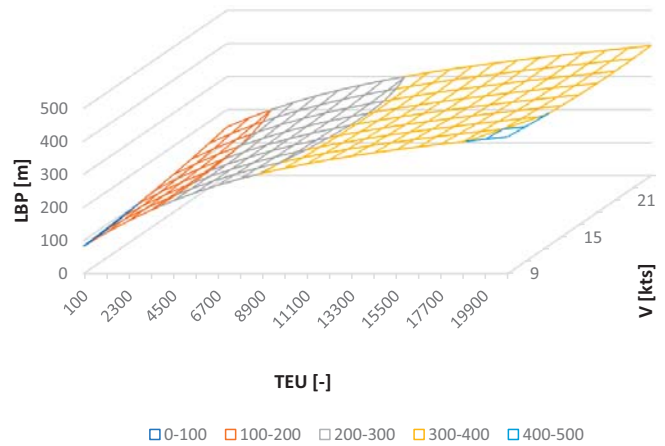


Fig. 3. Length (LBP) values estimated in the full range of TEU and V calculated using Eq. (8)

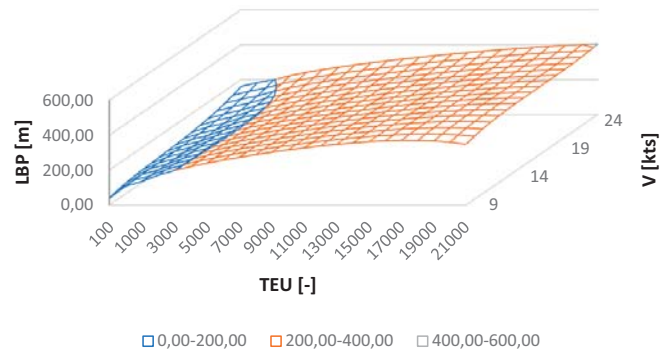


Fig. 4. Length (LBP) values estimated in the full range of TEU and V calculated using Eq. (14)

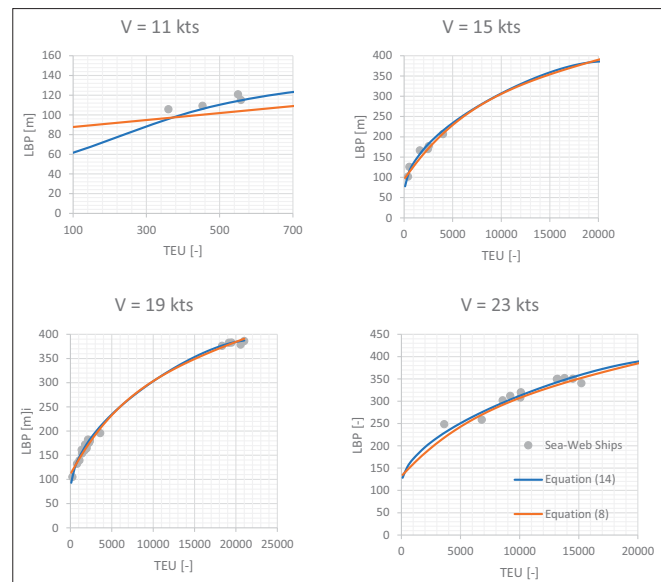


Fig. 5. Comparison of length (LBP) values estimated with sample ship data using Eqs. (8) and (14)

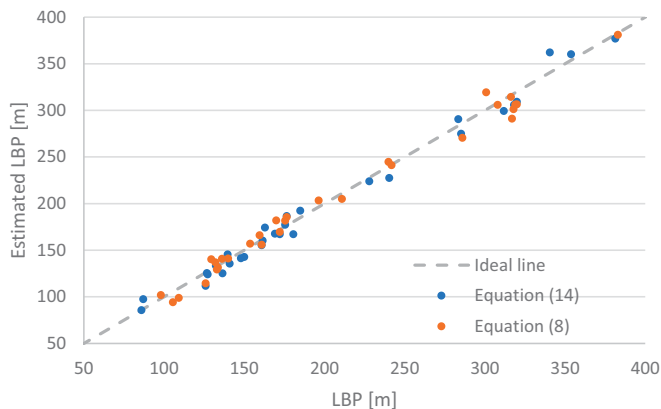


Fig. 6. Comparison of length (LBP) values calculated with sample data values using both methods

## AN EVALUATION OF METHODS IN TERMS OF EASE OF COMPUTATION AND MODEL SIMPLICITY

The equations presented in this article were developed for practical use by a ship designer. In this respect, one important factor was the possibility of using these formulas for manual calculations by a person with a basic knowledge of computer techniques. For this reason, model simplicity was an important criterion.

Research showed that Eq. (14) developed using the random search method had a simpler form than Eq. (8) developed using neural networks. Eq. (14) is based on only seven basic functions and six coefficients. The analytical relationships of independent variables are also clearly shown in this equation. The practical use of this equation requires only a basic knowledge of computer techniques. A scientific calculator or a simple spreadsheet can be used for calculating the LBP length based on Eq. (14).

In contrast, Eq. (8), which was developed using an ANN, is much more complex. Several calculations should be performed using the formulas in Eqs. (8) – (13) to estimate the length between perpendiculars in this case. The relationships between TEU capacity, ship velocity, and ship length presented in the formulas of Eqs. (9) - (12) are unclear. Eq. (8) ANN is more difficult to implement by a normal user. Indeed, the user must have an advanced knowledge of computer techniques to implement the ANN model, or alternatively, a specialised computer software may be used. The use of a scientific calculator to estimate LBP length using Eqs. (8) - (13) is more complicated and time-consuming than simply using Eq. (14).

## THE EVALUATION OF METHODS FOR THE USE OF DATA

Both methods presented here use heuristic techniques, so these methods do not offer an optimal solution. The complex equations developed using an ANN and a random search method may lead to overfitting. Therefore, overfitting was

detected using a test set which included 25% of the data in both methods. An ANN and random search method are the same in this respect.

However, an additional validation data set was used to develop the ANN. This validation set also included 25% of the data. In this research, ANNs lost 50% of data in total for validation and testing.

In contrast, the random search method did not require a validation set and lost only 25% of the data during the overfitting detection. In this regard, the random search method provides a more effective use of the data set than the ANN.

Table 4 shows a summarised method comparison in terms of different properties.

Tab. 3. A summarised method comparison in terms of different properties

Method	Equation no	Accuracy	Simplicity	Ease of computation	Data loss
ANN	(8)	high	complex	difficult	50%
Author's method	(14)	high, RMSE 2 metres smaller	simple	easy	25%

## CONCLUSIONS

In ship design, only DWT or TEU capacity are usually used to estimate a container ship's length. Over the last few years, economic and environmental factors have affected ship owner requirements. At present, ship velocity may be a second key design parameter in addition to TEU or DWT capacity. Therefore, alternative design equations for estimating a container ship's length based on TEU capacity and ship velocity have been proposed in this research. This provides a new approach in naval engineering. The equations presented in this work were developed based on the data of the most recent standard container ships built since 2014.

In this article, ANNs and a random search method based on MNLR were applied to estimate a container ship's length. The conclusions drawn from these compared methods may be summarised as follows:

- Both methods are characterised by a high estimation accuracy. The random search method is slightly more accurate and offers a RMSE error value less than 2 metres in length.
- Eq. (14) developed using the random search method is simpler and easier to compute than Eq. (8) developed using an ANN.
- The random search method used the data set more effectively than the ANN.
- The random search method also only used 25% of the data for testing while the ANN needed 50% of the data for validation and testing.

Estimates acquired with an equation developed using Multiple Nonlinear Regression (MNLR) may be as accurate as ones obtained using ANNs. The application of heuristic techniques for the development of MNLR by variable and

function randomisation automatically enables the discovery of a set of equations.

The methods presented in this article may be used to estimate the parameters of a container ship, such as breadth, side depth, or draught. In general, in the case of volume carriers, these dimensions are primarily determined by the ratio of length to breadth and side depth, and the displacement of the vessel. However, it seems that the use of these estimates could be helpful to assess the accuracy of the design calculations. The results presented in this paper and in [4] indicate the possibility of developing a neural network to predict all dimensions of a container ship and, potentially, other types of ships.

The algorithms described here may have practical applications for the commercial design of container vessels. However, these formulas can be inaccurate for the design of an innovative container ship and can only be used to estimate the length of container ships with design characteristic ranges listed out in Table 1. The use of algorithms to determine a ship's length for characteristics outside these ranges may possibly be associated with less reliable calculations.

## REFERENCES

1. D.G.M. Watson, "Practical Ship Design", Volume 1. Elsevier Science. 1998.
2. K.J. Rawson and E.C. Tupper, *Basic Ship Theory: Ship Dynamics and Design*. Butterworth-Heinemann. 2001.
3. A. Papanikolaou, *Ship Design: Methodologies of Preliminary Design*. Dordrecht: Springer. 2014.
4. J.H. Evans, *Basic Design Concepts*, Naval Engineers Journal, 1959.
5. D.J. Andrews, *An Integrated Approach to Ship Synthesis*, Trans. RINA. 1985.
6. W. Chądzyński, "Elements of contemporary design methods of floating objects", *Scientific Reports of Szczecin University of Technology*. (in Polish). 2001.
7. G.P. Piko, *Regression Analysis of Ship Characteristics*, Canberra: C. J. THOMPSON Commonwealth Government Printer. 1980.
8. H.O. Kristensen, "Determination of Regression Formulas for Main Dimensions of Container Ships based on IHS Fairplay data". Project no. 2010-56, Emissionsbeslutning sstøttesystem. Work Package 2, Report no. 03. Technical University of Denmark. 2013.
9. Sea-web Ships, IHS Markit, <https://maritime.ihs.com>, (accessed 8 Decemeber 2020)
10. S. Gurgen, I. Altin, I. and O. Murat, "Prediction of main particulars of a chemical tanker at preliminary ship design using artificial neural network", *Ships and Offshore Structures*, 13(5), 459-465, 2018.
11. A.D. Alkan, K. Gulez and H. Yilmaz, "Design of a robust neural network structure for determining initial stability particulars of fishing vessels", *Ocean Engineering* 31 761-777, 2004.
12. S. Ekinci, U.B. Celebi, M. Bal, M.F. Amasyali and U.K. Boyaci, "Predictions of oil/chemical tanker main design parameters using computational intelligence techniques", *Applied Soft Computing*, 11 2356-2366, 2011.
13. T. Abramowski, "Application of Artificial Intelligence Methods to Preliminary Design of Ships and Ship Performance Optimization", *Naval Engineers Journal*, 125 (3) 101-112, 2013.
14. T. Cepowski, "The prediction of ship added resistance at the preliminary design stage by the use of an artificial neural network", *Ocean Engineering* 195, 106657. 2020. doi.org/10.1016/j.oceaneng.2019.106657
15. J.G. Song, L.H. Liang, S.T. Zhang and J.M. Wang, "Design and experimental investigation of a GA-based control strategy for a low-speed fin stabilizer", *Ocean Engineering*, 2018. 10.1016/j.oceaneng.2020.108234
16. V. Sahin and N. Vardar, "Determination of Wastewater Behavior of Large Passenger Ships Based on Their Main Parameters in the Pre-Design Stage", *Journal of Marine Science and Engineering*, 8 (8), 2020. DOI: 10.3390/jmse8080546
17. Luan Thanh Le, Gunwoo Lee, Keun-Sik Park and Hwayoung Kim, "Neural network-based fuel consumption estimation for container ships in Korea", *Maritime Policy and Management*, 47:5, 615-632, 2020. DOI: 10.1080/03088839.2020.1729437
18. X. Cheng, S. Chen and C. Diao, "Simplifying Neural Network Based Model for Ship Motion Prediction: A Comparative Study of Sensitivity Analysis", *Proceeding of the ASME 36<sup>th</sup> International Conference on Ocean, Offshore and Arctic Engineering*, Vol. 1. 2017.
19. S. Haykin, "Neural Networks: A Comprehensive Foundation". New York: Macmillan Publishing. 1994.
20. J.H. Lee, T. Delbruck and M. Pfeiffer, "Training Deep Spiking Neural Networks Using Backpropagation", *Frontiers in Neuroscience*, 10, 508, 2016.
21. L. Fausett, *Fundamentals of Neural Networks*. New York: Prentice Hall. 1994.

22. D. Patterson, *Artificial Neural Networks*. Singapore: Prentice Hall. 1996.
23. C. Bishop, *Neural Networks for Pattern Recognition*, Oxford: University Press. 1995.
24. J. Shepherd, *Second-Order Methods for Neural Networks*. Springer: New York. 1997.
25. J. Adamowski, H.F. Chan, S.O. Prasher, B. Ozga-Zielinski and A. Sliusarieva, "Comparison of multiple linear and nonlinear regression, autoregressive integrated moving average, artificial neural network, and wavelet artificial neural network methods for urban water demand forecasting in Montreal", *Water Resources Research*, 48W01528, 2012.
26. E. Tsykin, "Multiple nonlinear regressions derived with choice of free parameters, *Applied Mathematical Modelling*", Volume 8 (4) 288-292, 1984.
27. T. Cepowski, ndCurveMaster n-dimensional Curve and Surface Fitting Software, <https://www.ndcurvemaster.com>, (accessed 13 December 2020).

## CONTACT WITH THE AUTHORS

### **Tomasz Cepowski**

*e-mail: t.cepowski@am.szczecin.pl*

Akademia Morska w Szczecinie,  
W.Chrobrego 1-2, 70-500 Szczecin,

**POLAND**

### **Paweł Chorab**

*e-mail: p.chorab@am.szczecin.pl*

Akademia Morska w Szczecinie,  
W.Chrobrego 1-2, 70-500 Szczecin,

**POLAND**

### **Dorota Łozowicka**

*e-mail: d.lozowicka@am.szczecin.pl*

Akademia Morska w Szczecinie,  
W.Chrobrego 1-2, 70-500 Szczecin,

**POLAND**

# NUMERICAL ESTIMATION OF HULL HYDRODYNAMIC DERIVATIVES IN SHIP MANEUVERING PREDICTION

Radosław Kołodziej\*

Maritime Advanced Research Centre, Gdańsk, Poland  
Gdańsk University of Technology, Poland

Paweł Hoffmann

Maritime Advanced Research Centre, Gdańsk, Poland

\* Corresponding author: [radoslaw.kolodziej@cto.gda.pl](mailto:radoslaw.kolodziej@cto.gda.pl) (R. Kołodziej)

## ABSTRACT

*Prediction of the maneuvering characteristics of a ship at the design stage can be done by means of model tests, computational simulations or a combination of both. The model tests can be realized as a direct simulation of the standard maneuvers with the free running model, which gives the most accurate results but is also the least affordable, as it requires a very large tank or natural lake, as well as the complex equipment of the model. Alternatively, a captive model test can be used to identify the hydrodynamic characteristics of the hull, which can be used to simulate the standard maneuvers with the use of dedicated software. Two types of captive model tests are distinguished: circular motion tests (CMT) and planar motion mechanism tests (PMM). The paper presents an attempt to develop a computational method for ship maneuverability prediction in which the hydrodynamic characteristics of the hull are identified by means of computational fluid dynamics (CFD). The CFD analyses presented here directly simulate the circular motion test. The resulting hull characteristics are verified against the available literature data, and the results of the simulations are verified against the results of free running model tests. Reasonable agreement shows the large potential of the proposed method.*

**Keywords:** Captive model tests, CFD tools in maneuvering prediction, MOERI Container ship (KCS), Hull hydrodynamic derivatives, Mathematical model of ship motion

## INTRODUCTION

In the literature, there are numerous algorithms regarding the simulation of ship planar motion. One of them, which has successfully been used for different types of vessels and propulsions [1] [2] [3], was first introduced by the Mathematical Modeling Group (MMG). The presented model uses two corresponding coordinate systems. The forces acting on the ship are calculated in reference to a ship-fixed coordinate system, which is then transformed into an Earth-fixed coordinate system.

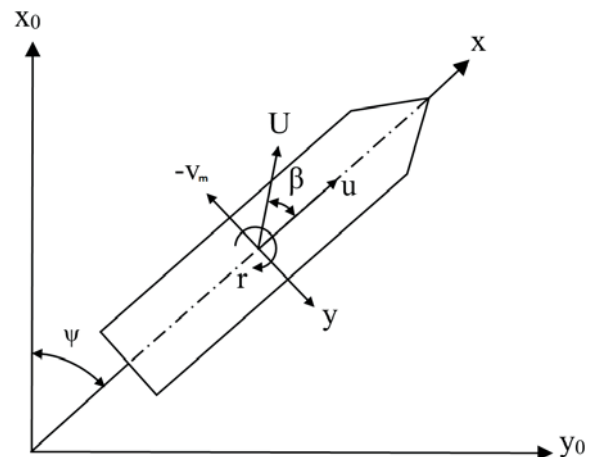


Fig. 1. Coordinate systems

As a result, the following equations are obtained:

$$F_x = (m + m_x)\dot{u} - (m + m_y)v_m r - mx_G r^2 \quad (1)$$

$$F_y = (m + m_y)\dot{v}_m + (m + m_x)ur + mx_G \dot{r}_m \quad (2)$$

$$N_z = (I_{zG} + mx_G^2 + J_z)\dot{r} + mx_G(\dot{v}_m + ur) \quad (3)$$

where  $m$  is the mass of the ship,  $v_m$  denotes the ship's lateral speed at midship,  $u$  is the longitudinal ship's speed,  $r$  is the yaw rate,  $x_G$  is the longitudinal coordinate of the center of gravity of the ship and  $I_{zG}$  is the moment of inertia of the ship around the center of gravity. The  $m_x$ ,  $m_y$  and  $J_z$  symbols stand for the added masses and added moment of inertia, which, for example, can be estimated based on Hoofft's formula [4]. The  $F_x$ ,  $F_y$  and  $N_z$  symbols represent, in order, the surge and sway forces as well as the yaw moment acting on the ship, which are a sum of the following components:

$$F_x = X_H + X_P + X_R \quad (4)$$

$$F_y = Y_H + Y_R \quad (5)$$

$$N_z = N_H + N_R \quad (6)$$

The subscripts H, R and P denote the forces and moments due to the hull, rudder and propeller, respectively.

## HULL FORCES

The forces acting on a hull during maneuvering can be expressed, for practical purposes, in a non-dimensional form as follows [1]:

$$X_H = 1/2\rho L_{pp} dU^2 X'_H(\beta, r') \quad (7)$$

$$Y_H = 1/2\rho L_{pp} dU^2 Y'_H(\beta, r') \quad (8)$$

$$N_H = 1/2\rho L_{pp}^2 dU^2 N'_H(\beta, r') \quad (9)$$

where  $\rho$  is the water density,  $L_{pp}$  is the length between perpendiculars,  $d$  stands for the ship draught and  $U$  is the ship velocity. The non-dimensional hull forces can now be expressed as polynomial functions using the drift angle  $\beta$  and  $r' = rL_{pp}/U$ :

$$X'_H = -R'_0 + X'_{\beta\beta}\beta^2 + X'_{\beta r'}\beta r' + X'_{rr}r'^2 + X'_{\beta\beta\beta\beta}\beta^4 \quad (10)$$

$$Y'_H = Y'_\beta\beta + Y'_{r'}r' + Y'_{\beta\beta\beta}\beta^3 + Y'_{rrr}r'^3 + (Y'_{\beta\beta r'}\beta + Y'_{\beta r'r'}r')\beta r' \quad (11)$$

$$N'_H = N'_\beta\beta + N'_{r'}r' + N'_{\beta\beta\beta}\beta^3 + N'_{rrr}r'^3 + (N'_{\beta\beta r'}\beta + N'_{\beta r'r'}r')\beta r' \quad (12)$$

The polynomial coefficients in equations (10), (11) and (12) are called hydrodynamic derivatives on maneuvering. There are various methods used in order to assess their value, such as captive model tests or numerical simulations. It has to be pointed out that the presented polynomial coefficients include added masses.

## PROPELLER FORCES

The surge force generated by a working propeller is expressed as

$$X_P = (1 - t_p)\rho n_p^2 D_p^4 K_T \quad (13)$$

where  $t_p$  is the thrust deduction factor,  $\rho$  is the density of water,  $n_p$  represents the propeller revolutions and  $D_p$  is the propeller diameter. The propeller thrust open water efficiency  $K_T$  is a function of the propeller advance ratio coefficient  $J_p$ , which can, for example, be calculated as a fourth order polynomial function:

$$K_T = k_4 J_p^4 + k_3 J_p^3 + k_2 J_p^2 + k_1 J_p + k_0 \quad (14)$$

$$J_p = \frac{u(1 - w_p)}{n_p D_p} \quad (15)$$

The inflow of water to the propeller changes considerably during maneuvering because of the ship's drift angle. This phenomenon is difficult to capture, and many algorithms were proposed in order to do so [1] [5]. In this paper, the wake fraction coefficient of the propeller is calculated using the following formula:

$$w_p = w_{p0} e^{-4\beta^2} \quad (16)$$

$$\beta_p = \beta - x'_p r' \quad (17)$$

## RUDDER FORCES

Hydrodynamic forces induced by the rudder during maneuvering can be calculated based on the rudder normal force according to the following equations:

$$X_R = -(1 - t_R)F_N \sin\delta \quad (18)$$

$$Y_R = -(1 + a_H)F_N \cos\delta \quad (19)$$

$$N_R = -(x_R + a_H x_H)F_N \cos\delta \quad (20)$$

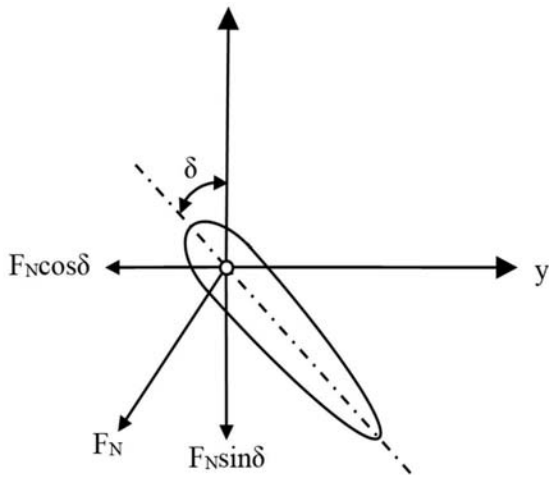


Fig. 2. Definition of rudder forces

The rudder normal force is expressed as

$$F_N = 0.5 \rho A_R f_a U_R^2 \sin \alpha_R \quad (21)$$

Here,  $A_R$  is the profile area of the moveable part of the rudder and  $f_a$  stands for the normal force coefficient:

$$f_a = \frac{6.13\Lambda}{2.25 + \Lambda} \quad (22)$$

The  $\Lambda$  coefficient in Eq. (22) is equal to  $\frac{h_R^2}{A_R}$ , where  $h_R$  is the rudder span. The effective angle of the  $A_R$  water attack to the rudder  $\alpha_R$  and the velocity of the water inflow to the rudder  $U_R$  are calculated according to:

$$\alpha_R = \delta - \tan^{-1} \frac{v_R}{u_R} \quad (23)$$

$$U_R = \sqrt{u_R^2 + v_R^2} \quad (24)$$

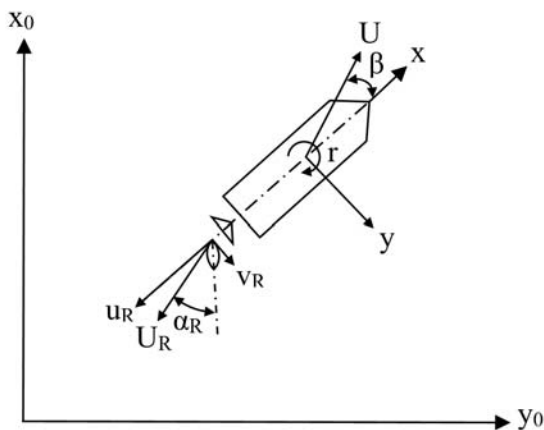


Fig. 3. Distribution of the water flow in the rudder area

The components of the water inflow to the rudder velocity are now calculated based on the following equations:

$$v_R = U \gamma_{R\pm} (\beta - r' l'_R) \quad (25)$$

$$u_R = (1 - w_P) \epsilon U \sqrt{\frac{D_P}{h_R} \left\{ 1 + \kappa \left( \sqrt{1 + \frac{8K_T}{\pi J_P^2}} - 1 \right) \right\}^2} + \left( 1 - \frac{D_P}{h_R} \right) \quad (26)$$

$$\epsilon = \frac{1 - w_R}{1 - w_P} \quad (27)$$

$$\kappa = \frac{0.55}{\epsilon} \quad (28)$$

where  $\gamma_{R\pm}$  is the flow straightening coefficient and  $l'_R$  is the effective longitudinal coordinate of the rudder position.

## INVESTIGATED SHIP

The subject of this study is a bare hull container ship KCS (Kriso Container Vessel) equipped with a rudder horn. This is a popular test case because many model experiments and various CFD simulations have been done for this geometry, which is open to the public [6]. Table 1 shows the main ship particulars in real and 1:30.455 scales; the latter was used in both free running model tests and numerical simulations. In contradiction to the method presented by the MMG, the model was not equipped with a rudder and propeller during numerical simulations.

Tab. 1. Main ship particulars

	Symbol	Unit	Real scale	Model scale
Scale	$\lambda$	[-]	1:1	1:30.455
Length between perpendiculars	$L_{pp}$	[m]	230.0	7.552
Breadth at waterline	B	[m]	32.2	1.057
Draught	d	[m]	10.8	0.355
Displacement volume	$V$	[m <sup>3</sup> ]	52030	1.842
Block coefficient	$C_B$	[-]	0.651	0.651
Longitudinal coordinate of the center of gravity	$x_G$	[m]	-3.4	-0.111
Radius of the gyration of the ship around the center of gravity (related to $L_{pp}$ )	$k'_{zz}$	[-]	0.25	0.25
Propeller diameter	$D_p$	[m]	7.9	0.259
Propeller direction of rotation	-	-	right	right
Rudder projected lateral moveable area	$A_R$	[m <sup>2</sup> ]	45.5	0.049
Rudder height	$h_R$	[m]	9.9	0.325
Rudder turn rate	-	[°/s]	2.32	12.8

## NUMERICAL SIMULATION

In this paper, simulations of circular motion tests (CMT) were conducted [7]. The tests were done for the constant ship's speed  $U_0 = 2.237$  m/s (equivalent to 24 knots in full scale). Prior to CMT tests, the propeller open water, resistance and propulsion model tests were done.

Tab. 2. Computational cases for the CMT

	Symbol	Unit	Computational cases
Rate of turn	$r$ ( $r'$ )	%s (-)	2 (0.118), 6 (0.354), 8 (0.471)
Drift angle	$\beta$	$^\circ$ (rad)	0, $\pm 5$ (0.087), $\pm 15$ (0.262), $\pm 25$ (0.436)

The Computational Fluid Dynamics (CFD) analysis is carried out using the STAR-CCM+ solver with the Reynolds Averaged Navier-Stokes (RANSE) method. The Volume of Fluid model is used to simulate multiphase flow with a High-Resolution Interface Capturing (HRIC) scheme for solving the free surface. Turbulence modeling was executed with a "Realizable k-epsilon Two-layer" model. The hull movement was computed in the rectangular domain. The size of the domain was matched to contain the whole circular trajectory with an additional margin of at least one length of the model; the height of the domain was over two lengths of the model. For the movement simulation, the Overset Mesh technique was used. The computational domain consisted of two blocks: the smaller one, which contained the hull and its small vicinity, and the background region, in which the movement trajectory was contained. The domain boundary conditions were set up as walls with an additional function set up to damp the waves in its vicinity in order to prevent the waves' reflections inside the computational domain. The time step was equal to  $2 \times 10^{-2}$  s, and at least two full circulations were completed before stopping the simulation to achieve the convergence of the monitored forces. A visualization of the computational domain is shown in the figure below:

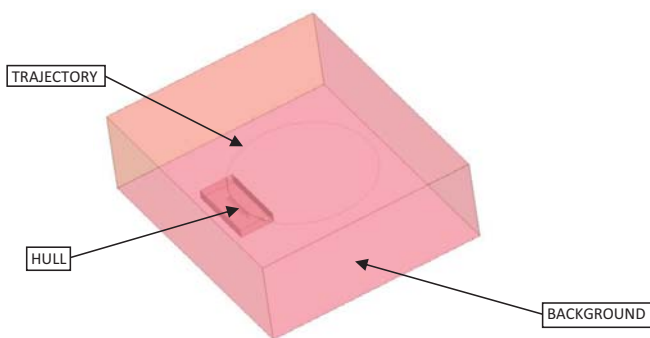


Fig. 4. Computational domain

Wave damping was applied at the boundaries to prevent the reflections of the waves inside the computational domain. The running trim and sinkage of the hull were not taken into account in the computations. The dynamic hull motions were not taken into account in the computations to reduce the time of the computations. A mesh of the hexahedral type was used. The mesh, depending on the case, included up to

8 000 000 cells. The mesh on the hull and the mesh on the free surface are presented below:



Fig. 5. Computational mesh on the KCS model surface

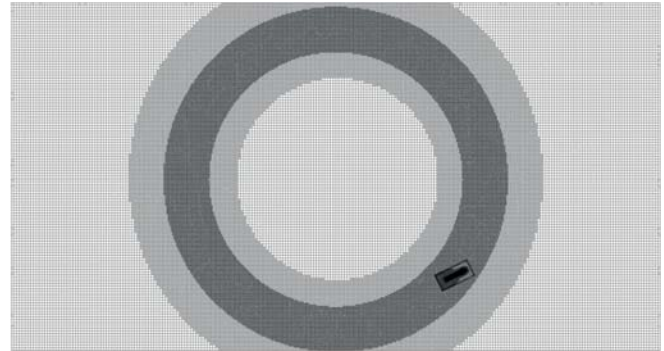


Fig. 6. Computational mesh on the free surface

## HULL HYDRODYNAMIC DERIVATIVES

During the tests, longitudinal (X) and lateral (Y) forces as well as the moment induced by the hull (N) were measured for different rates of the turn of the ship corresponding to the different drift angles. The results of numerical simulations in dimensionless form are presented in Table 3.

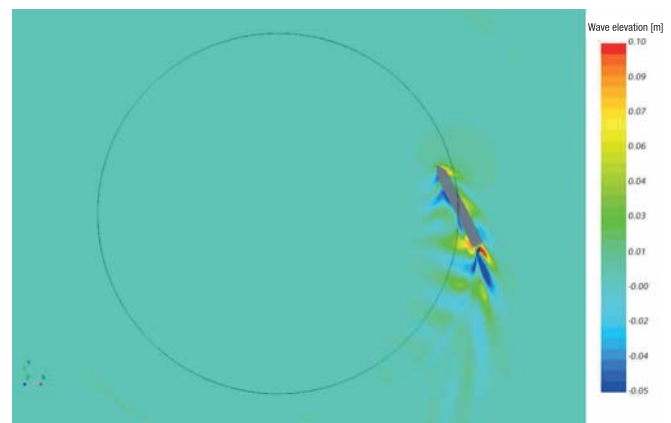


Fig. 7. Wave elevation and circular trajectory at  $-25^\circ$  drift angle

As stated in equations (10–12), the forces X and Y and the moment N can be presented as dimensionless polynomial functions of the drift angle  $\beta$  and the turn rate of the ship  $r'$ . In order to establish hydrodynamic derivatives of the hull, the surface was fitted on measured points using the least squares method, as shown in Fig. 8–10. The confidence bounds used for surface interpolation are equal to  $\pm 5\%$ . Fig. 11 shows a comparison of the received results with captive model tests done by Japan's Society of Naval Architects and Ocean Engineers (JASNAOE) [8].

Tab. 3. Results of CFD simulations

Drift angle [°]	$X'_H$			$Y'_H$			$N'_H$		
	Rate of turn [°/s]								
	2	6	8	2	6	8	2	6	8
-25	-0.0121	-0.0057	-0.0015	-0.1428	-0.1680	-0.1882	-0.0625	-0.0872	-0.0989
-15	-0.0128	-0.0080	-0.0057	-0.0712	-0.0941	-0.1060	-0.0384	-0.0576	-0.0660
-5	-0.0132	-0.0142	-0.0137	-0.0142	-0.0243	-0.0326	-0.0149	-0.0266	-0.0326
0	-0.0133	-0.0163	-0.0172	-0.0013	-0.0018	0.0007	-0.0036	-0.0145	-0.0216
5	-0.0149	-0.0196	-0.0213	0.0149	0.0227	0.0264	0.0058	-0.0029	-0.0090
15	-0.0190	-0.0271	-0.0305	0.0655	0.0754	0.0839	0.0238	0.0110	0.0042
25	-0.0220	-0.0355	-0.0412	0.1362	0.1546	0.1622	0.0425	0.0245	0.0139

$X'_H$  [-]

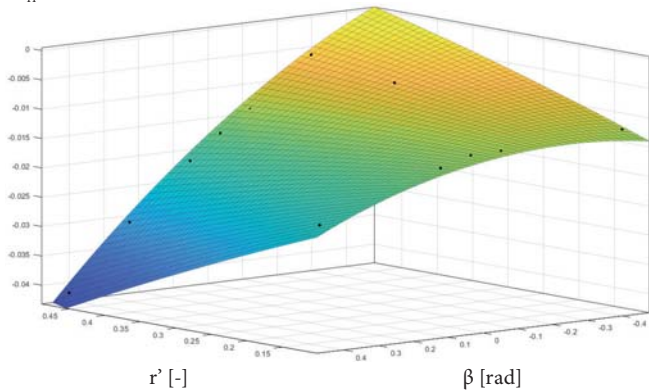


Fig. 8. Surface fitting for X hull forces

$Y'_H$  [-]

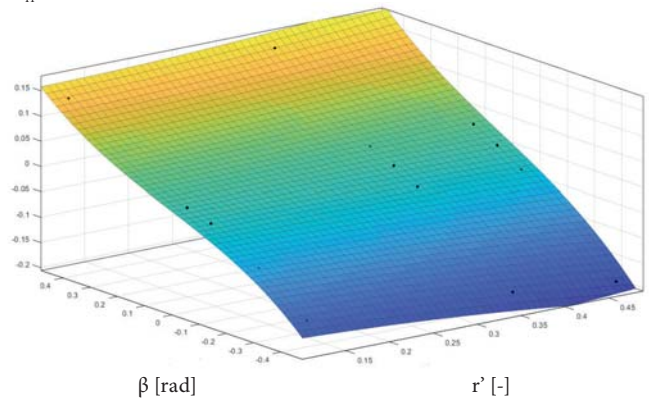


Fig. 9. Surface fitting for Y hull forces

$N'_H$  [-]

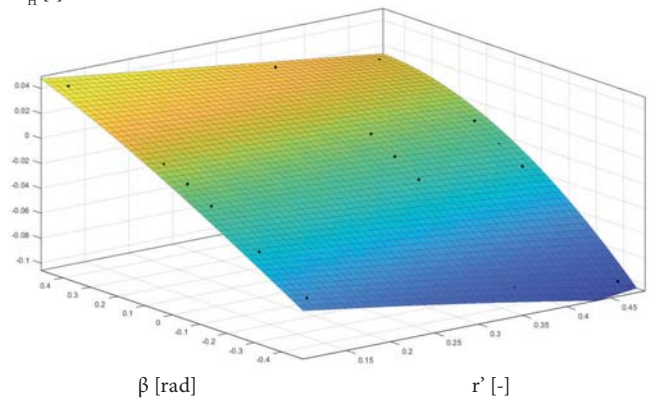


Fig. 10. Surface fitting for N hull moments

Tab. 4. Hull hydrodynamic derivatives

X force					
$R'_0$	$X'_{\beta\beta}$	$X'_{\beta r}$	$X'_{rr}$	$X'_{\beta\beta\beta\beta}$	
CFD simulation					
-0.0139	-0.0032	-0.0942	-0.0134	0.0794	
Captive model tests (JASNAOE)					
-0.0139	-0.0549	-0.1084	-0.0120	-0.0417	
Y force					
$Y'_{\beta}$	$Y'_r$	$Y'_{\beta\beta\beta}$	$Y'_{rrr}$	$Y'_{\beta\beta r}$	$Y'_{\beta r r}$
CFD simulation					
0.2526	0.0215	0.5779	0.0812	-0.0383	0.5199
Captive model tests (JASNAOE)					
0.2252	0.0398	1.7179	-0.0050	-0.4832	0.8341
N moment					
$N'_{\beta}$	$N'_r$	$N'_{\beta\beta\beta}$	$N'_{rrr}$	$N'_{\beta\beta r}$	$N'_{\beta r r}$
CFD simulation					
0.1141	-0.0468	-0.0596	-0.0616	-0.2749	0.0218
Captive model tests (JASNAOE)					
0.1111	-0.0465	0.1751	-0.0387	-0.6167	0.0512

The established hydrodynamic derivatives show considerable differences in comparison with the captive model tests presented by JASNAOE. Although the lower power coefficients, which have the biggest impact on the simulation, are a good match, the higher power coefficients, which have a lower impact, show large differences. The derivatives of correlated variables (like  $Y'_{\beta\beta r}$  and  $Y'_{\beta r r}$ ) that affect the growth rate of forces and the moment in the time domain diverge as well, which is understandable as they are also correlated with each other and are very sensitive to surface approximation. This, however, does not necessarily influence the simulations, as their general interaction can have a similar outcome, as proved in further paragraphs.

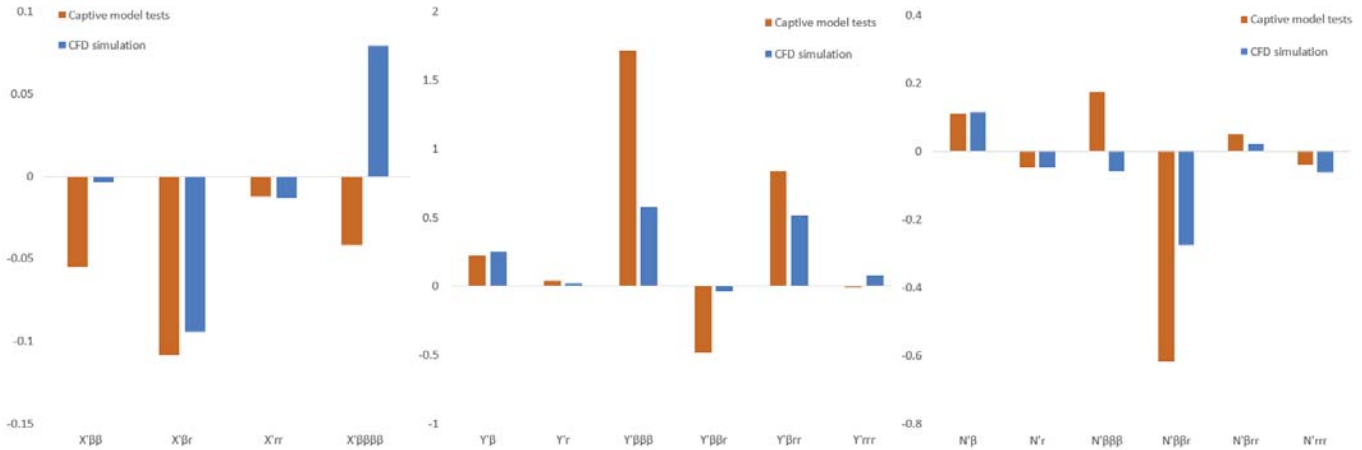


Fig. 11. Comparison of hydrodynamic derivatives received from CFD and captive model tests (JASNAOE)

## SIMULATION OF IMO STANDARD MANEUVERS

The IMO Standards are based on the assumption that the maneuverability of ships can be evaluated from the characteristics of conventional trial maneuvers [9]. Model tests such as the turning circle and zigzag duplicate the full-scale trial maneuvers, and the results can be compared directly with the IMO criteria [10]. In this paper, simulations of turning and zigzag tests are performed based on data received from CFD simulations and captive model tests presented by JASNAOE, and they are then compared with free running model tests. The ODE4 fixed step solver was used to simulate the maneuvers using MATLAB Simulink software. It has to be pointed out that using different types of solvers does not significantly influence the simulation results. The inertia terms of the ship used in both cases are included along with parameters used for the calculation of propeller and rudder forces in Table 5 [11]. The comparison of 10/10 and 20/20 zigzag maneuvers is shown in Fig. 12–15, and the trajectories for the turning circle test for  $\delta = \pm 35^\circ$  are presented in Fig. 16. Selected parameters for trial maneuvers are included in Table 6.

Tab. 5. Parameters used in simulations [11]

$m'_x$	$m'_y$	$J'_z$	$t_p$	$x'_p$	$t_R$	$a_H$	$x'_H$
0.013	0.138	0.006	0.179	-0.491	0.161	0.448	-0.444
$I'_R$	$w_{p0}$	$x'_R$	$\varepsilon$	$\kappa$	$\gamma_{R+}$	$\gamma_{R-}$	$f_a$
-0.751	0.274	-0.500	0.944	0.583	0.237	0.395	2.998

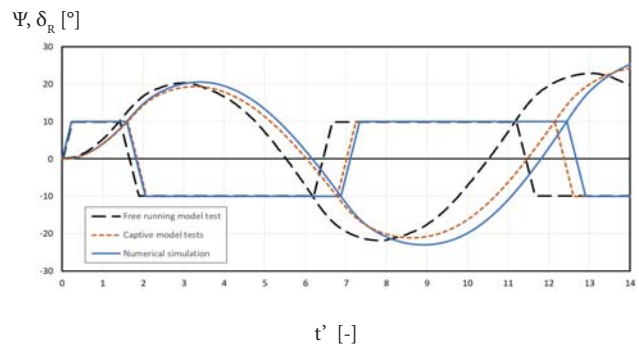


Fig. 12. Comparison of 10/10 zig-zag maneuvers, first turn to STBD

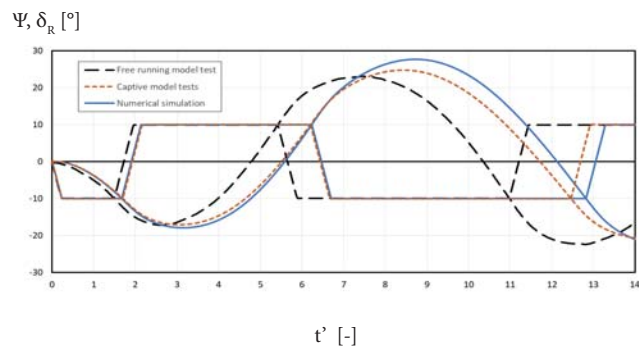


Fig. 13. Comparison of 10/10 zig-zag maneuvers, first turn to PS

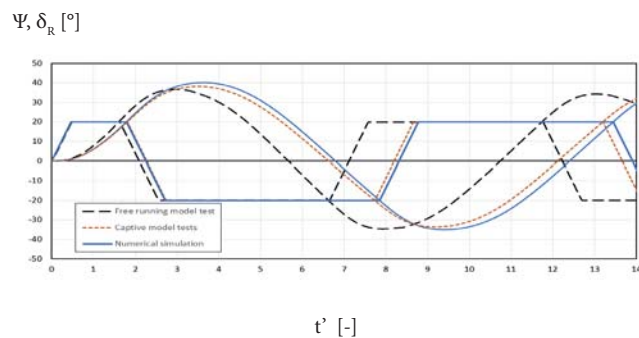


Fig. 14. Comparison of 20/20 zig-zag maneuvers, first turn to STBD

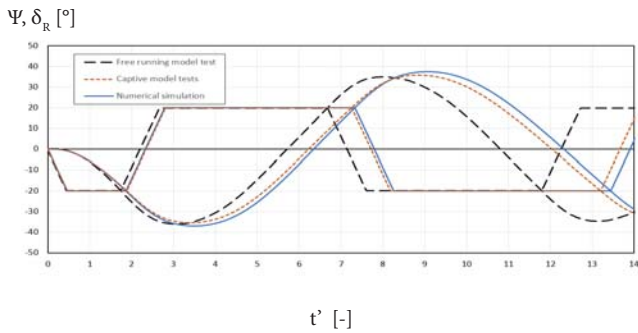


Fig. 15. Comparison of 20/20 zig-zag maneuvers, first turn to PS

where the non-dimensional time  $t' = t \frac{U_0}{L_{PP}}$ .

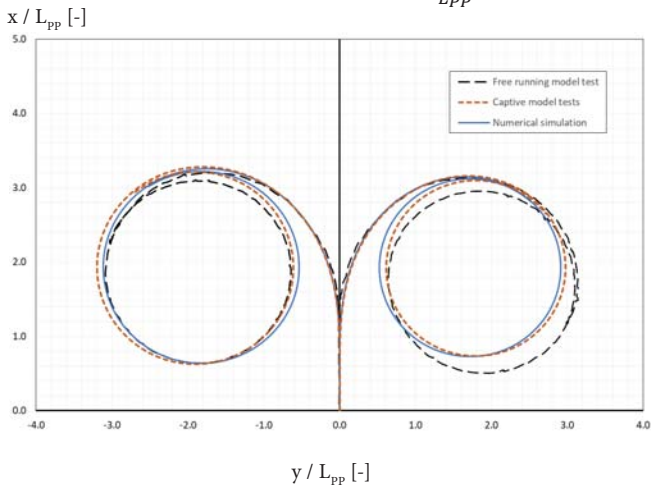


Fig. 16. Comparison of turning trajectories for  $\delta = \pm 35^\circ$

Tab. 6. Comparison of selected maneuvering criteria parameters [9]

Maneuver	Parameter	Free running model test	Captive model tests (JASNAOE)	Numerical simulation
zigzag 10°/10° (first turn to STBD)	$t'_a$	1.4	1.6	1.7
	1 st OSA	10.3	9.3	10.6
	2 st OSA	11.7	11.1	13.0
zigzag 10°/10° (first turn to PS)	$t'_a$	1.6	1.7	1.7
	1 st OSA	7.0	7.1	7.9
	2 st OSA	13.4	14.8	17.7
zigzag 20°/20° (first turn to STBD)	$t'_a$	1.6	1.8	1.8
	1 st OSA	15.8	17.2	19.0
	2 st OSA	14.8	13.0	14.4
zigzag 20°/20° (first turn to PS)	$t'_a$	1.8	1.9	1.9
	1 st OSA	16.1	14.6	16.7
	2 st OSA	14.9	15.1	16.0
turning 35° STBD	A'D	3.1	3.1	3.1
	D'T	3.1	3.0	2.9
	$D_C/L_{PP}$	2.4	2.4	2.5
	$U/U_0$	0.47	0.36	0.36

Maneuver	Parameter	Free running model test	Captive model tests (JASNAOE)	Numerical simulation
turning 35° PS	A'D	3.1	3.2	3.2
	D'T	3.0	3.2	3.1
	$D_C/L_{PP}$	2.5	2.6	2.6
	$U/U_0$	0.45	0.38	0.38

where  $t'_a$  is the initial turning ability time, OSA stands for Overshoot angle,  $A'_D$  is the Advance,  $D'_T$  is the tactical diameter,  $D_C/L_{PP}$  represent turning radius in reference to the length between perpendiculars and  $U/U_0$  represent speed in reference to the approach speed.

## CONCLUSIONS

The experimentally established values of hydrodynamic coefficients differ considerably from the values calculated with the use of regression formulas. This, however, does not seem to affect the final prediction of the maneuvers, as they show satisfying agreement in terms of practical purposes. It is assumed that the values of the hydrodynamic derivatives that show a large difference with regard to their origin method have a low impact on prediction, as the main discrepancies occur for coefficients of higher powers. The results of the predictions show a considerable difference in the drop of the speed of the ship, which means that the X forces are overestimated. What is more the underestimation of N moments can be noticed as rate of turn of ship (fig. 17) is lower for CFD and captive model tests in comparison to the free running model tests. This leads to conclusion that the Y forces are underestimated as well as turning radii are similar in each case. Other papers concerning this topic has provided similar results which further backs this theory [12].

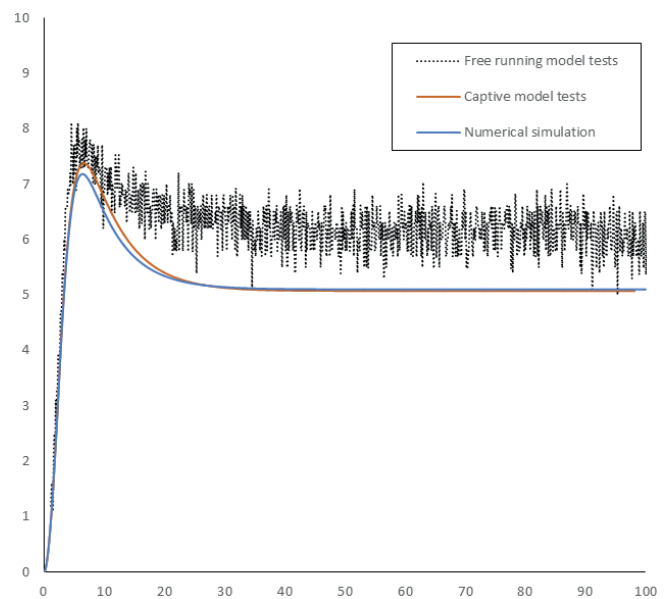


Fig. 17. Comparison of turning rates

## ACKNOWLEDGMENT

This paper has been elaborated within the framework of the internal research and support of the Maritime Advanced Research Centre (CTO S.A) in 2020.

## REFERENCES

1. H. Yasukawa and Y. Yoshimura, "Introduction of MMG standard method for ship maneuvering predictions", *Journal of Marine Science and Technology*, 2015, (DOI: 10.1007/s00773-014-0293-y).
2. M. Reichel, "Prediction of maneuvering abilities of 10000 DWT pod-driven coastal tanker", *Ocean Engineering*, vol. 136, pp. 201–208, 2017, (DOI: 10.1016/j.oceaneng.2017.03.025).
3. K. Dai and Y. Li "Manoeuvring prediction of KVLCC2 with hydrodynamic derivatives generated by a virtual captive test", *Polish Maritime Research* 4 (104) 2019 Vol. 26; pp. 16-26 (DOI: 10.2478/pomr-2019-0062).
4. J. P. Hooft and J. Pieffers, "Maneuverability of frigates in waves", *Marine Technology*, vol. 25, no. 4, pp. 262–271, 1988, (DOI: 10.5957/mt1.1988.25.4.262 ).
5. H. Lee and S. Shin, "The prediction of ship's maneuvering performance in initial design stage", *Hyundai Maritime Research Institute, Elsevier Science B. V.*, 1998, (DOI: 10.1016/s0928-2009(98)80205-9).
6. Y. Yoshimura, M. Ueno, and Y. Tsukada, "Analysis of steady hydrodynamic force components and prediction of maneuvering ship motion with KVLCC1, KVLCC2 and KCS", *Workshop on verification and validation of ship maneuvering simulation method, Workshop Proceedings*, vol. 1, Copenhagen, pp. E80–E86, SIMMAN 2008.
7. M. Ueno, Y. Yoshimura, Y. Tsukada, and H. Miyazaki, "Circular motion tests and uncertainty analysis for ship maneuverability", *The Japan Society of Naval Architects and Ocean Engineers*, 2009, (DOI: 10.1007/s00773-009-0065-2).
8. Report of the research committee on the standardization of mathematical models for ship maneuvering predictions (P-29), *The Japan Society of Naval Architects and Ocean Engineers*, 2013.
9. IMO Res MSC: Standards for Ship Maneuverability, vol.37, no. 76, 2002.
10. IMO MSC/Circ.: Explanatory Notes to the Standards for Ship Maneuverability, 2002.
11. R. Kołodziej, "Numerical approach to assessment of maneuvering properties of ship with a single propeller", *Coastal, Offshore and Ocean Conference*, 2019.
12. B. Mei, L. Sun, G. Shi, X. Liu, "Ship maneuvering prediction using grey box framework via adaptive RM-SVM with minor rudder" *Polish Maritime Research* 3 (103) 2019 Vol. 26; pp. 115-127 (DOI: 10.2478/pomr-2019-0052).

## CONTACT WITH THE AUTHORS

**Radosław Kołodziej**

*e-mail: radoslaw.kolodziej@cto.gda.pl*

Centrum Techniki Okrętowej S.A.,  
Szczecińska 65, 80-396 Gdańsk,

Politechnika Gdańska,  
Gabriela Narutowicza 11/12, 80-233 Gdańsk,  
**POLAND**

**Paweł Hoffmann**

*e-mail: pawel.hoffmann@cto.gda.pl*

Centrum Techniki Okrętowej S.A.,  
Szczecińska 65, 80-396 Gdańsk,  
**POLAND**

# BLADE CUP METHOD FOR CAVITATION REDUCTION IN MARINE PROPELLERS

**M. Burak Samsul**

Istanbul Technical University, Türkiye

\* Corresponding author: [samsul@itu.edu.tr](mailto:samsul@itu.edu.tr) (M.B. Samsul)

## ABSTRACT

*Energy efficiency has become more important in every industry and daily life. Designing and building a more efficient marine vehicle can lead to lower fuel consumption and a longer lifetime for the components of the vehicle. Erosion caused by cavitation reduces the service life of the propeller and the related components in the propulsion and maneuvering system. Reducing cavitation leads to a longer life for these components. This paper aims to explain and investigate propeller blade cup as a cavitation reduction method for marine propellers. A cavitating no-cup propeller is created and analyzed then the cupped version of this propeller is generated and analyzed to compare with the no-cup propeller. Cavitation results of these propellers are investigated. In addition, the thrust, torque, and efficiency of the propellers are compared.*

**Keywords:** Marine Propeller, Computational Fluid Dynamics, Propeller Cup, Cupping, Cavitation, Propeller Efficiency, Vibration, Noise, Erosion

## INTRODUCTION

A propeller is expected to create the required thrust to overcome the ship resistance at a specified speed. The main engines supply the torque to the propeller. The torque is limited by the engine power and rotational speed of the propeller. Basic propeller design principles give the designer general ideas for how to design a propeller for a particular vessel. In most cases, the propulsion system and components design are made for building a new ship. A newly designed ship provides great flexibility to the Naval Architect to modify most of the design inputs. Propeller diameter, pitch, and blade area ratio can be determined in the design of the propeller. Also, if the propeller design process is started at the very early stages of

the project, engine power and gearbox reduction ratio can be determined more accurately. Even hull stern shape can be optimized because the hull-induced velocity distribution has a critical effect on the propeller [1] [2].

For the propeller design, the most important goals are satisfying the speed and efficiency expectations based on the operating conditions and requirements of the vessel. For some of the design processes on marine propellers, the operating conditions of the propeller may need to be forced to the limits. This can be a necessity for reaching the design goals. Cavitation is a critical design limit for marine propellers. Operating in the cavitating zone leads to noise, vibration, and erosion problems, which cause permanent damage to the propeller and on related components [3] [4]. Also, propeller

performance is affected by cavitation [5]. Any propeller that suffers from the mentioned problems may not be able to meet the speed and comfort expectations after a while of operation. In addition, propeller replacement may be needed because of the damage caused by erosion on the propeller. Nevertheless, in some cases, propeller design may have more strict limitations and challenges. For instance, the propeller diameter can be limited because of the hull geometry. The shaft angle may create diameter restrictions to the propeller coming from shaft installation restrictions on the boat. In order to meet the speed expectations, the propeller may be forced to work in cavitating conditions. Propeller section modification can be the only option to eliminate the cavitation while satisfying the speed and efficiency requirements if all of the mentioned limitations and difficulties are considered [6].

Blade pitch increment is an option to create more thrust if the diameter is not able to be increased. It is well-known that increased blade pitch increases the likelihood of creating cavitation. Cavitation reduction can be achieved by modifying the pitch distribution on a blade starting from the root to the tip. High loading of the blade tips and unloading the midsections of the blade provide a reduction in sheet cavitation. However, this method leads to increased tip loading and propulsive efficiency loss [7].

In this study, cavitation reduction is achieved by not changing the shaft depth, rotational speed of the propeller, or blade area ratio of the propeller. The only modified parameter is the blade trailing edge shape and angle of attack of the blade. Blade trailing edge deflection, which is called the propeller blade cup, is a beneficial option to modify the pressure distribution on the blade. Also, the propeller cup method provides the opportunity to decrease the angle of attack of the propeller, which has a significant effect on cavitation reduction [6] [8].

For this study, two propellers are created. The first is a no-cupped propeller and the second is the cupped version of the first propeller, which has a decreased angle of attack. Propeller cupping increases the effective pitch [6] [8] [9], so the blade angle of attack is decreased in the cupped propeller in order to have the same effective pitch with the initial no-cup cavitating propeller. These two propellers with the same effective pitch provide the same open water characteristics if the cupping level and angle attack decrement is correctly applied [8] [10]. The specified no cupped conventional propeller is a cavitating propeller. The cupped version of this propeller has a blade cup on the trailing edge, and the angle of attack of the blade is reduced to match the produced thrust [9].

This paper investigates the cavitation reduction effect of the blade cup by the Computational Fluid Dynamics (CFD) solution. In addition, previous studies in this field do not provide a CFD solution that examines how to modify the angle of attack of the blade for cavitation reduction [6] [8] [10] [11]. Cupping is an effective solution to modify the cavitation characteristic of a propeller without decreasing its efficiency. The study shows that the cupping application

provides a good opportunity to modify the peak low pressure values on the blade.

## CAVITATION

Cavitation is a fluid mechanics phenomenon that can occur whenever a liquid is used in a machine, inducing pressure and velocity fluctuations in the fluid. Where the pressure is significantly low due to the high local velocities, the fluid phase changes from liquid to vapor, which causes the cavitation to occur.

If cavitation inception is investigated at a point A, the local pressure of the point is defined by  $P_A$ , then;

$$P_A \leq P_V ; \frac{P_0 - P_A}{\frac{1}{2}\rho V^2} \geq \frac{P_0 - P_V}{\frac{1}{2}\rho V^2}$$

where  $P_A$  and  $V_A$  are local flow pressure and velocity,  $P_0$  and  $V$  are the fluid pressure and velocity at the far upstream flow area where the flow is not affected by the geometry, in the so-called infinity.

By using the Bernoulli equation, a simple criterion for cavitation is defined as the cavitation number.  $\sigma$  is the cavitation number and  $C_p$  is the non-dimensional pressure coefficient .

$$\sigma = \frac{p - p_v}{\frac{1}{2}\rho V^2} , C_p = \frac{P_0 - P_A}{\frac{1}{2}\rho V^2} \quad C_p = -\frac{\Delta P}{q}$$

$$\sigma \leq \frac{\Delta P}{q} ; \text{cavitation occurs} , \quad \sigma \geq \frac{\Delta P}{q} ; \text{cavitation does not occur}$$

The types of cavitation depend on the location on the blade of the propeller and the physical appearance itself. Cavitation that depends on the location on the blades are back cavitation and face cavitation. Cavitation that depends on the physical appearance are tip/hub vortex cavitation, sheet cavitation, bubble cavitation, root cavitation, propeller-hull vortex cavitation, and unsteady sheet cavitation. This study mainly examines sheet cavitation and bubble cavitation, with a focus on reducing them on the propeller. These two types of cavitation are generated by low-pressure distribution on the suction side of the blades. Cavitation can occur on a ship component where the local pressures are lower than the evaporation pressure of the water. Because of the creation of high local velocities and low pressures, propellers are one of the main sources of cavitation for marine vehicles.

There are several effects of the cavitation on the propellers, such as performance breakdown, noise, vibration, and erosion. This study mainly focuses on reducing/eliminating blade erosion by reducing the cavitation while keeping the propeller performance constant.

## HOW TO REDUCE CAVITATION

There are several methods to reduce the cavitation on the propeller, such as decreasing the blade rotational speed, changing the shaft depth, anti-fouling, and pitch reduction.

If the propeller rotation speed is reduced to create a lower local speed distribution around the blade, then the local pressure values are going to be increased. The increment for the local pressures provides an opportunity to create higher pressures than the vapor pressure of the water. Propeller rotational speed reduction, likewise, brings loss in thrust. Enlarging the propeller diameter is an option to gain the lost thrust back; however, physical limits may prevent application of this solution in some cases.

Increasing the depth increases hydrostatic pressure. This means that cavitation occurrence risk is reduced when the depth of the propeller is increased. The depth-increasing method for cavitation reduction is not an applicable solution for the specified cases defined in this paper.

Fouling leads to an increased probability for cavitation and also reduces propeller efficiency [12]. However, if a propeller creates cavitation when it is new, this situation shows that cavitation reduction should be achieved by amending the propeller characteristics. This study focused on the cavitation reduction solutions for the propellers that are already non-fouled.

For both fixed-pitch conventional propellers and controllable pitch propellers, decreasing the angle of attack leads to higher local pressure distribution on the suction side of the blade. Fig. 1 shows a typical pressure distribution on a blade section that has a positive angle of attack.

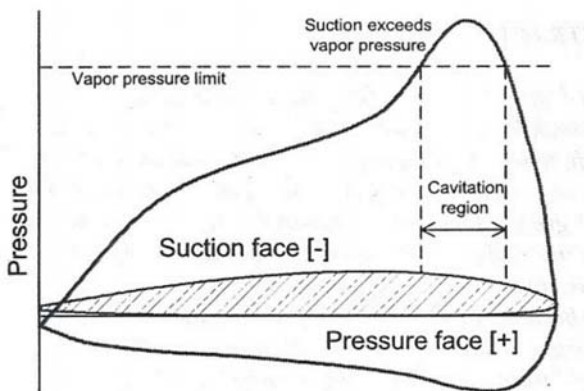


Fig. 1. Typical pressure distribution on a blade section [13]

In order to decrease or eliminate the cavitation, manipulating the pitch by amending the angle of attack is always an option. But pitch decrement is going to bring loss in thrust. If there is no available option to gain back the lost thrust, the pitch reduction application leads to loss in produced thrust.

Modifying the pitch distribution on an existing propeller and creating a new blade that has the same overall pitch but a different angle of attack distribution on the sections of

the blade is an option to reduce the cavitation. In addition, cloud cavitation can be prevented or reduced by increasing tip loading and distributing the blade loads more evenly from the maximum pitch region to the tip. The tip loading method to reduce cavitation on the blade provides sheet cavitation reduction. However, high tip loading can also bring up tip vortex cavitation and propulsive efficiency loss from the tip vortex [7].

## EFFECT OF ANGLE OF ATTACK ON CAVITATION

Propellers produce thrust by creating a pressure difference between the suction side and the thrust side of the blades. Increasing the pressure difference between these two faces increases the thrust generated by the propeller. Increasing the angle of attack of the blades, which means increasing the pitch of the propeller, also leads to the generation of a relatively higher pressure difference and thrust. This additional thrust may be needed on a vessel that has requirements and design restrictions, as mentioned in the previous section. However, as shown in Fig. 2, an increased angle of attack leads to cavitation risk on the back (suction side) of the propeller blade.

On the suction side of the blade, especially in the mid-chord area, the flow velocity is at the highest level, which means that peak low-pressure values are observed in this zone.

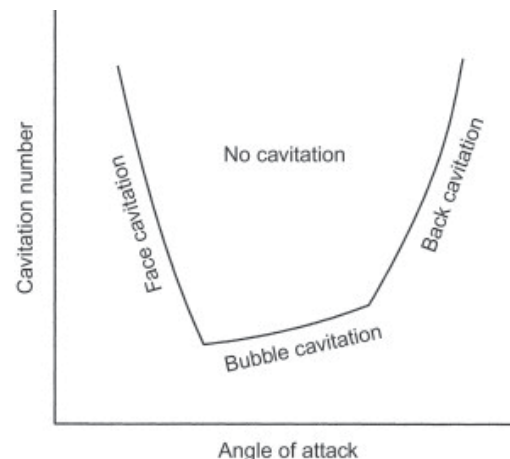


Fig. 2. Angle of attack vs. cavitation number [14]

## CUPPING METHODOLOGY

### AIM OF CREATING PROPELLER CUP

For the specified cases for a boat that are defined in the previous sections, there might be no opportunity to change the propeller characteristics to avoid cavitation. However, cavitation reduction might be needed on these specified challenging cases. In these cases, reducing the rotational speed or angle of attack is going to reduce or eliminate the cavitation as known. But applying these methods leads to thrust and efficiency losses. At this point, the propeller cup

is very advantageous when the propeller cavitation needs to be reduced while the propeller thrust and efficiency need to be preserved [6].

The purpose of the cupping application on the blades of the propeller is to spread the low pressure on the suction side of the blade to have the pressure distribution above the vapor pressure without changing the total pressure difference between the faces of the blade. With the help of the cup application, local pressure values around the mid-chord are increased where the minimum pressure values are expected to be observed on a conventional propeller. As a result of the blade cup, the local pressure values around the trailing edge of the propeller are decreased compared with a no-cupped conventional blade section [6] [8]. In addition, a blade cup is an anti-singing option. The anti-singing chamfer is typically applied to the suction side of the blade; however, there are some anti-singing edge forms that are applied to both sides [15].

Fig. 3 shows the pressure distribution difference between a conventional blade section and a cupped blade section.

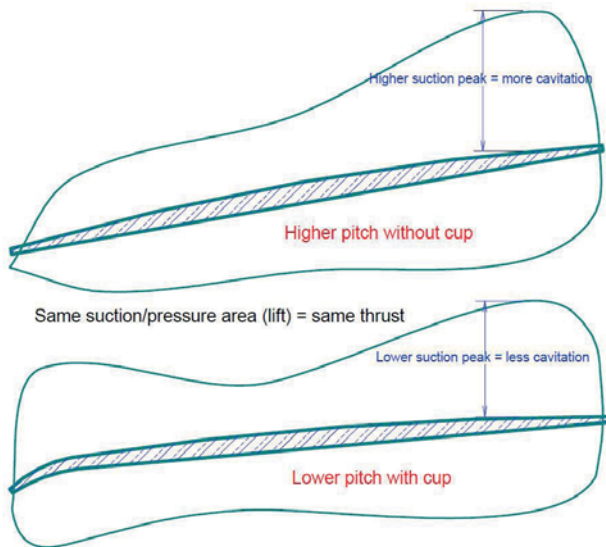


Fig. 3. Pressure distribution on cupped and no-cup blade sections [8]

A propeller cup is simply the deformation of a propeller's trailing edge toward the pressure face. Providing an additional camber to the blade trailing edge changes the pressure distribution along the blade's chord length, adding lift toward the trailing edge. Typically, there is a peak in the lift distribution around the leading half of the blade. This peak lift zone is also the lowest pressure area, in general, for a conventional Fixed Pitch Propeller (FPP). The main purpose is to create a suction side pressure distribution that is above the vapor pressure at the specified condition. It is possible to eliminate/reduce the cavitation, which can be achieved by spreading the lowest pressure values (around the peak lift area on the suction side) to the blade chord. This also means spreading the lift distribution on the chord instead of loading it around the mid-chord zone [7]. Propeller cupping provides an opportunity to modify the pressure distribution on the

blade chord. Because effective pitch increases with the effect of cupping, the angle of attack of the blade can be reduced to reach the effective pitch value of the initial no-cup propeller. With the help of this, the lowest pressure value can be changed while keeping the total pressure difference constant, which means keeping the thrust constant.

## CUPPING CREATION METHOD

There is no established and agreed methodology to create a cup on the propeller blades. Different companies make definitions based on their rates. However, the experiments performed at the David W. Taylor Naval Ship Research and Development Center provide extensive data to examine the cupping and cavitation relationship, and also provide a formulation for the cupping vs. effective pitch relationship [6]. In this study, blade cup definitions are made in agreement with Hydrocomp. Fig. 4 shows the propeller diameter /cup drop ratio definition of Hydrocomp [11].

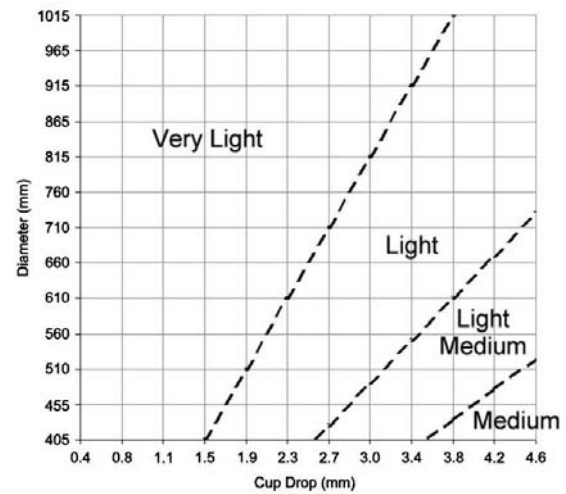


Fig. 4. Propeller diameter vs. cup drop [11]

The total deflection that is given to the trailing edge of the blade is defined as a ratio of the diameters of the propeller. As shown on the cup drop /diameter graph, cup levels are named as very light, light, light medium, medium, medium heavy, and heavy cup. All of these levels are defined as a ratio of propeller diameters. Chord deflection is applied to start from 0.9 C to 1.0 C. That means 0–0.9 C of the blade section is the same as the original section. When a chord deflection between 0.9–1.0 C is applied, propeller thrust and torque increased at the same advance coefficient. Then, the blade angle of attack should be decreased on the applied cup version of the propeller to match the effective pitch.

In the following chapters, a cavitating conventional fixed-pitch propeller is investigated. Then, that specified propeller is solved after applying the cup and reducing the blade angle of attack. This study provides an opportunity to compare cavitation characteristics of two different propellers that have the same thrust, torque, and efficiency values at the same advance coefficient.

## CAVITATION REDUCTION BY CUP METHOD

### NO CUPPED AND CUPPED PROPELLER COMPARISON

To observe the cavitation reduction capability of the blade cup, a FPP cavitating propeller is defined by using the lifting surface code. Once the cavitating propeller is obtained and solved at defined advance coefficients, then the cupped version of this propeller is created by following the same procedure. However, the critical point of creating the cupped propeller is to find the angle of attack decrement. The angle of attack optimization can be carried out by two tools. One is the effective pitch-geometric pitch conversion formula, which provides a very basic idea, and the second one is the lifting surface method. The angle of attack decrement for the cupped propeller should be compatible with the applied cupping because the additional torque that is created by the cupping should be adjusted by the angle of attack decrement in order to not exceed the torque of the initial no-cup propeller. After creating the propellers with the help of the lifting surface code, sections of the propeller are converted into a 3D model.

The camber distribution of the section is selected as NACA66 for the initial conventional propeller. The NACA66 camber is modified to create the determined cup deformation on the blade section. To compare the cavitation characteristics, firstly, the conventional propeller is solved with CFD for two different advance coefficients. The advance coefficients are shown in Table 1.

Tab. 1. Solution advance coefficients, inlet velocities, and propeller revolutions

Advance Coefficient	Inlet Velocity (m/s)	Propeller Revolution (rps)
0.82	10.28	25
0.87	8.7	20

Once the thrust and torque values are calculated for the conventional no-cup cavitating propeller, the cupped version of the propeller is created. Several cupping levels are applied on the blade and the angle of attack of the blades is reduced relative to the cupping level of each propeller. Pitch ratio (P/D) tuning is done by the lifting surface code. The lifting surface model forms a reliable basis for designing blade section profiles and screw propeller blades [16]. As emphasized, thrust, torque, and efficiency results should be the same as the initial conventional propeller.

There is a practical formulation that proposes a pitch conversion for cupping applications [8] [10]. This formulation does not guarantee that the effective pitch of the propeller can be accurately found. However, the formulation provides an accurate starting point for the CFD calculations. After solving the cupped propeller, which is generated with the help of the formulation, final tuning can be performed with CFD studies.

$$P_{EFF} = P_{GEO} + 21(X_{CUP}) [8]$$

where,

$P_{EFF}$  = effective pitch

$P_{GEO}$  = geometric (uncupped) face pitch

$X_{CUP}$  = trailing edge deformation (drop)

Table 2 shows the general characteristics of the created no-cup and cupped propeller. The no-cup propeller has a 675 mm mean pitch, which is 1.35 in terms of P/D. After applying the cup to the blades, the cupped propeller mean pitch value should be decreased with the help of the formulation in order to match the effective pitch values of these two propellers. In this case, the trailing edge deformation is 6.2 mm. If a 6.2 mm cup drop is applied to the blade, which has a 675 mm mean pitch, the cupped blade mean pitch should be decreased to 675 mm – (21 × 6.2 mm) = 544.8 mm. In this case, the cupped propeller P/D is determined to be 1.1, which is equal to 550 mm.

As emphasized, the blade angle of attack of the cupped propeller should be checked with CFD, and then, final tuning of the cup drop can be achieved.

Tab. 2. No-cup and cupped propeller general characteristics

No-Cup and Cupped Propeller	
Diameter (mm)	500
No-Cup P/D	1.35
Cupped P/D	1.1
Number of Blades	3
Expanded Area Ratio	0.6
Hub Diameter (mm)	100
Camber	NACA66

The sections of the no-cup and cupped propeller are created according to the values shown in Table 3. The pitch values on the table show the blade section pitches. The effective pitch of the cupped propeller is the same as the initial no-cup propeller with the help of the cup trailing edge deformation.

Tab. 3. No-cup and cupped propeller section details

r/R	Chord / D	P/D (No-Cup)	P/D (Cupped)	$F_{max} / C$	$T_{max} / C$
0.24	0.349	1.296	1.056	0.021	0.124
0.25	0.357	1.302	1.061	0.021	0.119
0.30	0.380	1.320	1.075	0.022	0.101
0.40	0.420	1.347	1.098	0.023	0.078
0.50	0.449	1.365	1.112	0.024	0.063
0.60	0.465	1.372	1.118	0.022	0.051
0.70	0.466	1.369	1.116	0.018	0.041
0.80	0.442	1.360	1.108	0.014	0.033
0.90	0.373	1.344	1.095	0.010	0.026
0.95	0.312	1.333	1.086	0.009	0.024
0.98	0.245	1.326	1.080	0.008	0.025
1.00	0.124	1.320	1.076	0.012	0.042

The no-cup and cupped propeller 3D files are modeled. Fig. 5 shows the geometries of the propellers. The cup deflection can be observed on the trailing edge of the cupped propeller.

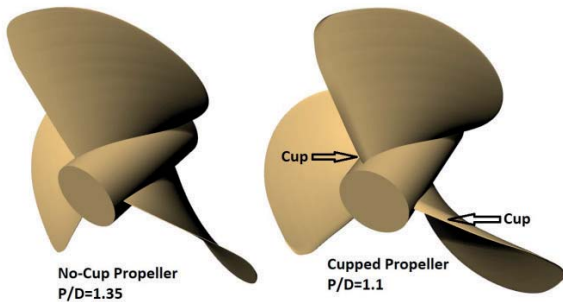


Fig. 5. No-cup propeller and cupped propeller view

In Fig. 6, the blade sections of the analyzed propellers are shown. The trailing edge deflection is defined by the manipulation of the camber function. The blade section of the cupped propeller indicates that the cup deflection starts from 0.95 C of the section.

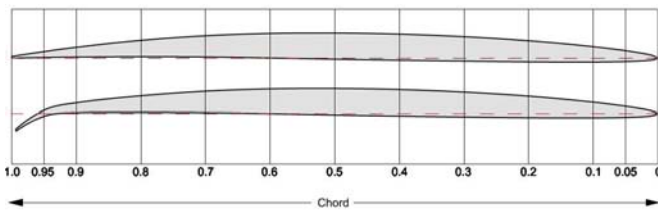


Fig. 6. No-cup and cupped propeller blade sections

The created cupped blade section has a lower angle of attack compared with the no-cup blade section. The reason for decreasing the angle of attack in the cupped propeller is to match the produced thrust with the no-cup propeller. The trailing edge deflection leads to a higher flow velocity on the trailing edge area and creates additional thrust [9]. However, the lower angle of attack reduces the peak velocity around the mid-chord. With the help of the cup and angle of attack optimizations, the cupped propeller is expected to produce the same open water results while creating a reduction in cavitation. The angle of attack difference of the propellers is shown in Fig. 7.

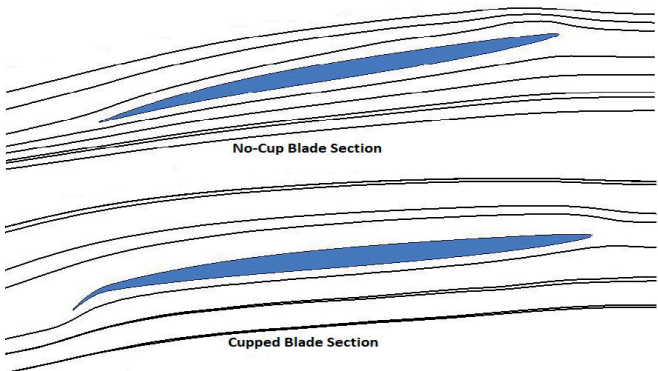


Fig. 7. Angle of attack comparison

Fig. 8 shows the computational domain dimension in terms of propeller diameter.

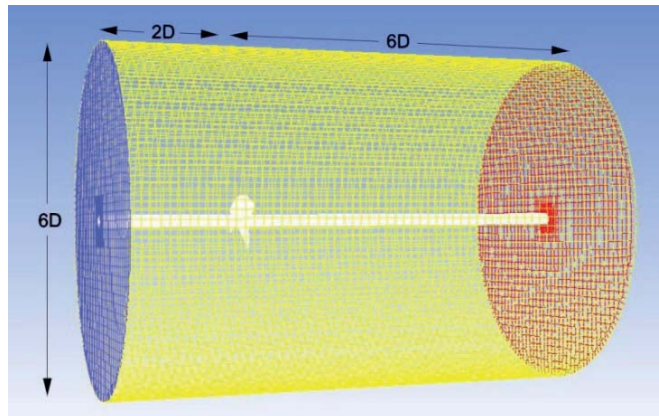


Fig. 8. Computational domain

The same calculation procedure and parameters are used in the analysis. The vaporization pressure is 3540 Pa, which is the same for both the no-cup and cupped propeller calculation in order to compare the cavitation occurrence for the same depth conditions. The K- $\omega$  Shear Stress Transport (SST) turbulence model and Schnerr-Sauer cavitation model is used for the Reynolds Averaged Navier Stokes (RANS) calculations of both propellers [17] [18]. If the cavitation of a propeller is simulated using the RANS solver combined with the K- $\omega$  SST turbulence model and Schnerr-Sauer cavitation model, the behavior of the propeller cavitation is in good agreement with the test results [19]. CFD calculations are performed by using Ansys Fluent. The single-rotating-frame method is selected for the solutions. The first layer thickness of the viscous layer is  $9 \times 10^{-5}$  mm and 10 layers are applied with a stretching ratio of 1.2. The  $y^+$  value is between 30–110 on the major part of the blades, and  $y^+$  is reduced to 6–12 approximately around the roots of the blades. A  $10^{-8}$  residual error for continuity and  $10^{-7}$  residual errors for x-y-z velocity, k-omega, and vf-phase-2 are achieved in the calculations.

Mesh sizes, which are defined as the surfaces of the propeller and shaft, are shown in Table 4. The blade trailing edge cell size is reduced in order to create a fine mesh around the cupping area compared with the blade faces. The calculation domain has a full structured hexahedral mesh, which is created by Hexpress.

For the no-cup propeller mesh, the minimum orthogonal quality is 0.205 and the maximum skewness is 0.795. For the cupped propeller mesh, the minimum orthogonal quality is 0.216 and the maximum skewness is 0.784.

Tab. 4. Mesh parameters

Mesh	No-Cupped	Cupped
Blades	3 mm	3 mm
Blade Trailing Edge	0.3 mm	0.3 mm
Root	2 mm	2 mm
Shaft	5 mm	5 mm
Total Cell	7547218	7672828

Fig. 9 shows the surface mesh view of the propeller. As shown on the mesh parameters table, the trailing edge mesh is finer.

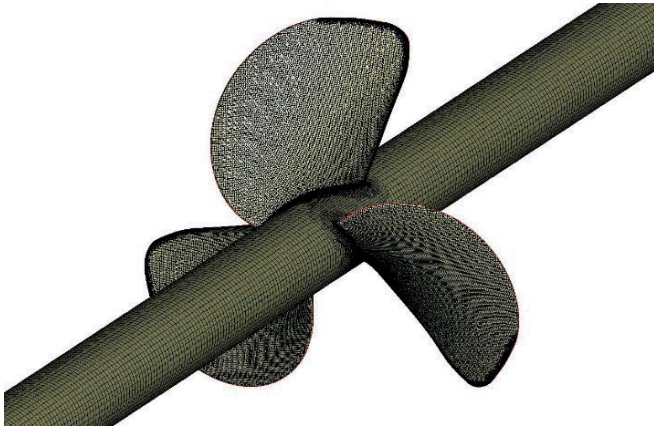


Fig. 9. Cupped propeller cells on suction side

The calculations are performed as steady. The analyses are solved without the vapor phase first. In this initial analyses, which provides a converged start to cavitation calculations, Simplec segregated solver is used. Discretization schemes are least-square cell-based for the gradient and second-order for pressure, momentum, turbulent kinetic energy, and specific dissipation rate. After convergence is satisfied to  $10^{-7}$  residual error, the multiphase model is solved with Simplec solver. The same discretization schemes are used but Presto for pressure and Quick for volume fraction is selected additionally.

## RESULTS AND DISCUSSION

Two different propellers that are working in two different advance coefficients are solved with CFD. The calculation results are shown in Fig. 10 as open water curves. The  $K_T$ ,  $K_Q$ , and efficiency results indicate that one of the main goals is satisfied. The first main goal is creating a cupped propeller that is producing the same thrust that can be replaced by the no-cup propeller without any additional revisions or replacements on the propulsion components of the boat.

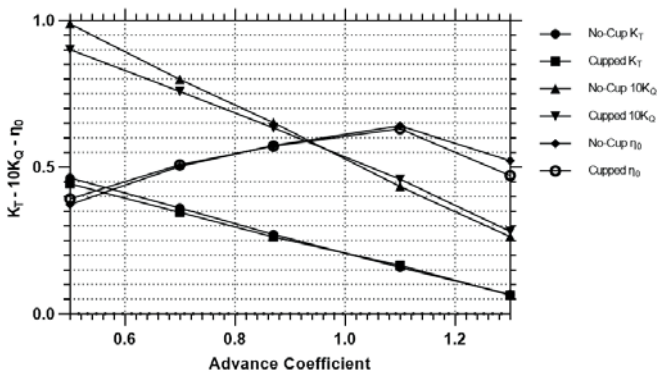


Fig. 10. Open water curves of no-cup and cupped propellers

$$K_T = \frac{T}{\rho n^2 D^4}, \quad K_Q = \frac{Q}{\rho n^2 D^5}, \quad \eta_0 = \frac{J K_T}{2 \pi K_Q}$$

Table 5 shows that the efficiency values of the defined propellers are almost the same for the advance coefficients where the cavitation comparison is performed.

Tab. 5. Propeller efficiency comparison

J	No-Cupped	Cupped
0.82	55.1%	56.6%
0.87	56.7%	56.5%

The cavity patterns of the no-cup propeller for the 0.82 and 0.87 advance coefficients, which are created by the lifting surface, are shown in Fig. 11. The cavity patterns are expected to be in agreement with the CFD cavitation plots.

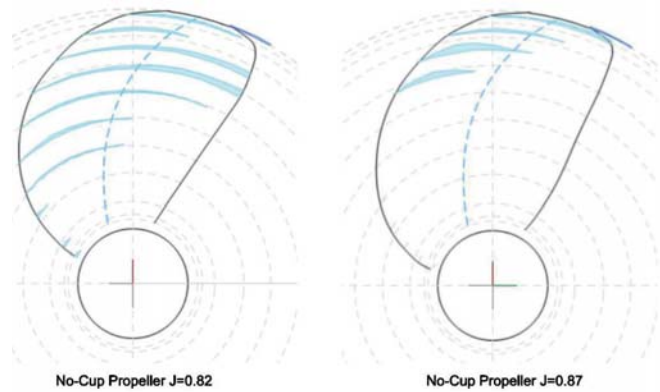


Fig. 11. Cavitation patterns of no-cup propeller at 0.82 and 0.87 advance coefficients by the lifting surface method

The second goal is to observe a reduction in cavitation. Figs. 12 and 13 show the vapor fraction comparison of the propellers at advance coefficients 0.82 and 0.87. For  $J = 0.82$ , cavitation risk is observed starting from  $0.5R$  of the blade to the tip (left). However, on the cupped version of the specified propeller (right), only the trailing edge and the tip of the blade generate cavitation risk. The agreement between the lifting surface method and CFD can be noticed for the no-cup results [20].

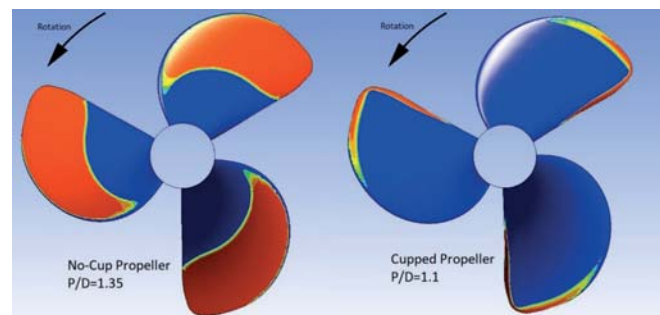


Fig. 12. Vapor fraction comparison at  $J = 0.82$

Compared with the 0.82 advance coefficient, 0.87 has a lower cavitation-producing potential because of the lower local velocities on the blades. Even having a lower rotational speed and inlet velocity at 0.87, a vapor fraction over 0.5 can be observed from 0.7R to the tip (left). However, the cupped version propeller (right) almost eliminated the cavitation occurrence. The phase change is found only on the trailing edge area between the 0.7R and tip, as shown in Fig. 13.

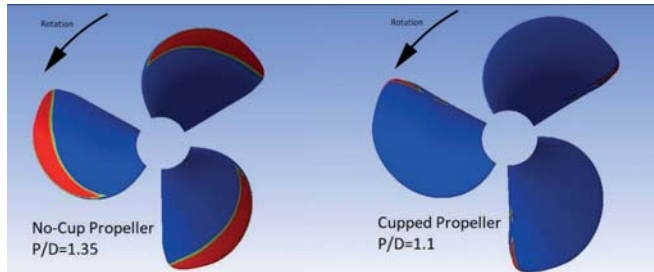


Fig. 13. Vapor fraction comparison at  $J = 0.87$

The iso-surface plot at vapor fraction 0.5 is shown in Fig. 14 at advance coefficient 0.87. The cupped version of the propeller, which has a lower blade angle of attack, creates a better cavitation characteristic at the defined advance coefficient.

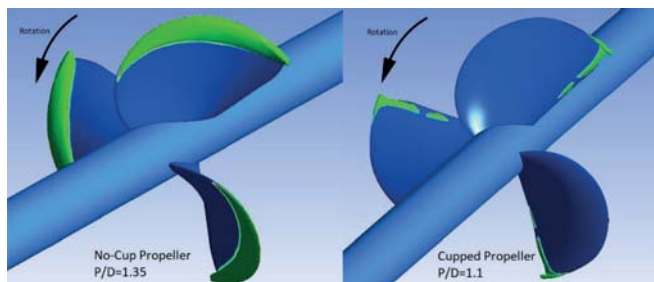


Fig. 14. 0.5 vapor fraction comparison at  $J = 0.87$

Figs. 15 and 16 show the pressure coefficient plots of the propellers at advance coefficients 0.82 and 0.87. If the pressure coefficient plots are checked according to the defined  $\sigma$  values in the figures, the agreement in the vapor fraction plots and pressure coefficient can be observed.

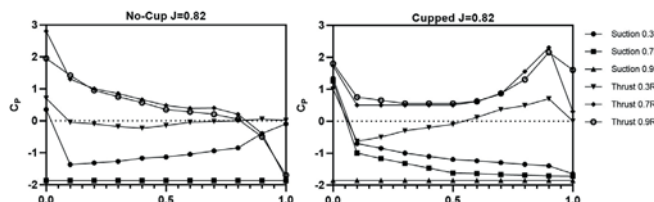


Fig. 15. Pressure coefficient distribution at  $-\sigma = 1.85$

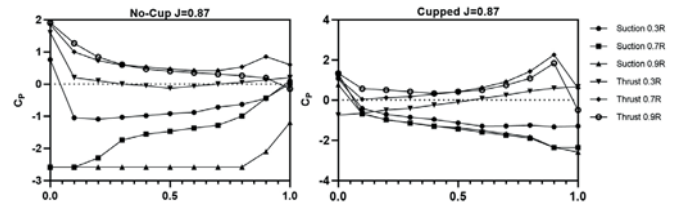


Fig. 16. Pressure coefficient distribution at  $-\sigma = 2.59$

## CONCLUSION

Erosion is a crucial issue for marine propellers. In order to provide a long life-time, cavitation elimination is fundamental. As detailed in the previous sections, there are several methods for cavitation reduction on the blades. However, all of these mentioned methods for cavitation reduction are able to be applied at the initial stages of the design of the boat.

Hull speed, hull stern shape, propeller-hull clearance, engine power, and gearbox reduction ratio should be correctly examined. However, for the specific cases where there are solid design restrictions, modifying the pressure distribution on the blade by propeller cup could be an alternative cavitation elimination method. By virtue of the propeller cup, the angle of attack of the blades is reduced after determining the cavitation distribution of the conventional propeller. A well-optimized blade cup compensates for the lost thrust that comes from the blade angle of attack decrement.

The total pressure difference between the low-pressure side and the high-pressure side of the propeller is kept constant. The critical point of the cup determination is to examine the influence of the different cup levels on the angle of attack alteration of the blades. Several CFD calculations should be performed for a range of P/D values to adjust the pitch of the cupped version of the studied cavitating propeller.

The thrust and torque coefficients and efficiency comparison tables for the specified cases show that a no-cup propeller can be converted to a cupped propeller that provides the same performance characteristics and has the same diameter and rotational speed but a different angle of attack.

Vapor fraction and cavitation coefficient plots indicate a significant reduction in the cavitation occurrence on the blades, which are found for two different advance coefficients. Determination of the cup level and P/D modification are the main objectives and also the main challenges. The  $P_{EFF} = P_{GEO} + 21(X_{CUP})$  formulation provides a solid starting point and offers an opportunity to identify a range for P/D modification [8] [10].

CFD calculations should be performed for the final tuning of the modified (cupped) propeller. Thrust, torque, and efficiency values should be examined attentively as well as the cavitation results. In order to create a systematic cup creation method, the blade pitch conversion formulation should be tested with CFD calculations for a P/D range, which should be the focus of future work.

## REFERENCES

1. T. Koronowicz, Z. Krzemianowski, T. Tuskowska, J.A. Szanty, "A Complete Design of Ship Propellers Using New Computer System" *Polish Maritime Research* 1(59), vol. 16, pp. 29-34, 2009.
2. T. Koronowicz, Z. Krzemianowski, "Investigation of Influence of Screw Propeller Operation on Water Flow Around Stern Part of Ship Hull" *Polish Maritime Research* 1(51), vol 14, pp. 3-8, 2007.
3. A. Peters, U. Lantermann, O. el Moctar, "Numerical Prediction of Cavitation Erosion on a Ship Propeller in Model- and full-scale" *Wear*, vol. 408-409, pp. 1-12, 15 August 2018.
4. B. Aktas, M. Atlar, S. Turkmen, W. Shi, R. Sampson, E. Korkut, P. Fitzsimmons, "Propeller Cavitation Noise Investigations of a Research Vessel Using Medium Size Cavitation Tunnel Tests and Full-Scale Trials" *Ocean Engineering*, vol. 120, pp. 122-135, 1 July 2016.
5. J.W. Lindau, D.A. Boger, R.B. Medvitz, R.F. Kunz, "Propeller Cavitation Breakdown Analysis" *Journal of Fluids Engineering*, vol. 127(5), pp. 995-1002, Sep 2005.
6. J. G. Peck, B. L. Fisher, "Cavitation Performance of Propellers With and Without Cupping" David W. Taylor Naval Ship Research and Development Center, Sep 1976
7. K. W. Shin, P. Andersen "CFD Analysis of Cloud Cavitation on Three Tip-Modified Propellers With Systematically Varied Tip Geometry" *J. Phys. :Conf. Ser* 656 012139, 2015.
8. Donald M. MacPherson, HydroComp Technical Report, Small Propeller Cup, Presented at the Propeller/Shafting Symposium, 1997
9. Jing-Fa Tsai, "Study on the Cavitation Characteristics of Cupped Foils" *Journal of Marine Science and Technology*, vol. 2, pp. 123-134, 1997.
10. Hwang, J. L, Tsai, J: F., Li C. Y., "Cupped Propeller Test and Analysis", vol. 42, issue 4, pp. 186-192, October 1995
11. HydroComp Technical Report, Correlating Michigan Wheel Cup Gages
12. E. Korkut, M. Atlar, "An Experimental Study into the Effect of Foul Release Coating on the Efficiency, Noise and Cavitation Characteristics of a Propeller" First International Symposium on Marine Propulsors smp'09, Trondheim, Norway, June 2009
13. E. V. Lewis, Principles of Naval Architecture, Volume II, Resistance, Propulsion, and Vibration, Society of Naval Architects and Marine Engineers, Jersey City, NJ, 1988.
14. E. C. Tupper, "Introduction to Naval Architecture" , Fifth Edition, 2013
15. J. Carlton, 2007, "Marine Propellers and Propulsion", Second Edition, Butterworth-Heinemann
16. P. Krol, "Blade Section Profile Array Lifting Surface Design Method for Marine Screw Propeller Blade" *Polish Maritime Research* 4 (104), vol. 26, pp. 134-141, 2019.
17. D.-C. Liu, W.-X. Zhou, "Numerical Predictions of the Propeller Cavitation Pressure Fluctuation behind Ship and Comparison with Experiment", *Journal of Ship Mechanics*, vol. 23(3), pp. 245-254, March 2019.
18. N. Lu, G. Bark, U. Svennberg, R. Bensow, "Numerical Simulations of the Cavitating Flow on a Marine Propeller", Proceedings of the Eighth International Symposium on Cavitation, pp. 338-343, 2012.
19. L.Guangnian, Q. Chen, Y. Liu "Experimental Study on Dynamic Structure of Propeller Tip Vortex" *Polish Maritime Research* 2 (106), vol. 27, pp. 11-18, 2020.
20. S. Sezen, A. Dogrul, S. Bal, "An Empirical Approach For Propeller Tip Vortex Cavitation Noise", *Sigma J Eng & Nat Sci*, vol. 36 (4), pp. 1127-1139, 2018.

## CONTACT WITH THE AUTHOR

**M. Burak Samsul**

*e-mail: samsul@itu.edu.tr*

Istanbul Technical University,  
Maslak, 34467 Istanbul  
**TÜRKİYE**

# IMPLEMENTING SIMULATIONX IN THE MODELLING OF MARINE SHAFTING STEADY STATE TORSIONAL VIBRATIONS

Nenad Vulić\*

Karlo Bratić

Branko Lalić

Ladislav Stazić

Faculty of Maritime Studies, Split, Croatia

\* Corresponding author: [nenad.vulic@pfst.hr](mailto:nenad.vulic@pfst.hr) (N. Vulić)

## ABSTRACT

*Marine propulsion shafting systems are exposed to torsional vibrations originating from excitations in their prime movers and propellers. It is essential to analyse their steady state response in the earliest stage of ship design. The paper describes the implementation of SimulationX software based upon simulation modelling for these calculations. This software can be used either by the design office of the shipyard or by the classification society for verification within the plan approval phase. Some specifics of the input data preparation are briefly discussed. In addition, the simulation results depend on the modelling approach chosen. For these reasons, the real two-stroke Diesel engine ship propulsion system was chosen and several different models were implemented for system modelling. SimulationX calculation results are compared with those of two well-known and field-proven programs that use an analytical approach. Finally, the results are compared with the measurements performed on the actual newly built ship. Discussion reviews the selected SimulationX model, and its verification and validation in the case of engine cylinders with normal ignition.*

**Keywords:** mechanical dynamic system, critical speeds, torsional stress amplitudes, two-stroke marine Diesel engine, normal firing

## INTRODUCTION

Marine propulsion shafting systems are exposed to dynamic excitations from their propulsion engines (usually diesel engines) and propellers. It is essential to analyse their torsional vibrations stationary response, as well as to verify calculated results within the plan approval process at the classification society in charge of classing the vessel. Furthermore, according to the classification rules, these results must also be validated by measurements of the torsional stress amplitudes of the shafts on board the ship over the operating speed range of the engine [1].

Marine classification societies are required to conduct a timely verification of the submitted calculations during the plan approval and to supervise validation of these verified results on board the first ship of the sister ship series. These

calculations result from the propulsion system design concept, the dimensions, the material properties and their dynamic loading. The results shall include natural frequencies, vibration modes, critical speeds, torsional stress amplitudes in the shaft sections, allowable stresses and barred speed ranges, if any. Verification of the results shall be based on the criteria specified in IACS Unified Requirements [2] as implemented in the technical rules of the classification society. Validation shall be performed by measuring the torsional stress amplitudes in an attainable section of the selected shaft and comparing them with the calculated values.

The first failures of marine propulsion systems shafting elements which can be attributed to the adverse effect of torsional vibrations were reported a long time ago, i.e. at the beginning of the 20<sup>th</sup> century, even before the first Diesel engine powered ocean-going ship entered into service [3].

These failures initiated the development of calculation and measurement methods for torsional vibrations. A systematic and methodical presentation of the calculation methods was published by Ker Wilson in 1935, with its 3<sup>rd</sup> edition in 1963 [4]. In 1968, Lloyd's Register published detailed instructions for calculating the torsional vibration characteristics of shafts within their classification rules [5]. This enabled the development of the computer program by Butković et al. [6], which was extensively used for these calculations in Croatia by Diesel engine manufacturers and the local classification society. An important contribution was the 1985 textbook by Hafner and Maass, which comprehensively presented the details of torsional vibration calculations and dedicated computer codes based on analytical methods [7]. Implementing his own analytical approach, Magazinović developed a powerful and user-friendly computer program [8] based on analytical methods, which is widely implemented in torsional vibration calculations in Croatia, especially in new constructions of the Croatian Shipyard Brodosplit. This program and its later extensions have been used and referred to in many publications, e.g. [9, 10, 11]. An important contribution to the analytical methods was brought out by Murawski and Charchalis, who proposed their simplified method for torsional vibrations calculations which was extensively elaborated in [12]. The last significant encirclement of the systematic analytical approach was brought out in the guidance VDI 2039 [13].

Simulation modelling approach for the calculations of torsional vibrations has been implemented by ESI-Group (formerly: ITI-Software) Dresden as the part of their platform for modelling, simulating and analysing of technical systems, SimulationX [14]. This software platform has been approved by several IACS classification societies by allowing the implementation of SimulationX for ships they classify. The basic implementation of SimulationX for these calculations was described in [15].

SimulationX enables the modelling and simulation of complex multiphysics systems, e.g. mechanical translational or rotational, 2D or 3D systems and to perform virtual tests of these models by evaluating their response. The basic procedure is to assemble the system from the elements already available in SimulationX. Users' self-developed elements in Modelica, the object-oriented programming language for modelling of physical systems, may also be used. The way in which these elements are connected within the model determines whether a variable in the model will be input or output. The number of equations in these elements, describing the variables which may be either input or output values, is to be equal to the number of variables. It is irrelevant whether these equations are expressed in their implicit or explicit form, algebraic, differential or discrete. This enables the user to perform complicated types of linear or nonlinear analyses.

This paper aims to describe possibilities and advantages, with some possible ambiguities and disadvantages, of implementing the TVA module of SimulationX simulation modelling-based software in the procedure of torsional vibration calculations. Some essential details about the

modelling of damping and excitation and the preselection of the actual calculation model have already been published [16, 17]. Implementing simulation modelling to the problem of finding steady-state response of marine main propulsion shafting torsional vibrations compared with their solution in a closed analytical form (although the analytical solution is usually complicated and demanding) shows certain advantages, especially when any element in the system, e.g., a highly flexible coupling with a silicone elastic element or a spring-viscous torsional vibration damper, behaves nonlinearly in terms of its rotation-torque response. Simulation modelling software, such as SimulationX, is easy to use in the handling of these situations, because it is not critically important whether the problem is linear or nonlinear, just that the convenient solver has been selected. On the other hand, the disadvantage of SimulationX lies in the fact that its result is always expressed in the form of point values forming the final solution, without functional dependencies of the output values in analytical form. However, this is not a major problem, because the final results in the analytical approach are usually presented in the form of graphs consisting only of points showing the results. SimulationX software comprises its TVA module intended for torsional vibration analysis of rotational mechanical systems in general [14] and this module has been used for the modelling of the actual real systems presented hereafter.

## MATERIAL AND METHODS

Torsional vibration simulation modelling starts from the actual propulsion shafting general arrangement drawing (prepared early within the ship machinery systems design phase). Its main objective is to create an equivalent discretised mechanical model composed of point inertias, massless elastic elements (torsional springs), massless damping elements (torsional dampers), and somewhat specific elements of engine cylinders together with the system excitation loads. These excitations comprise gas forces (due to combustion in the engine cylinders), inertia forces (due to accelerations of reciprocating components in the engines), and propeller forces (consisting of their steady-state and vibrational part).

In general, the torsional vibrations of marine propulsion shafting with  $n$  rotational inertias can be described by the following system of  $n$  ordinary differential equations of second order:

$$\mathbf{J}\ddot{\boldsymbol{\varphi}}(t) + \mathbf{C}\dot{\boldsymbol{\varphi}}(t) + \mathbf{K}\boldsymbol{\varphi}(t) = \mathbf{T}(t) \quad (1)$$

where:

$\mathbf{J}$ ,  $\mathbf{C}$ ,  $\mathbf{K}$  – matrices of rotational inertias, damping (absolute and relative), stiffness;

$\boldsymbol{\varphi}$ ,  $\dot{\boldsymbol{\varphi}}$ ,  $\ddot{\boldsymbol{\varphi}}$  – vectors of angular displacements, rotational velocities, rotational accelerations;

$\mathbf{T}$  – vector of time dependent excitation torques in the cylinders and on the propeller.

In general, depending on the form of the vector of excitation torques, an analytical solution of the system (Eq. 1) can be practically obtained when the elements of the matrices **C** and **K** are constant. However, if their dependence on, for example, the rotational velocity is nonlinear, the implementation of a simulation modelling approach would be easier than trying to solve the system of differential equations in an analytical closed form.

## MATERIAL

The shafting general arrangement drawing, prepared by the shipyard, usually contains all of the information necessary to model shaft parts in terms of their discretised point inertia elements and the massless springs interconnecting these elements. However, the modelling of massless damping elements requires some additional knowledge, as their damping values are not always uniquely defined, but based on results from practice and previous cases. However, there are several references in the literature suggesting proper values to be used, e.g. [18].

Engine licensors generally provide sufficient data needed to model their Diesel engines, such as cylinder bore, stroke, connecting rod length, reciprocating masses, cylinder firing order, torsional elastic models of engine crankshafts, and engine cylinder pressures (or crank tangential forces) vs. crank angle. Propeller manufacturers provide documentation that contains the necessary information about the propeller, such as number of blades, propeller diameter and mean pitch, propeller mass, and its material. These propeller data are necessary to obtain the correct value of the mass moment of inertia of the propeller together with the entrained water vibrating with the propeller, which is used in the calculations.

## METHODS

This paper has been focused exclusively on marine propulsion systems with two-stroke diesel engines, due to some important specifics regarding the modelling of absolute damping, as described in [17]. Simulation modelling of the actual system is based on the elements available in the TVA module of the SimulationX software [14]. This software is based on Modelica, the object-oriented language for modelling of physical systems.

The modelling procedure consists of selecting the proper TVA module elements that will faithfully and correctly represent the behaviour of the real system. TVA L-cylinder elements represent engine cylinders and the marine propeller element represents the actual propeller. Shaft elements represent thrust shaft, intermediate shaft and propeller shaft. The next step is entering the input data into each element representing quantities relevant to inertia, elastic properties, damping properties and excitation. After that, model elements are to be properly connected the same way as in the real system. It is essential to transfer the actual position of the

crankshaft to the engine cylinder elements, to connect the injection of fuel to them properly, and to correctly correlate damping elements in the engine cylinders to their relevant inertia. Once the reference quantity, period variable and the compensation parameter have been set, and the required diagrams of the system response variables selected, the model is ready for the analysis of the torsional vibration steady-state response.

Several different SimulationX TVA models have been tested to find the one that is the most suitable for modelling of the actual system. The description of this procedure is too extensive and has already been partially presented in [17]. The two models of cylinder excitation gas forces finally remain: cylinder pressure excitation and crank torque excitation. The former uses actual cylinder pressure values over the entire crank angle ranges (-180 to +180 degrees) and the latter implements the forces acting on the crankpin in the tangential direction due to ignition in the cylinders over the same crank angle range. These two models produce slightly different results in SimulationX.

The reciprocating mass in the engine cylinders can be taken into account by means of either the physical model, or the nonreactive approach by crank angle. The latter model was considered in the calculations presented below.

The most convenient solution algorithm of the four available in SimulationX steady state simulation is the „Linear method with interpolation”. It was shown to produce final results quite quickly over the entire speed range of the engine without compromising quality.

## RESULTS

Calculation results consist of the free and forced steady-state torsional vibrations response. Although possible, the analysis in the time domain was not found to be necessary.

The free vibration results can be expressed in the tables of natural frequencies, vibration modes and Campbell diagram. These results give an important insight into at which engine speeds the problems with resonance can be expected.

Far more important are the calculation results for forced vibrations expressed in the form of, for example, torsional stress amplitudes for the particular shafts within the drive system over the shaft speed ranges. These results also include the allowable stresses calculated in accordance with the IACS Unified Requirement M68 [2]. By comparing the actual calculated stresses with the allowable ones, the designer of the system decides whether it will be necessary to introduce barred speed ranges or even to introduce a torsional vibration damper.

## CALCULATION EXAMPLE

To present torsional vibration simulation modelling results, the container/reefer vessel of 12,913 DWT with a propulsion shafting system composed of one two-stroke 7-cylinder



determined.

Fig. 3 shows the amplitudes of the torsional stresses in the elastic massless rotational spring element of the model representing the intermediate shaft.

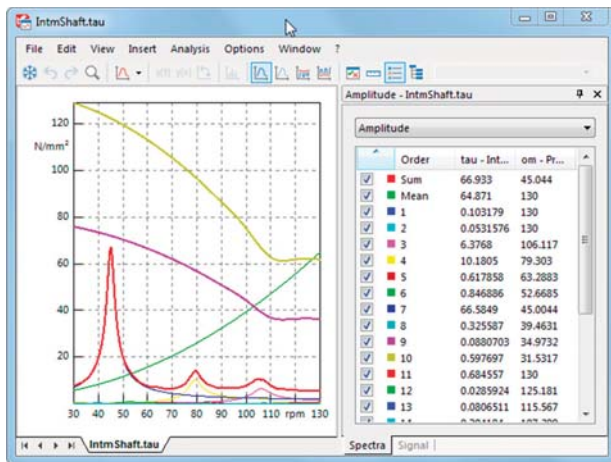


Fig. 3. SimulationX calculated and allowable torsional stress amplitudes in the intermediate shaft

Presented values are obtained by simulation modelling of the steady-state response of the system by SimulationX TVA module, together with the values of the allowable stress amplitudes based upon IACS UR M68 [2] obtained within the same calculation. Fig. 4 shows the same results for the propeller shaft.

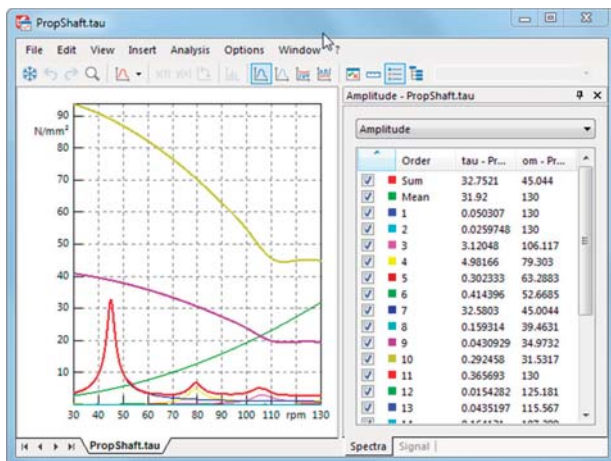


Fig. 4. SimulationX calculated and allowable torsional stress amplitudes in the propeller shaft

## DISCUSSION OF THE RESULTS

The basic idea of this paper is to verify the calculation results obtained by the TVA module of SimulationX by means of the two selected well-known torsional vibration calculation programs based on conventional analytical approach and proven in practice. These programs are GTorsi, developed by MAN Energy Solutions from Copenhagen [19], and TorViC,

developed by CADEA from Split [8]. The former has been in practical use for a long time and implemented in many calculations of two-stroke propulsion systems. The latter is an excellent, reliable and user-friendly commercial program purchased long ago by the Croatian Register of Shipping (CRS), having also been implemented for a very long time within the CRS for the approval of marine propulsion and auxiliary systems torsional vibrations calculations.

Thus, if the simulation modelling by the SimulationX TVA module provides results that successfully pass verification by both GTorsi and TorViC (for this reason CRS gave the allowance to the research team to use the results obtained by TorViC within the CRS plan approvals), as well as the validation against measurement results on board, as normally required by classification rules, then the use of SimulationX TVA module in the plan approval of torsional vibrations calculations will be justified.

## VERIFICATION OF THE FREE VIBRATIONS CALCULATION RESULTS

It has been found that the natural frequencies determined by means of SimulationX differ slightly from case to case, dependent even upon the actually selected model of excitation in the engine cylinders (cylinder pressure vs. crank torque model). This dependency is against the basic physical understanding of natural frequencies themselves, but it is present. On the other hand, when these natural frequencies are calculated by one of the two proven-in-practice programs (GTorsi and TorViC), the natural frequencies correctly remain the same from one calculation case to another and independent of excitation, which is correct. This finding would be a drawback of the implementation of SimulationX, though the differences found have been rather small.

Table 1 shows the comparison of the natural frequencies obtained by SimulationX with the results of GTorsi and TorViC. There are no differences between GTorsi and TorViC themselves, which proves that both of them perform a correct calculation of the natural frequencies. From Table 2, it can also be concluded that the differences of SimulationX natural frequencies compared to the two conventional programs are very modest (max. 0.5%), so this justifies the use of SimulationX to calculate the natural frequencies in the example presented here, regardless of its possible drawback as mentioned before.

## VERIFICATION OF THE FORCED VIBRATIONS CALCULATION RESULTS

The proper selection of the calculation model for the forced torsional vibration response of the actual system in order to compare the results of SimulationX model with the analytical programs is also essential. For this comparison, the maximal torsional stress amplitudes in the thrust shaft, intermediate shaft (see Fig. 3) and propeller shaft (see Fig. 4) were selected as the main representatives with the results presented in Table 2.

Taking the TorViC results as a reference, with respect to

Table 2. Verification of the calculation results

SimulationX evaluation of TVA Normal firing			Comparison of results vs. TorViC Propeller law torque load factor: default = 0.96								
			Natural freq.			Total torsional stress max. amplitude					
case	program	system	excitation	n1 [rpm]	n2 [rpm]	n3 [rpm]	critical speed [rpm]	thrust shaft [MPa]	intm. shaft [MPa]	prop. shaft [MPa]	note
1	TorVic, v1.11	7x cyl.	tang. press. coeff. LARGE_2S	315.4	1501.7	2939.9	44.9	21.0	74.2	36.3	reference
2	GTORSI , v3.6.4	7x cyl.	tang. press. coeff. 240860	315.4	1501.7	2939.9	44.9	20.4	72.0	35.2	best match
3	SimX, v3.8	7x TVAcyl, cyl. press. nonreact.	excit 240860: p(0 18 bar)	313.9	1500.5	2939.3	44.8	18.5	65.3	31.9	
4	SimX, v3.8	7x TVAcyl, crnk. torq. nonreact.	excit 240860: Te(0 18 bar)	314.2	1503.3	2939.3	45.0	18.9	66.9	32.8	
5	SimX, v3.8	7x TVAcyl, cyl. press. nonreact.	excit LARGE_2S: p(0 18 bar)	313.9	1500.5	2939.3	44.7	18.9	66.7	32.6	
6	SimX, v3.8	7x TVAcyl, crnk. torq. nonreact.	excit LARGE_2S: Te(0 18 bar)	314.2	1503.3	2939.4	45.0	19.4	68.5	33.5	2 <sup>nd</sup> match
Relative values [%]											
case	program	system	excitation	n1	n2	n3	critical speed	thrust shaft	intm. shaft	prop. shaft	
1	TorVic, v1.11	7x cyl.	tang. press. coeff. LARGE_2S	0.0%	0.0%	0.0%	0.0%	0.0%	0.0%	0.0%	reference
2	GTORSI , v3.6.4	7x cyl.	tang. press. coeff. 240860	0.0%	0.0%	0.0%	0.0%	-2.9%	-2.9%	-2.9%	best match
3	SimX, v3.8	7x TVAcyl, cyl. press. nonreact.	excit 240860: p(0 18 bar)	-0.5%	-0.1%	0.0%	-0.3%	-11.9%	-12.1%	-12.0%	
4	SimX, v3.8	7x TVAcyl, crnk. torq. nonreact.	excit 240860: Te(0 18 bar)	-0.4%	0.1%	0.0%	0.3%	-9.8%	-9.8%	-9.8%	
5	SimX, v3.8	7x TVAcyl, cyl. press. nonreact.	excit LARGE_2S: p(0 18 bar)	-0.5%	-0.1%	0.0%	-0.4%	-10.0%	-10.1%	-10.1%	
6	SimX, v3.8	7x TVAcyl, crnk. torq. nonreact.	excit LARGE_2S: Te(0 18 bar)	-0.4%	0.1%	0.0%	0.3%	-7.8%	-7.7%	-7.7%	2 <sup>nd</sup> match

the maximal torsional stress amplitudes, the best match is expectedly obtained with GTorsi (max. 2.9% of absolute difference), with the closest (2<sup>nd</sup>) match yielding the SimulationX crank torque excitation model, with exactly the same excitations as in TorViC. The maximum absolute difference of 7.8% may seem rather high, so an additional comparison was made in the form of comparing the graphs of calculation results over the entire engine speed range.

Fig. 5 shows the amplitudes of the torsional stresses in the thrust shaft, intermediate shaft and propeller shaft over the whole speed range (30 to 130 rpm) obtained by SimulationX compared to the analytically calculated results by TorViC. These results show a very good agreement justifying the implementation of the SimulationX TVA module.

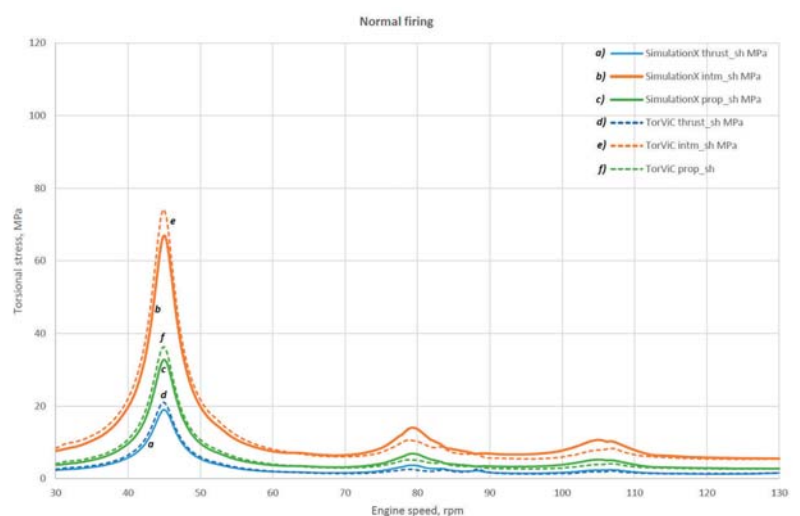


Fig. 5. Verification of the obtained SimulationX calculation results in terms of torsional stress graphs

## VALIDATION OF CALCULATED RESULTS

Verification of any simulation modelling results by comparing them to other calculation results obtained by any means does not mean much unless these calculated results are somehow validated by actual practical measurements on a real propulsion system. This means that the only proper confirmation of a certain calculation approach is its validation by measurements of the stresses on the actual propulsion system on-board the ship itself.

Classification rules always prescribe that the calculations of torsional vibrations of ship propulsion shafting systems must be verified not only during the plan approval phase, but also validated by the measurements on-board the first ship in the series of identical new ships (so-called sister ships).

Validation results from the measurements actually performed on the first ship in the series of the two sister ships in the analysed example have been taken from [20]. These results were obtained by strain gauge measurements on the reachable surface of the intermediate shaft.

The measurement results in terms of torsional stress amplitudes in MPa over the actual engine operating speed range (30 to 110 rpm) are presented by circles in Fig. 6 together with the lines representing the results calculated by SimulationX, TorViC and GTorsi. It is obvious that this comparison of the calculated vs. measured torsional stress amplitudes shows excellent agreement, which further justifies the implementation of SimulationX for the presented calculations.

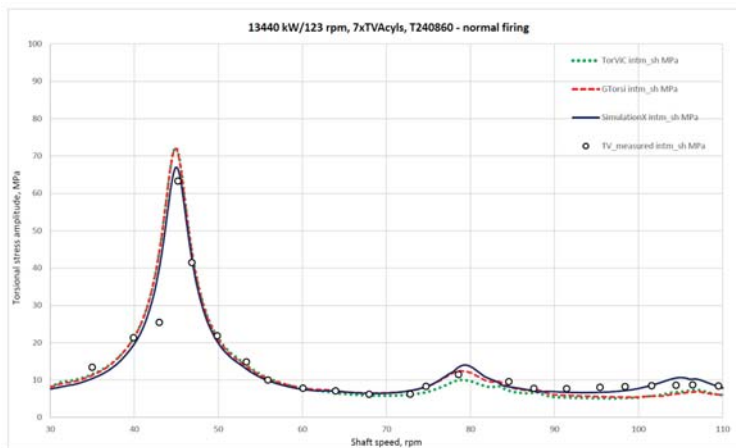


Fig. 6. Validation of SimulationX calculation results vs. engine speed compared with the measurements on-board ship

## CONCLUSIONS

This research was initiated with the aim of judging whether the TVA module of simulation modelling based software SimulationX can be correctly applicable within a classification society plan approval process of the torsional vibrations calculations for marine propulsion shafting

systems and under what conditions. The basic idea of the paper is to present the methodology and results obtained by SimulationX software TVA module to the calculation of torsional vibrations steady-state responses. In addition, the SimulationX results have been verified by means of the calculation results obtained using the two computer programs already proven in practice for this purpose. These have been in use for a long time and validated by the available results of shipboard measurements.

The research is focused on the propulsion systems with the two-stroke slow-speed marine diesel engines with the fixed pitch propellers, which are common in bulk carriers and tankers. The important fact is that the stated problem can be expressed in an analytical form of the system of ordinary linear differential equations and solved analytically in closed form. However, these calculations are extensive, especially with respect to the input data preparation and require dedicated technical specialists in order to implement such programs in a proper way. On the other hand, the TVA module of SimulationX does not require deep skills and extensive training to be used, especially when the software is already available in the company, such as a classification society, for different other purposes. There are some important items to be taken care of, so the implementation of SimulationX had to be properly verified and validated. This was the reason and the background for selecting the proper comparable systems to be analysed by SimulationX, for which the actual validation measurements have also been already performed in the shipyard on board the newly built vessels.

The simulation modelling computer program selected for this task is SimulationX, developed by ESI Group, Dresden. It is based on Modelica, a unified object-oriented language for modelling of different physical systems. Important issues related to the selection of appropriate modelling elements have been described. The discretisation of the real system into „lumped masses” and „massless shafts” was briefly explained. It was practically impossible to obtain correct results by SimulationX in terms of stress amplitudes in the shafts, because the absolute damping element as available in SimulationX does not provide proper outcome. For the correct modelling of damping based upon the dynamic magnification values, a special self-developed element relating the damping dynamic magnification factor to a particular mass had to be developed and implemented in SimulationX calculations, with all the details that have already been presented in [17].

Furthermore, it was also important to present modelling of the excitation forces, originating from the gas and inertia forces in the engine cylinders. Modelling of the loading caused by the propeller also had to be considered.

The selection of the actual model from the various models available in SimulationX was not presented in detail, but only the finally selected model, to avoid too extensive a presentation.

Calculation results were presented using a real example of a two-stroke, 7-cylinder, slow-speed marine diesel engine

propulsion system, in terms of free and forced vibrations basic calculation results. These results were then compared for verification with the results of two world-renowned calculation programs based on an analytical approach that has long been proven in practice.

Free vibrations are expressed by the calculated natural frequencies (eigenvalues), where the SimulationX results show excellent agreement with the analytical results. It should be noted that the eigenvalues obtained by SimulationX are different for various excitations implemented in selected model, contrary to the definition and physical meaning of natural frequencies. However, they follow those of the two analytical programs very well.

Forced vibrations are presented in terms of maximal amplitudes of the steady-state torsional stresses in the thrust shaft, intermediate shaft and propeller shaft of the actual system and also show very good agreement with the values obtained by the two analytical programs.

Finally, the validation of the calculation results by comparing them with the measured results, expressed in the stresses in the intermediate shaft over the achievable engine speed range finally justifies that SimulationX proves to be a suitable tool for modelling of steady-state torsional vibrations.

However, in the case of the misfiring of one of the engine cylinders (which is also a common case to be considered in these calculations), the implementation of SimulationX requires special attention and a somewhat different approach than one might expect. This will be a matter for future work of the research group, together with the extensive analyses of four-stroke engine-based systems with all of the possible causes that will force the use of nonlinear elements within SimulationX models.

## ACKNOWLEDGEMENTS

Part of the research for this article was performed using the equipment and software obtained within the scope of the scientific research project named: "Functional integration of the University of Split, PMF-ST, PFST and KTF-ST through development of scientific and research infrastructure in the building of the three faculties", contract number KK.01.1.1.02.00182.2.

The authors would like to express sincere thanks to the Croatian Register of Shipping (CRS) for the given allowance to use the calculation verification results obtained within the CRS plan approval process of the newbuilding in the presented example by means of the CRS owned program TorViC, developed by CADEA, Split.

The authors also want to thank DIV Brodosplit, Split for providing the results of validation measurements obtained during the sea-trials of the newbuilding in the presented example.

## REFERENCES

1. Croatian Register of Shipping, "Rules for the Classification of Ships, Part 7-Machinery Installation (Amd 1, 2021)," Croatian Register of Shipping, 2021. [Online]. Available: <http://www.crs.hr/en-us/links/rulesfortheclassification.aspx>. [Accessed: April 15th, 2021].
2. International Association of Classification Societies, "UR M68 Dimensions of propulsion shafts and their permissible torsional vibration stresses (Rev. 2, April 2015)," International Association of Classification Societies, 2015. [Online]. Available: <https://www.iacs.org.uk/publications/unified-requirements/ur-m/ur-m68-rev2-cln/>. [Accessed: April 15th, 2021]
3. Y. Batrak, "Torsional vibration calculation issues with propulsion systems," SKF Solution Factory-Marine Services-Shaft Designer, 2010. [Online]. Available: <http://www.shaftdesigner.com/support/papers.html>. [Accessed: April 15th, 2021]
4. W. K. Wilson, "Practical Solution of Torsional Vibration Problems, 3rd edition," London: Chapman & Hall Ltd, 1963.
5. Lloyd's Register of Shipping, "Rules and Regulations for the Classification of Ships, Part 5 - Main and Auxiliary Machinery," London: Lloyd's Register of Shipping, 1968.
6. M. Butković, and Z. Jeličić, "Computer calculation of torsional vibrations for oil engine installations," Technical Information of Jugoturbina, vol. 2-4, pp. 26-35, 1969.
7. K. E. Hafner, and H. Maass, "Torsionschwingungen in der Verbrennungs-kraftmaschine," Wien: Springer-Verlag, 1985.
8. G. Magazinović, "User's manual for TorViC v1.1: A computer system for propulsion system torsional vibration analysis," Split: CADEA, 2000.
9. G. Magazinović, "Propulsion system forced torsional vibration calculation," Shipyard Brodosplit, Split, Tech. Rep. 85N11706, 1988.
10. G. Magazinović, "Shaftline design considerations of five-cylinder low-speed propulsion plants," in Proceedings I. of 13th Symposium on Theory and Practice of Shipbuilding Sorta'98, In memoriam prof. Leopold Sorta, 1998. pp. 141-151.
11. I. Senjanović, I. Ančić, G. Magazinović, N. Alujević, N. Vladimir, and D. S. Cho, "Validation of analytical methods for the estimation of the torsional vibrations of ship power transmission systems," Ocean Engineering, vol. 184, pp. 107-120, 2019.

12. L. Murawski and A. Charchalis, "Simplified method of torsional vibration calculation of marine power transmission system," *Marine Structures*, vol. 39, pp. 335-349, 2014.
13. Verein Deutscher Ingenieure, "VDI 2039 Torsional vibration of drivelines - Calculation, measurement, reduction," Düsseldorf: Verein Deutscher Ingenieure e.V, 2016.
14. ITI-Software GmbH, "SimulationX Library Manual-Torsional Vibration Analysis," Dresden: ITI-Software GmbH, 2015.
15. J. Huet, "Torsional vibration analysis of marine installations," *Ship & Offshore*, no. 5, pp. 18-20, 2011.
16. N. Vulić, Đ. Dobrota and I. Komar, "Damping and excitation in the torsional vibrations calculation of ship propulsion systems," in *Proceedings of the Contemporary Issues in Economy & Technology Conference, CIET 2016*, Split, Croatia, 16th-18th June 2016. pp. 165-174.
17. N. Vulić, I. Komar and P. Jurišić, "Selection and evaluation of marine shafting torsional vibrations calculation software," in *Book of Proceedings of the 7th International Maritime Science Conference (IMSC 2017)*, Split, Croatia, 20th-21st April, 2017. pp. 221-229.
18. E. Sandberg, "Classification rules for torsional vibrations," Høvik: Det norske Veritas AS, 2005.
19. MAN Energy Solutions, "Torsional Vibration Calculation Program GTORSI, Version 3.6.4 External," Copenhagen: MAN Energy Solutions, 2018.
20. M. Kramar, I. Beatović and N. Bobanac, "Shafting Torsional Vibration Test," Shipbuilding Institute, Zagreb, Croatia, Tech. Rep. A100-LF01-02-071, 1999.

## CONTACT WITH THE AUTHORS

**Nenad Vulić**

*e-mail: nenad.vulic@pfst.hr*

**Karlo Bratić**

*e-mail: kbratic@pfst.hr*

**Branko Lalić**

*e-mail: blalic@pfst.hr*

**Ladislav Stazić**

*e-mail: lstazic@pfst.hr*

Faculty of Maritime Studies  
Boškovićeve 37  
HR21000 Split  
**CROATIA**

# ENERGY ANALYSIS OF THE PROPULSION SHAFT FATIGUE PROCESS IN A ROTATING MECHANICAL SYSTEM PART III DIMENSIONAL ANALYSIS

Zbigniew Korczewski\*

Konrad Marszałkowski

Gdańsk University of Technology, Poland

\* Corresponding author: [zbigniew.korczewski@pg.edu.pl](mailto:zbigniew.korczewski@pg.edu.pl) (Z.Korczewski)

## ABSTRACT

*This article presents the third and last part of the problem of diagnosing the fatigue of marine propulsion shafts in terms of energy with the use of the action function, undertaken by the authors. Even the most perfect physical models of real objects, observed under laboratory conditions and developed based on the results of their research, cannot be useful in diagnostics without properly transferring the obtained results to the scale of the real object. This paper presents the method of using dimensional analyses and the Buckingham theorem (the so-called  $\pi$  theorem) to determine the dimensionless numbers of the dynamic similarity of the physical model of the propulsion shaft and its real ship counterpart, which enable the transfer of the results of the research on the energy processes accompanying the ship propulsion shaft fatigue from the physical model to the real object.*

**Keywords:** ship propulsion shaft, dimensional analysis, Buckingham theorems, similarity criteria.

## INTRODUCTION

Within the previous parts of the article, the results of model and experimental studies of the fatigue process of the propulsion shaft were presented [6,7]. The active experiments were carried out on the especially designed and built physical model of the rotary propulsion system which was mapping an operation of full-size real object. There has been proved that changes in the deflection of the rotary propulsion line are reflected in the amount of dissipated kinetic energy of masses in rotational motion and the accumulated internal energy of construction materials. After exceeding the critical values of these energies, a fatigue damage occurs, the course of which is characterized by energy residual processes: vibroacoustic and thermal. They cause, inter alia, observable diagnostic symptoms of changes in the fatigue state of the structural material from which the propulsion shaft is made. There has been proposed to adopt the high-cycle fatigue syndrome consisting of diagnostic symptoms determined from the function of the propulsion shaft action related to the transformation of mechanical energy

into the way of work and heat, and the generation of mechanical vibrations and elastic waves of acoustic emission. In order to assess the diagnostic information contributed by the defined characteristics of the fatigue condition of the propulsion shaft, a program of experimental tests was developed and performed, in which two statistical hypotheses were verified: the significance of the influence of the quantities forcing the fatigue process [6] and the adequacy of the regression equation describing the fatigue life of the propulsion shaft in term of energy [7].

Experimental studies carried out on physical models that reflect the work of a real full-size object have one fundamental weakness; namely they may not consider certain phenomena and processes that have been unconsciously eliminated due to their transition to a small scale [1]. To be able to fully transfer the measurement results characterising the work of the physical model to real objects, it is not enough to simply multiply them by the dimensional scale of the model. Therefore, appropriate criteria (dimensionless numbers) for their geometric, kinematic, and dynamic similarities should be developed. An effective tool in the way of analytical solution

of this problem for the considered process of fatigue of marine propulsion shafts can be its dimensional analysis, which has been widely included in publications providing theoretical guidance [2,3] and successfully used, for example, in modelling the dynamics of vehicle movement [4,5]. It allows the form of the function describing the examined process to be determined in a situation where only its arguments are known. It is then assumed that there must be full compliance of the dimension of this function (physical quantity) with the dimension of the power product created from the considered arguments, significantly affecting the course of the fatigue process which has already been partially described by the authors [6-8]. Nevertheless, there is still a noticeable lack of bibliographic items describing the problems of fatigue durability of marine propulsion systems based on the results of experimental tests carried out on a small scale.

## DIMENSIONAL ANALYSIS OF THE FATIGUE DURABILITY OF THE PROPULSION SHAFT

For a rotating propulsion shaft subjected to set bending-torsional loads, one can write the relationship describing its fatigue durability  $\tau_w$  as a function of the recorded physical parameters<sup>1</sup>, each of which has its own dimension, according to the International System of Units:

$$\tau_w = f(m, I, M, F, y, \omega) \quad (5.1)$$

Both the dimension of the function being searched for and the dimensions of its arguments (parameters) can be represented by the power products of three basic dimensions: length [L], mass [M], and time [T]<sup>2</sup>:

- $\tau_w$  – fatigue durability (operating time to the development of a detectable crack on the shaft's surface),  $s \rightarrow [L^0 \cdot M^0 \cdot T^1]$ ,
- $m$  – propulsion shaft mass (without the mass of the propeller),  $kg \rightarrow [L^0 \cdot M^1 \cdot T^0]$ ,
- $I$  – moment of inertia (polar around the shaft axis),  $kg \cdot m^2 \rightarrow [L^2 \cdot M^1 \cdot T^0]$ ,
- $M$  – transmitted torque (by the propulsion shaft),  $kg \cdot m^2 / s^2 \rightarrow [L^2 \cdot M^1 \cdot T^{-2}]$ ,
- $F$  – the bending force acting on the propulsion shaft (resulting from reactions in bearing nodes),  $kg \cdot m / s^2 \rightarrow [L^1 \cdot M^1 \cdot T^{-2}]$ ,
- $y$  – shaft deflection (assumed for the middle of the shaft length, as in Fig. 1),  $m \rightarrow [L^1 \cdot M^0 \cdot T^0]$ ,
- $\omega$  – angular speed of the propulsion shaft,  $1/s \rightarrow [L^0 \cdot M^0 \cdot T^{-1}]$ .

The relationship (5.1) connects  $m = 7$  physical dimensional quantities characterising the tested fatigue process of the propulsion shaft in the dynamic aspect, the dimensions of which

include  $n = 3$  basic dimensions. Thus, according to the method developed by Edgar Buckingham [9, 10] in 1914 (the so-called  $\pi$  theorem)<sup>3</sup>, the fatigue life of the shaft can be described by  $k = m - n$ , i.e., four dimensionless similarity numbers  $\pi_k$ , starting from the dimensional formula in the form of the product of the powers of the important basic physical quantities in the studied process [11]:

$$\tau_w = C \cdot m^A \cdot I^B \cdot M^D \cdot F^E \cdot y^F \cdot \omega^G \quad (5.2)$$

where:  $A \dots G$  – constant.

According to the Fourier dimensional consistency principle, to maintain the size equation, the dimensions of the physical quantities on the left and right side of the equation (5.2) must be the same. After replacing all the physical quantities with their basic dimensions in it, we get:

$$T = C \cdot M^A \cdot L^{2B} \cdot M^B \cdot L^{2D} \cdot M^D \cdot T^{-2D} \cdot L^E \cdot M^E \cdot T^{-2E} \cdot L^F \cdot T^{-G} \quad (5.3)$$

and after transformation:

$$T = C \cdot M^{A+B+D+E} \cdot L^{2B+2D+E+F} \cdot T^{-2D-2E-G} \quad (5.4)$$

To obtain the dimensionless form of the equation for the fatigue life of the propulsion shaft, the sum of the exponents of each physical quantity must be zero:

$$\begin{aligned} \text{for } T &\rightarrow 1 + 2D + 2E + G = 0 \\ \text{for } M &\rightarrow A + B + D + E = 0 \\ \text{for } L &\rightarrow 2B + 2D + E + F = 0 \end{aligned}$$

Since there are six unknowns (exponents) and only three independent equations, it is impossible to solve the given problem without eliminating some of the arguments<sup>4</sup> or assuming at least three values of the sought exponents<sup>5</sup> as the parametric solution to the system of linear equations. On the other hand, three basic units were used for the dimensional analysis. This means that three out of the six analysed arguments of the searched persistence function may be dimensionally independent<sup>6</sup>. The mass  $m$ , the shaft deflection  $y$ , and the angular velocity  $\omega$  were selected for further analysis, for which the dimensional independence was checked. For this purpose, the value of the determinant of the matrix composed of exponents was calculated with the dimensions of these arguments. Since the value of the determinant is different from zero, it can be assumed that these arguments are dimensionally independent:

3 Buckingham's Theorem, also known as the  $\pi$  Theorem, is a key law used in dimensional analyses. It states that "if one has an equation described by a certain number of independent physical parameters, then this equation can be expressed by dimensionless modules  $\pi$ , the number of which is equal to the number of these physical parameters minus the number of fundamental dimensions".

4 This is not a rational procedure as it reduces the level of detail in the dimensional analysis.

5 For example, the exponent  $F = -1$ , which means that the fatigue durability of the shaft is inversely proportional to its deflection

6 None of their units can be expressed in combination with the others.

1 Assuming that the fatigue durability depends only on the specified physical parameters, and the function describing this durability is dimensionally invariant and homogeneous.

2 This is the standard assumption of dimensional analyses in mechanics.

$$\begin{vmatrix} 0 & 1 & 0 \\ 1 & 0 & 0 \\ 0 & 0 & -1 \end{vmatrix} = 1 \neq 0 \quad (5.5)$$

In the next step of the calculations, successive dimensionless variables  $\pi_1 \dots \pi_4$  are determined using the remaining arguments and the selected arguments that are independent of the dimensions:

**1. Dimensionless variable  $\pi_1$  due to fatigue durability  $\tau_w$ :**

$$\pi_1 = \tau_w \cdot m^A \cdot y^B \cdot \omega^C \quad (5.6)$$

Inputting basic units on both sides of equation (5.6) we get:

$$\frac{L^0 \cdot M^0 \cdot T^0}{(L^1 \cdot M^0 \cdot T^0)^B \cdot (L^0 \cdot M^0 \cdot T^{-1})^C} = \frac{L^0 \cdot M^0 \cdot T^0}{(L^0 \cdot M^1 \cdot T^0)^A} \quad (5.7)$$

By comparing exponents with appropriate dimensions:

$$\begin{aligned} \text{for } T \rightarrow 0 &= 1 - C \Rightarrow C = 1 \\ \text{for } M \rightarrow 0 &= A \Rightarrow A = 0 \\ \text{for } L \rightarrow 0 &= B \Rightarrow B = 0 \end{aligned}$$

the following is obtained:

$$\pi_1 = \tau_w \cdot m^0 \cdot y^0 \cdot \omega^1 \quad (5.8)$$

and finally:

$$\pi_1 = \tau_w \cdot \omega \quad (5.9)$$

**2. Dimensionless variable  $\pi_2$  due to the moment of inertia  $I$ :**

$$\pi_2 = I \cdot m^A \cdot y^B \cdot \omega^C \quad (5.10)$$

By inserting the base units on both sides of equation (5.10) we get:

$$\frac{L^0 \cdot M^0 \cdot T^0}{(L^1 \cdot M^0 \cdot T^0)^B \cdot (L^0 \cdot M^0 \cdot T^{-1})^C} = \frac{L^0 \cdot M^1 \cdot T^0}{(L^0 \cdot M^1 \cdot T^0)^A} \quad (5.11)$$

By comparing the exponents with appropriate dimensions:

$$\begin{aligned} \text{for } T \rightarrow 0 &= -C \Rightarrow C = 0 \\ \text{for } M \rightarrow 0 &= 1 + A \Rightarrow A = -1 \\ \text{for } L \rightarrow 0 &= 2 + B \Rightarrow B = -2 \end{aligned}$$

the following is obtained:

$$\pi_2 = I \cdot m^{-1} \cdot y^{-2} \quad (5.12)$$

and finally:

$$\pi_2 = \frac{I}{m \cdot y^2} \quad (5.13)$$

**3. Dimensionless variable  $\pi_3$  due to the transmitted torque  $M$ :**

$$\pi_3 = M \cdot m^A \cdot y^B \cdot \omega^C \quad (5.14)$$

By inserting the base units on both sides of equation (5.14) we get:

$$\frac{L^0 \cdot M^0 \cdot T^0}{(L^1 \cdot M^0 \cdot T^0)^B \cdot (L^0 \cdot M^0 \cdot T^{-1})^C} = \frac{L^2 \cdot M^1 \cdot T^{-2}}{(L^0 \cdot M^1 \cdot T^0)^A} \quad (5.15)$$

By comparing the exponents with appropriate dimensions:

$$\begin{aligned} \text{for } T \rightarrow 0 &= -2 - C \Rightarrow C = -2 \\ \text{for } M \rightarrow 0 &= 1 + A \Rightarrow A = -1 \\ \text{for } L \rightarrow 0 &= 2 + B \Rightarrow B = -2 \end{aligned}$$

the following is obtained:

$$\pi_3 = M \cdot m^{-1} \cdot y^{-2} \cdot \omega^{-2} \quad (5.16)$$

and finally:

$$\pi_3 = \frac{M}{m \cdot y^2 \cdot \omega^2} \quad (5.17)$$

**4. Dimensionless variable  $\pi_4$  due to the bending force  $F$ :**

$$\pi_4 = F \cdot m^A \cdot y^B \cdot \omega^C \quad (5.18)$$

Putting the base units on both sides of equation (5.18) we get:

$$\frac{L^0 \cdot M^0 \cdot T^0}{(L^1 \cdot M^0 \cdot T^0)^B \cdot (L^0 \cdot M^0 \cdot T^{-1})^C} = \frac{L^1 \cdot M^1 \cdot T^{-2}}{(L^0 \cdot M^1 \cdot T^0)^A} \quad (5.19)$$

By comparing the exponent of powers with appropriate dimensions:

$$\begin{aligned} \text{for } T \rightarrow 0 &= -2 - C \Rightarrow C = -2 \\ \text{for } M \rightarrow 0 &= 1 + A \Rightarrow A = -1 \\ \text{for } L \rightarrow 0 &= 1 + B \Rightarrow B = -1 \end{aligned}$$

the following is obtained:

$$\pi_4 = F \cdot m^{-1} \cdot y^{-1} \cdot \omega^{-2} \quad (5.20)$$

and finally:

$$\pi_4 = \frac{F}{m \cdot y \cdot \omega^2} \quad (5.21)$$

Thus, a functional relationship that binds all dimensionless variables can be determined as:

$$\pi_1 = f(\pi_2, \pi_3, \pi_4) \quad (5.22)$$

which, when expanded, takes the following dimensionless form:

$$\tau_w \cdot \omega = f\left(\frac{I}{m \cdot y^2}, \frac{M}{m \cdot y^2 \cdot \omega^2}, \frac{F}{m \cdot y \cdot \omega^2}\right) \quad (5.23)$$

and dimensional form:

$$\tau_w = f\left(\frac{I}{m \cdot y^2}, \frac{M}{m \cdot y^2 \cdot \omega^2}, \frac{F}{m \cdot y \cdot \omega^2}\right) \cdot \frac{1}{\omega} \quad (5.24)$$

In the next step, by introducing the replacement dimensionless variable  $\pi_{2-3}$ , which is determined from the ratio of the variables  $\pi_3$  and  $\pi_2$  i.e.  $\pi_3/\pi_2$ , one obtains:

$$\tau_w = f\left(\frac{M}{I \cdot \omega^2}, \frac{F}{m \cdot y \cdot \omega^2}\right) \cdot \frac{1}{\omega} \quad (5.25)$$

Analysing the expression (5.25) for the fatigue durability of the propulsion shaft, it can be seen that the dimensionless modulus  $\pi_{2-3}$  has the form of a Newton number for its rotational

motion  $Ne_{(ROT)}$ , while the dimensionless modulus  $\pi_4$  has the form of a Newton number for the transverse movement of the shaft  $Ne_{(TRANS)}$ <sup>7</sup>. The physical sense of the first one is determined by the ratio of the transmitted torque to the accumulated kinetic energy, and the second by the ratio of the forces acting on the shaft: bending to centrifugal forces. In such a situation, formula (5.25) takes the final form:

$$\tau_w = f(Ne_{(ROT)}, Ne_{(TRANS)}) \cdot \frac{1}{\omega} \quad (5.26)$$

## CRITERIA OF SIMILARITY

Considering the problem of the geometric, kinematic, and dynamic similarities of the fatigue process of the physical model ( $M$ ) of the propulsion shaft and its real ship counterpart ( $R$ ), which is made of the same material and which is subjected to analogous forces and moments, appropriate similarity scales can be defined, according to which the results obtained from the research of the physical model can be transferred to the real object:

- length scale (diameter)  $S_{L/D}$ :

$$\frac{L_R}{L_M} = \frac{D_R}{D_M} \rightarrow L_R = L_M \cdot \frac{D_R}{D_M} \rightarrow L_R = 8 \cdot D_R \quad (5.27)$$

where:

- $L_R$  – length of the real object propulsion shaft,
- $L_M$  – length of the propulsion shaft of the physical model (64 mm),

- $D_R$  – real object propulsion shaft diameter,
- $D_M$  – diameter of the propulsion shaft of the physical model (8 mm).

- scale of masses (moments of inertia)  $S_{m/I}$ :

$$\frac{m_R}{m_M} = \frac{I_R}{I_M} \rightarrow m_R = m_M \cdot \frac{I_R}{I_M} \rightarrow m_R = 0.115 \text{mm}^{-2} \cdot I_R \quad (5.28)$$

where:

- $m_R$  – propulsion shaft mass of the real object,
- $m_M$  – mass of the propulsion shaft of the physical model (0.028 kg),
- $I_R$  – moment of inertia of the real object's propulsion shaft,
- $I_M$  – moment of inertia of the propulsion shaft of the physical model (0.244 kg·mm<sup>2</sup>).

- speed scale  $S_{\omega/u}$ :

$$\frac{\omega_R}{\omega_M} = \frac{u_R}{u_M} \rightarrow \omega_R = \omega_M \cdot \frac{u_R}{u_M} \rightarrow \omega_R = 250 \text{m}^{-1} \cdot u_R \quad (5.29)$$

where:

- $\omega_R$  – angular speed of the real object's propulsion shaft,
- $\omega_M$  – angular velocity of the propulsion shaft of the physical model (157 s<sup>-1</sup>),
- $u_R$  – peripheral speed of the propulsion shaft of the real object,
- $u_M$  – peripheral speed of the propulsion shaft of the physical model (0.628 m/s).

<sup>7</sup> Newton's Power Number, which, for mechanical systems is the ratio of the force (moment) of the resistance to motion to the force (moment) of inertia, can be determined from Newton's Second Law of Dynamics for the translational (rotational) motion of a rigid body.

The comparison of the proposed scales of similarity is presented in Figure 1, with the example of a direct propulsion system, typical for cargo sea vessels.

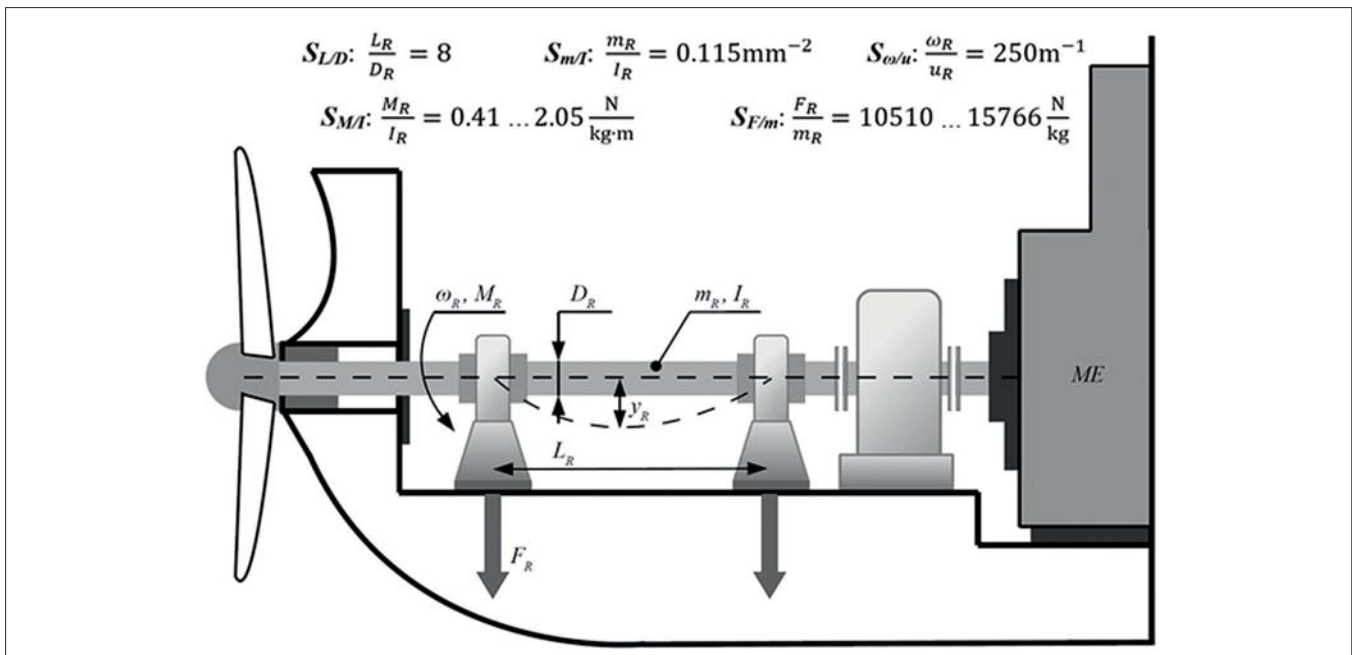


Fig. 1. Graphical interpretation of the applied scales of similarity of the physical model of the rotary propulsion shaft to the full-size ship shaft:  $D_R$  – propulsion shaft diameter,  $F_R$  – bending force acting on the propulsion shaft,  $I_R$  – moment of inertia of the propulsion shaft,  $L_R$  – propulsion shaft length,  $m_R$  – propulsion shaft mass, ME – main propulsion internal combustion engine,  $M_R$  – torque transmitted by the propulsion shaft,  $\omega_R$  – angular speed of the propulsion shaft,  $y_R$  – deflection of the propulsion shaft

On the other hand, the basic invariant of the dynamic similarities of the physical model of the propulsion shaft and its real ship counterpart will be the Newton number considered in the scope of shaft rotation:

- Newton's number for a real object in rotation:

$$Ne_{R(ROT)} = \frac{M_R}{I_R \cdot \omega_R^2} \quad (5.30)$$

where:

- $M_R$  – torque transmitted by the propulsion shaft of the real object,
- $I_R$  – moment of inertia of the real object's propulsion shaft,
- $\omega_R$  – angular speed of the real object's propulsion shaft.

- Newton's number for a physical model in rotational motion:

$$Ne_{M(ROT)} = \frac{M_M}{I_M \cdot \omega_M^2} \quad (5.31)$$

where:

- $M_M$  – torque transmitted by the propulsion shaft of the physical model,
- $I_M$  – moment of inertia of the propulsion shaft of the physical model,
- $\omega_M$  – angular velocity of the propulsion shaft of the physical model.

The following condition follows from the identity of these numbers:  $Ne_{R(ROT)} = Ne_{M(ROT)}$ . Assuming that the values of the angular velocity ( $\omega_R, \omega_M$ ) for the real object and its physical model, and the range of variability of the torque transmitted by the propulsion shaft of the physical model are invariant  $M_M = 0.1 \dots 0.5$  N·m, the scale of the  $S_{MI}$  torques reflects the following relationship:

$$M_R = I_R \cdot \frac{M_M}{I_M} \rightarrow M_R = 0.41 \dots 2.05 \frac{\text{N}}{\text{kg} \cdot \text{m}} \cdot I_R \quad (5.32)$$

Another analysed invariant of dynamic similarities of the physical model of the prop shaft and its real counterpart is the Newton number considered for the transverse movement of the shaft:

- Newton's number for a real object in lateral motion:

$$Ne_{R(TRANS)} = \frac{F_R}{m_R \cdot y_R \cdot \omega_R^2} \quad (5.33)$$

where:

- $F_R$  – bending force acting on the propulsion shaft of the real object,
- $m_R$  – mass of the real object's propulsion shaft,
- $y_R$  – deflection of the real object's propulsion shaft.

- Newton's number for a physical model in lateral motion:

$$Ne_{M(TRANS)} = \frac{F_M}{m_M \cdot y_M \cdot \omega_M^2} \quad (5.34)$$

where:

- $F_M$  – bending force acting on the propulsion shaft of the physical model,
- $m_M$  – mass of the propulsion shaft of the physical model,
- $y_M$  – deflection of the propulsion shaft of the physical model.

The identification of these numbers requires the following condition:  $Ne_{R(TRANS)} = Ne_{M(TRANS)}$ . By making analogous transformations and assuming that the deflection ( $y_M, y_R$ ) and the angular velocity ( $\omega_R, \omega_M$ ) of the real object shaft and its physical model are invariant, as well as assuming that the range of variability of the bending force acting on the propulsion shaft of the physical model  $F_M = 294.3 \dots 441.45$  N, the relationship representing the scale of bending forces  $S_{F/m}$  is obtained in the following form:

$$F_R = m_R \cdot \frac{F_M}{m_M} \rightarrow F_R = 10510 \dots 15766 \frac{\text{N}}{\text{kg}} \cdot m_R \quad (5.35)$$

## FINAL REMARKS AND CONCLUSIONS

The method of mathematical description of the fatigue life of the rotary propulsion shaft presented in this article by means of designated Newton dynamic similarity numbers enables the transfer of the diagnostic test results of its physical model to full-size ship shafts, while considering appropriate geometric and kinematic similarity criteria. However, it should be noted that the dimensional method used for identification purposes has significant limitations, as it does not penetrate into the essence of mechanical fatigue as a physical phenomenon, but only determines arbitrarily (often intuitively) the physical quantities that affect its course [12]. Hence, the dimensional analysis of the physical quantities of marginal or key significance can be accidentally included or excluded, respectively. Only their dimensions are considered, which makes it impossible to collect numerical data on the determined invariants of physical similarities. The results obtained in this way should always be confirmed experimentally or theoretically (from the analysis of mathematical equations resulting from the laws of physics).

## REFERENCES

1. Z. Korczewski, "The conception of energetic investigations of the multisymptom fatigue of the simple mechanical systems constructional materials", *Journal of Polish CIMAC*, 1/2012, p. 99–108, 2012.
2. G.A. Vignaux, "Dimensional Analysis in Data Modelling", in: Smith C.R., Erickson G.J., Neudorfer P.O. (eds) *Maximum Entropy and Bayesian Methods. Fundamental Theories of Physics (An International Book Series on The Fundamental Theories of Physics: Their Clarification, Development and Application)*, vol 50. Springer, Dordrecht, 1992.

3. E.S. Taylor, *Dimensional Analysis for Engineers*. Oxford University Press, 1974.
4. K. Parczewski and H. Wnęk, "The use of the theory of similarity to analyze the vehicle motion stability based on the research of the mobile model" (in Polish). *Logistyka*, 3/2012.
5. K. Romaniszyn, "A mobile model for car dynamics research" (in Polish). *The Archives of Automotive Engineering*, 1(59)/2013.
6. Z. Korczewski and K. Marszałkowski, "Energy analysis of propulsion shaft fatigue process in rotating mechanical system. Part I. Testing significance of influence of shaft material fatigue excitation parameters", *Polish Maritime Research*, Vol.25, Special issue S1(97), pp. 211–217, DOI: 10.2478/pomr-2018-0044, 2018.
7. Z. Korczewski and K. Marszałkowski "Energy analysis of propulsion shaft fatigue process in rotating mechanical system. Part II. Identification studies – developing the fatigue durability model of a propulsion shaft", *Polish Maritime Research*, Vol. 27, 2(106), pp. 120–124, DOI: 10.2478/pomr-2020-0033, 2020.
8. K. Marszałkowski, "Energy processes modelling in a rotating mechanical system for the purpose of diagnosing the fatigue of ship propulsion shafts" (in Polish), Ph.D. dissertation, Gdansk University of Technology, 2019.
9. E. Buckingham, "On Physically Similar Systems: illustrations of the use of dimensional equations", *Physical Review*, 4, pp. 345–376, 1914.
10. E. Buckingham, "Physically similar systems", *Academy of Sciences*, 93, pp. 347–353, 1914.
11. S. Drobot, *About dimensional analysis* (in Polish). 1954.
12. L. Müller, *Application of dimensional analysis in model studies* (in Polish). 1983.

## CONTACT WITH THE AUTHORS

**Zbigniew Korczewski**

*e-mail: z.korczewski@gmail.com*

Gdańsk University of Technology  
Narutowicza 11/12  
80-233 Gdańsk  
**POLAND**

**Konrad Marszałkowski**

*e-mail: konmarsz@pg.edu.pl*

Gdańsk University of Technology  
Narutowicza 11/12  
80-233 Gdańsk  
**POLAND**

# OPTIMISATION OF THE TOPPING-UP PROCESS OF LUBRICATING OIL IN MEDIUM-SPEED MARINE ENGINES

Andrzej Młynarczyk  
Krzysztof Rudzki\*  
Gdynia Maritime University, Poland

\* Corresponding author: [k.rudzki@wm.umg.edu.pl](mailto:k.rudzki@wm.umg.edu.pl) (K. Rudzki)

## ABSTRACT

*In this paper, we examine the problem of optimising the process of topping up lubricating oil in medium-speed marine engines. This process is one of the methods that can be applied to improve the properties of lubricating oil. The amount of fresh oil added to lubricating oil system always balances its consumption, but the method used to top up depends on the marine engineer. Small amounts of fresh oil can be added at short intervals, or large ones at long intervals, and the element of randomness often plays a significant role here. It would therefore be valuable to find a method that can help the mechanical engineer to choose the right strategy. We apply a multi-criteria optimisation method for this purpose, and assume that the criterion functions depend on the concentration of solid impurities and the alkalinity, which are among the most important aspects of the quality and properties of lubricating oil. These criterion functions form the basis for multi-objective optimisation carried out with the use of the MATLAB computer program.*

**Keywords:** multi-objective optimisation, medium-speed marine engine, lubricating oil, solid impurities, alkalinity, topping-up process

## INTRODUCTION

The performance and reliability of a marine engine and its components are of primary importance to the user, i.e. the marine engineer, and lubricating oil should therefore be considered an integral part of the engine and its systems.

As time passes, the oil in the lubricating system of a medium-speed marine engine loses its properties. Maintaining these properties within acceptable limits or tolerances requires a knowledge of the additive package reserve of the oil, the degree of contamination from the products of engine combustion, wear engine elements or other extraneous sources, excessive consumption of lubricating oil due to leakage or poor engine maintenance, and the frequency and amounts in which fresh oil is added to the system [1].

An extended life or increased running hours can be obtained for the lubricating oil by optimising all of these influences to ensure that the properties of the oil are maintained within the acceptable limits set by the engine manufacturer.

The topping-up process is one of the methods that can be used to improve the properties of lubricating oil and to keep these within acceptable limits, as they define the conditions for safe engine operation. However, the optimal use of lubricating oil should not only ensure that the changes in the properties of the oil are limited to these safe levels, but also that its properties are as close as possible to those of fresh oil, to allow it to fulfil its functions more effectively and over a longer period. This can reduce the wear on the engine elements and the consumption of lubricating oil (as a result of decreasing the wear on the piston rings and cylinder liners) and can ultimately reduce the costs of engine operation.

The amount of fresh oil added to the lubricating oil system always balances its consumption, but the method used to top up depends on the marine engineer. Small amounts of fresh oil can be added at short intervals, or large ones at longer intervals (Fig. 1). It is also possible to maintain a constant amount of oil in the lubrication system by continuous topping up.

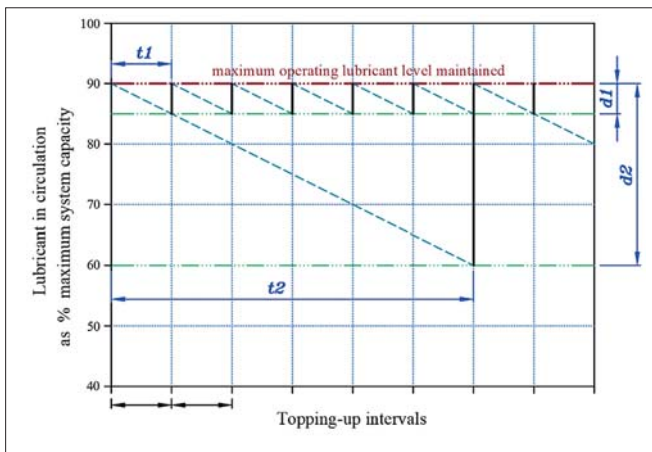


Fig. 1. Two different topping-up methods [2]

The aim of this article is to determine the influence of topping up methods on the base number and mass concentration of solid impurities. A literature review and the authors' personal experience show that the alkalinity level of the lubricating oil considerably influences the corrosive damage to cylinder liners, which is mainly caused by acid reacting with the cast iron surfaces, removing the protective oxide layer and leaving a reactive surface. The softer components of the cast iron liner are preferentially removed, and the acid also attacks the phase boundaries. The harder material then protrudes, and may fall away or be mechanically removed by the piston rings. These hard particles fall between the piston rings and cylinder liners, and accelerate the wear of these elements [3], [4], [5], [6], [7], [8].

According to new rules introduced by the International Maritime Organisation (IMO) for sulphur oxides in shipping emissions (the so-called "sulphur directive") beginning 1st January 2020, the allowable sulphur content in marine fuel in the other seas of the world has been reduced from 3.5% to 0.5% by weight [9]. To meet these new regulations, ships have been forced to switch to cleaner low-sulphur fuel, to install an exhaust gas cleaner (or "scrubber"), or to be rebuilt to allow them to be powered by alternative fuels such as gas or methanol [10]. In each case, the cost of shipping has increased. Using a purification method such as a scrubber drastically reduces sulphur emissions [9], [11], [12], [13], and a further advantage of this approach compared to other methods of fulfilling the "sulphur directive" is that the ship can continue to be driven by cheaper high-sulphur fuel while still meeting the stricter regulations. To the authors' knowledge, several shipping companies have decided to use scrubbers, meaning that the problem of corrosive damage to cylinder liners still exists.

In addition, the concentration, size and hardness of the solid impurities can considerably influence the abrasive wear of engine matching elements [2], [6], [7], [14]. The combustion of lubricating oil containing solid impurities also contributes to the total particulate emissions. These particulate emissions and other ash constituents from the fuel may affect the use of exhaust gas treatment equipment (e.g. scrubbers), their operation and efficiency [1]. According to Corbett et al. [15], the emission of particles from shipping causes about 60,000 deaths globally each year. The coastal regions along major

trade routes are the most strongly affected, and mortality is the highest in Europe and Asia, where large populations and high levels of particulate emissions coexist.

For these reasons, we believe that scientific research that focuses on exploring the influence of topping-up practices on changes in the base number and mass concentrations of solid impurities in lubricating oil is important from both a theoretical and a practical point of view.

## PROPOSED METHOD OF SOLVING THE PROBLEM

In this case, we are faced with a typical multi-objective optimisation problem (MOOP). In shipbuilding, multi-objective optimisation methods are widely used, for example to improve:

- voyage routes [16] [17], [18],
- the shape of a ship's hull [19],
- the arrangement of machines and devices inside a ship [20], and
- fuel consumption during a voyage [21], [22].

Solving this type of task involves identifying decision variables, defining criterion functions and limitations, adopting an objective function and finally finding the optimal values of the decision variables [23].

## CHOOSING THE OPTIMISATION CRITERIA

To solve the problem of optimising the lubricating oil topping-up process, we need to determine the properties of the oil that have the greatest impact on the scope and the importance of the tasks fulfilled by the oil in the engine. We also need to construct the objective function, which represents the dependence of the criterion quantity on the quantity used as a control. In this case, the criterion is the quality of the lubricating oil, which is characterised by a selected set of properties, and the control is the parameter that defines the method of topping up.

The objective function defined in this way can be expressed in general form as:

$$J = fc(X, Y) \quad (1)$$

where:

- $J$  – is the objective function that characterises the condition of the lubricating oil (oil quality) in the operation process,
- $X$  – is the set of controls, and
- $Y$  – is the set of independent parameters (i.e. parameters determining the operating conditions of the marine engine).

For the general objective function in Eq. (1), the desired outcome of the topping-up method is to obtain the best possible oil quality (under the given operating conditions), and this is characterised by the utility properties, which are chosen

here as the base number and the mass concentration of solid impurities.

A topping-up method characterised by parameter  $d$  was assumed as the control. This parameter determines the amount of oil added to the system as a proportion of the initial amount of oil. It is defined as in Eq. (2) [24], [25], [26]:

$$d = \frac{G_o \cdot \Delta t}{m_o} \quad \text{for: } 0 < \Delta t < \frac{m_o}{G_o} \quad (2)$$

where:

- $d$  – is the amount of added oil relative to the amount of initial oil in the lubricating oil system [-],
- $m_o$  – is the initial mass of oil in the engine lubrication system [kg],
- $G_o$  – is the hourly oil consumption [kg/h],
- $\Delta t$  – is the time between the following topping-up practices [h].

## OBJECTIVE FUNCTIONS

Based on the mass balance equations for the properties of the lubricating oil and the model of the experimental unit (a trunk-piston marine engine) adopted in [24], mathematical models were developed to assess the initial changes in the mass concentration of solid impurities and the base number depending on the method used to top up the oil and the parameters that characterise the lubrication system. These models have the following forms:

- for the concentration of solid impurities:

$$\Delta x = \left| x_o - \frac{q_z}{\left(\frac{1}{2} - \frac{1}{d}\right) \cdot (Q_w \cdot \psi + G_o) \cdot \ln(1 - d)} \cdot 100\% \right| \quad \text{for: } 0 < d < 1 \quad (3)$$

where:

- $\Delta x$  – is the change in the solid impurity content of the oil relative to the initial impurity content [%],
- $x_o$  – is the initial content of solid impurities in the oil [%],
- $Q_w$  – is the capacity of the oil purifier [kg/h],
- $q_z$  – is the inflow of contaminants to the lubrication system [kg/h],
- $\psi$  – is an oil purification factor [-].

- for the base number:

$$\Delta K = \left| \left(\frac{1}{2} - \frac{1}{d}\right) \cdot \frac{b}{G_o} \cdot \ln |1 - d| \right| \quad \text{for: } 0 < d < 1 \quad (4)$$

where:

- $\Delta K$  – is the change in the base number for the oil relative to the base number for fresh oil [mg KOH/g],
- $b$  – is the rate of consumption of alkaline additives used to neutralise the acid products of fuel combustion and oil oxidation [mg KOH/h].

Both criteria are functions of several variables. In addition, the parameters  $G_o$ ,  $Q_w$ ,  $\psi$ ,  $q_z$  and  $b$  that characterise the engine's lubrication system are dependent on time, although under the conditions described in [24], we can assume that these are constant. This assumption transforms the problem into the much easier task of static optimisation with a single decision variable, the parameter  $d$ , which characterises the method of topping up the oil. The minima in the functions in Eqs. (3) and (4) then determine the desired effect of the topping-up method in the form of the smallest change in the initial value of solid impurity content in the lubricating oil (criterion 1) or the smallest change in the initial value of the alkalinity of the oil (criterion 2).

## LIMITATIONS OF THE OBJECTIVE FUNCTIONS

The objective functions in Eq. (3) and Eq. (4) have minimum values in their domain of determinancy, at which the optimal values of the parameter  $d$  (i.e. for  $0 < d < 1$ ) are possible solutions. In practice, there are also additional limitations (resulting from the topping-up methods that can be applied in practice), and these also define the range of possible and desired solutions. This can be expressed as the following inequality:

$$d_{min} \leq d \leq d_{max} \quad (5)$$

The value of  $d_{min}$  results from the smallest top-up that can be applied in practice, whereas  $d_{max}$  results from the minimum permissible oil level in the engine crankcase or sump tank. The amount of oil in the lubrication system must not drop below the minimum required for proper lubrication, and  $d_{max}$  therefore has a characteristic value for a specific engine and lubrication system, as specified by the engine manufacturer.

## CALCULATION EXAMPLE

### PREPARATION OF THE OPTIMISATION TASK

Using the mathematical models Eqs. (3) and (4), we carried out a numerical simulation of a Pielstick 12PC2-5V trunk piston marine diesel engine (with a maximum continuous rating of 5740 kW at 520 rpm), operating on sulphated fuels ( $S = 2\%$ ). Various methods of topping up the lubricating oil were applied, and the following system parameters were used:  $G_o = 6$  kg/h;  $Q_w = 880$  kg/h;  $\psi = 0.15$ ;  $q_z = 1,41$  kg/h;  $b = 30625$  mg KOH/h [24]. The simulation results are shown in Figs. 2A and 2B.

Calculations were carried out for values of the parameter  $d$  from  $d = 0.01$  (continuous oil dosing adjusted to the current consumption rate) to  $d = 0.99$  (consumption of practically all the oil in the lubricating system and then replenishment to the initial level). The range of changes in the parameter  $d$  was purely theoretical.

In practice, for the Pielstick 12PC2-5V engine considered here, the value of the parameter  $d$  ranged from  $d = 0.05$

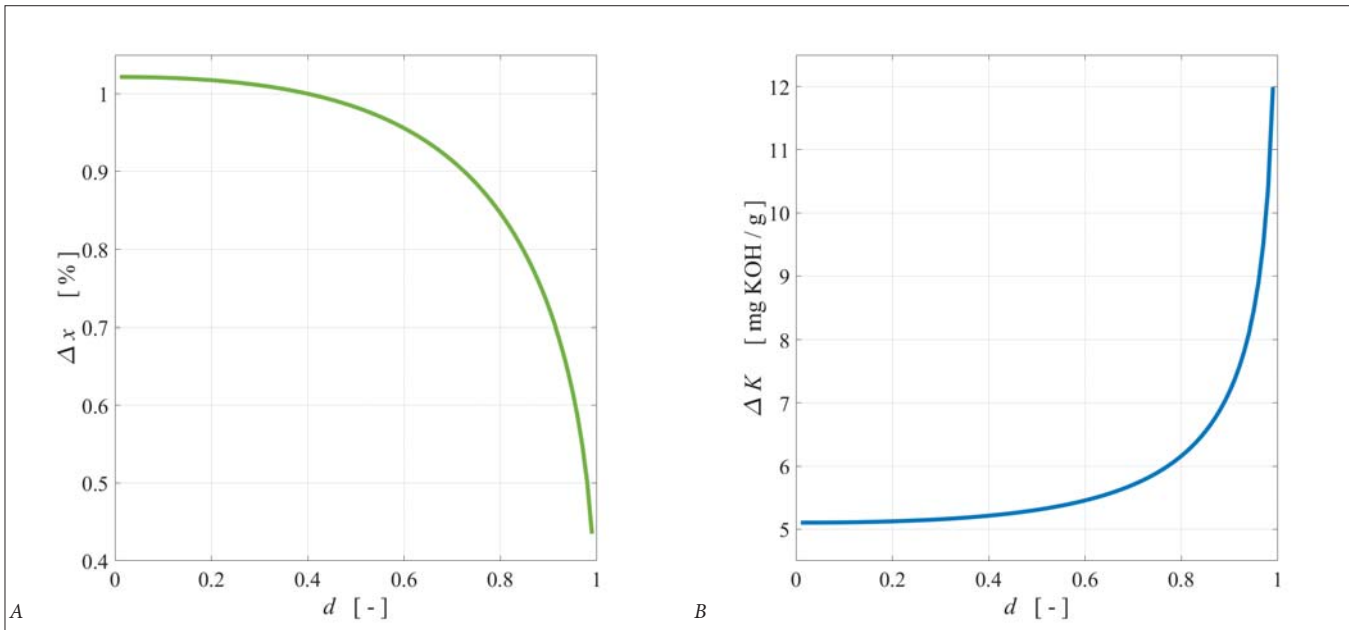


Fig. 2. Graphical interpretation of the objective functions – changes in the concentration of solid impurities (Fig.2A) and alkalinity (Fig.2B) of the lubricating oil of a PIELSTICK 12PC2-5V engine versus parameter  $d$

(corresponding to a minimum replenishment of about 400 kg of oil, resulting from the rationality of the operation) to  $d = 0.5$  (corresponding to a maximum replenishment of about 4000 kg of oil, calculated based on the low-level alarm in the lubricating oil sump tank) [24].

The objective functions in Eqs. (3) and (4) clearly define the influence of the topping-up method on the changes in the base number and mass concentration of the solid impurities. However, the influence is inverse: an increase in the parameter  $d$  (the amount of added oil relative to the initial amount of oil in the lubricating system) has a beneficial effect on the solid impurity content change  $\Delta x$  (Fig. 2A), but change of  $\Delta K$  is negative (Fig. 2B). Hence, in the following, the objective functions in Eqs. (3) and (4) will form the basis for multi-objective (two-objective) optimisation. One of the most intuitive ways of obtaining a single unique solution to a MOOP is the weighted sum method, in which all of the objective functions are combined to form a single function.

We then seek the minimum or maximum of this single function. The value scales of the summed criterion functions can vary considerably, and to ensure that none of the functions dominates the desired solution, the criterion function values are normalised, typically using a linear function of between zero and one. This is purely a technical procedure, and the function created in this way has no physical interpretation.

The following actions need to be performed to achieve this:

- Formulate a synthetic (substitute) objective function consisting of the two previously developed objective functions Eq. (3) and Eq. (4) as criteria functions for the optimisation task;
- Accept the weights in order to find a compromise solution to the criterion functions that is dependent on the sulphation of the fuel;

- Choose a compromise solution search method and carry out a numerical simulation.

The synthetic objective function  $f_c(X)$  was formulated in the form of a weighted sum of the criterion functions:

$$f_c(X) = w_1 \cdot k_1(X) + w_2 \cdot k_2(X) \quad (6)$$

where:

- $k_1(X)$  – is the normalised criterion 1, i.e. the change in the concentration of solid impurities  $\Delta x$  in Eq. (3);
- $k_2(X)$  – is the normalised criterion 2, i.e. the change in the base number  $\Delta K$  in Eq. (4);
- $X$  – is the set of independent variables (the parameter  $d$ ),
- $w_1, w_2$  – are the weighting factors of the criterion functions ( $w_1 + w_2 = 1$ ).

The criterion functions are continuous functions of a single variable, the parameter  $d$ . This parameter can take values from zero to one, but in practice, due to the limitations on the engine used in this case, its values range from 0.05 to 0.5. Sufficient accuracy can be obtained by changing the value of  $d$  with a step of 0.001. The objective function in the area of feasible solutions can therefore take several hundred values, and a search for the optimum value was performed using the complete review method in MATLAB. The preliminary calculations were carried out by changing the parameter  $d$  from 0.05 to 0.5 with a step of 0.001 and changing the weight factor  $w$  from 0 to 1 with a step of 0.1.

Based on these calculations, it was observed that the substitute objective function was less sensitive to changes in  $d$  than to changes in the weighting factor  $w$ . The criterion functions after normalisation are almost symmetric with

respect to the straight line  $fc(d) = 0.5$ , meaning that after summation they give a graph that is close to a horizontal straight line (as shown by the red dashed line in Fig. 3).

This means that the minimum value of the objective function (the optimum) for most values of the weighting factor  $w$  lie on the extreme left- or right-hand sides (i.e. at the minimum or maximum allowable values of the parameter  $d$ ).

In order to increase the sensitivity of the substitute objective function to changes in the parameter  $d$ , we applied a general utility function, which can be expressed in its simplest form as a weighted exponential sum:

$$fu(d) = (1 - w) \cdot k1(d)^2 + w \cdot k2(d)^2 \quad (7)$$

Fig. 3 shows the differences between the substitute objective functions in Eqs. (6) and (7), for three values of the weighting factor ( $w = 0.45, w = 0.5, w = 0.55$ ).

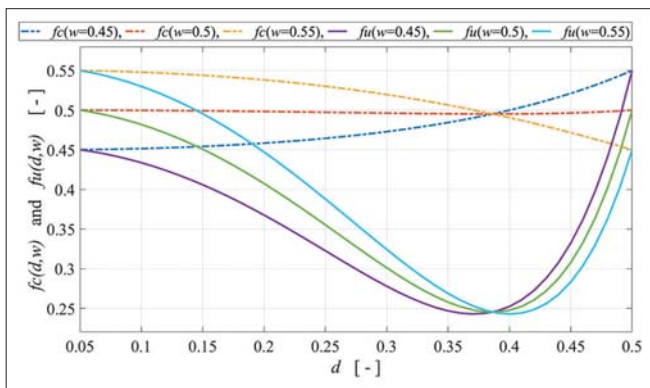


Fig. 3. Substitute objective functions in the form of weighted linear sum: equation 6 (dashed lines), equation 7 (continuous lines), for three weighting factors:  $w=0.45, w=0.5, w=0.55$

## OPTIMISATION CALCULATIONS

Due to the small number of acceptable solutions, the search for the optimum of the objective function was carried out using a complete review method. Fig. 4 shows the optimum points (shown as black circles) determined for different weighting factors. The weighting factor was varied from  $w = 0$  to  $w = 1$  with a step of 0.1.

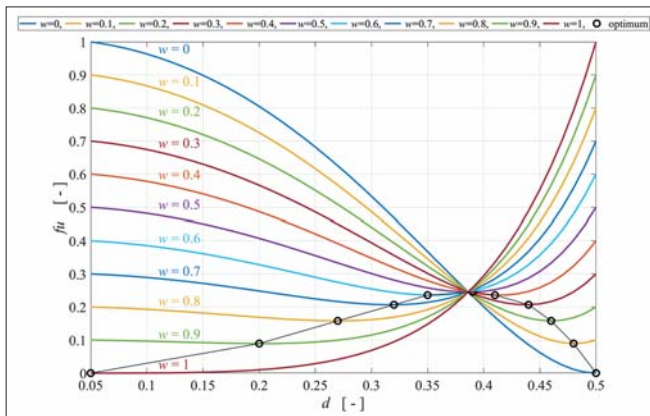


Fig. 4. Review of optimal solutions for weighting factors  $w$  over the interval  $\{0:1\}$  with a step of 0.1. The parameter  $d$  was varied in the interval  $\{0.05:0.5\}$

A weighting factor of  $w = 1$  means that the topping-up strategy takes into account only the change in the oil alkalinity (criterion 2),  $\Delta K$ . We seek the lowest possible value of this parameter, and pay no attention to the increase in solid impurities  $\Delta x$ . On the other hand, with a weighting factor of  $w = 0$ , we minimise the concentration of solid impurities  $\Delta x$  and do not pay attention to the alkalinity level of the lubricating oil. For intermediate values, we find compromise solutions in which we consider both optimisation criteria to different extents.

## PRACTICAL APPLICATION OF OPTIMISATION

We can relate the weighting factor used in the substitute objective function to the degree of sulphation of the fuel oil used in the marine engine. This will make it easier for the mechanical engineer to choose the right strategy for topping up the lubricating oil.

In this example, we assume a linear relationship between the fuel oil sulphur content and the weight coefficient. We assume that a weight coefficient of  $w = 1$  corresponds to the sulphur content of heavy fuels,  $S = 2\%$ , while a weight coefficient of  $w = 0$  corresponds to gas oils with minimum sulphur content,  $S = 0.1\%$ .

Fig. 5 shows the optimum values of the parameter  $d$  for varying fuel oil sulphur content  $S$ .

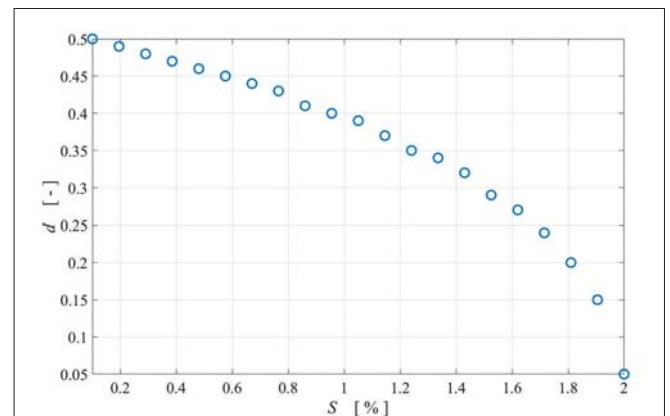


Fig. 5. Optimal values of the parameter  $d$  for varying fuel oil sulphur content  $S$ , for weight factors  $w$  varying in the range  $w=0$  to  $w=1$  with a step of 0.05 (where the sulphur content has a linear relationship with the weight factor: for  $w=0, S=0.1\%$ ; for  $w=1, S=2\%$ )

For instance, for a fuel oil with sulphur content  $S = 0.4\%$ , the optimal value of the parameter  $d = 0.469$  (Fig. 5). The change in the solid impurity content of the oil in relation to the initial impurity content for a Pielstick 12PC2-5V engine will then be  $\Delta x = 0.989\%$  from Eq. (3), and the change in the base number of the lubricating oil relative to the base number for fresh oil will be  $\Delta K = 5.274 \text{ mg KOH/g}$  from Eq. (4).

## SUMMARY

The proposed method of optimising the scheme used to top up lubricating oil in medium-speed marine diesel engines is an attempt to solve the problem by taking into account the

influence of the topping-up method on the quality of the oil (in terms of the mass concentration of solid impurities and the base number). The quality of the oil influences the friction conditions of the engine (for example the piston/piston ring/cylinder liner) and ultimately the wear of the elements. In addition, during combustion, the solid impurities in lubricating oil contribute to the total particulate emissions.

This complex issue was formulated as a simple problem of static two-criteria optimisation (where these criteria represent the properties of the lubricating oil, i.e. the concentration of solid impurities and the alkalinity) with one decision variable (parameter  $d$ ). The optimisation was carried out using MATLAB software. The aim was to enable the operator (the mechanical engineer) to choose the optimal strategy for topping up the oil depending on the quality (sulphur content) of the fuel oil. For engines powered by DMX/DMA-type gas oils, the problem of sulphur corrosion is negligible, as the sulphur content is below 0.1%. In this case, the dominant criterion should be criterion 1, i.e. the change in the concentration of solid impurities. As the fuel quality deteriorates, mainly due to the increase in sulphur content, the oil alkalinity changes (criterion 2, Eq. (4)) and becomes more important. For intermediate values, we have compromise solutions in which we consider both optimisation criteria to a different extent (Fig. 5).

The proposed method should be seen as a way of selecting an appropriate strategy for topping up lubricating oil of medium-speed marine diesel engines. Under real operating conditions, other factors such as the engine manufacturer's recommendations, the potential risk of sludge precipitation, and difficulties in interpreting analytical data on the oil when samples are taken should also be considered.

## REFERENCES

1. CIMAC, "Guidelines for the lubrication of medium speed diesel engines," *Int. Counc. Combust. Engines*, no. 29, 2008.
2. P.G. Casale, D. Davidson, and G. Lane, "Marine lubrication and the user connection," in *20<sup>th</sup> International Congress on Combustion Engines*, CIMAC, London, 1993.
3. W. Cyulin and W.J. Lemski, "Effect of operating influences on wearing speed of marine diesel engine elements," in *II International Scientifically-Technical Conference EXPLOR-Diesel & Gas Turbine*. Gdańsk-Międzyzdroje-Kopenhaga, 2001.
4. J.F. Thomas, C. Scott Sluder, M.D. Kass and T. Theiss, "A guide to fuel, lubricant, and engine concerns relative to the IMO 2020 Fuel Oil Sulfur Reduction Mandate," Oak Ridge National Laboratory, 2019.
5. V. Macian, B. Tormos, P. Olmeda, and L. Montoro, "Analytical approach to wear rate determination for internal combustion engine condition monitoring based on oil analysis," *Tribology International*, vol. 36, 2003.
6. J. Senatorski, "Assessment of the impact of mineral abrasive particles on the wear of lubricated sliding associations" (in Polish), *Tribologia*, no. 2, 2002.
7. J.K. Włodarski, "Fundamentals of operation of marine machinery: Friction and wear" (in Polish), *Wydawnictwo Akademii Morskiej w Gdyni*, Gdynia 2006.
8. P. Tonon, et al., "Tribology in a big medium speed engine", Paper No. 105, presented at the 24th CIMAC Congress, Kyoto 2004.
9. IMO Annex 14, Resolution MEPC.320(74) (adopted 17 May 2019), "2019 Guidelines for Consistent Implementation of the 0.50% Sulphur Limit Under Marpol Annex VI." [Online]. Available: [https://www.wcdn.imo.org/localresources/en/KnowledgeCentre/IndexofIMOResolutions/MEPCDocuments/MEPC.320\(74\).pdf](https://www.wcdn.imo.org/localresources/en/KnowledgeCentre/IndexofIMOResolutions/MEPCDocuments/MEPC.320(74).pdf). [Accessed April 2, 2021].
10. R. Bergqvist, M. Turesson, and A. Weddmark, "Sulphur emission control areas and transport strategies – The case of Sweden and the forest industry," *Eur. Transp. Res. Rev.*, vol. 7, no. 2, 2015. doi: 10.1007/s12544-015-0161-9.
11. EMSA, "The 0.1 % sulphur in fuel requirement as from 1 January 2015 in SECAs – An assessment of available impact studies and alternativemeans of compliance," *European Maritime Safety Agency, Technical Report*, 13 December 2010.
12. A. Half, L. Younes, and T. Boersma, "The likely implications of the new IMO standards on the shipping industry," *Energy Policy*, vol. 126, 2019. doi: 10.1016/j.enpol.2018.11.033.
13. EC, "Directive 2012/33/EU of the European Parliament and of the Council of 21 November 2012 amending Council Directive 1999/32/EC as regards the sulphur content of marine fuels," OJL, 2012.
14. M. Guatam, K. Chitor, M. Durbha, and J.C. Sommers, "Effect of diesel soot contaminated oil on engine wear-investigation of novel oil formulation," *Tribology International*, vol. 32, 1999.
15. J.J. Corbett, J.J. Winebrake, E.H. Green, P. Kasibhatla, V. Eyring, and A. Lauer, "Mortality from ship emissions: A global assessment," *Environmental Science & Technology*, vol. 41, no. 24, pp. 8512–8518, 2007. doi: 10.1021/es071686z.
16. R. Szłapczyński and H. Ghaemi, "Framework of an evolutionary multi-objective optimization method for planning a safe trajectory for a marine autonomous surface ship," *Polish Maritime Research*, 2020. doi: 10.2478/pomr-2019-0068.
17. E. Sobocka, R. Szłapczyński, and M. Zyczkowski,

“Evolutionary multi-objective weather routing of sailboats,” *Polish Maritime Research*, 2020. doi: 10.2478/pomr-2020-0054.

18. A. Cheaitou and P. Cariou, “Greening of maritime transportation: A multi-objective optimization approach,” *Ann. Oper. Res.*, 2019. doi: 10.1007/s10479-018-2786-2.
19. Z. Baoji, “Research on ship hull optimization of high-speed ship based on viscous flow/potential flow theory”, *Polish Maritime Research*, 2020. doi: 10.2478/pomr-2020-0002.
20. S. Su, Y. Zheng, J. Xu, and T. Wang, “Cabin placement layout optimization based on systematic layout planning and genetic algorithm,” *Polish Maritime Research*, 2020. doi: 10.2478/pomr-2020-0017.
21. K. Rudzki and W. Tarelko, “A decision-making system supporting selection of commanded outputs for a ship’s propulsion system with a controllable pitch propeller,” *Ocean Eng.*, 2016. doi: 10.1016/j.oceaneng.2016.09.018.
22. W. Tarelko and K. Rudzki, “Applying artificial neural networks for modelling ship speed and fuel consumption,” *Neural Computing and Applications*, 2020. doi: 10.1007/s00521-020-05111-2.
23. W. Stadler, *Multicriteria Optimization in Engineering and in the Sciences*. Boston, MA: Springer US, 1988.
24. A. Młynarczak, “Optimisation of the using process of lubricating oils in marine engines” (in Polish), PhD dissertation, *Gdynia Maritime University*, Gdynia 2006.
25. A. Młynarczak, “Modelling of alkalinity changes in lubricating oils used in marine diesel engines”, *J. KONES*, vol. 16, no. 2, 2009.
26. A. Młynarczak, “Modeling of mass concentration of solid impurities changes in Lubricating oils used in trunkpiston marine diesel engines during various lubricating oil refilling methods”, *Joint Preceedings no. 21, August 2008, Gdynia Maritime University & Hochschule Bremerhaven*, pp. 29–36, Wydawnictwo Uczelniane AM Gdynia 2008.

## CONTACT WITH THE AUTHORS

**Andrzej Młynarczak**

*e-mail: a.mlynarczak@wm.umg.edu.pl*

Gdynia Maritime University  
Morska 81-87, 81-225 Gdynia

**POLAND**

**Krzysztof Rudzki**

*e-mail: k.rudzki@wm.umg.edu.pl*

Gdynia Maritime University  
Morska 81-87, 81-225 Gdynia

**POLAND**

# INVESTIGATIONS OF THE EMISSION CHARACTERISTICS OF A DUAL-FUEL GAS TURBINE COMBUSTION CHAMBER OPERATING SIMULTANEOUSLY ON LIQUID AND GASEOUS FUELS

Serhiy Serbin\*

Badri Diasamidze

Viktor Gorbov

Admiral Makarov National University of Shipbuilding, Ukraine

Jerzy Kowalski

Gdańsk University of Technology, Poland

\* Corresponding author: [serbin1958@gmail.com](mailto:serbin1958@gmail.com) (S. Serbin)

## ABSTRACT

*This study is dedicated to investigations of the working process in a dual-fuel low-emission combustion chamber for a floating vessel's gas turbine. As the object of the research, a low-emission gas turbine combustion chamber with partial premixing of fuel and air inside the outer and inner radial-axial swirls was chosen. The method of the research is based on the numerical solution of the system of differential equations which represent the physical process of mass and energy conservation and transformations and species transport for a multi-component chemically reactive turbulent system, considering nitrogen oxides formation and a discrete ordinates model of radiation. The chemistry kinetics is presented by the 6-step mechanism of combustion. Seven fuel supply operating modes, varying from 100% gaseous fuel to 100% liquid fuel, have been analysed. This analysis has revealed the possibility of the application of computational fluid dynamics for problems of dual-fuel combustion chambers for the design of a floating vessel's gas turbine. Moreover, the study has shown the possibility of working in different transitional gaseous and liquid fuel supply modes, as they satisfy modern ecological requirements. The dependencies of the averaged temperature, NO, and CO concentrations along the length of the low-emission gas turbine combustion chamber for different cases of fuel supply are presented. Depending on the different operating modes, the calculated emission of nitrogen oxides NO and carbon monoxide CO at the outlet cross-section of a flame tube are different, but, they lie in the ranges of 31–50 and 23–24 mg/nm<sup>3</sup> on the peak of 100% liquid fuel supply mode. At operating modes where a gaseous fuel supply prevails, nitrogen oxide NO and carbon monoxide CO emissions lie in the ranges of 1.2–4.0 and 0.04–18 mg/nm<sup>3</sup> respectively.*

**Keywords:** gas turbine engine, dual-fuel combustion, combustion chamber, liquid and gaseous fuels

## INTRODUCTION

The problem of the design and exploitation of marine power plants of Floating Production, Storage, and Offloading (FPSO) vessels is of interest to the Offshore Gas and Oil industry. A forecast from 2020 to 2024 expects 60 new FPSO vessels projects to go forward, with an expectation that 29 of them will have new-built hulls [1]. Gas turbines are frequently used as FPSO marine power plants, so there is a strong need to create both efficient and ecologically-friendly gas turbines. Despite the existing research on FPSO power plant

enhancement [2-8], the current data investigating the burning of dual-fuel in the modern gas turbine combustion chamber and its operating modes applied to FPSO power plants is insufficient. One of the challenging tasks of developing dual-fuel combustion chambers is to provide the required nitrogen oxides concentrations [9] while sustaining low emissions of carbon monoxide and unburned hydrocarbons when operating on various transitional modes of gaseous and liquid fuel supply. Experimental work to investigate the dual-fuel combustion of diesel fuel and methane [10] in internal combustion engines (ICE) has revealed that burning dual-fuel provides lower emission of nitrogen oxide compared to the

diesel fuel operation mode due to the lower flame temperature and lower heat capacity of methane.

This work uses computational fluid dynamics (CFD) methods and is dedicated to the investigation of transitional gaseous and liquid fuel supply modes combining advanced methods of mathematical modelling and the idea of the preliminary simultaneous mixing of liquid and gaseous fuels and air in the radial-axial swirls of a flame tube. Revealing the behaviour of transitional gaseous and liquid fuel supply modes is important for the exploitation of gas turbine engines as they could cause flame instability and flame blowout.

## MATHEMATICAL MODELLING

The mathematical modelling of combustion processes in a dual-fuel low-emission combustion chamber for an FPSO includes modelling of the physical and chemical processes. This is based on the solution of the differential equations of mass, impulse, and energy conservation for the multi-component, turbulent, chemically reacting system. The main equations of the gaseous phase model are continuity, the equation of momentum conservation, the energy conservation equation, and the equation for the conservation of chemical components. A detailed description of the equations and methods of solving them in the case of gaseous fuel is given in [7, 11-16]. The transfer equations for the kinetic energy of turbulence  $k$  and the dissipation rate of turbulent energy  $\epsilon$  for the Renormalization Group (RNG) turbulence model [17] have been chosen. In this article equations that are applied directly to dual-fuel combustion and the interaction of gaseous and liquid phases are noted:

– the continuity equation:

$$\frac{\partial \rho}{\partial t} + \frac{\partial}{\partial x_i} (\rho u_i) = \dot{\rho}^s \quad (1)$$

– the equation of momentum conservation:

$$\frac{\partial}{\partial t} (\rho u_j) + \frac{\partial}{\partial x_i} (\rho u_i u_j) = \frac{\partial}{\partial x_i} \left[ \mu \left( \frac{\partial u_i}{\partial x_j} + \frac{\partial u_j}{\partial x_i} \right) \right] - \frac{\partial p}{\partial x_j} + \rho g_i + \dot{F}^s + \frac{\partial}{\partial x_i} (\overline{\rho u_i u_j}) \quad (2)$$

– the energy conservation equation:

$$\frac{\partial}{\partial t} (\rho h_0) + \frac{\partial}{\partial x_i} (\rho u_i h_0) = \frac{\partial}{\partial x_i} \left[ \frac{k_m + k_t}{c_p} \left[ \frac{\partial (h_0 - u^2/2)}{\partial x_i} - \sum_j h_j \frac{\partial X_j}{\partial x_i} \right] - \frac{\partial}{\partial x_i} \sum_j h_j J_{ji} + \frac{\partial p}{\partial t} - \frac{\partial}{\partial x_i} (\tau_{ik} u_k) + S_h + \dot{Q}^s \right] \quad (3)$$

– the equation for the conservation of chemical components:

$$\frac{\partial}{\partial t} (\rho Y_i) + \frac{\partial}{\partial x_i} (\rho u_i Y_i) = \frac{\partial}{\partial x_i} J_i + R_i + \dot{\rho}^s \delta_i \quad (4)$$

In Eqs. (1)–(4),  $t$  is the time;  $x_i$  and  $x_j$  are the coordinates;  $\rho$ ,  $u$ ,  $\mu$ ,  $p$ , and  $g$  are the density, velocity, viscosity, pressure, and gravity acceleration;  $\dot{\rho}^s$ ,  $\dot{F}^s$ ,  $\dot{W}^s$ , and  $\dot{Q}^s$  are the sources for

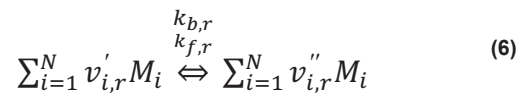
the interaction of the gas and liquid phases;  $G_k$  is the source describing the generation of turbulent energy;  $C_1$ ,  $C_2$ , and  $C_3$  are the empirical constants;  $h_0$  is the stagnation enthalpy;  $h_j$  is the component's enthalpy;  $k_m$  and  $k_t$  are the coefficients of molecular and effective thermal conductivity;  $c_p$  is the specific heat of the mixture at constant pressure;  $\tau_{ik}$  is the shear stress tensor;  $J_{ji}$  is the component  $j$  flow in the  $i$  direction;  $S_h$  is the source term from the chemical reaction;  $Y_i$  is the mass fraction of component  $i$ ;  $R_i$  is the rate of the component's formation or destruction;  $J_j$  is the diffusion component's flow; and  $\delta_i$  is the Dirac delta function.

The net source of chemical species  $i$  due to the reaction is computed as the sum of the Arrhenius reaction sources over the  $N_r$  reactions in which the species participate:

$$R_i = M_{w,i} \sum_{r=1}^{N_R} R_{i,r} \quad (5)$$

where  $M_{w,i}$  is the molecular weight of species  $i$  and  $R_{i,r}$  is the Arrhenius molar rate of creation/destruction of species  $i$  in reaction  $r$ .

Consider the  $r$ -th reaction written in the general form:



where  $N$  is the number of chemical species in the system;  $v'_{i,r}$  is the stoichiometric coefficient for reactant  $i$  in reaction  $r$ ;  $v''_{i,r}$  is the stoichiometric coefficient for the product  $i$  in reaction  $r$ ;  $M_i$  is the symbol denoting species  $i$ ;  $k_{f,r}$  is the forward rate constant for reaction  $r$ ; and  $k_{b,r}$  is the backward rate constant for reaction  $r$ .

For a non-reversible reaction, the molar rate of creation/destruction of species  $i$  in reaction  $r$  is given by

$$R_{i,r} = \Gamma (v''_{i,r} - v'_{i,r}) \cdot \left( k_{f,r} \prod_{j=1}^N [C_{j,r}]^{\eta'_{j,r} + \eta'_{j,r}} \right) \quad (7)$$

where  $C_{j,r}$  is the molar concentration of species  $j$  in reaction  $r$ ;  $\eta'_{j,r}$  is the rate exponent for reactant species  $j$  in reaction  $r$ ;  $\eta''_{j,r}$  is the rate exponent for product species  $j$  in reaction  $r$ ; and  $\Gamma$  presents the net effect of third bodies on the reaction rate:

$$\Gamma = \sum_j^{N_r} \gamma_{j,r} C_j \quad (8)$$

where  $\gamma_{j,r}$  is the third-body efficiency of the  $j$ -th species in the reaction  $r$ .

Modelling of nitrogen oxides emissions was carried out using transfer equations which include convection, diffusion, formation, and decomposition of NO and related compounds. The influence of the reaction volume's residence time on the mechanism of nitrogen oxide formation is considered in the convection terms of the defining equations written in the Euler reference system. For thermal and prompt nitrogen oxides, it is necessary to solve the NO transfer equation [11, 16]:

$$\frac{\partial}{\partial t} (\rho Y_{NO}) + \nabla \cdot (\rho \vec{v} Y_{NO}) = \nabla \cdot (\rho D \nabla Y_{NO}) + S_{NO} \quad (9)$$

where  $Y_{NO}$  is the NO mass fraction;  $D$  is the diffusion coefficient;  $\vec{v}$  is the velocity vector; and  $S_{NO}$  is the source term depending on the NO formation mechanism.

The eddy dissipation combustion (EDC) model [18] and its detailed chemical mechanisms in turbulent flows are included in this research. It assumes that the reaction occurs in small turbulent structures, called fine scales. The length fraction of the fine scales is modelled as

$$\xi^* = C_\xi (v\varepsilon/k^2)^{0.75} \quad (10)$$

where  $C_\xi = 2.1377$  is the volume fraction constant and  $v$  is the kinematic viscosity.

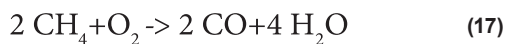
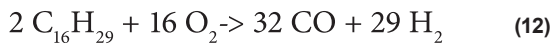
Species are assumed to react in the fine structures over a time scale

$$\tau^* = C_\tau (v/\varepsilon)^{0.5} \quad (11)$$

where  $C_\tau = 0.4082$  is the time-scale constant.

The length fraction of the fine scales is modelled as reactions proceed over the time scale, governed by the Arrhenius rates, and are integrated numerically using the ISAT algorithm [19]. The validity of the EDC approach for modelling physicochemical processes is demonstrated for two-phase turbulent swirling liquid spray burning in a complex gas turbine combustion chamber [20] and for a model gas turbine combustor [21].

To simulate the formation of carbon monoxide and molecular hydrogen inside a dual-fuel gas turbine combustion chamber, it is proposed to use the 6-step kinetic mechanism for simultaneous combustion of liquid and gaseous fuels:



The reaction rate constants of the proposed kinetic mechanism are presented in Table 1.

Tab. 1. Reaction rate constants for a six-stage oxidation mechanism of diesel fuel and methane

Reaction	A	E, J/mol	$\beta$	The order of the reaction			
$2 C_{16}H_{29} + 16 O_2 \rightarrow 32 CO + 29 H_2$	1.1206e+19	1.2238e+08	2.541	$C_{16}H_{29}$	2.066	O2	1.953
$2 H_2 + O_2 \rightarrow 2 H_2O$	9.1048e+14	2.7007e+08	0.467	$H_2$	0.57	O2	1.178
$2 CO + O_2 \rightarrow 2 CO_2$	6.2327e+14	8.4199e+07	-0.309	CO	1.736	O2	1.804
$2 H_2O \rightarrow 2 H_2 + O_2$	6.5724e+19	3.6931e+08	-0.068	$H_2O$	2.868		
$2 CO_2 \rightarrow 2 CO + O_2$	6.7299e+11	3.5065e+08	-0.255	$CO_2$	1.871		
$2 CH_4 + O_2 \rightarrow 2 CO + 4 H_2O$	9.9126e+14	2.9825e+08	2.618	$CH_4$	1.109	O2	1.572

Validation of similar global chemical mechanisms for the conditions of a gas turbine combustion chamber was carried out in several investigations [11, 22-24]. These works have shown the applicability of kinetic mechanisms to study the combustion of liquid and gaseous fuels in gas turbine combustion chambers in a wide range of variations of the governing parameters.

For calculations of liquid fuel combustion in a low-emission combustion chamber, the Discrete Phase Model (DPM), which calculates the trajectories of motion for individual particles, was selected [18, 25, 26]. The model predicts the particle trajectories of the discrete phase by integrating their motion equations written in the Lagrange form [18, 25-27].

In this study, the discrete ordinates (DO) radiation model is chosen. The DO model (20) considers the radiative transfer equation (RTE) (19) as a field equation and solves it for nine discrete solid angles, each associated with a vector direction  $\vec{s}$  fixed in the global Cartesian system ( $x, y, z$ ).

The radiative transfer equation for an absorbing, emitting, and scattering medium at the position  $\vec{r}$  in the direction  $\vec{s}$  as field equation [28]:

$$\frac{\partial I(\vec{r}, \vec{s})}{\partial s} + (a + \sigma_s)(I\vec{r}\vec{s}) = an^2 \frac{\sigma T^4}{4\pi} + \frac{\sigma_s}{4\pi} \int_0^{4\pi} (I(\vec{r}, \vec{s}')) \Phi(\vec{s} \cdot \vec{s}') d\Omega' \quad (18)$$

where  $\vec{r}$  is the position vector;  $\vec{s}$  is the direction vector;  $s'$  is the scattering direction vector;  $s$  is the path length;  $a$  is the absorption coefficient;  $n$  is the refractive index;  $\sigma_s$  is the scattering coefficient;  $\sigma$  is the Stefan-Boltzmann constant;  $I$  is the radiation intensity, which depends on the position  $\vec{r}$  and direction  $\vec{s}$ ;  $T$  is the local temperature;  $\Phi$  is the scattering phase function;  $\Omega$  is the solid angle. The discrete ordinates model equation

$$\nabla \cdot (I\vec{r}\vec{s})\vec{s} + (a + \sigma_s)(I\vec{r}\vec{s}) = an^2 \frac{\sigma T^4}{4\pi} + \frac{\sigma_s}{4\pi} \int_0^{4\pi} (I(\vec{r}, \vec{s}')) \Phi(\vec{s} \cdot \vec{s}') d\Omega' \quad (19)$$

where  $(I\vec{r}\vec{s})$  is the total intensity;  $\Phi$  is the scattering phase function.

For simplicity, it is assumed that the temperature of the droplet does not change when boiling. The energy required for evaporation is taken into consideration as a source term in the equation for the energy conservation of the gas phase. Liquid evaporation is also a source of chemical component for the gas phase. A detailed description of the research object and verification of the mathematical model are given in [7].

We should note that some submodels of the general mathematical model were used by the authors to analyse the working processes of various fuel combustion devices [29-32].

## INVESTIGATION OF CHARACTERISTICS OF WORKING PROCESSES IN A DUAL-FUEL COMBUSTION CHAMBER

A low-emission combustion chamber with partial preliminary mixing of fuel and air for a 25 MW UGT25000 gas turbine engine produced by Zorya-Mashproekt was chosen as the object of investigation [16, 33]. The combustion chamber has a cannular counterflow structure (Fig. 1), which implements the principle of dry combustion of a partially mixed lean mixture. The combustion chamber has 16 flame tubes evenly spaced around the engine axis. The total airflow through a combustion chamber at the nominal operating mode is 69.68 kg/s. Compressed air goes to the flame tube through the air inlet and is mixed with a mixture of gaseous and liquid fuel. Gaseous fuel is supplied through a series of holes made in the blades of the radial-axial swirlers of the first and second channels. Liquid fuel is injected using 30 injectors evenly spaced in the sections of the inner and outer swirlers. The design of the flame tube is presented in Fig. 2.

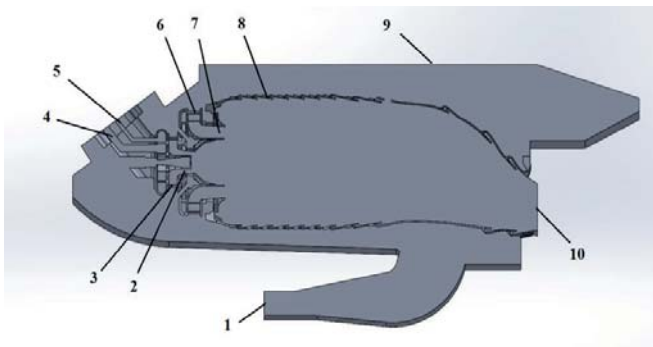


Fig. 1. Longitudinal section of the combustion chamber: 1 – compressed air inlet; 2, 7 – sectors for supplying liquid fuel into the swirlers; 3, 6 – inner and outer radial-axial swirlers; 4, 5 – first and second gaseous fuel channels; 8 – flame tube; 9 – casing; 10 – outlet

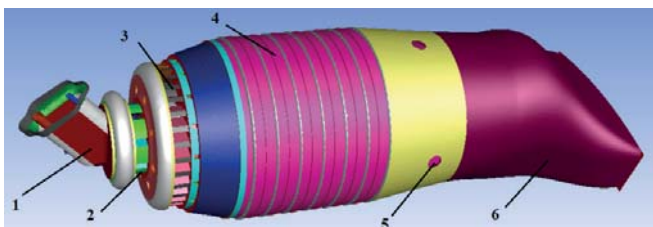


Fig. 2. Flame tube design features: 1 – burner; 2 – inner swirler; 3 – outer swirler; 4 – cooled shells; 5 – dilution air holes; 6 – flame tube diffuser

Since all flame tubes have an identical design, three-dimensional CFD calculations in order to reduce computing resources were carried out for a 1/16 part of a combustion chamber. The initial conditions for a 1/16 part of a low-emission combustion chamber of a 25 MW gas turbine engine

are set as follows: the air temperature at the compressed air inlet of 770 K, the pressure of 2.0523 MPa, the airflow of 4.355 kg/s. In the calculations in which the mass fraction of liquid fuel exceeds the mass fraction of gaseous fuel, the liquid fuel consumption through the fuel supply pipes was 358.02 kg/h. In the calculations where the mass fraction of gaseous fuel exceeds the mass fraction of liquid, the consumption was taken as equal to 320.46 kg/h. These parameters correspond to the nominal mode of operation of the gas turbine engine. To simplify the calculations, the flame tube walls were taken as adiabatic. Typical root mean square (RMS) residuals to establish the solution convergence are about  $1e^{-4}$ .

Fig. 3 shows the locations of the injectors for spraying liquid fuel into the combustion chamber. In the simulation of liquid fuel, a hollow-cone fuel injection method is used, which simulates the spraying of injectors installed in radial-axial swirlers. Parameters of diesel fuel spraying that are common to all operating modes where liquid fuel is supplied are as follows: droplet velocity 15 m/s, the temperature of the diesel fuel 313 K, fuel spray angle  $5^\circ$ . The initial diameters of the fuel droplets are taken from 5 to 75  $\mu\text{m}$ , with an average diameter of 35  $\mu\text{m}$ . Such parameters could be provided by air-mechanical spray nozzles, which are widely used to intensify the processes of breaking liquid fuel droplets and mixing them with an oxidant. Note that 95% of the liquid fuel is fed in the axial direction through fifteen injectors located in the outer swirlers, and 5% of the fuel – through fifteen nozzles located in the inner swirlers.

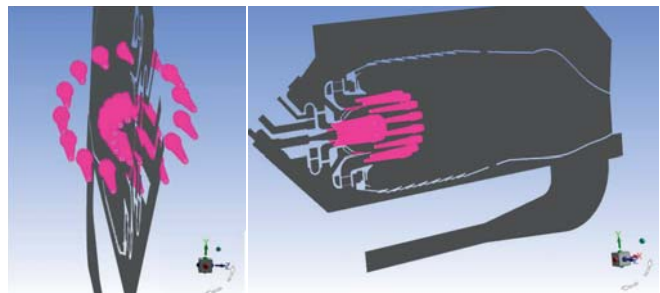


Fig. 3. Injector layout

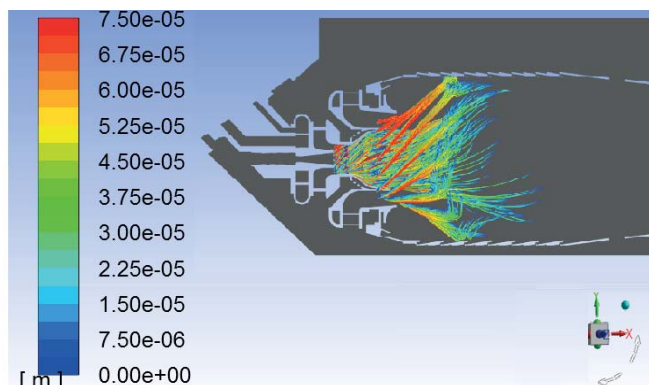
Modes of simultaneous operation on liquid and gaseous fuels at different ratios of their mass flow through the flame tube were studied. Let us denote by numbers the various modes of fuel supply to the combustion chamber. Mode 1 corresponds to 100% gaseous fuel feeding, mode 2 – 90% gaseous fuel and 10% liquid fuel, mode 3 – 70% gaseous fuel and 30% liquid fuel, mode 4 – 50% gaseous fuel and 50% liquid fuel, mode 5 – 30% gaseous fuel and 70% liquid fuel, mode 6 – 10% gaseous fuel and 90% liquid fuel, and mode 7 – 100% liquid fuel feeding. In all cases, the temperature of the gaseous fuel was taken equal to 288 K.

The gaseous and liquid fuel consumption is presented in Table 2.

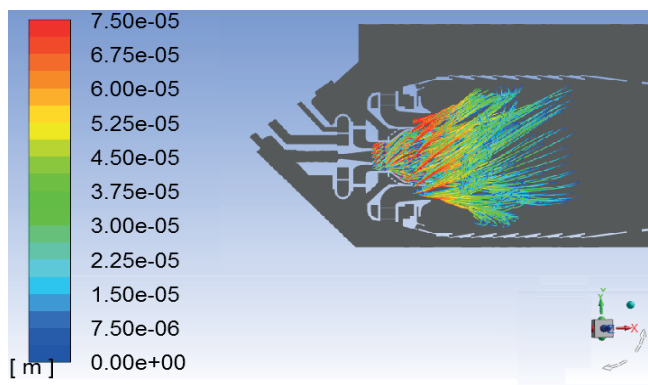
Tab. 2. Fuel consumption through the flame tube

Modes of fuel supply	Fuel consumption through the flame tube, kg/s			
	Gaseous fuel		Liquid fuel	
	Outer swirler	Inner swirler	Outer swirler	Inner swirler
1	0.084567	0.004451	0	0
2	0.076110	0.004006	0.000564	0.000029
3	0.059197	0.003116	0.001691	0.000089
4	0.047239	0.002486	0.003149	0.000166
5	0.028343	0.001492	0.004409	0.000232
6	0.009448	0.000497	0.005669	0.000298
7	0	0	0.094477	0.004972

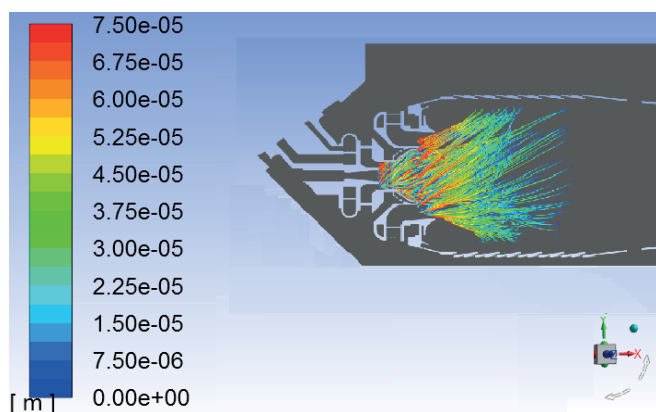
Fig. 4 shows liquid particle traces in the longitudinal section of the flame tube, depending on the modes of fuel supply, taking into consideration the features of mixing the liquid fuel with the mixture of the gaseous fuel and the oxidiser in the channels of the radial-axial swirlers. Due to the nature of the gaseous fuel and its calorific value, modes where the mass fraction of gaseous fuel exceeds 50% are characterised by more intense evaporation of liquid fuel particles.



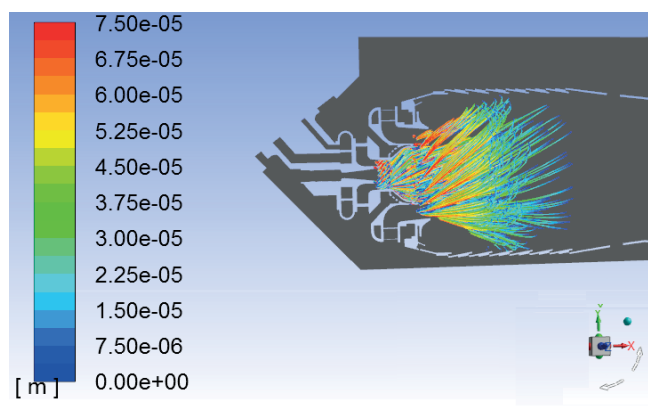
(a)



(b)



(c)



(d)

Fig. 4. Particle diameter distribution for different modes of fuel supply: a) 2; (b) 4; (c) 6; (d) 7

The parameters of the combustion products for the outlet section of the flame tube (average temperature of gases  $T_{exit}$ , the mass concentrations of nitrogen oxides NO and carbon monoxide CO, the average coefficient of the temperature field non-uniformity  $\delta$ ) are presented in Table 3.

a lower proportion of liquid fuel compared to gaseous fuel are characterised by lower concentrations of carbon monoxide.

Fuel supply modes in which the amount of liquid fuel dominates are characterised by higher concentrations of nitrogen oxides in the outlet section of the flame tube due

Tab. 3. Parameters at the outlet combustion chamber section

Mode of fuel supply	1	2	3	4	5	6	7
$T_{exit}$ , K	1564	1555	1532	1610	1608	1578	1565
NO, mg/nm <sup>3</sup>	4.59	1.2359	4.8785	19.226	31.332	36.219	49.823
CO, mg/nm <sup>3</sup>	0.0438	5.6408	17.813	25.2	23.608	21.083	24.452
$\delta$	0.1407	0.1029	0.1436	0.105	0.1803	0.1267	0.13

The results of three-dimensional modelling are presented in Figs. 5–10.

Figs. 5–7 represent the distribution of the temperature, the mass fractions of carbon monoxide and nitrogen oxide on the axis of the combustion chamber. It can be seen that the temperature in the cross-section of the flame tube for all cases is in the range from 1170 to 1750 K (Fig. 5). Modes of supply in which the amount of gaseous fuel exceeds the amount of liquid fuel are characterised by better mixing of fuel with oxidant and a higher rate of the chemical reaction. Along the length of the flame tube, the concentrations of carbon monoxide decrease monotonically (Fig. 6), which indicates the active combustion of fuel. Note that modes with

to the increase in the residence time of reagents in high-temperature zones as a result of delaying the evaporation of liquid fuel and mixing of the evaporated fraction with air. The concentrations of nitrogen oxides NO along the length of the combustion chamber increase (Fig. 6). This is due to the increase in the residence time of the reagents in the primary and secondary zone of the chamber. In the cross-sections of the dilution air supply (the distance from the beginning of the flame tube is 0.32 m) there is a decrease in NO concentrations even on the axis of the chamber as a result of mixing the air and reducing the temperature of the mixture (Fig. 5), and then their further growth is observed. A characteristic trend is that with the increase of liquid fuel content, the concentrations of nitrogen oxides and carbon monoxide in the outlet cross-sections of the flame tube are increasing (Figs. 6, 7).

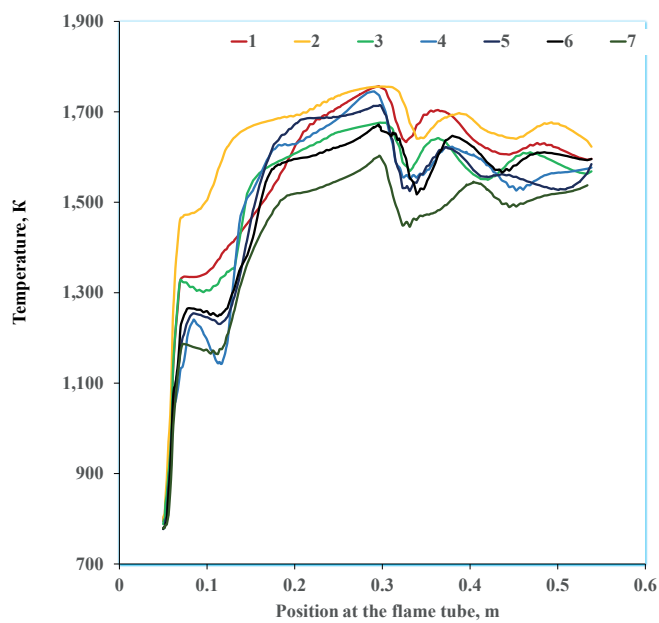


Fig. 5. Distribution of the temperatures (K) along the length of the low-emission combustion chamber for different modes of fuel supply

Figure 8 shows the temperature contours in the longitudinal section of a dual-fuel combustion chamber for four modes of supply of gaseous and liquid fuels. It is seen that the processes of fuel combustion in the cases of the gaseous fuel supply are completed faster, as evidenced by the greater filling of the primary zone with combustion products with high temperatures. As the amount of liquid fuel increases, the flame front is concentrated with the zones corresponding to the trajectories of the fuel droplets, which gradually evaporate and burn in the stream. Moreover, for modes with the vast majority of liquid fuel the maximum combustion products temperature lies in the range of 2100–2280 K, and for modes with a greater amount of gaseous fuel the peak temperatures in the longitudinal cross-section of the combustion chamber are in the range of 1900–2000 K (Fig. 8).

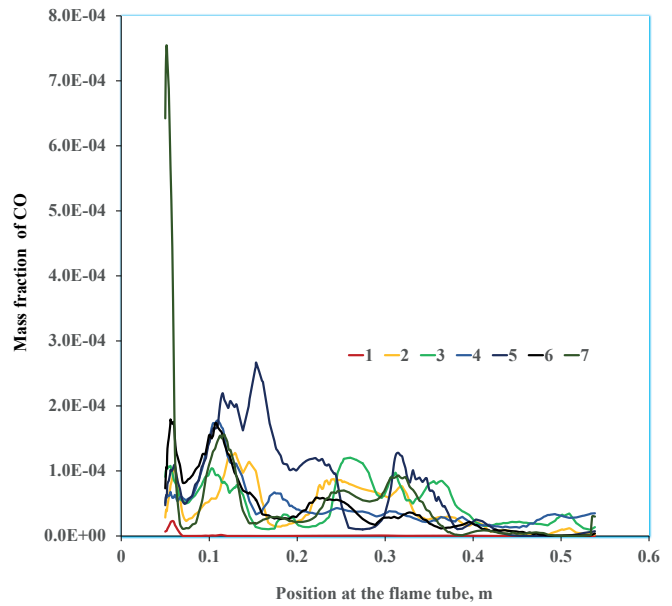


Fig. 6. Distribution of the averaged mass fractions of carbon monoxide along the length of the low-emission combustion chamber for different modes of fuel supply

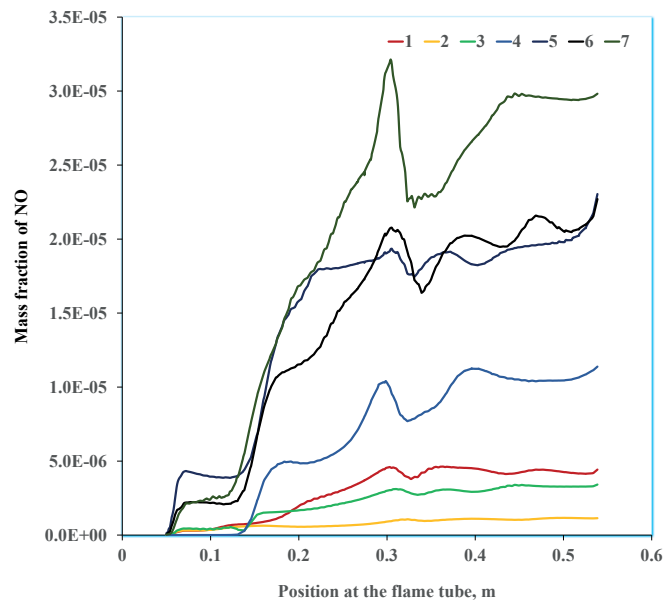


Fig. 7. Distribution of the averaged mass fractions of nitrogen oxide along the length of the low-emission combustion chamber for different modes of fuel supply

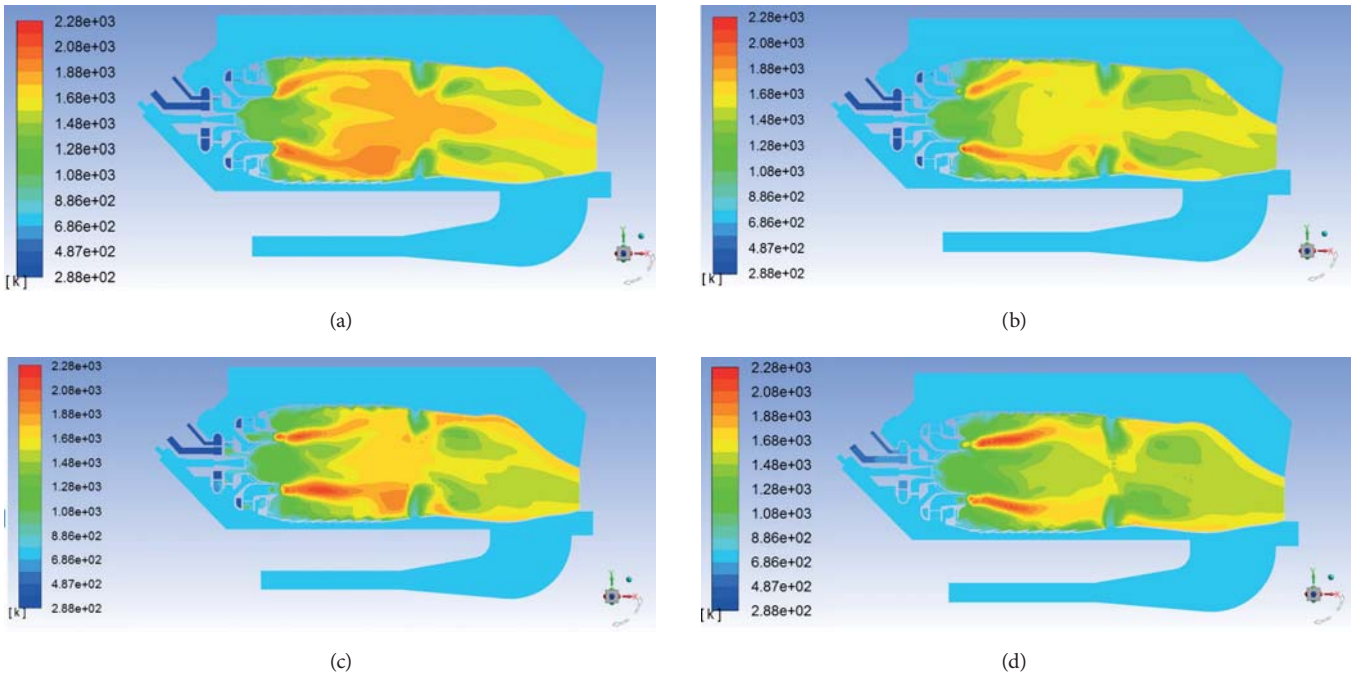


Fig. 8. Distribution of gas temperatures along the flame tube at different fuel supply modes: (a) – 1; (b) – 3; (c) – 5; (d) – 7

Fig. 9 shows the contours of the mass fractions of nitrogen oxides NO in the longitudinal section of the flame tube of the dual-fuel combustion chamber for four modes of supply of gaseous and liquid fuels. In the case of the supply of only gaseous fuel (operating mode 1), the formation of nitrogen oxides is negligible. As the amount of liquid fuel increases,

the concentrations of nitrogen oxides increase, and their maximum value is observed in the primary zone of the combustion chamber in the area of the flame front. This confirms that the main mechanism of formation of nitrogen oxides is thermal, which is determined by the maximum temperatures in the flame front.

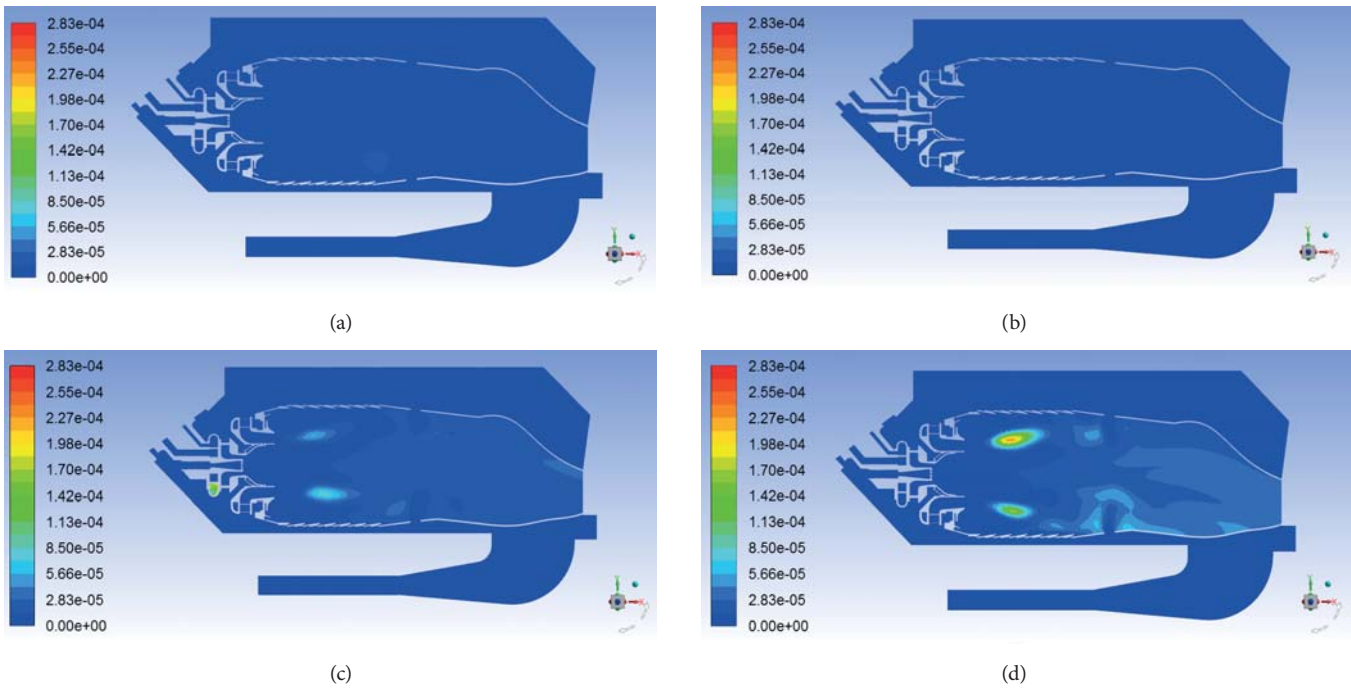


Fig. 9. Distribution of mass fraction of NO along the flame tube at different fuel supply modes: (a) – 1; (b) – 3; (c) – 5; (d) – 7

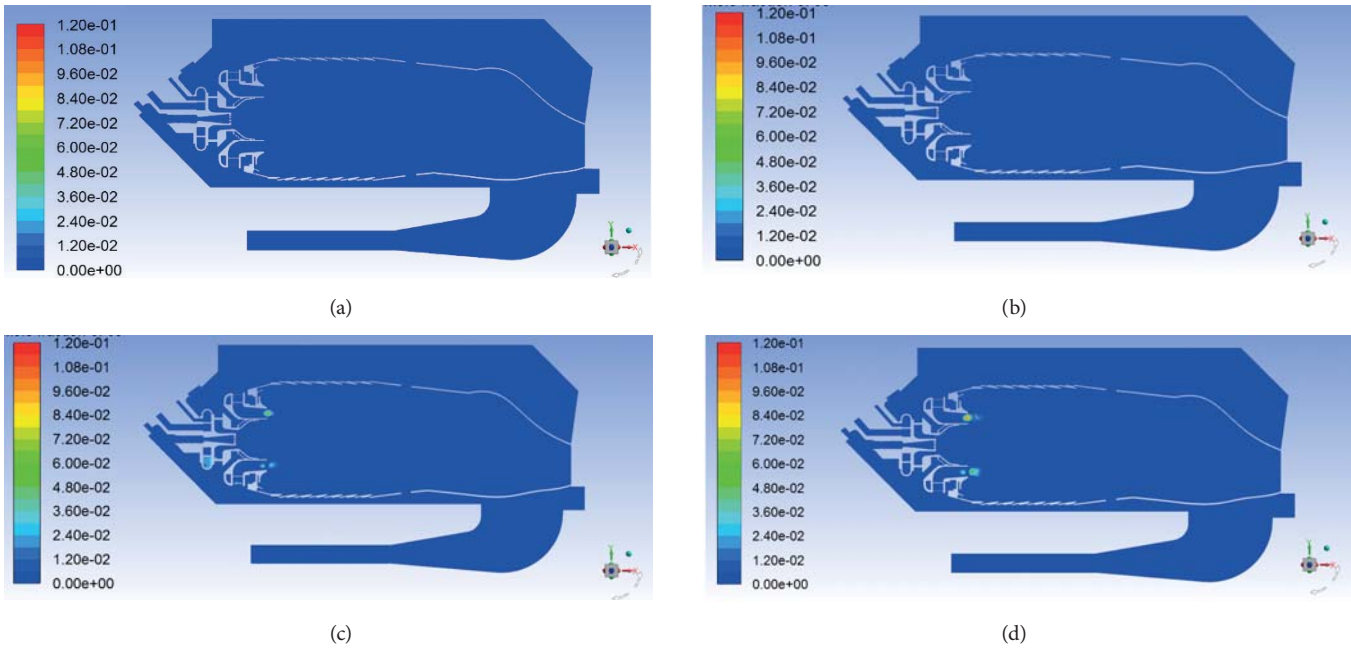


Fig. 10. Distribution of mass fraction of CO along the flame tube at different fuel supply modes: (a) – 1; (b) – 3; (c) – 5; (d) – 7

Fig. 10 shows the contours of the carbon monoxide mass fraction in the longitudinal section of the flame tube for the same modes of supply of gaseous and liquid fuels. It is seen that with the increasing amount of liquid fuel, carbon monoxide CO is mostly formed in local areas located behind the outer swirler. Later, as a result of the active chemical reaction, the CO concentrations decrease sharply.

Fig. 11 shows the calculated dependencies of the NO and CO concentrations (at 15% O<sub>2</sub>, dry basis) and the average coefficient of the temperature field non-uniformity  $\delta$  at the outlet combustion chamber's section on the fuel supply modes.

It should be noted that the coefficient of the average temperature field non-uniformity is determined by the formula

$$\delta = \frac{T_{max} - T_{min}}{T_{av}} \quad (21)$$

where  $T_{max}$ ,  $T_{min}$  and  $T_{av}$  are the maximum, minimum, and average gas temperature in the outlet flame tube's section.

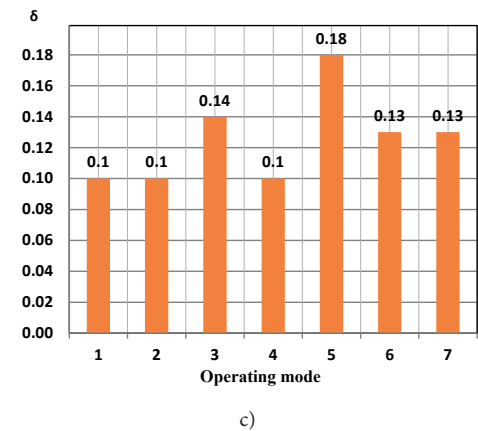
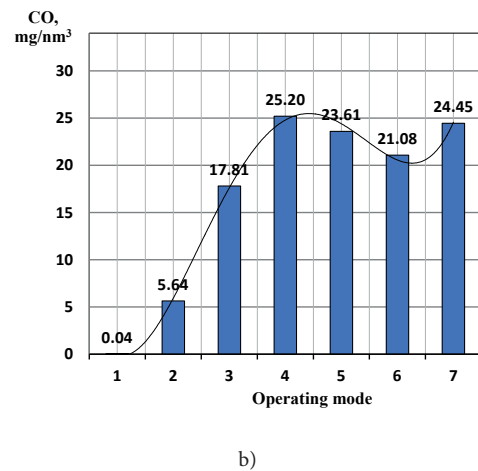
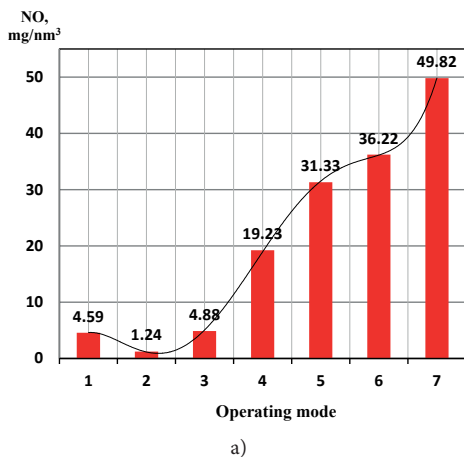


Fig. 11. Combustion chamber's outlet parameters at different fuel supply modes: (a) and (b) – NO and CO concentration at 15% O<sub>2</sub>, dry basis; (c) – coefficient of the temperature field non-uniformity

The graphic data in the diagrams of Fig. 11 show a significant dependence of the emission of toxic components on the fuel supply mode. The emission of nitrogen oxides increases monotonically with increasing liquid fuel content, while the emission of carbon monoxide in modes with a significant amount of liquid diesel fuel is stabilising. The rate of non-uniformity of the temperature field behind the combustion chamber tends to increase slightly during the transition from gaseous to liquid fuel.

The performance of a dual-fuel combustion chamber can be improved by using various combustion intensifiers, including plasma-chemical devices [34-37]. This is especially important when working on liquid fuel, when there is a need for additional stabilisation of the flame front and an increase in the rate of combustion of evaporating fuel.

## CONCLUSIONS

To sum up, the results that have been obtained in this article are as follows:

1. The distributions of temperatures, concentrations of complete combustion products, and toxic components in sections of a dual-fuel combustion chamber for a floating vessel's gas turbine when working on different modes of supply of liquid and gaseous fuels are obtained.
2. To model the process of hydrocarbons burning in a dual-fuel combustion chamber a six-step kinetic mechanism is proposed.
3. The results of mathematical modelling of the workflow processes in a dual-fuel combustion chamber are obtained. The need to use air-mechanical spray nozzles is shown, which can provide a spray spectrum of fuel droplets from 5 to 75  $\mu\text{m}$  with an average diameter of 35  $\mu\text{m}$  or less.
4. Three-dimensional modelling made it possible to identify trends in the formation of toxic components in transient combustion modes from gaseous to liquid fuel. For transient modes with a higher content of gaseous fuel, the estimated emissions of nitrogen oxides NO in the outlet cross-section of the flame tube are 1.2-4.8 mg/nm<sup>3</sup>, and carbon monoxide 0.04-18 mg/nm<sup>3</sup>. For transient modes with a higher content of liquid fuel, the estimated emissions of nitrogen oxides NO are 31-50 mg/nm<sup>3</sup>, and carbon monoxide 23-24 mg/nm<sup>3</sup>, respectively.
5. The obtained concentrations of the main toxic components of a dual-fuel gas turbine combustion chamber satisfy modern European requirements for emissions of toxic components.
6. High-quality spraying of liquid fuel provides decent overall temperature-field non-uniformity in the outlet section. Still, it could be optimised by using plasma-assisted combustion, which could be a topic for further investigation.

## REFERENCES

1. A. Duggal and J. Minnebo, 'The Floating Production, Storage and Offloading system – past, present and future', in *Offshore Technology Conference, Houston, Texas, USA, May 05, 2020*, 2020, doi.org/10.4043/30514-MS.
2. M. M. L. Reis and W. L. R. Gallo, 'Study of waste heat recovery potential and optimization of the power production by an organic Rankine cycle in an FPSO unit', *Energy Convers. Manag.*, vol. 157, pp. 409–422, 2018, doi.org/10.1016/j.enconman.2017.12.015.
3. O. Cherednichenko, S. Serbin, and M. Dzida, 'Application of thermo-chemical technologies for conversion of associated gas in diesel-gas turbine installations for oil and gas floating units', *Pol. Marit. Res.*, vol. 26, no. 3, pp. 181–187, 2019, doi.org/10.2478/pomr-2019-0059.
4. M. Aligoodarz, M. Soleimanitehrani, H. Karrabi, and F. Ehsaniderakhshan, 'Numerical simulation of SGT-600 gas turbine combustor, flow characteristics analysis, and sensitivity measurement with respect to the main fuel holes diameter', *Proc. Inst. Mech. Eng. G J. Aerosp. Eng.*, vol. 230, no. 13, pp. 2379–2391, 2016, doi.org/10.1177/0954410015625663.
5. O. Cherednichenko, S. Serbin, and M. Dzida, 'Investigation of the combustion processes in the gas turbine module of an FPSO operating on associated gas conversion products', *Pol. Marit. Res.*, vol. 26, no. 4, pp. 149–156, 2019, <http://doi.org/10.2478/pomr-2019-0077>, doi.org/10.2478/pomr-2019-0077.
6. J. A. Vidoza, J. G. Andreasen, F. Haglind, M. M. L. dos Reis, and W. Gallo, 'Design and optimization of power hubs for Brazilian off-shore oil production units', *Energy (Oxf.)*, vol. 176, pp. 656–666, 2019.
7. C. Waldhelm, 'Application of gas turbines on floater vessel for power generation service', in *ASME 1998 International Gas Turbine and Aeroengine Congress and Exhibition, Volume 2: Aircraft Engine; Marine; Microturbines and Small Turbomachinery*, 1998.
8. S. Serbin, B. Diasamidze, and M. Dzida, 'Investigations of the working process in a dual-fuel low-emission combustion chamber for an FPSO gas turbine engine', *Pol. Marit. Res.*, vol. 27, no. 3, pp. 89–99, 2020.
9. Directive 2013/39/EU of the European Parliament and of the Council, *Europa.eu*, 2008. [Online]. Available: <https://eur-lex.europa.eu/LexUriServ/LexUriServ.do?uri=OJ:L:2013:226:0001:0017:EN:PDF>. [Accessed: 05 Mar 2021].
10. S. Di Iorio, A. Magno, E. Mancaruso, and B. M. Vaglieco, 'Analysis of the effects of diesel/methane dual fuel

- combustion on nitrogen oxides and particle formation through optical investigation in a real engine', *Fuel Process. Technol.*, vol. 159, pp. 200–210, 2017.
11. S. I. Serbin, 'Modeling and experimental study of operation process in a gas turbine combustor with a plasma-chemical element', *Combust. Sci. Technol.*, vol. 139, no. 1, pp. 137–158, 1998.
  12. B. T. Diasamidze, S. V. Vilkul, and S. I. Serbin, 'Theoretical investigations of a dual-fuel low-emission gas turbine combustor', *NTU KhPI Bull. Power Heat Eng. Process. Equip.*, no. 1, pp. 27–33, 2020.
  13. C. K. Law, *Combustion Physics*. Cambridge, England: Cambridge University Press, 2010.
  14. J. Warnatz, U. Maas, and R. W. Dibble, *Combustion: Physical and chemical fundamentals, modeling and simulation, experiments, pollutant formation*, 3rd ed. Berlin, Germany: Springer, 2013.
  15. B. E. Launder and D. B. Spalding, *Lectures in Mathematical Models of Turbulence*. London: Academic Press.
  16. S. I. Serbin, I. B. Matveev, and G. B. Mostipanenka, 'Investigations of the working process in a 'lean-burn' gas turbine combustor with plasma assistance', *IEEE Trans. Plasma Sci. IEEE Nucl. Plasma Sci. Soc.*, vol. 39, no. 12, pp. 3331–3335, 2011.
  17. D. Choudhury, *Introduction to the Renormalization Group Method and Turbulence Modeling*. Fluent Incorporated, 1973.
  18. B. Magnussen, 'On the structure of turbulence and a generalized eddy dissipation concept for chemical reaction in turbulent flow', in *19th Aerospace Sciences Meeting, St Louis, MO, USA*, 1981.
  19. S. B. Pope, 'Computationally efficient implementation of combustion chemistry using in situ adaptive tabulation', *Combust. Theory Model.*, vol. 1, no. 1, pp. 41–63, 1997.
  20. F. Wang, Y. Huang, and T. Deng, 'Gas turbine combustor simulation with various turbulent combustion models', in *ASME Turbo Expo 2009: Power for Land, Sea, and Air, June 8–12, 2009, Orlando, Florida, USA, Volume 2: Combustion, Fuels and Emissions*, 2009.
  21. A. C. Benim, S. Iqbal, W. Meier, F. Joos, and A. Wiedermann, 'Numerical investigation of turbulent swirling flames with validation in a gas turbine model combustor', *Appl. Therm. Eng.*, vol. 110, pp. 202–212, 2017.
  22. Turbulence, heat and mass transfer: *Proceedings of the Seventh International Symposium on Turbulence, Heat and Mass Transfer*, ed. by K. Hanjalic, Palermo, Italy, 24-27 September, 2012.
  23. I. V. Novoselov and P. C. Malte, 'Development and application of an eight-step global mechanism for CFD and CRN simulations of lean-premixed combustors', *J. Eng. Gas Turbines Power*, vol. 130, no. 2, 2008.
  24. I. Matveev, S. Matveeva, S. Serbin, 'Design and Preliminary Test Results of the Plasma Assisted Tornado Combustor', *Collection of Technical Papers - 43rd AIAA/ASME/SAE/ASEE Joint Propulsion Conference, Cincinnati, OH, AIAA 2007-5628*, vol. 6, 2007, pp. 6091-6098.
  25. G. M. Faeth, 'Structure and atomization properties of dense turbulent sprays', *Symp. (Int.) Combust.*, vol. 23, no. 1, pp. 1345–1352, 1991.
  26. S. James, M. Anand, and S. Pope, 'The Lagrangian PDF transport method for simulations of gas turbine combustor flows', in *38th AIAA/ASME/SAE/ASEE Joint Propulsion Conference & Exhibit, Indianapolis, Indiana, USA*, 2002.
  27. G. Faeth, 'Spray combustion models - A review', in *17th Aerospace Sciences Meeting, New Orleans, USA*, 1979.
  28. W. A. Fiveland and A. S. Jamaluddin, 'Three-dimensional spectral radiative heat transfer solutions by the discrete-ordinates method', *J. Thermophys. Heat Transf.*, vol. 5, no. 3, pp. 335–339, 1991.
  29. S. I. Serbin, A. V. Kozlovskiy, and K. S. Burunsuz, 'Investigations of nonstationary processes in low emissive gas turbine combustor with plasma assistance', *IEEE Trans. Plasma Sci. IEEE Nucl. Plasma Sci. Soc.*, vol. 44, no. 12, pp. 2960–2964, 2016.
  30. I. B. Matveev, S. I. Serbin, V. V. Vilkul, and N. A. Goncharova, 'Synthesis gas afterburner based on an injector type plasma-assisted combustion system', *IEEE Trans. Plasma Sci. IEEE Nucl. Plasma Sci. Soc.*, vol. 43, no. 12, pp. 3974–3978, 2015.
  31. I. Matveev, S. Serbin, T. Butcher, N. Tutu, 'Flow Structure investigation in a "Tornado" Combustor,' *Collection of Technical Papers - 4th International Energy Conversion Engineering Conference*, vol. 2, 2006, pp. 1001-1013.
  32. S. Serbin., A. Kozlovskiy, K. Burunsuz, 'Influence of plasma-chemical products on process stability in a low-emission gas turbine combustion chamber', *International Journal of Turbo and Jet Engines*, 2021. Available from: <https://doi.org/10.1515/tjeng-2020-0046>.
  33. G. F. Romanovsky, S. I. Serbin, V. M. Patlaychuk, *Modern Gas Turbine Units of Russia and Ukraine*. Mikolayiv: NUK, 2005.

34. S. I. Serbin, I. B. Matveev, and G. B. Mostipanenکو, 'Plasma-assisted reforming of natural gas for GTL: Part II—modeling of the methane–oxygen reformer', *IEEE Trans. Plasma Sci. IEEE Nucl. Plasma Sci. Soc.*, vol. 43, no. 12, pp. 3964–3968, 2015.
35. S. I. Serbin, I. B. Matveev, and N. A. Goncharova, 'Plasma-assisted reforming of natural gas for GTL—part I', *IEEE Trans. Plasma Sci. IEEE Nucl. Plasma Sci. Soc.*, vol. 42, no. 12, pp. 3896–3900, 2014.
36. I. B. Matveev, A. A. Tropina, S. I. Serbin, and V. Y. Kostyuk, 'Arc Modeling in a Plasmatron Channel', *IEEE Trans. Plasma Sci. IEEE Nucl. Plasma Sci. Soc.*, vol. 36, no. 1, pp. 293–298, 2008.
37. I. Matveev, S. Serbin, A. Mostipanenکو, 'Numerical Optimization of the "Tornado" Combustor Aerodynamic Parameters', in *45th AIAA Aerospace Sciences Meeting and Exhibit, Reno, Nevada, AIAA 2007-391*, 2007.

## CONTACT WITH THE AUTHORS

**Serhiy Serbin**

*e-mail: serbin1958@gmail.com*

Admiral Makarov National University of Shipbuilding,  
Geroes of Ukraine, 54025 Mikolayiv,

**UKRAINE**

**Badri Diasamidze**

*e-mail: badri.diasamidze@nuos.edu.ua*

Admiral Makarov National University of Shipbuilding,  
Geroes of Ukraine, 54025 Mikolayiv,

**UKRAINE**

**Viktor Gorbov**

*e-mail: viktor.gorbov@nuos.edu.ua*

Admiral Makarov National University of Shipbuilding,  
Geroes of Ukraine, 54025 Mikolayiv,

**UKRAINE**

**Jerzy Kowalski**

*e-mail: jerzy.kowalski@pg.edu.pl*

Gdańsk University of Technology,  
11/12 Gabriela Narutowicza Street, 80-233 Gdańsk,

**POLAND**

# MINIMIZING GREENHOUSE GAS EMISSIONS FROM SHIPS USING A PARETO MULTI-OBJECTIVE OPTIMIZATION APPROACH

Zygfryd Domachowski

Gdańsk University of Technology, Poland

\* Corresponding author: [domachow@pg.edu.pl](mailto:domachow@pg.edu.pl) (Z.Domachowski)

## ABSTRACT

*To confront climate change, decarbonization strategies must change the global economy. According to statements made as part of the European Green Deal, maritime transport should also become drastically less polluting. As a result, the price of transport must reflect the impact it has on the environment and on health.*

*In such a framework, the purpose of this paper is to suggest a novel method for minimizing emissions from ships, based on so-called Pareto multi-objective optimization. For a given voyage by a ship, the problem is to minimize emissions on the one hand and minimize fuel consumption or passage time on the other. Minimizing emissions is considered as the preferred objective. Therefore, the objective of minimizing fuel consumption or passage time needs to be reformulated as a constraint. Solving such a problem consists of finding most favourable path and speed for the ship and satisfying the optimization criteria.*

*Relatively new systems such as hybrid diesel–electric systems have the potential to offer significant emissions benefits. A hybrid power supply utilizes the maximum efficiency of the direct mechanical drive and the flexibility of a combination of combustion power from the prime mover and stored power from energy storage from an electrical supply, at part load and overload.*

*A new report by the American Bureau of Shipping suggests that maritime transport is likely to meet the International Maritime Organization's target by 2030, solely by using current technology and operational measures. However, this would not be enough to attain the target of reducing CO<sub>2</sub> emissions by 2050 by at least 50% compared to 2008. New technologies and operational methods must be applied.*

**Keywords:** Minimizing emissions from ships; Pareto multi-objective optimization; Minimizing emissions as preference objective; Ship routing optimization; Hybrid power to lower emissions

## INTRODUCTION

Reducing emissions of the greenhouse gases that cause global warming should be humanity's first reaction to the threat of human-caused climate change. It is necessary for humanity to be forward-looking to take responsibility for managing the climate. This can be viewed as the responsibility to ensure that conditions are created in which life can flourish.

In such a view, the decarbonization of the global economy is commonly discussed all over the world. However, on the one hand carbon dioxide is not the only greenhouse gas. On the other hand, there are other pollutants (such as heavy metals, nitrogen and sulphur oxides and coal ash) produced

during the energy production cycle that have an impact on the environment. In many ways these are the more tangible and immediate concerns for the public. This is not the only problem, but unfortunately it is the main one.

Mitigating carbon dioxide emissions does not solve all the detrimental effects of energy production on public health and the environment.

The COVID-19 pandemic has derailed the global economy. Even if mitigation efforts are ramped up soon, they may be insufficient to prevent dangerous impacts. Therefore, society may be tempted to try to control the climate directly. This may be done only if individual states, industries and corporations are making attempts to curb the harm, recognizing past

harms and changing everything. As some have argued [1], COVID-19 has presented society with an opportunity to respond to climate change through 'planned degrowth' that prioritizes the well-being of people over profit margins.

The Paris Convention requires a significant reduction in CO<sub>2</sub> emissions to avoid global warming above 2°C. However, if no measures are taken, CO<sub>2</sub> emissions are projected to increase by between 50% and 250% by 2050 [2].

According to the European Green Deal Communication [3], transport should become drastically less polluting. Among other measures, the European Commission will take action in relation to maritime transport. The regulations should aim to accelerate the deployment of low-emission or zero-emission vessels [3]. The European Green Deal Communication also states that the price of transport must reflect the impact it has on the environment and on health. The European Commission will look closely at current tax exemptions, including those for maritime fuels. Moreover, the Commission will propose the extension of the European emissions trading system to the maritime sector. This will be coordinated with action on a global level, notably through the International Maritime Organization [4].

## PERFORMANCE CRITERIA FOR DESIGN AND OPERATION OF SHIPS' POWER PLANTS

The operating profile of ships is diverse. In spite of such diverse operating profiles, a ship's power plant has to satisfy many performance criteria, including those relating to:

1. ship safety;
2. propulsion availability;
3. manoeuvrability;
4. fuel consumption;
5. pollutant emissions;
6. comfort arising from minimal noise, temperature, vibration and smell;
7. maintenance cost; and
8. purchase cost.

From the point of view of a ship's operation, the first six criteria should be considered. The criterion of a vessel's safety prevails over all other criteria for any operation. Furthermore, the propulsion availability and manoeuvrability criteria must be satisfied to make the ship's operation possible. It should be a matter of interest that criteria relating to fuel consumption, pollutant emissions, discomfort arising from noise, vibration and smell, and maybe maintenance cost are minimized.

The aim of ship control strategies in international shipping is to reduce fuel consumption and emissions. The role of the ship's control system is to adapt the ship's power and propulsion for a specific operation. At the same time, emissions should be limited according to the International Maritime Organization regulations. Since 1997, when Annex VI to the Marpol Convention was first adopted, more and more stringent changes have limited emissions from ships.

In regard to sustaining shipping in the short term, the

ambition is to reduce total greenhouse gas emissions by at least 50% by 2050 compared to 2008 [4]. Among other measures, a reduction of ships' speed is discussed as a candidate [5].

On the one hand, the profit should be maximized by minimizing fuel consumption. On the other hand, environmental emissions should be minimized. Complying with the criterion of minimizing power production costs with merely legal constraints can make matters worse from the climate change point of view. Like most other industries, shipping prioritizes profit margins in the short term over the well-being of people. Ultimately, some of the dangerous impacts of greenhouse gases would be catastrophic for the future of the planet.

The fact of the matter is that minimizing greenhouse gas emissions and fuel consumption, and maybe discomfort arising from noise, vibration, and smell, is a set of goals representing an example of Pareto multi-objective optimization. Finding a solution to such a problem on which decision makers can agree is a topic in Multiple Criteria Decision Analysis.

## PARETO MULTI-OBJECTIVE APPROACH TO MINIMIZING GREENHOUSE GAS EMISSIONS FROM SHIPS

A multi-objective optimization problem is given, for example, by the following problem statement [6]:

minimize  $f_1(x), \dots$ , minimize  $f_m(x)$

in which  $f_1(x), \dots, f_m(x)$  are called the objective functions,  $x \in X$ , and  $X$  is called the decision space. This definition does not explicitly state any constraint functions. In practice, such functions have to be incorporated. In general,  $m > 1$ , but in practice  $m \leq 3$ , and usually  $m = 2$ . Then the goal is:  $\min f_1(x)$ ,  $\min f_2(x)$ .

Let us consider an industrial process in which, on the one hand, profit should be maximized and, on the other hand, environmental emissions should be minimized. Solving such a problem is an example of multi-objective optimization. The so-called Pareto-optimal solution refers to a solution for which there is no way of improving any one objective without degrading at least one other objective. A situation is called Pareto-optimal if no change would lead to improved satisfaction for all the objectives.

The Pareto front is the set of choices that are Pareto-optimal. The decision maker can make trade-offs within this set. Finding the Pareto front is particularly useful in engineering. It is conventionally shown graphically, which is possible for  $m = 2$  and sometimes for  $m = 3$ .

Without additional subjective preference information, all Pareto-optimal solutions are considered equally good. The goal may be to find a representative set of Pareto-optimal solutions, or to find a single solution that satisfies the subjective preferences of a human decision maker.

In the shipping industry, a Pareto multi-objective optimization problem is to minimize the greenhouse gas

emissions from a ship and minimize its fuel consumption. The last objective represents the maximization of profit.

## MINIMIZING GREENHOUSE GAS EMISSIONS FROM SHIPS

In the nineteenth century steam engines were introduced for the mechanical propulsion of ships. Driving engines developed from reciprocal steam engines and steam turbines to diesel engines and gas turbines. Nowadays, most ships use diesel engines because of their high efficiency. Moreover, mechanical propulsion is particularly efficient at the design point (between 80% and 100% of the rated speed). This is the most efficient working point of a diesel engine. It is the point of minimum fuel consumption and, for the same reason, of minimum emissions.

In addition, mechanical propulsion consists of only three power conversion stages: the main engine, the gearbox and the propeller. This leads to low conversion losses. Therefore, mechanical propulsion is mostly used for transport ships such as tankers. For such ships, over 80% of the energy is converted in the main diesel engine. Thus fuel consumption, and by the same count emissions, can best be reduced by recovering the waste heat in the exhaust gas and cooling water to generate auxiliary electrical power and heat [7].

Mechanical propulsion remains the preferred method for ships that sail at a single cruise speed most of the time, because its fuel efficiency at full load is high. Cargo ships are ships of this type.

Consider an engine that operates close to the optimal working point from a fuel consumption point of view. However, when sailing in heavy weather or under other propulsion load, disturbances can provoke an overloading of the engine. Such an off-design condition represents an increase in fuel consumption and emissions. Providing a margin of load between the propeller load and the engine load from, for example, a battery or super capacitor can reduce the increase in fuel consumption and emissions. This additional electrical power might be generated from renewable energy sources.

This is an example of hybrid propulsion, using a combination of mechanical and electrical propulsion. Hybrid propulsion can benefit from the advantages of both. In the type of hybrid power supply discussed, the mechanical part consists of the supply of combustion power from a diesel engine, gas turbine or steam turbine. The electrical part is represented by the supply of stored power from an energy storage system such as a battery or super capacitor.

Several other ship types with mechanical propulsion operate at low power in certain operating modes [7]. For example, during transit tugs (over 50% of tugs operating around the globe use mechanical propulsion) only require 20% of the maximum power they require for towing. Offshore vessels perform numerous tasks, such as transit and dynamic positioning operations; naval ships perform traditional patrol operations in open sea as well as being deployed in littoral

operations. Unfortunately mechanical propulsion has low fuel efficiency and produces high emissions at speeds below 70% of top speed. In particular, engine fuel consumption increases significantly at below 50% of the rated power. For these ship types, mechanical propulsion leads to high specific fuel consumption and high emissions.

Energy storage can provide the required electrical power and enables one or more engines to be switched off when they would be running inefficiently at part or no load. This can even enable the ship to sail temporarily without emissions. The energy storage can then be recharged when the engine is running at an operating point when less power is required. In such a situation, the specific fuel consumption and emissions are low.

Hybrid propulsion with a hybrid power supply utilizes the maximum efficiency of the direct mechanical drive and the flexibility of a combination of combustion power from the prime movers and stored power from energy storage from an electrical supply.

Batteries have only recently been used in maritime applications, but their popularity is growing very quickly.

## SHIP ROUTING OPTIMIZATION TO PLAN THE MOST FUEL-EFFICIENT PASSAGE

All ocean-going ships are required to operate all year around in different circumstances. Any ship's routing must take into account conditions such as:

1. ocean currents;
2. ocean tides;
3. ship traffic volume;
4. land obstacles on shallow waters;
5. 'piracy threats' to be avoided; and
6. forecast weather conditions.

These factors are related to the movement of the ship. Keeping the crew, cargo, and the ship itself safe and secure is the primary goal. The most favourable paths and speed profiles then have to be investigated. Any choice of them affects the efficiency of the propulsion system in terms of fuel consumption and attainable passage time. For a given ship, its motion and propulsion efficiency are strictly related to the weather conditions through which it is navigating. Thus, the ship's route optimization requires a trustworthy forecast as well as an adequate mathematical model for the ship. The aim is to be able to assess the ship's behaviour in any given sea-state.

In general, there are three criteria to be optimized: safety, passage time, and fuel consumption. These define a multi-objective optimization problem. To solve this, the Pareto method has been adopted for several years. The goal is to find the Pareto-optimal set of routes for a given voyage of the ship [8]. The resulting Pareto-optimal set of routes enables the user (the human decision maker) to choose a trade-off between the optimization goals.

Over the years a large amount of research has been dedicated to methods that are generally referred to as weather

routing. Their goal has been the development of reliable algorithms to search for the most favourable route, depending on the weather forecast. The urgent global need to reduce emissions has boosted research into advanced methods [9]. The aim is to enable strategies for the control of the ship, to improve the ship's operational efficiency.

## PRACTICAL APPLICATION OF PARETO MULTI-OBJECTIVE OPTIMIZATION TO MINIMIZING EMISSIONS FROM A SHIP

For a given voyage of a ship, the aim is to solve the problem of minimizing the environmental emissions on the one hand and maximizing the profit on the other. This is a problem of multi-objective optimization, to which it is possible to apply the Pareto method. In the shipping industry, solving such a problem consists of finding the most favourable path and speed for the ship, satisfying the optimization criteria and constraints.

### OPTIMIZATION CRITERIA FOR THE GIVEN VOYAGE OF A SHIP

The following particular criteria have to be taken into account:

1. maximizing safety; let us represent this as the relationship:  
 $f_{\text{safety index}} \rightarrow \max$
2. minimizing emissions, represented as:  
 $f_{\text{emissions}} \rightarrow \min,$
3. minimizing fuel consumption, represented as:  
 $f_{\text{fuel consumption}} \rightarrow \min$
4. minimizing passage time, represented as:  
 $f_{\text{passage time}} \rightarrow \min$
5. maximizing profit, represented as:  
 $f_{\text{profit}} \rightarrow \max.$

The safety of the ship and cargo, as well as the comfort of the passengers and crew, are paramount constraints in any ship's routing. The decision maker must choose the safety criterion in preference to any other.

The so-called safety index may be defined as having normalized values in the range 0.0-1.0. The value 1.0 means that the ship is hypothetically absolutely safe and the value 0.0 depicts a completely unstable situation.

Shipping is still largely weather-dependent, especially with regard to schedule, reliability, and control of emissions and fuel consumption. Actual hull stress and vertical or transverse accelerations influence the ship's safety and the comfort of crew. All such constraints may even determine the speed of the ship itself. Ultimately, the goal is to find a solution with which the decision maker can agree.

In a single-objective optimization, the optimal solution is usually clearly defined. However, in a multi-objective optimization the objectives can be conflicting. Therefore, instead of a single optimum, there is a set of trade-off solutions, generally called Pareto-optimal solutions. In this

paper it is assumed that in the shipping industry the decision maker is asked to make a pairwise comparison of a set of Pareto-optimal solutions. In any such pair, one objective is to minimize emissions, and the other is, in practice, to minimize fuel consumption or passage time.

Whenever fuel costs are a predominant component of operational costs, fuel consumption may be the second objective in a Pareto trade-off solution. However, when the freight rate prevails as a component of the operational costs, then passage time should be considered as such an objective in the Pareto trade-off solution.

### THE ROLE OF THE PARETO FRONT

Let us take into account a so-called space of possible solutions, also known as the feasible decision space. These solutions are typically obtained using the values of the objective functions, or they may be the results of experiments. In the problem under consideration one of the axes represents the emissions function values, and the other the fuel consumption or the passage time function values. Denoting by  $f_1$  the emissions function ( $f_1 = f_{\text{emissions}}$ ), and by  $f_2$  the fuel consumption or passage time function ( $f_2 = f_{\text{fuel consumption}}$  or  $f_{\text{passage time}}$ ), it is possible to depict the so-called Pareto front, which is a set of trade-off solutions, generally known as Pareto-optimal solutions, see Fig. 1. These solutions are optimal in the sense that no other solutions are better than them when all the objectives are considered.

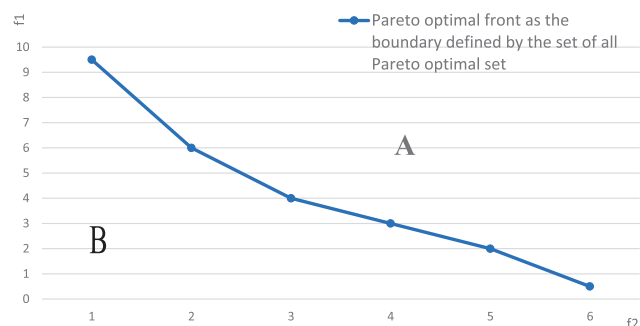


Fig.1 Graphical Depiction of Pareto-optimal Solutions

**A** – the solutions in this area are enclosed within the boundary of the decision space but are worse than the Pareto-optimal solutions

**B** – there are points that are better than the Pareto-optimal solutions, but they are outside the boundary of the decision space

The Pareto front enables the decision maker to choose a trade-off between the optimization goals. The Pareto-optimal solution refers to a situation around which there is no way

of improving any objective without degrading at least one other objective. Without additional subjective preference information, all the Pareto-optimal solutions are considered equally good. In the situation under consideration this preference information results from the goal of minimizing the environmental emissions criterion. Therefore, the objective of the preference is minimal emissions. The other objective must then be reformulated as a constraint.

### CONSTRAINTS ON THE TRADE-OFF SOLUTIONS

Generally, in practical applications, constraints have to be handled. When the fuel cost is predominant among the operational costs, then fuel consumption may be the objective that should be reformulated as a constraint. Then, for economic reasons, to satisfy a request for a minimum profit for the shipowner, the fuel consumption has to be limited.

Constraints on passage time may occur when, for example, shippers want their agricultural or perishable products shipped more quickly, or when there are scheduling or timetabling requirements for serving specific ports or meeting feeder connections [5].

A possible side effect of speed reduction, and of increasing the time for the same journey, may be that shippers are provoked to shift to other modes of transportation. If ships go more slowly, then shippers may be induced to choose road or railway alternatives, or even aircraft. This means, among other things, that a potential reduction in the ship's speed may also increase the overall greenhouse gas emissions.

### WEIGHTED SUM METHOD FOR SOLVING MULTI-OBJECTIVE OPTIMIZATION PROBLEM

Several numerical algorithms for solving multi-objective optimization problems use the so-called weighted sum method, also known as the scalarization technique. Scalarization means that the objective functions are aggregated or reformulated as constraints. It is then possible to use single-objective numerical optimization methods to find different points on the Pareto front. A simple means to scalarize the problem is to attach non-negative weights to each objective function and then to minimize the weighted sum of the objective functions. Hence, the multi-objective optimization problem is reformulated as a linear scalarization problem. In the case considered above it takes the following form:

In this way a trade-off between the two objectives is given. It can be proved that, no matter which weights  $w_1, w_2$  are chosen, the solution to the linear scalarization problem is

$$\text{minimize } f(x) = \sum_{i=1}^2 w_i \cdot f_i(x),$$

where  $x \in X, w_i \in [0, 1], \sum_{i=1}^2 w_i = 1$

on the Pareto front [6].

## CONCLUSIONS

It is enormously important to reduce the total annual greenhouse gas emissions from international shipping as soon as possible. According to a new report by the American Bureau of Shipping entitled *Setting the Course to Low Carbon Shipping – Pathways to Sustainable Shipping* and the comments on that report [10], the shipping industry is likely to meet the IMO's target of reducing CO<sub>2</sub> emissions by at least 40% by 2030, compared to the 2008 emissions, by using current technologies and operational measures.

In such circumstances a novel method of minimizing emissions from ships is suggested in this paper. It is based on so-called Pareto multi-objective optimization. A ship's operation is optimized to minimize its emissions with respect to unavoidable constraints determined by the human decision maker.

By 2050 international shipping will be dependent on fossil fuels for about 40% of its fuel requirements. On the basis of forecasts for energy consumption and trade, current technology alone will not be enough to reduce CO<sub>2</sub> emissions by at least 50% by 2050. New technologies and operational methods must be applied to find significant benefits related to the reduction of greenhouse gas emissions.

## REFERENCES

1. J. Attali, 'Non à la décroissance, oui a une tout autre economie', Les Echos, 10 October 2019.
2. IPCC (Intergovernmental Panel on Climate Change), 'Special report on the impacts of global warming of 1.5°C'. <https://www.ipcc.ch/sr15/download/> (access 28.02.2021).
3. EU, 'Communication on The European Green Deal', 11 December 2019. [https://ec.europa.eu/info/publications/communication-european-green-deal\\_en](https://ec.europa.eu/info/publications/communication-european-green-deal_en) (access 28.02.2021).
4. IMC. International Convention for the Prevention of Pollution from Ships (MARPOL), Annex VI. <http://library.arcticportal.org/1699/> (access 28.02.2021).
5. H.N. Psaraftis, 'Speed optimization vs speed reduction: The choice between speed limits and a bunker levy', Sustainability. 2019, 11, pp. 3-18.
6. M.T. Emmerich and A.H. Deutz, 'A tutorial on multi-objective optimization: Fundamentals and evolutionary methods', Natural Computing. 2018, 17, pp. 585-609.
7. R.D. Geertsma, R.R. Negenborn, K. Visser, and J.J. Hopman, 'Design and control of hybrid power and propulsion systems for smart ships: A review of developments', Applied Energy. 2017, 194, pp. 30-54.

8. J. Szlapczynska, 'Multi-objective weather routing with customized criteria and constraints', *The Journal of Navigation*. 2015, 68(2), pp. 338-354.
9. M. Zyczkowski, J. Szlapczynska, R. Szlapczynski, 'Review of weather forecast services for ship routing', *Polish Maritime Research*. 2019, 4(104), pp. 80-89.
10. G. Plevrakis, 'Setting the course to low-carbon shipping', *Maritime Reporter and Engineering News*. June 2020.

#### **CONTACT WITH THE AUTHOR**

**Zygfryd Domachowski**

*e-mail: domachow@pg.edu.pl*

Gdańsk University of Technology

Narutowicza 11/12

80-233 Gdańsk

**POLAND**

# REVIEW OF RESEARCH RESULTS CONCERNING THE MODELLING OF SHIPPING NOISE

Xiaowei Yan<sup>\*1)</sup>

Hao Song<sup>1)</sup>

Zilong Peng<sup>2)</sup>

Huimin Kong<sup>2)</sup>

Yipeng Cheng<sup>2)</sup>

Linjiang Han<sup>2)</sup>

<sup>1)</sup> Systems Engineering Research Institute, China

<sup>2)</sup> Jiangsu University of Science and Technology, China

\* Corresponding author: yanxwseri@163.com (X. Yan)

## ABSTRACT

*The effect of underwater radiated noise (URN) pollution (produced by merchant ships) on marine ecology has become a topic of extreme concern for both the academic community and the general public. This paper summarises some research results and modelling about shipping noise published over several decades, which comprises the research significance of low-frequency ambient noise and shipping noise, shipping noise source levels (SL), empirical models and the measurement standards of shipping noise. In short, we try to present an overall outline of shipping noise and ocean ambient noise for related research.*

**Keywords:** shipping noise, noise source level model, measurement standard, ocean ambient noise

## INTRODUCTION

The National Research Council [1] states that it is an important research task to evaluate the effect of man-made noise and natural noise on overall ambient marine noise and to study the long-term trend of ambient noise levels. The prosperity brought by industrialisation and the shipping industry since the middle of the 19<sup>th</sup> century has led to increasing levels of ambient noise, which was predicted to continue to increase in recent years, but there is a lack of sufficient evidence. Studies have shown that noise from different ship classes greatly increase the level of ambient marine noise, at frequencies of 25 Hz~16 kHz with a horizontal distance of 60 m~1 km [2]. Ross [3] analysed noise levels

measured in the mid-20<sup>th</sup> century and pointed out that the low-frequency noise was increasing at an average growth rate of 0.5 dB/year. It was later proved, by the measured data, that this growth rate was actually closer to 0.2 dB/year [4]. Some recent measurements by Andrew *et al.* in the northeast Pacific Ocean indicate a slight decrease [5].

In recent years, with the extensive usage of vibration and noise control technology in submarines, both their radiated noise and the target strength (TS) were significantly reduced, which greatly increases detection difficulty for active or passive sonars. Although some acoustic stealth techniques can reduce the target strength and radiated noise level (RNL) at medium-high frequencies, it seems to have no significant effect at low frequencies, below several hundred Hertz [6]. Some of the

measured data indicates that 90% of the noise below 300 Hz radiated from submarines or merchant ships is abundant, with strong tones and instantaneous signal components, which are of great significance for the identification and tracking of submarines or merchant ships. Therefore, low-frequency acoustic detection will be an important trend, especially for long-range detection, and some new challenges will also be brought. One of the bottlenecks is the basic research on the low-frequency ocean ambient noise field, at present there is still a lack of more scientific theories and effective methods.

As indicated in Wenz' classical deep-sea ambient noise spectrum [7], the low-frequency ambient noise is generated by widely distributed, multiple and complex sources including wind noise, merchant ships, crustal movements, ocean turbulence and human industrial activities, etc. These noise sources are the main disturbance for the active and passive sonars. Meanwhile, they also provide important shelter for submarine and unmanned underwater vehicles (UUV), to achieve stealth activities. The low-frequency acoustic waves, no higher than several hundred Hertz but higher than the cut-off frequency for certain depths of ocean channel, can travel long distances with relatively little attenuation [8]. Thus, for a certain receiving point in the ocean, there are abundant contributory sources from low-frequency ambient noise fields with a large distribution range [9]. Due to the diversity and distribution of the noise sources in different sea areas, the spectral components of low-frequency, ambient noise are more complex than those at medium-high frequencies.

The shipping noise and the wind noise are dominant at low frequencies, and their proportion mainly depends on the busyness of routes as well as wind intensity. The shipping noise presents great variability in both space and time, of which the spatial variability mainly depends on the distribution of routes and the time variability mainly depends on the time arrangement of shipping operations. Shipping noise has a great influence on the spatial distribution of low-frequency ambient noise, for example, the vertical directivity of the noise field shows 'groove' characteristics in the deep sea [10-11].

In the present paper, we intend to provide an appraisal of some measurements and modelling of shipping noise. It is considered by the authors that such a review will be of value to developing the subject of shipping noise as an introduction to the field, consolidating the literature on this topic which is spread among ambient ocean noise and underwater acoustic journals. The paper is structured as follows: (2) a description of the research significance of shipping noise, (3) an overall review of the research work on shipping noise, (4) a summary and analysis of empirical source level models, collected from some published papers and reports and compared, and (5) a collection of standards and methods for the measurement of shipping noise.

## THE RESEARCH SIGNIFICANCE OF SHIPPING NOISE

In the published academic papers and scientific reports, there are nearly ten models for modelling the shipping noise, and at least seven models nominally can predict shipping noise under 100 Hz, but needs more measured data to verify their accuracy. Some comparison results of some measured data and predictions using the above models are presented, and the SL obtained from underwater noise radiated from four cargo ships observed in the area of the East China Sea [12,13]. Table 1 summarises the design and operational conditions for the transiting ships. The SLs of transiting ships listed in Tab.1 are predicted using several empirical models (Urick model [14], Ross model [15], W&H model [16] and RANDI-3 model [17]), and the measured SLs are the combination of received level (RL) and transmission loss (TL) estimated using Normal Modes or Ray Method combining with the realistic geoacoustic parameters and sound speed profile (SSP), that is  $SL=RL+TL$ , and the estimations and measurements of these four merchant ships are presented in Fig. 1.

Tab. 1. Summary of commercial ship characteristics

Ship type	MMSI	Length/ Draught (m)	Speed (kt)	Range at CPA (m)	Measured date
Bulk carrier	412378670	173.0/7.0	9.1	806.7	Jan., 2015
Container ship	372748000	140.0/8.0	13.8	617.7	Feb., 2015
Bulk carrier	413794000	140.0/4.5	9.1	855.3	Mar., 2015
Container ship	412499000	136.0/7.6	7.5	1122.6	Apr., 2015

As illustrated in Fig. 1, even for the same ship, the predictions with Ross model, W&H model and Urick model are different (the maximum difference is ~ 20 dB), not to mention how consistent are these predictions with the measured results. Measured SLs above 100 Hz decreased approximately with  $-N \lg f$ , and N is about 16.6~32.5. But for the frequencies below 100 Hz, the frequency dependency of source level is not monotonous and relatively complicated. In general, there is a significant hump whose shape, position and level will be influenced by the shipping speed as shown in measured results by U.S. Surface Warfare Center in Fig. 2 [18]. Although the trends of the measured results above 100 Hz are basically consistent with those of the empirical models, there is still a great gap in levels.

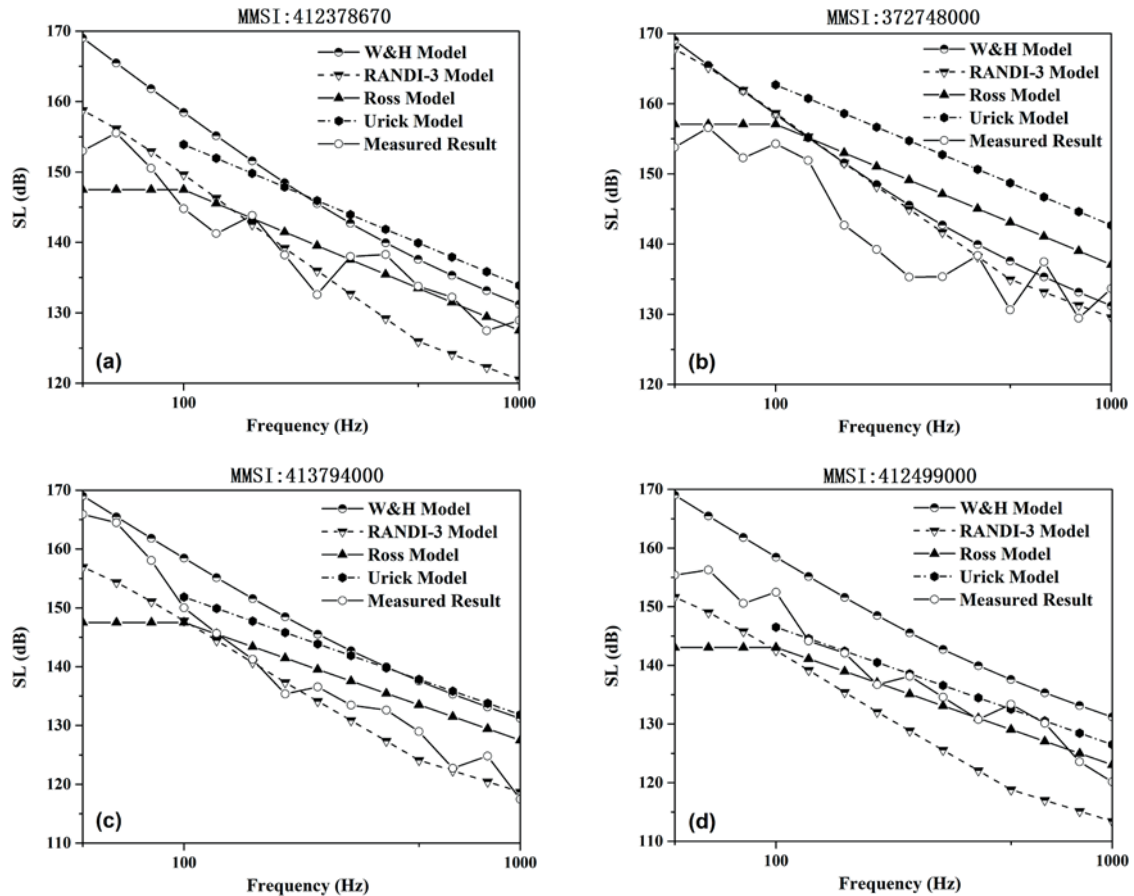


Fig. 1. Comparisons between estimations and measurements of selected ships [11,12]

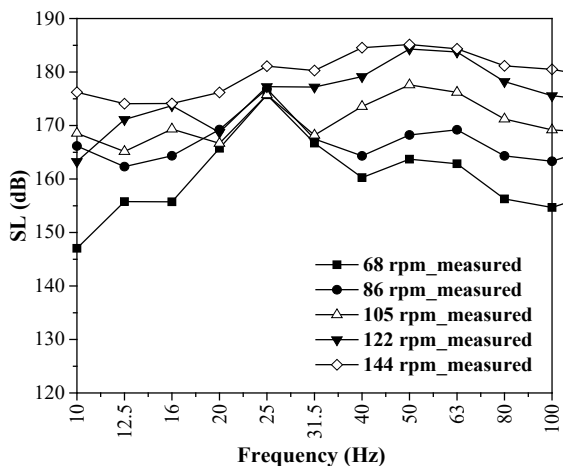


Fig. 2. Source level of cargo ship "Ov. Harriette" measured by U.S. Navy [17]

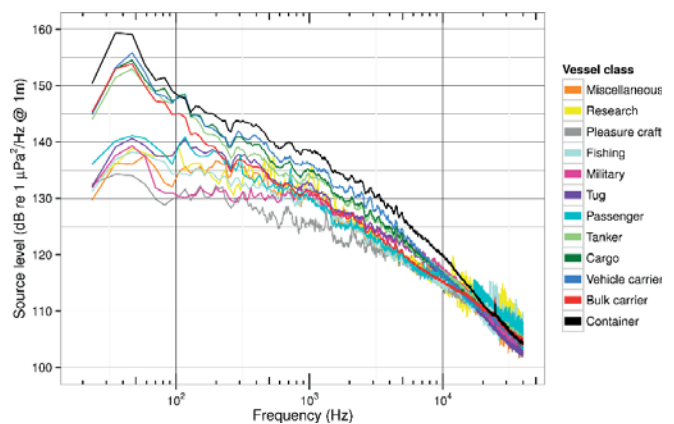


Fig. 3. Median source spectra of ship noise for different classes of ships [18]

Furthermore, the median SLs of different ship types are also different greatly. Scott Veirs *et al.* [19] estimated underwater sound pressure levels for 1,582 unique ships that transited the core critical habitat of the endangered Southern Resident killer whales during 28 months in Haro Strait (WA, USA), and presented the median source spectra of ship noise for different classes of ships as illustrated in Fig. 3.

## AN OVERALL REVIEW ON THE RESEARCH WORKS OF SHIPPING NOISE

The research on the spectrum level of ambient noise was started during the World War II. A vast amount of measured data and theoretical results were classified. The wartime research was summarised by Knudsen [20]. After the war, a graphical or schematic deep-sea noise spectrum

was published by Wenz [7], and some efforts on the shallow-sea noise spectrum were made by Piggot [21]. Ross [15] and Urick [14] analysed the measured noise data of merchant ships and warships during World War II, respectively, and finally some empirical SL models of merchant ships and warships were summarised dependent on the shipping speed and ship length.

There are almost nine kinds of ship source level models published so far [14-17, 22-27], which can be roughly categorised into two groups, according to modelling mechanism. One model tries to establish the fitting relationship between SL and ship speed, ship length (or tonnage) and frequency from the statistical law of amount of measured data, and the others emphasise the noise-generated mechanism, namely the superposition of mechanical noise, propeller cavitation noise and non-cavitation noise, as illustrated in Table 2.

Tab. 2. Comparison of URN models of merchant ship

Model	Urlick	Ross	W&H	RANDI-2 RANDI-3	ANATRA	Wittekind	AQUO project	Three parameters	Lurton
Speed/length	√	√	×	Depending on the type of ship	×	√	√	×	×
Ship types	Passenger ships	Merchant ships	Merchant ships	Super Cruises, Large Cruises, Cruises, Merchant Ships, Fishing Vessels	Noise (quiet, Standard noisy)	Merchant ships	Merchant ships	Merchant ships (Adjustable pitch propeller)	Merchant ships
Fitness <100(Hz)	×	×	√	√	√	√	√	√	√
Modelling Mechanism	Statistics Regulation	Statistics Regulation	Statistics Regulation	Statistics Regulation	Statistics Regulation	Noise Mechanism	Noise Mechanism	Statistics Regulation	Statistics Regulation

Although there are already many models of shipping noise, some problems still exist. At first, almost all the models cannot predict low-frequency shipping noise below 100 Hz very well. Secondly, as pointed out by Yvan Simard [28], these models were established on insufficient measured data over ten years and cannot predict data for newly-built larger merchant ships worldwide. Gaggero [29] also compared the predictions using these models and the measured results. Thirdly, although both the AQUO project's model and the Wittekind's model are based on the noise mechanism [23, 30], the related parameters and modelling conditions are not easy to obtain. For the AQUO project's model, three main noise sources are assumed as functions of frequency and speed (at least two different speeds are required), which are difficult to obtain during the measurement of non-cooperative ships [24]. The required parameters in the Wittekind's model are much more detailed, whether the main engine is equipped with a vibration isolator is even considered.

The SL models and noise regularity must rely on a large amount of accurately measured data. Some organisations, such as ASA (Acoustical Society of America), DNV (Det Norske Veritas), ICES (International Council for the Exploration of the Sea) and ISO (International Organization for Standardization), have made a series of measurement standards or restriction standards for the URN of merchant ships [31-34]. In addition, some experts [35-37] pointed out that all the SLs of merchant ships can be categorised into

monopole source level and dipole source level (equivalent source level). The dipole source level is the most commonly used type, the significant differences between them being whether the Lloyd mirror effect of the sea surface is taken into consideration, which must be given enough attention when comparing the SLs of different ships in different publications [35].

As early as the low-frequency acoustic propagation international conference held in 1970s, the U.S. Navy initiated a new project to measure the narrowband noise of merchant ships, which aimed to develop a parametric noise model of surface ships. Supported by the U.S. Navy, the noise of the transportation ship, Ov. Harriette, was measured in 1980 [18] and this was recognised as being a considerably accurate measurement. The measurement system was deployed in the TOTO area of the Bahamas with a depth of 1,830 m.

The noise data showed that high levels are attributed to service diesel generators, marine engines and cavitation blades of the propeller; the low-frequency noise radiation usually appears as a dipole pattern.

Since the 1990s, research on shipping noise has already become one of the major subjects in the international acoustic community. One of the probable reasons is that the impact of man-made noise on the marine environment has attracted more attention from supervision departments, which can be well accounted for by the content of shipping strategy framework guidance [38]. In almost all the busy shipping channels and areas worldwide, noise measurements have been made: the Mediterranean [16, 39], the North Atlantic near Europe [39], the southern Baltic [40], the ocean around the United States [41], Canada [42] and the northern Indian ocean [43]. In recent years, there has been some published research on shipping noise in the Arctic Ocean [44].

Scrimger *et al.* [39] measured the radiated noise of 50 merchant ships passing through the sea near Genoa. The measured median spectrum level and its shape in the range of 70~700 Hz were roughly consistent with the classical Ross model. In the Mediterranean Sea and the East Atlantic Ocean, Wales *et al.* [16] measured the noise at 30~1200 Hz, radiated from 272 merchant ships and obtained the median spectral level. Mckenna and Ross [41] measured the radiated noise of 593 container ships near the Santa Barbara Channel and studied the impact on the radiated noise of ship shape

lines, operational configurations and sea states. Among these measured ships, bulk carriers have higher SLs near 100 Hz, while the highest levels of container ships and tankers present at frequencies below 40 Hz, which accounts for the influence of different ship classes on the SLs. By taking measurements on the 1,363 voyages of ships with AIS passing through Puget Sound, Bassett *et al.* [45] indicated that cargo ships contribute the most to the noise field, followed by tugboats and passenger ships. Coward *et al.* [42] made a measurement of a small cargo ship in the shallow waters of the Oslo Fjord and modified its SL to monopole form with the RAM transmission model. Roth [44] measured the underwater radiation noise of an icebreaker in the Arctic Ocean, which showed that the radiation noise of 20 Hz~2 kHz increased by nearly 10 dB during icebreaking work. Trevorrow *et al.* [46] measured the radiated noise of a small, single-screw oceanographic vessel and studied the variation rule of shipping noise under manoeuvring conditions, such as steering. Gaggero *et al.* [47] developed a post-processing software tool capable of processing the output data of the vertical array, which provided some information such as vertical directivity and horizontal directivity of the underwater radiated noise from transiting ships. Grelowska *et al.* [48] carried out experimental research on the underwater noise radiated from a small ship using classical propulsion and identified the main sources. In 2016, Simard *et al.* [28] carried out shipping noise measurement in the St. Lawrence channel, to a depth of 350 m, and obtained the source spectrum levels of 255 merchant ships. The predicted source spectral levels were sensitive to the transmission loss models. In 2018, Zilong Peng *et al.* [49] made extensive measurements on the URN of a small fishing boat in the South China Sea, to 87 m depth, and proposed a predictive model to be applied to a typical fishing boat.

In recent years, with the support of the European Union, several large cooperative research teams (SILENV (Ship Innovative soLutions to rEduce Noise and Vibrations) project [50], AQUO (Achieve QUIeter Oceans) project [30,51-56], SONIC (Suppression Of underwater Noise Induced by Cavitation) project [38,57], and the MEPF (Marine Environment Protection Fund) project [58]) have carried out a large number of studies on shipping noise in European waters [59]. The AQUO project [30] can be divided into three stages: URN modelling of noise sources; noise mapping of merchant ships in specific sea areas; assessment of the impact of shipping noise on marine mammals. This project produced a series of reports and papers, which are an important reference for the research of shipping noise.

On the basis of SL empirical models, Hamson [60], Etter [61], Anon [62], Courtois [63], Colin [64], Audoly [65], Aulanier [66], Jones [67], Folegot [68], Soares [69], Erbe [70], Sertlek [71], and Buszman [72,73], devoted studies to the noise field produced by merchant ships in specific sea areas. Ainslie [35] and Carey [9] introduced the noise mapping of merchant ships in *Principles of Sonar Performance Modelling* and *Ocean Ambient Noise Measurement and Theory*, respectively. Kozaczka and Grelowska [74, 75] carried out an assessment of a range of acoustic disturbances generated by a ship sailing

in shallow seas and developed a new, complex system for improving the security of the maritime infrastructure by means of many methods of observation, including acoustical methods in water.

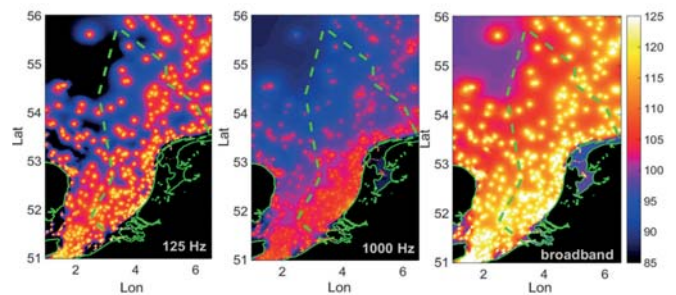


Fig. 4. Sound maps for the isovelocity case. Ship source depth is 5 m. The wind generated sound is added to all maps [71]

## A SUMMARY OF EMPIRICAL SOURCE LEVEL MODELS

Table 2 lists some of the SL empirical models. Their specific expressions, applicable conditions and the relations between these models are systematically sorted and summarised here. It should be noted that the ‘three-parameter’ model [25, 26] is not included here as it mainly deals with the adjustable pitch propeller used in a portion of current merchant ships. The basic relationships of the other SL models are shown in Fig. 5. In the dashed box, the AQUO project’s model and the Wittekind’s model are the representative SL models, based on a noise-generated mechanism. Among these models, the Wittekind’s model was proposed earlier and it is the most complex model which takes some detailed ship parameters into consideration.

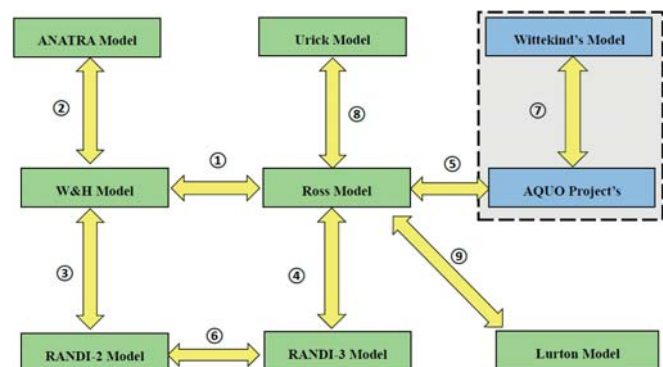


Fig. 5. Basic relationships of SL empirical models

## THE INTRODUCTION OF EMPIRICAL SOURCE LEVEL MODELS

### (1) Ross model

Ross [15] concluded several formulas for estimating the radiated noise of merchant ships in his classic publication

*Mechanics of Underwater Noise.* He summarised the relationship between total sound pressure level (SPL) and the speed of ships within 8 ~ 24 kt during World War II. At frequencies above 100 Hz, the average curve fitting equations drawn (based on these data) are listed as follows,

$$SL(f) = 190 + 53\lg(U_a/10kt) - 20\lg f, \quad (1)$$

$$SL(f) = 199 + 53\lg(U_a/15kt) - 20\lg f$$

where  $U_a$  is the speed (kt) and  $f$  is the frequency (Hz). In the above formula, the average SL of different ships deviates from the average curve by about  $\pm 4$  dB. Gaggero [76] called the first expression in Eq. (1) the Ross Speed model (R-S model).

In addition, Ross also derived several formulas for tonnage,

$$SL(f) = 132 + 50\lg(U_a/10kt) + 15\lg DT - 20\lg f, \quad (2)$$

$$SL(f) = 154 + 60\lg(U_a/10kt) + 9\lg DT - 20\lg f$$

where  $DT$  is vessel tonnage (t). Both formulas gave similar results for ships during World War II. However, the displacements of modern supertankers have increased by more than 20 times and, for ships of this size, the SL difference predicted by these two formulas is as large as 10 dB. As a result, these formulas are not suitable for vessels exceeding 30,000 tonnes. Gaggero [76] called the first expression in Eq. (2) the Ross Tonnage model (R-ST model). At the same time, these formulas only apply to spectral levels above 100 Hz, the part below 100 Hz is generally considered to be flat.

In addition, Ross [15] believed that the cavitation noise power of the propeller is proportional to the total number of cavitation blades and propeller diameter. When studying shipping noise during World War II, for large ships, it was found that the average trend was significantly related to blade tip velocity  $U_t$  and blade number  $B$ , but had nothing to do with other quantities. For ships with a length of more than 100 m (blade velocity range of 15 ~ 50 m/s), the SL can be expressed as follows:

$$SL(f) = 195 + 60\lg\left(\frac{U_t}{25}\right) + 10\lg\left(\frac{B}{4}\right) - 20\lg(f) \quad (3)$$

### (2) Urick model

Urlick [14] obtained the following fitting formula, according to 157 voyages of 77 ships of 11 different types, most being cargo ships, tankers and large warships:

$$SL = 51\lg V + 15\lg T - 20\lg f_{kHz} + 20\lg D - 13.5 \quad (4)$$

where  $V$  is the velocity of propeller blade tip (ft/s),  $T$  is the displacement of the vessel (ton),  $f_{kHz}$  is the frequency (kHz), and  $D$  is the distance (yards). It should be noted that the predicted results of the above formula have a standard deviation of 5.4 dB with individual measured values, which

is only applicable when the propeller cavitation is the main noise source above 1 kHz.

When the speed of the propeller blade is unknown, a more convenient formula for calculating spectral level with ship speed can be used,

$$RNL(f) = RNL_{1K} - 20\lg\left(\frac{f}{1000}\right) \quad (5)$$

where  $K$  is the speed (kt). This formula is consistent with the measurement level of passenger ships, transport ships and warships at 5 kHz, with a standard deviation of 5.5 dB, but not applicable to cargo ships and tankers.

### (3) Lurton model

In his book *An introduction to underwater acoustics: principles and applications*, Lurton [8] presented a simplified version of the Ross empirical model. There are two key parameters in the description of shipping noise level, i.e. the noise level at 1 kHz ( $RNL_{1k}$ ) and the average or highest level of line spectrum at low frequencies below 100 Hz ( $RNL_{sl}$ ). The low-frequency noise spectrum below 100 Hz is considered to be flat. The radiated noise levels above 100 Hz can be expressed as follows:

$$RNL(f) = RNL_{1K} - 20\lg\left(\frac{f}{1000}\right) \quad (6)$$

### (4) W&H model

By measuring the shipping noise in the Mediterranean Sea and the Eastern Atlantic Ocean, Wales and Heitmeyer [16] gave the average SL in the frequency range of 30~1200 Hz. The SLs in other frequency bands were obtained by interpolation, and the expression is:

$$\bar{S}(f) = 230 - 35.9\lg f + 9.17\lg\left(1 + \left(\frac{f}{340}\right)^2\right) \quad (7)$$

### (5) ANRTRA model

In 1980-1990, the French CERDSM research centre measured the noise data from 167 ships using sonobuoys. The SLs of all ships can be categorised into three levels: quiet, standard and noisy, i.e. the so-called ANATRA model [27]. The three types of source levels are defined as follows:

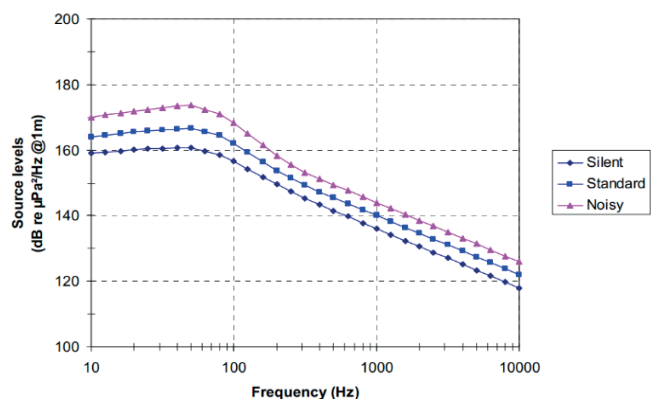


Fig. 6. URN patterns of merchant vessels for use in the ANATRA model [27]

**(7) RANDI-2 model**

The RANDI-2 [17] model was developed by the U.S. Naval Research Laboratory on the basis of the W&H model and Ross model. The specific expression is given as follows:

$$SL = Sv(f) + 60 \lg\left(\frac{v}{12}\right) + 20 \lg\left(\frac{L}{300}\right) \quad (8)$$

where  $Sv(f)$  is given by the W&H model.  $L$  and  $v$  are ship length (ft) and ship speed (kt), respectively.

**(8) RANDI-3 model**

On the basis of the RANDI-2 model, Breeding [17] made a further improvement. The ship length and the speed can be described by a uniform random distribution function and ships can be divided into five categories, according to length and speed: fishing boat, merchant ships, tankers, large tankers and super large tankers. The expressions are:

$$L_s(f, v, l_s) = L_{so}(f) + 60 \lg\left(\frac{v}{12}\right) + 20 \lg\left(\frac{L}{300}\right) + df \times dl + 3.0 \quad (9)$$

and

$$df = \begin{cases} 8.1, & 0 \leq f \leq 28.40 \\ 22.3 - 9.77 \lg f, & 28.4 \leq f \leq 284.0, \quad dl = l_s^{1.15} / 3643.0 \\ 0, & f > 191.6 \end{cases} \quad (10)$$

The expression of the average SL is

$$L_{so}(f) = \begin{cases} -10 \lg(10^{-1.06 \lg f - 14.34} + 10^{3.32 \lg f - 21.425}), & f < 500\text{Hz} \\ 173.2 - 18.0 \lg(f), & f > 500\text{Hz} \end{cases} \quad (11)$$

**(8) Wittekind's model**

Wittekind [23] was the first to attempt to model shipping noise according to noise-generating mechanisms. Shipping noise can be made up of low-frequency propeller cavitation noise, medium-high frequency propeller cavitation noise and medium-frequency diesel engine noise. By establishing a connection between some primary parameters influencing the shipping noise (displacement, critical speed of cavitation, block coefficients, mass of main engine and whether the main engine is installed elastically) and three major underwater radiation noise sources, the total source level is given by

$$SL = 10 \lg\left(10^{\frac{F_1}{10}} + 10^{\frac{F_2}{10}} + 10^{\frac{F_3}{10}}\right) \quad (12)$$

where  $F_1$ ,  $F_2$  and  $F_3$  are the low-frequency cavitation noise, medium-high frequency cavitation noise and diesel engine noise, respectively.

According to the work by Arveson and Vendittis, Wittekind [23] believed that the low-frequency noise component should be a function of speed, square coefficient and ship dimension,

$$F_1 = 2.2 \times 10^{-10} f^5 - 2 \times 10^{-7} f^4 + 6 \times 10^{-5} f^3 - 8 \times 10^{-3} f^2 + 0.35 f + 125 + A + B, \\ A = 80 \lg((v/v_{cIS}) \cdot 4 \cdot c_B), B = 10 \lg(\Delta/\Delta_{ref})^{2/3} \quad (13)$$

where  $A$  is the coefficient factor about the shipping speed and the square coefficient.  $B$  and  $c_B$  are the displacement factor and the square coefficient, respectively.  $v$  and  $v_{cIS}$  are the speed (kt)

and the cavitation critical speed (kt), respectively.  $\Delta$  and  $\Delta_{ref}$  are displacement and reference displacement, respectively.

The medium-high frequency propeller noise can be expressed as follows:

$$F_2 = -5 \ln(f) - \frac{1000}{f} + 10 + B + C, \quad C = 60 \lg\left(\frac{1000 c_B v}{v_{cIS}}\right) \quad (14)$$

where  $C$  is another coefficient factor about the shipping speed and the square coefficient.

The medium-frequency diesel engine noise can be expressed as follows:

$$F_3 = 10^{-7} f^2 - 0.01 f + 140 + D + E, \quad D = 15 \lg(m) + 10 \lg(n) \quad (15)$$

where  $D$  is the simulation factor about the mass and the number of main engines.  $E=0$  means elastic installation for the main engines and  $E=15$  means rigid installation for the main engines.  $m$  and  $n$  are the mass ( $t$ ) and the number of main engines.

**(9) AQUO project's model**

The AQUO project's model [24] fully draws lessons from the Wittekind's model and Ross model but is different, in that the AQUO project's model takes into account the propeller non-cavitation noise. Audoly *et al.* believed that the shipping noise source mainly includes the mechanical noise, propeller non-cavitation noise and cavitation propeller noise. The total source level can be expressed as follows:

$$SL_t(f, V, L) = 10 \lg\left(10^{SL_{mach}(f, V, L_{ref})/10} + 10^{SL_{prop}(f, V, L_{ref})/10} + 10^{SL_{cav}(f, V, L_{ref})/10}\right) + 25 \lg(L/L_{ref}) \quad (16)$$

where each term can be expressed in terms of speed  $V$  (kt) and frequency  $f$  (Hz).  $L$  is the ship length (m) and  $L_{ref}$  is the referenced ship length (m). Finally, 17 unknowns are determined by matching the measured data with the prediction formula.

**THE RELATIONSHIPS AMONG THESE EMPIRICAL SL MODELS**

**(1) Relationship ① between the Ross model and W&H model**

The W&H model gives the average SL and its variation rule is only related to frequency  $f$ , while the Ross model gives an expression about ship speed, tonnage and frequency. Assuming that the average speed and the average tonnage are known, the Ross model can be degenerated into an average SL. Different from the Ross model, the effective frequency range of the W&H model is 30 ~1200 Hz and the SL at other frequencies are obtained by linear interpolation.

**(2) Relationship ② between the W&H model and ANATRA model**

The ANATRA model gives three different definitions of the SL of merchant ships: quiet, standard and noisy. However,

unlike the W&H model, the ANATRA model lacks a specific expression, only presenting several average SL curves.

### (3) Relationship ③ between the W&H model and RANDI-2 model

The RANDI-2 model completely adopts the average SL spectrum of the W&H model as  $S_v(f)$ . Therefore, the W&H model is a degenerated form of the RANDI-2 model and the RANDI-2 model also absorbs the rules of the Ross model on ship speed and ship length.

### (4) Relationship ④ between the Ross model and RANDI-3 model

Here we adopt the Ross tonnage model (R-ST model) in the second expression of Eq. (2). There is a certain relationship between ship length and tonnage,  $DT = 10^{-2.1}L^{2.96}$ . Thus the Ross formula can be completely transformed into an expression about the ship length  $L$  (m),

$$SL = 154 + 60\lg(v/10) + 9\lg(DT) - 20\lg f = 75.1 + 60\lg v + 27\lg L - 20\lg f \quad (17)$$

For the RANDI-3 model, the frequency band above 500 Hz is first investigated with the expression:

$$SL = 72.2 + 60\lg v + 20\lg L - 18\lg f \quad (18)$$

It should be noted that the ship length  $L$  is converted into metres.

By comparing Eq. (17) with Eq. (18), it can be found that the Ross model and RANDI-3 model can be converted to completely similar forms for the frequencies higher than 500 Hz, but the coefficients will be different. The SL predictions of the merchant ship with an assumed length of 100 m, at 1 kHz, will have a discrepancy of 10.9 dB using the two models.

Secondly, for the frequencies of 100~500 Hz, the RANDI-3 model has a relatively complex expression and only  $L_{SO}$  is considered here:

$$L_{SO}(f) = -10\lg(10^{-1.06\lg f - 14.34} + 10^{3.32\lg f - 21.425}) \quad (19)$$

$$= -10\lg[10^{3.32\lg f - 21.425}(10^{-4.38\lg f + 7.08} + 1)] \approx -33.2\lg f + 214.3$$

Although the initial form is non-linear, with respect to the logarithmic frequency, it can still be converted to a linear expression, which will be consistent with the Ross model. This is because the RANDI-3 model takes the hump characteristic below 100 Hz into account, rather than being flat as the Ross model suggests. However, it is also found that the RANDI-3 model has two different slopes in the two frequency bands above 500 Hz and 100~500 Hz, and the latter has a steeper slope.

### (5) Relationship ⑤ between the AQUO project's model and Ross model

The AQUO project's model is based on noise mechanisms and each term is a function of speed and frequency. Although these relationships cannot be directly obtained from the Ross

model, they still draw lessons from Ross's early works. In addition, the relationship of SL with respect to ship length or tonnage adopts the Ross model, as indicated in Eq. (17).

### (6) Relationship ⑥ between the RANDI-2 model and RANDI-3 model

By comparing Eq. (8) and Eq. (9), it is obvious that the forms of both models are very close. Furthermore, the RANDI-2 model employs the average SL spectrum of the W&H model completely. In contrast, the RANDI-3 model defines the average SL spectrum segmented in frequency bands and the low-frequency part in the model can also reflect the typical 'hump' characteristics.

### (7) Relationship ⑦ between the AQUO project's model and Wittekind's model

Both the AQUO project's model and the Wittekind's model are based on noise-generated mechanisms. The difference between them is that the former requires the measured noise data of a specific ship to obtain the coefficients of noise sources through optimisation. The Wittekind's model is a series of empirical formulas, which have not been fully verified.

### (8) Relationship ⑧ between the Urick model and Ross model

By comparing Eq. (2) with Eq. (4), it is obvious that the coefficients about tonnage and frequency obtained by both models are exactly the same, but the Urick model employs the blade tip velocity of the propeller. Since the propeller tip velocity and the shipping speed are connected through an advanced ratio, it can be generally considered that the coefficients of both models about shipping speed are basically the same.

### (9) Relationship ⑨ between the Ross model and Lurton model

The Lurton model was developed on the basis of the Ross model. The model takes two key parameters into account, namely the noise level at 1 kHz ( $RNL_{1k}$ ) and the average or maximum level of line spectrum below 100 Hz ( $RNL_{SL}$ ). Accordingly, the dependency of noise levels for a frequency above 100 Hz is completely consistent with the Ross model, as shown in Eq. (6).

## STANDARDS AND METHODS FOR MEASUREMENT OF SHIPPING NOISE

The ANSI/ASA S12-64 (2009) measurement standard developed by the Acoustical Society of America (ASA) is the most widely used [31]. The standard is categorised into A, B and C grades to satisfy different accuracy requirements. In Grade C, a measurement method using a single hydrophone is recommended for investigation. A three-element array, with depression angles of 15°, 30° and 45° are recommended for Grade A (accurate method) and Grade B (engineering method), and the closest distance shall not be less than 100 m or 1 times the ship length. Finally, the SL of a measured ship is

the average SLs obtained from the three elements in the array. Figure 7 shows the measurement methodology specified in the ANSI/ASA S12-64 (2009) standard. The standard requires replicated, far-field, broadside measurements along three aspect angles, centred on a fixed closest point of approach (CPA). The measurements should be performed in a deep basin, 1 to 3 times the ship length (depending on the target grade level of the SL estimate), allowing free-field propagation between the source and receiver, with no interference from other sources and reverberation. The propagation loss from CPA to 1 m is estimated with spherical spreading. The SSLs averaged over the three measurement angles should be reported by integrating the energy per one-third octave bands, which facilitates inter-ship comparisons by smoothing the SSL narrowband variability. Other acoustic metrics commonly used for ship SLs are broadband levels integrated over a large bandwidth (e.g. 20 Hz to 1 kHz, or per octave bands) and narrow band SSL (for spectral levels in 1 Hz bands) [28,41].

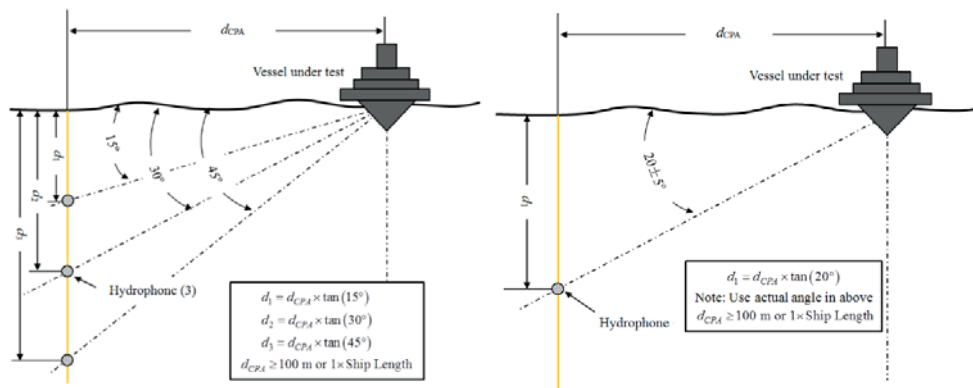


Fig. 7. measurement methodology presented in ANSI/ASA S12-64 (2009) (a) Grade A and B (b) Grade C [31]

Figure 8 shows the trajectory of the target vessel and the position of the hydrophone specified in the ANSI/ASA S12-64 (2009) standard. The target vessel travels at a constant speed along a straight line, turns away from two times the Data Window Length (DWL), and then continues the next round trip. The time window is taken to be  $\pm 30^\circ$  near the closest point.

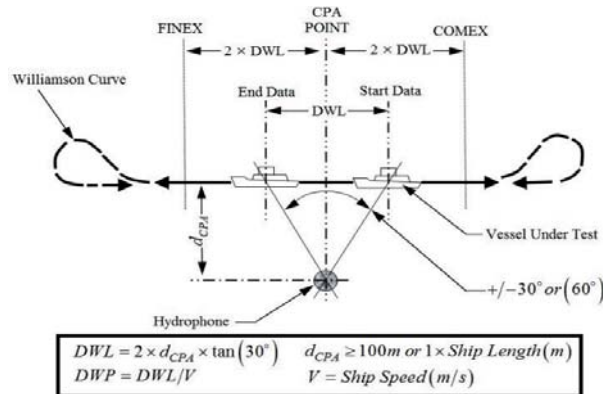


Fig. 8. The shipping trajectory of target vessel and position of hydrophone defined in ANSI/ASA S12-64(2009) [31]

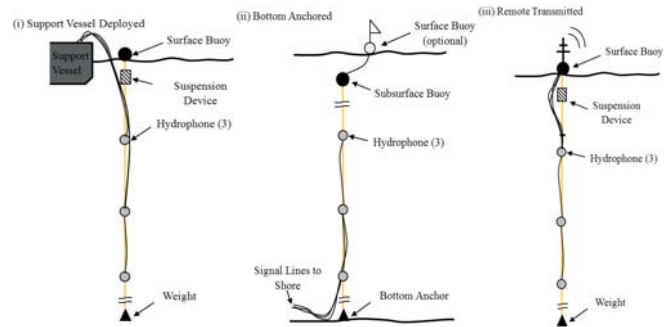


Fig. 9. Hydrophone deployment arrangements [31]

As shown in Fig. 9, the hydrophones are generally arranged in the above three ways. In September 2013, with the support of the SONIC project, Brooker and Humphrey [38] conducted underwater radiated noise measurements of the target ship

Princess Royal, using the first method. A slight difference was that, in order to prevent the buoy and the measuring system from being carried away by the current, and also to isolate the vibration of the mother vessel to the measuring system, the buoy was connected with elastic ropes. The second measurement method is often applicable to the long-time noise monitoring for the observatory stations

near the coast. Andrew *et al.* [5] used a method similar to the second method to observe ship noise on the west coast of North America for 13 years (1994–2007), but the hydrophone array was horizontally arranged on the seabed. The third measurement method, suitable for the simultaneous observation of a wide range of multiple measurement points, has been adopted by the CERDSM research centre in France [27]. In 1980–1990, they used the sonobuoy system to measure the noise of 167 ships and obtained the ANATRA model.

The DNV measurement standard [32] is mainly used for the classification and evaluation of the underwater radiation noise level of various ships; a single hydrophone is arranged on the seabed with a closest distance of 150–250 m, as shown in Fig. 10. The measurement can also be carried out in relatively shallow waters but the standard requires that the water depth below the keel should be more than 30 m.

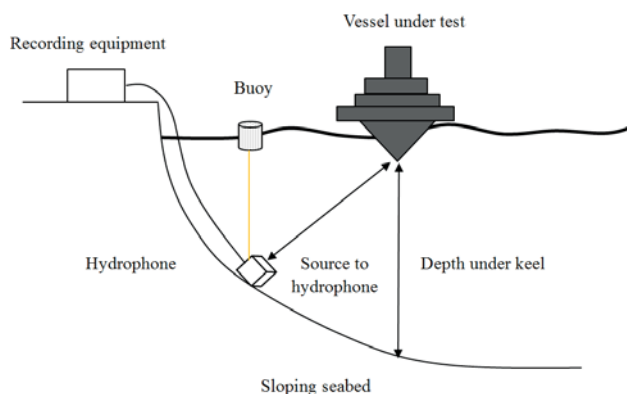


Fig. 10 Hydrophone deployment arrangements defined in DNV document

## CONCLUSIONS

The aim of the present work has been to outline the empirical models and measurement techniques developed over recent years for studying shipping noise. These applications and research into shipping noise (both in the ocean and river channels) is still in an ongoing developmental phase and there are limitations and shortcomings that need to be overcome; further applications need to be explored. Presented in this section is a brief discussion regarding present limitations and the requirement for future developments.

### MORE ACCURATE EMPIRICAL SL MODELS

The current empirical SL models listed in this paper were all developed based on numerous measurements. For the ship traffic noise mapping, the SL models of merchant ships are all treated as a monopole source, or equivalent monopole source considering radiation direction. However, this cannot reflect the real noise radiation patterns at different frequencies, especially at higher frequencies. Thus, a more accurate empirical SL model, regarding the noise generated from a whole merchant ship as being a combination of spatially separated monopole sources, dipole sources and multipole sources, is necessary to study and develop it further; this may generate more accurate, radiated noise field propagation in the ocean channels.

### THE CONNECTIONS BETWEEN EMPIRICAL MODELS AND NOISE SOURCE GENERATION MECHANISMS

The current empirical models were always produced from measurements and statistics, and the coefficients used to fit the formulas lack practical physical meaning. For example, what does the dependence of source level on shipping speed or ship length represent? How can we create the connections between empirical models and noise source generation mechanisms? The present limitations require development for the future.

## ACKNOWLEDGEMENTS

This work was supported by the Foundation Strengthening Program Area Fund of Science and Technology Commission of the Central Military Commission (No. 2020-JCJQ-JJ-228), Natural Science Foundation of Jiangsu Province (BK20200995), Scientific Research Start-Up Fund for Young Teachers of Jiangsu University of Science and Technology (1142931805) and the Institute of Acoustics of the Chinese Academy of Sciences (IOA, CAS). The authors would like to thank Professor Jun Fan from Shanghai Jiao Tong University for their suggestions. Finally, we would like to thank the anonymous reviewers for their insightful comments and helpful suggestions made.

## REFERENCES

1. National Research Council: *Ocean noise and marine mammals*. National Academies Press (US), 2003.
2. Hermannsen, L., Beedholm, K., Tougaard, J., Madsen, P. T.: *High frequency components of ship noise in shallow water with a discussion of implications for harbor porpoises (Phocoena phocoena)*, The Journal of the Acoustical Society of America, vol. 136(4), pp. 1640-1653, 2014.
3. McKenna, D.: *Ship sources of ambient noise*. IEEE Journal of Oceanic Engineering, 30(2), 257-261, 2005.
4. Chapman, N. R., Price, A.: *Low frequency deep ocean ambient noise trend in the Northeast Pacific Ocean*. The Journal of the Acoustical Society of America, 129(5), EL161-EL165, 2011.
5. Andrew, R. K., Howe, B. M., Mercer, J. A.: *Long-time trends in ship traffic noise for four sites off the North American West Coast*. The Journal of the Acoustical Society of America, 129(2), 642-651, 2011.
6. Zhu Beili, Huang Xiuchang.: *Key Technologies for Submarine: Stealth Design of Acoustic Coating*, Shanghai Jiao Tong University Press: Shanghai, China, 2012. (In Chinese)
7. Wenz, G. M.: *Acoustic ambient noise in the ocean: Spectra and sources*. The Journal of the Acoustical Society of America, 34(12), 1936-1956, 1962.
8. Lurton. X.: *An Introduction to Underwater Acoustics*. Berlin, Germany: Springer-Praxis, 2010.
9. Carey, W. M., Evans, R. B.: *Ocean ambient noise: measurement and theory*. Springer Science & Business Media, 2011.

10. Harrison, C. H.: *Formulas for ambient noise level and coherence*. The Journal of the Acoustical Society of America, 99(4), 2055-2066, 1996.
11. Harrison, C. H.: *CANARY: A simple model of ambient noise and coherence*. Applied Acoustics, 51(3), 289-315, 1997.
12. Zilong Peng, Bin Wang, Jun Fan.: *Assessment on source levels of merchant ships observed in the East China Sea*. Ocean Engineering, 156: 179-190, 2018.
13. Zilong Peng.: *Measurement and modelling on the underwater noise radiated from ships in the area of Zhoushan Archipelago*. Ph.D. Dissertation of Shanghai Jiao Tong University, 2018.
14. Urick, R. J.: *Principles of Underwater Sound*. McGraw-Hill Co, New York, 1983.
15. Ross, D.: *Mechanics of Underwater Noise*. Pergamon, New York, 1976.
16. Wales, S. C., Heitmeyer, R. M.: *An ensemble source spectra model for merchant ship-radiated noise*. The Journal of the Acoustical Society of America, 111(3), 1211-1231, 2002.
17. Breeding Jr, J. E., Pflug, L. A., Bradley, M., Walrod, M. H.: *Research Ambient Noise Directionality (RANDI) 3.1 Physics Description (No. NRL/FR/7176--95-9628)*. Naval Research Lab Stennis Space Center MS, 1996.
18. Arveson, P. T., Vendittis, D. J.: *Radiated noise characteristics of a modern cargo ship*. The Journal of the Acoustical Society of America, 107(1), 118-129, 2000.
19. Veirs S, Veirs V, Wood J. D.: *Ship noise extends to frequencies used for echolocation by endangered killer whales*. PeerJ, 4: e1657, 2016.
20. Knudsen, V. O., Alford, R. S., Emling, J. W.: *Underwater ambient noise*. J. Mar. Res., 7, 410-429, 1948.
21. Piggott, C. L.: *Ambient sea noise at low frequencies in shallow water of the Scotian Shelf*. The Journal of the Acoustical Society of America, 36(11), 2152-2163, 1964.
22. Hamson, R. M., Wagstaff, R. A.: *An ambient-noise model that includes coherent hydrophone summation for sonar system performance in shallow water (No. SAACLANTCEN-SR-70)*. SAACLANT ASW RESEARCH CENTRE LA SPEZIA (ITALY), 1983.
23. Wittekind, D. K.: *A simple model for the underwater noise source level of ships*. Journal of Ship production and design, 30(1), 7-14, 2014.
24. Audoly, C., Rizzuto, E.: *AQUO: Achieve Quieter Oceans by shipping noise footprint reduction FP7-Collaborative project n°314227, WP 2: Noise Sources, Task T2.1, "Ship underwater radiated noise patterns"*, URL: www.aquo.eu., 2018.
25. Traverso, F., Gaggero, T., Rizzuto, E., Trucco, A.: *Spectral analysis of the underwater acoustic noise radiated by ships with controllable pitch propellers*. In OCEANS 2015-Genova (pp. 1-6). IEEE, 2015.
26. Traverso, F., Gaggero, T., Tani, G., Rizzuto, E., Trucco, A., Viviani, M.: *Parametric analysis of ship noise spectra*. IEEE Journal of Oceanic Engineering, 42(2), 424-438, 2016.
27. Esperandieu, J. S.: *Prediction of horizontal ambient shipping noise directionality with an analytical model: ANATRA*, 1990.
28. Simard, Y., Roy, N., Gervaise, C., Giard, S.: *Analysis and modelling of 255 source levels of merchant ships from an acoustic observatory along St. Lawrence Seaway*. The Journal of the Acoustical Society of America, 140(3), 2002-2018, 2016.
29. Gaggero, T., Rizzuto, E., Traverso, F., Trucco, A.: *Comparing ship underwater noise measured at sea with predictions by empirical models*. In proc. of 21st International Congress on Sound and Vibration: 1510-1516, 2014.
30. Audoly, C., Gaggero, T., Baudin, E., Folegot, T., Rizzuto, E., Mullor, R. S., ... Kellett, P.: *Mitigation of underwater radiated noise related to shipping and its impact on marine life: A practical approach developed in the scope of AQUO project*. IEEE Journal of Oceanic Engineering, 42(2), 373-387, 2017.
31. ANSI/ASA.: *Quantities and Procedures for Description and Measurement of Underwater Sound from Ships-Part 1: General Requirements*, 2009.
32. Veritas, D. N.: *Rules for classification of ships - part 6 chapter 24: Silent Class Notation*, 2010.
33. Mitson, R. B.: *Underwater noise of research vessels: review and recommendations*. ICES Cooperative Research Report No.209. ISSN 1017-6195, 1995.
34. ISO 17208-1.: *Underwater acoustics -- Quantities and procedures for description and measurement of underwater sound from ships -- Part 1: Requirements for precision measurements in deep water used for comparison purposes*, 2016.
35. Ainslie, M. A.: *Principles of sonar performance modelling*. Berlin: Springer, 2010.

36. De Jong, C. A. F.: *Characterization of ships as sources of underwater noise*. In NAG/DAGA International Conference on Acoustics, Rotterdam, The Netherlands, 2009.
37. Coward, S.: *A method for remote sensing of acoustic ship noise*. Master's thesis, 2013.
38. Brooker, A., Humphrey, V.: *Measurement of radiated underwater noise from a small research vessel in shallow water*. Ocean Engineering, 120, 182-189, 2016.
39. Scrimger, P., Heitmeyer, R. M.: *Acoustic source-level measurements for a variety of merchant ships*. The Journal of the Acoustical Society of America, 89(2), 691-699, 1991.
40. Grelowska, G.: *Study of Seasonal Acoustic Properties of Sea Water in Selected Waters of the Southern Baltic*, Polish Maritime Research, 23(1), 25-30, 2016.
41. McKenna, M. F., Ross, D., Wiggins, S. M., Hildebrand, J. A.: *Underwater radiated noise from modern commercial ships*. The Journal of the Acoustical Society of America, 131(1), 92-103, 2012.
42. Coward, S., Tollefsen, D., Dong, H.: *Radiated ship noise level estimates from measurements in a fjord*. The Journal of the Acoustical Society of America, 134(5), 4150-4150, 2013.
43. Das, A.: *Shallow ambient noise variability due to distant shipping noise and tide*. Applied Acoustics, 72(9), 660-664, 2011.
44. Roth, E. H., Schmidt, V., Hildebrand, J. A., Wiggins, S. M.: *Underwater radiated noise levels of a research icebreaker in the central Arctic Ocean*. The Journal of the Acoustical Society of America, 133(4), 1971-1980, 2013.
45. Bassett, C., Polagye, B., Holt, M., Thomson, J.: *A vessel noise budget for Admiralty Inlet, Puget Sound, Washington (USA)*. The Journal of the Acoustical Society of America, 132(6), 3706-3719, 2012.
46. Trevorrow, M. V., Vasiliev, B., Vagle, S.: *Directionality and maneuvering effects on a surface ship underwater acoustic signature*. The Journal of the Acoustical Society of America, 124(2), 767-778, 2008.
47. Gaggero, T., Bassetti, M., Firenze, E., Tesei, A., Trucco, A.: *Processing strategies for evaluating the ship radiated noise using an underwater vertical array*. In proc. of 2nd Int. Conf. and Exhibition on Underwater Acoustics, 329-336, 2014.
48. Grelowska, G., Kozaczka, E., Kozaczka, S., Szymczak, W.: *Underwater noise generated by a small ship in the shallow sea*. Archives of Acoustics, 38(3): 351-356, 2013.
49. Zilong Peng, Jun Fan, Bin Wang.: *Analysis and Modelling on Radiated Noise of a Typical Fishing Boat Measured in Shallow Water Inspired by AQUO Project's Model*. Archives of Acoustics, 38(3): 351-356, 2018.
50. SILENV.: *Ships oriented Innovative Solutions to Reduce Noise and Vibrations*, FP7-EC Collaborative Research Project, 2009-2012.
51. Rizzuto, E., Audoly, C.: *AQUO: Achieve QUIeter Oceans by shipping noise footprint reduction FP7-Collaborative project n°314227, WP 2: Noise Sources, Task T2.2, "Predictive theoretical models for propeller"*, URL: [www.aquo.eu](http://www.aquo.eu), 2015.
52. Hallander, J., Audoly, C.: *AQUO: Achieve QUIeter Oceans by shipping noise footprint reduction FP7-Collaborative project n°314227, WP 2: Noise Sources, Task T2.3, "Propeller noise experiments in model scale"*, URL: [www.aquo.eu](http://www.aquo.eu), 2015.
53. Salinas, R., Audoly, C.: *AQUO: Achieve QUIeter Oceans by shipping noise footprint reduction FP7-Collaborative project n°314227, WP 2: Noise Sources, Task T2.5, "Synthesis: Impact of propeller noise on global"*, URL: [www.aquo.eu](http://www.aquo.eu), 2015.
54. Moreno, A., Audoly, C.: *AQUO: Achieve QUIeter Oceans by shipping noise footprint reduction FP7-Collaborative project n°314227, WP 2: Noise Sources, Task T3.1, "European URN Standard Measurement Method"*, URL: [www.aquo.eu](http://www.aquo.eu), 2015.
55. Salinas, R., Audoly, C.: *AQUO: Achieve QUIeter Oceans by shipping noise footprint reduction FP7-Collaborative project n°314227, WP 2: Noise Sources, Task T3.2, "On-site measurements -Experimental data for accurate identification and quantification of Cavitation Noise and other sources"*, URL: [www.aquo.eu](http://www.aquo.eu), 2015.
56. Andre, M., Audoly, C.: *AQUO: Achieve QUIeter Oceans by shipping noise footprint reduction FP7-Collaborative project n°314227, WP 2: Noise Sources, Task T3.4, "In-situ measurements of ambient underwater noise along time in different areas with record of AIS data"*, URL: [www.aquo.eu](http://www.aquo.eu), 2015.
57. Brooker, A., Humphrey, V., Jansen, E.: *Suppression of underwater Noise Induced by Cavitation*, FP7-314394-SONIC, Deliverable D2.5: Full Scale Radiated Noise Measurement, 2015.
58. Loughborough University Institutional Repository.: *Measurement of underwater noise arising from marine aggregate dredging operations*. Marine Aggregate Levy Sustainability Fund (MALSF), 2011.
59. Wright, E. B., Cybulski, J.: *Low-frequency acoustic source levels of large merchant ships (No. NRL-8677)*. NAVAL RESEARCH LAB WASHINGTON DC, 1983.

60. Hamson, R. M.: *The modelling of ambient noise due to shipping and wind sources in complex environments*. Applied Acoustics, 51(3), 251-287, 1997.
61. Etter, P. C.: *Underwater Acoustics Modelling and Simulation: Principle, Techniques and application*. Spon Press, New York, 2003.
62. Anon.: *Ocean noise and marine mammals (National Research Council of the National Academies)*. The National Academies Press, Washington, D.C, 2003.
63. Hom, F. L. C., Kinda, F. G. B., Hom, S.: *Statistical Ambient Noise Maps from Traffic at World and Basin Scales*. Institute Of Acoustics, Cambridge, UK, 2016.
64. Colin, M. E., Ainslie, M. A., Binnerts, B., de Jong, C. A., Karasalo, I., Östberg, M., ... Clorennec, D.: *Definition and results of test cases for shipping sound maps*. IEEE, 2015.
65. Audoly, C., Flikeema, M.: *Suppression of underwater Noise Induced by Cavitation, FP7-314394-SONIC, Deliverable D5.4: Guidelines for regulation on UW noise from commercial shipping*, 2015.
66. Aulanier, F., Simard, Y., Roy, N., Bandet, M., Gervaise, C.: *Groundtruthed probabilistic shipping noise modelling and mapping: Application to blue whale habitat in the Gulf of St. Lawrence*. In Proceedings of Meetings on Acoustics 4ENAL (Vol. 27, No. 1, p. 070006). ASA, 2016.
67. Jones, E. L., Hastie, G. D., Smout, S., Onoufriou, J., Merchant, N. D., Brookes, K. L., Thompson, D.: *Seals and shipping: quantifying population risk and individual exposure to vessel noise*. Journal of applied ecology, 54(6), 1930-1940, 2017.
68. Folegot, T., Clorennec, D., Brunet, P., Six, L., Chavanne, R., van der Schaar, M., André, M.: *Monitoring long term ocean noise in European waters*. In OCEANS 2015-Genova:1-7, 2015.
69. Soares, C., Zabel, F., Jesus, S. M.: *A shipping noise prediction tool*. In OCEANS 2015-Genova:1-7, 2015.
70. Erbe, C., MacGillivray, A., Williams, R.: *Mapping cumulative noise from shipping to inform marine spatial planning*. The Journal of the Acoustical Society of America, 132(5), EL423-EL428, 2012.
71. Sertlek, H. Ö., Binnerts, B., Ainslie, M. A.: *The effect of sound speed profile on shallow water shipping sound maps*. The Journal of the Acoustical Society of America, 140(1), EL84-EL88, 2016.
72. Buszman K., Gloza M.: *Detection of Floating Objects Based on Hydroacoustic and Hydrodynamic Pressure Measurements in the Coastal Zone*, Polish Maritime Research, 27(2), 168-175, 2020.
73. Buszman K.: *Analysing the Impact on Underwater Noise of Changes to the Parameters of a Ship's Machinery*, Polish Maritime Research, 27(3), 176-181, 2020.
74. Kozaczka, E., Grelowska, G.: *Propagation of Ship-Generated Noise in Shallow Sea*, Polish Maritime Research, 25(2), 37-46, 2018.
75. Kozaczka, E., & Grelowska, G.: *Autonomous Platform to Protect Maritime Infrastructure Facilities*, Polish Maritime Research, 26(4), 101-108, 2019.
76. Gaggero, T., Rizzuto, E., Traverso, F., Trucco, A.: *Comparing ship underwater noise measured at sea with predictions by empirical models*. In proc. of 21st International Congress on Sound and Vibration: 1510-1516, 2014.

## CONTACT WITH THE AUTHORS

**Xiaowei Yan**

*e-mail: yanxwseri@163.com*

Systems Engineering Research Institute,  
16 Cuiwei Road, Haidian District, 100036 Beijing,  
**CHINA**

**Hao Song**

*e-mail: songhaox@163.com*

Systems Engineering Research Institute,  
16 Cuiwei Road, Haidian District, 100036 Beijing,  
**CHINA**

**Zilong Peng**

*e-mail: zlp\_just@sina.com*

Jiangsu University of Science and Technology,  
No.2 Mengxi Road, 212003 Zhenjiang,  
**CHINA**

**Huimin Kong**

*e-mail: kongcnn@126.com*

Jiangsu University of Science and Technology,  
No.2 Mengxi Road, 212003 Zhenjiang,  
**CHINA**

**Yipeng Cheng**

*e-mail: 346256152@qq.com*

Jiangsu University of Science and Technology,  
No.2 Mengxi Road, 212003 Zhenjiang,  
**CHINA**

**Linjiang Han**

*e-mail: 892328443@qq.com*

Jiangsu University of Science and Technology,  
No.2 Mengxi Road, 212003 Zhenjiang,  
**CHINA**

# DESIGN CRITERIA FOR SCANTLING OF LONGITUDINAL AND TRANSVERSE CONNECTIONS IN THE TORSION BOX UNDER FATIGUE LOADING

Arturo Silva-Campillo\*

Juan Carlos Suárez-Bermejo

Miguel Ángel Herrerros-Sierra

Universidad Politécnica de Madrid, Spain

\* Corresponding author: [a.silva@upm.es](mailto:a.silva@upm.es) (A. Silva-Campillo)

## ABSTRACT

*Fatigue is one of the main failure modes in marine structures, and it is caused by the strong cyclic characteristics of the loads they support. This failure mode is amplified in areas of high stress concentration, such as at the intersection of primary and secondary elements. In this paper, a two-phase study is proposed that compares numerical and experimental results using a digital image correlation technique. The described procedure establishes selection, design, and scantling criteria and provides recommendations for the design of the transverse structure using specimens with different geometries. These geometries correspond to different designs for the transverse primary structure that use a longitudinal secondary stiffener with variable thickness and longitudinal spacing to transverse in a dynamic and quasi-static regime. The stress state for this regime is calculated based on the biaxiality indication concept, which uses the fatigue phenomenon (safety factor and sensitivity curves) and fracture mechanics (parameters of the Paris crack propagation law, correlation value, and law of variation of the stress intensity factor).*

**Keywords:** Fatigue life; ship structures; crack growth; fracture.

## INTRODUCTION

Fatigue is a local phenomenon caused by fluctuating stresses on the structure that originate from global and local loads on the hull girder. In terms of the fatigue event, structural details that have high stress concentrations are of particular interest. To this end, the cut-outs made in the primary transverse structure to allow passage of the element structure (longitudinal stiffeners), which is a structural element in all ships and offshore structures, has been widely studied and investigated to optimize it in terms of structural performance [1].

This structure has been analyzed under the influence of adjoining substructures [2], wherein the cut-out geometry and lug or collar plate presence with the respective longitudinal stiffener are established using finite element models (FEM) and hypotheses with shell and solid elements. To this end, different approaches have been used [3], including nominal stress, structural or hot-spot stress, notch stress and notch

intensity, notch strain, and the crack propagation process. Over the years, several procedures have been developed to implement the most appropriate study methodology [4] for a structural hot-spot in welded joints based on the results of different experimental tests involving four different geometries.

These structural details have been studied for all types of vessels. For example, Fricke and Paetzold [5] tested different constant and variable amplitude history loads to determine the fatigue phenomenon in different areas of container ships (hatch corner and upper wing torsional box) for identifying the intersection of the primary and secondary structure for different load values. The results were validated with those obtained via FEM using the structural hot-spot stress and effective notch stress approaches. Lotsberg [6] presented a summary with different methodologies to evaluate fatigue life based on the hot-spot stress approach and the corresponding SN curve – in engineering practice, fatigue strength is defined from the so-called SN curves [7] – for this structural detail in floating,

production, storage, and offloading (FPSO) units. SN curves are used to calculate the fatigue life of this type of structure [5], where the results are validated through experimental tests. The damage and fatigue life of this structure is studied using FEM of the structural details of double hull oil tankers based on the notch stress approach; furthermore, the nonlinear corrosion effect on fatigue life was investigated [8].

It is common to use numerical analysis by FEM to evaluate the stresses via fatigue analysis; it is possible to view a detailed analysis of this type of structure that considers the welding between elements using the FEM analysis [9]. The results of the fatigue analysis performed using the FEM of the structural detail are verified through comparison of different procedures to evaluate fatigue life [10]. Fatigue life analysis has been conducted using a fracture mechanics approach [11], wherein the effects of misalignment on the weld of the structure or intersection are investigated, and a FEM tool is proposed to calculate the weld effect on the sub model without considering crack propagation.

This research proposes scantling criteria that are based on obtaining structural results via the evaluation of the different alternatives of the design variables (spacing of the longitudinal stiffeners and thickness of primary supporting member in the torsion box of a container ship; Fig. 1) of two different geometries that are commonly used in the shipbuilding industry. Experimental tests are conducted to validate the numerical results, provide maximum reliability, and to allow the results for scantlings of ship structures to be used.

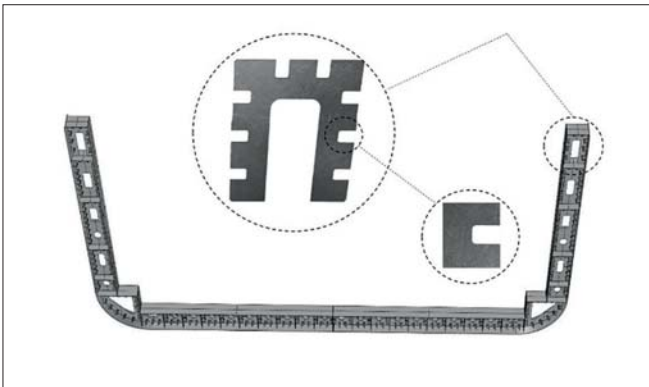


Fig. 1. Midship section of the container ship with an upper wing torsional box and cut-out detail

The study is outlined as follows: Section 2 gives the mathematical basis and section 3 introduces the experimental tests by presenting the specimens and their coupling in the testing machine. Section 4 details the finite element modelling of the specimens and compares it with the test specimens to validate the obtained results. Section 5 presents the results with respective discussion, and finally, section 6 provides the conclusions resulting from this research.

## FATIGUE DAMAGE ASSESSMENT

The study is conducted in two phases based on the state of the structure in terms of damage. The first level corresponds to the analysis of crack initiation from the perspective of

the fatigue phenomenon (using the Palmgren–Miner linear damage hypothesis), and the second phase is characterized by the study of crack propagation based on fracture mechanics.

## MIXED-MODE CRACK GROWTH PATH

Several analytical models have been developed for isotropic solids from various mathematical developments [12–14] to establish the direction of crack propagation [15–16]. The maximum circumferential stress (MCS) theory is the most widely used due to its simple, easily implementable, and good results [17]. This theory proposes the following concept to obtain the direction of crack propagation from the circumferential tensile stress ( $\partial\sigma_{\theta\theta}$ ):

$$\frac{\partial\sigma_{\theta\theta}}{\partial\theta} = 0 \Rightarrow \theta | \sigma_{\theta\theta, \max} \quad (1)$$

To find the angle of propagation  $\theta$ , it is necessary to identify the direction in which the tangential stress ( $\tau_{r\theta}$ ) is zero, that is,

$$\begin{aligned} \frac{\partial\sigma_{\theta\theta}}{\partial\theta} = 0 \Rightarrow \tau_{r\theta} = 0 \\ \frac{1}{4}K_I \left( \sin\frac{\theta}{2} + \sin\frac{3\theta}{2} \right) + \frac{1}{4}K_{II} \left( \cos\frac{\theta}{2} + 3\cos\frac{3\theta}{2} \right) = \\ \frac{1}{2}\cos\frac{\theta}{2} \left[ K_I \sin\theta + K_{II} (3\cos\theta - 1) \right] = 0 \end{aligned} \quad (2)$$

The following solutions are proposed using the presented criterion:

$$\begin{cases} \theta = \pm\pi \\ K_I \sin\theta + K_{II} (3\cos\theta - 1) = 0 \end{cases} \quad (3)$$

The first solution is trivial and corresponds to the faces of the crack. The most common way in which the second solution can be found corresponds to

$$\begin{aligned} \theta | \sigma_{\theta\theta, \max} = \Delta\theta = 2 \tan^{-1} \left[ \frac{K_I - \sqrt{K_I^2 + 8K_{II}^2}}{4K_{II}} \right] \text{ if } K_{II} < 0 \\ \theta | \sigma_{\theta\theta, \max} = \Delta\theta = -2 \tan^{-1} \left[ \frac{K_I - \sqrt{K_I^2 + 8K_{II}^2}}{4K_{II}} \right] \text{ if } K_{II} < 0 \\ \theta | \sigma_{\theta\theta, \max} = \Delta\theta = 0 \text{ if } K_{II} = 0 \end{aligned} \quad (4)$$

For the crack to extend, the maximum circumferential tensile stress obtained in Eq. (4) must reach a critical value, which is obtained by rearranging the components as

$$\sigma_{\theta\theta} \sqrt{2\pi r} = K_{IC} = \cos\frac{\theta}{2} \left[ K_I \cos^2\frac{\theta}{2} - \frac{3}{2}K_{II} \sin\theta \right] \quad (5)$$

Eq. (5) can be normalized as

$$\frac{K_I}{K_{IC}} \cos^3\frac{\theta}{2} - \frac{3}{2} \frac{K_{II}}{K_{IC}} \cos\frac{\theta}{2} \sin\theta = 1 \quad (6)$$

Finally, Eq. (7) is used to define an equivalent stress intensity factor based on the implementation of each of the fracture modes as

$$K_{eq} = K_I \cos^3\frac{\theta}{2} - \frac{3}{2} K_{II} \cos\frac{\theta}{2} \sin\theta \quad (7)$$

## TESTING

### DESIGN AND FABRICATION OF TEST SPECIMENS

Three values of longitudinal spacing ( $s$ ) (400, 500, and 600 mm) are established to study and characterize the structural behavior. The initial structure comprising multiple cut-outs is simplified and modeled by the assumption adopted in Fig. 2, which allows a single cut-out under the influence of the proximity of contiguous cut-outs to be analyzed by following a procedure similar to Fricke et al. [1].

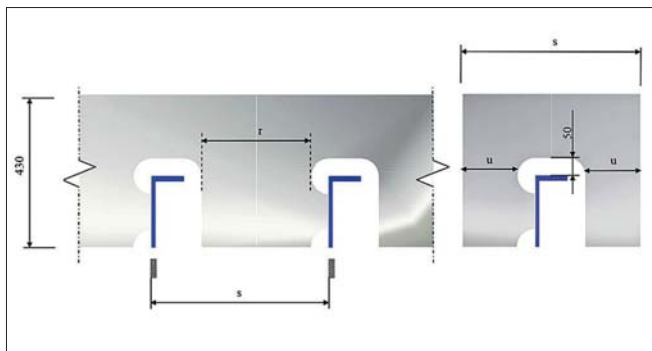


Fig. 2. Modelling of isolated structure of interest. Dimensions in mm

Table 1 shows the dimensions of each of the specimens as a function of the longitudinal spacing values.

Tab. 1. Dimensions (in mm) of the sub model for each different spacing value

s	r	u
400	210	105
500	310	155
600	410	205

The specimen is adjusted based on the numerical results for the 500 mm spacing with the correcting geometric scale factor between the original ship structure and that measured in the test laboratory. This study involves two typical geometries commonly used in the shipbuilding industry. These geometries are for the primary supporting members that allow the secondary longitudinal stiffener to pass under a uniformly distributed tensile load. This issue is simulated by four point loads acting on each of the eight holes in the specimen that serve to distribute the design load and establish the structure in the testing machine. Fig. 3 shows the two test specimens and their respective dimensions located on a steel plate with dimensions  $360 \times 215 \times 10$  mm (the initial design geometry is located on a  $430 \times 500 \times 20$  mm plate; it is scaled with a geometric scale factor of two in all three dimensions to couple it to the testing machine). The material properties (provided by the manufacturer's certificate) are a Young's modulus and Poisson's ratio of 206 GPa and 0.3, respectively, with a 250 MPa yield stress and a steel density of  $7.85 \text{ t/m}^3$ .

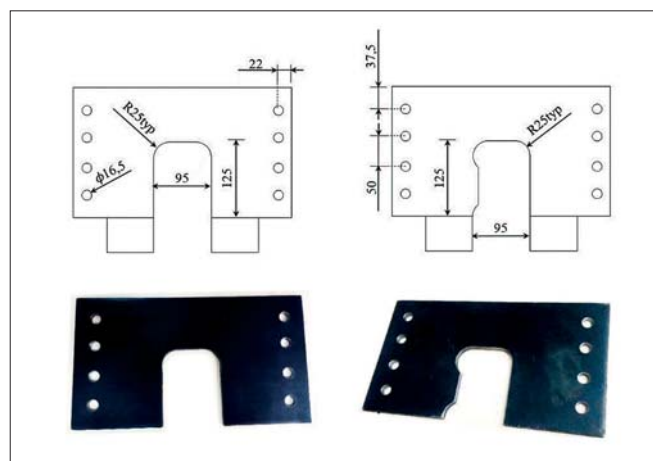


Fig. 3. Sketch and dimensions (in mm). (left) Specimen 1, (right) Specimen 2

The crack growth rate in a linear regime is established as a criterion for comparison between the two specimens; therefore, a pre-crack is located to focus on crack propagation, as reported by Carpintieri [18]. Using the same criteria employed by Strandberg [19], the same pre-crack dimension (6 mm) is located for each of the proposed models, and they are oriented perpendicular to the upper region of the cut out. Using the same principles as those in the establishment of the geometries of the test specimens (single-edge notched tension, SENT), the initial regular load condition undergoes the same scaling process under a factor of 2.5 and within the range of  $\pm 25\%$  about the mean stress ( $R = 0.6$ ). The design fatigue load is defined using a value  $R = -1$ .

### INSTRUMENTATION AND CONDITIONING OF THE SPECIMENS

The test procedure is performed using the digital image correlation (DIC) technique widely used in fatigue phenomenon [20], which allows validation criteria to be established by obtaining displacements and deformations to provide the maximum reliability to the process. The distribution of the strains and displacements in the specimens are obtained using the Open-Source 2D software Ncorr<sup>®</sup> together with MATLAB<sup>®</sup> [21]. The procedure is performed in a quasi-static regime (constant load speed of 0.5 kN/s until a generic calibration load of 130 kN is reached), and it requires some prerequisites in terms of surface treatment through a previous cleaning with acetone. The application of the white contrast paint (PFINDER<sup>®</sup> 280) and the indirect spraying of black paint serves as a random mesh for each of the specimens (Fig. 4).

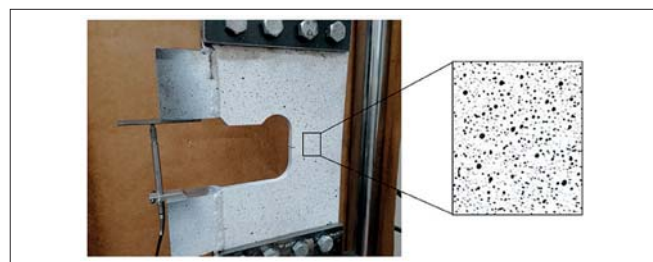


Fig. 4. Experimental specimen 2 meshing for digital image correlation application

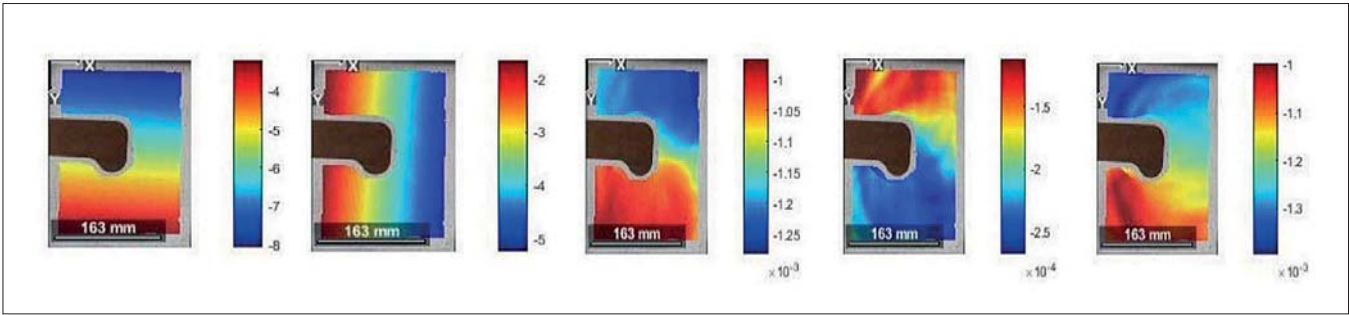


Fig. 5. Displacement and strain distributions for quasi-static load 130 kN ( $U(mm)$ ,  $V(mm)$ ,  $\epsilon_{xx}(mm/mm)$ ,  $\epsilon_{yy}(mm/mm)$ )

The process is recorded with a video camera, and the video is decomposed into a set of images. These images are processed using the program, and the meshes of the points of each image are compared; they correspond to different moments of the test. Fig. 5 shows the obtained output parameters of the program for a previous calibration specimen. The procedure is assessed using the inclusion of another calibration load and the two remaining specimen geometries.

## FATIGUE TESTING

The test specimens are fitted in the dynamic testing machine by machining two transition blocks coupled in the parts of the machine intended for this purpose (Fig. 6); the upper transition block is connected to the specimen (previously drilled in four points) through four bolts subjected to double shear throughout the process, whereas the connection with the upper load cell is achieved by the joint combination of a lyre shackle with its respective pin and rotating eyebolt. This approach is employed to absorb the possible imperfections of the arranged welds (between different elements that constitute the transition blocks) or possible misalignments (concentric or angular) of the testing machine, which can induce undesirable bending loads in the model that may interfere with the results and reduce the reliability of the process.

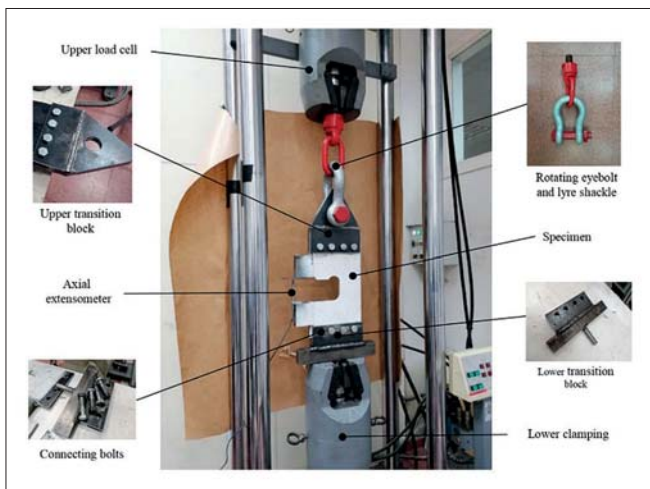


Fig. 6. Testing machine (INSTRON® 500kN) arrangement

The connection of the model with the lower clamp is achieved through a lower transition block composed of a U-shaped machined piece (previously drilled in four points in an identical

manner as the upper transition block) that fits the model using four bolts. The connection of the transition block with the lower clamping is developed by including a parallelepiped element to which a threaded hole is drilled where a cylindrical component is subsequently welded to the previous element, which is then attached using the lower clamp. To characterize the results, the design frequency of the regular load introduced to the model from the upper load cell is set to 5 Hz based on the procedure reported by Branco et al. [22].

The original model of study is characterized by a welding in the mouth of the same one that is included in the numerical simulation by means of a fixed support. Owing to the characteristics of the testing machine, the boundary conditions are modified by suppressing the fixed support that corresponds to the lower clamp of the testing machine; the previous idealization that corresponds to the welding located in the lower mouth is suppressed to ensure correct correlation and achieve accurate results. The initial design load is simulated by means of four point loads whose contribution is the total load (Fig. 7).

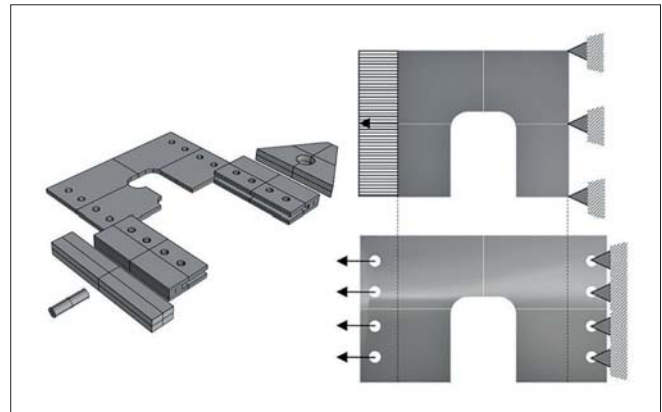


Fig. 7. (left) Arrangement of transition pieces for adaptation and coupling to the testing machine.(right) Comparison between initial and adapted geometry

## FINITE ELEMENT MODELLING

Numerical modelling based on the extended finite element method (XFEM) by linear analysis (that is widely used in the process of fracture and crack growth) is used to obtain the results. However, this modelling approach has limitations in that it incurs a high computational cost and it is difficult to achieve convergence in some scenarios [23]. This approach incorporates certain degrees of freedom of the nodes that

belong to the elements that contain the crack as obtained using enrichment functions, which are defined as the set of functions that allow for the establishment of any displacement near the crack as a combination of the same functions [24]. This research uses the XFEM employed by ANSYS® APDL 20 from the unstructured mesh method (UMM) implemented in the separating, morphing, adaptive, and remeshing technology (SMART) module. A standard coarse mesh is set using default 10-node (quadratic) tetrahedral [25, 26] and solid elements [27, 28] and two refined elements at two levels; on the one hand, it is done in the eight drilled holes of the model, and on the other hand, a mesh of local character is achieved that adapts to the contour of the crack (Fig. 8) under a generic area of influence with a radius of 20 mm (whose aim is to refine the meshing near the crack and improve the quality of the results) and a standard element size of 2 mm.

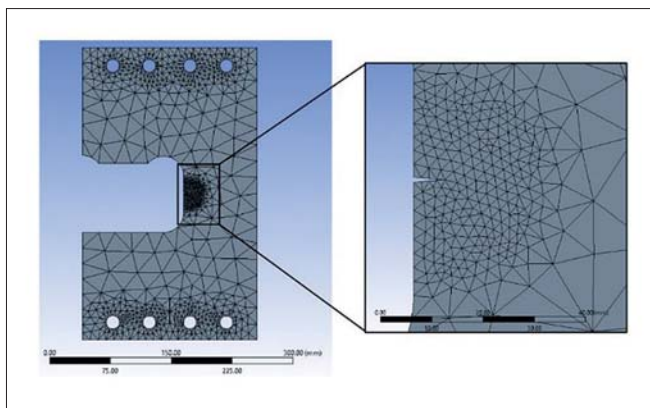


Fig. 8. Meshing (coarse and fine) pattern of specimen 2

Local meshing is updated during the crack propagation process (Fig. 9). The numerical model referring to specimen 1 comprises 17,858 nodes and 9,996 elements, while the numerical model referring to specimen 2 comprises 17,573 nodes and 9,866 elements.

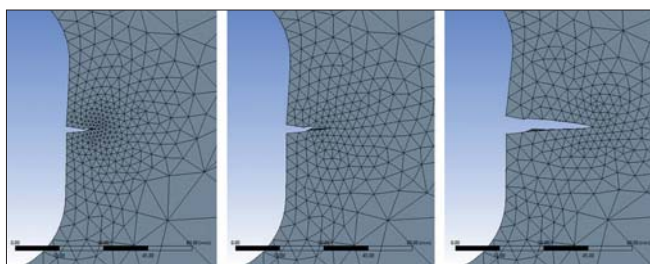


Fig. 9. Adaptive re-meshing technique in the fracture process in specimen 2

The correct structural correspondence between geometries shown in Fig. 7 is established by comparing the most representative values (von Mises stress and maximum displacement) of the two static regime tests, thereby obtaining differences in stresses and displacements that are translated into percentages of 3.31 and 4.5 %, respectively. The comparison, in terms of displacements, is done between the maximum displacements of the whole specimen (Fig. 10), while the comparison between von Mises stresses is carried out at the crack location.

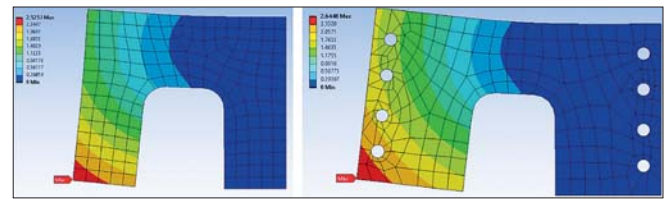


Fig. 10. Comparison between both geometries when determining the value of the maximum displacement of specimen 1

To assess the structural design and the results derived from it, the correlation between the two main geometric variables that occur in the testing process – crack length ( $a$ ) and cut-out opening (crack mouth opening displacement, CMOD) – are studied. Figs. 11 and 12 show the numerical and test models for each specimen.

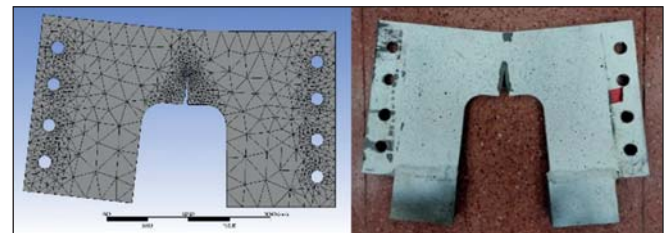


Fig. 11. Specimen 1 fracture process. (left) numerical model (right) test model

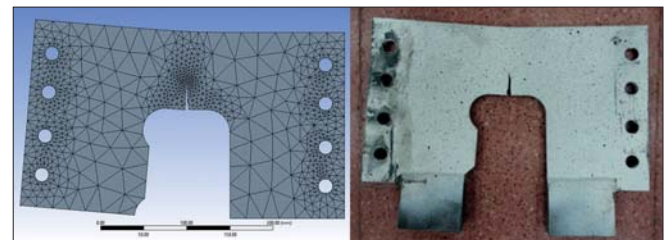


Fig. 12. Specimen 2 fracture process. (left) numerical model (right) test model

The analysis of both variables validates the numerical results obtained through the experimental tests and the correct arrangement of the specimens in the testing machine (Table 2).

Tab. 2. Comparison between numerical and experimental analysis for both specimens

Specimen	Analysis	Crack length, $a$ (mm)	CMOD (mm)	Difference (%)
1	Numerical	32	124.85	3.96
	Experimental		130	
2	Numerical	30	109.95	2.69
	Experimental		113	

Table 2 shows the differences between both analyses (numerical and experimental) for each of the specimens; larger values in the experimental tests are attributed to uncertainties inherent to the physical crack growth mechanism derived from the fatigue phenomenon. Other uncertainties are associated with imperfections of the material at the microstructural level and the constrained plasticity effect. Eventually, others may be due to the testing machine and the way the dynamic load was applied. Another validation analysis to reveal the

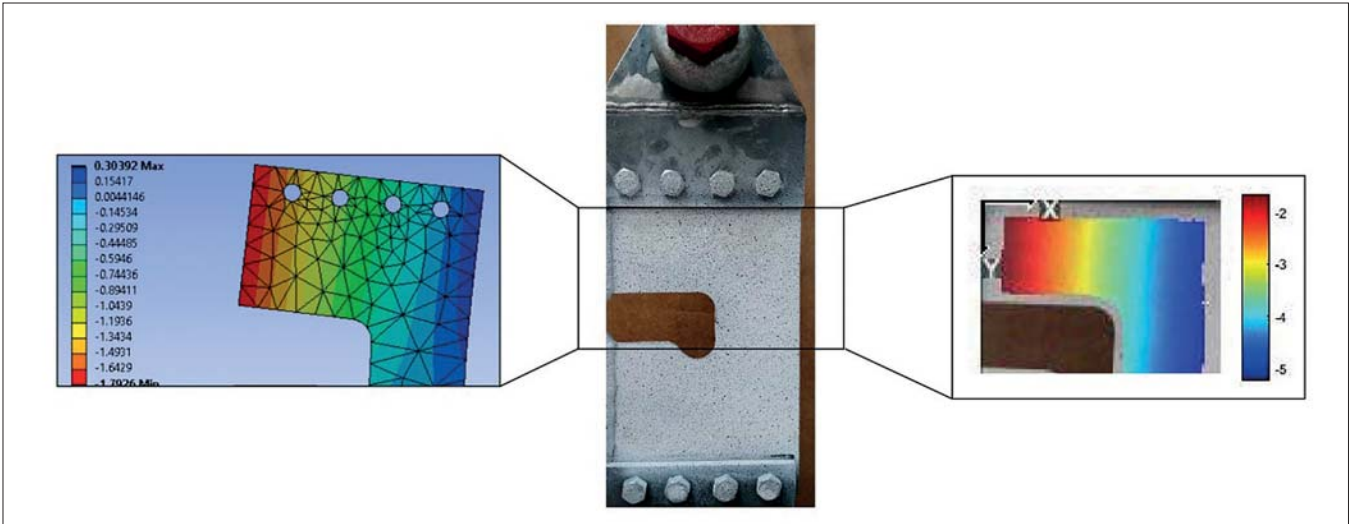


Fig. 13. Correspondence between DIC and FEM results from the strain field distribution (dimensions in mm/mm)

model accuracy is carried out by comparing results at the experimental level by establishing the strain field distribution obtained by DIC (1.85 mm/mm) and using the FEM technique (1.79 mm/mm), with a difference between both procedures of 3% (Fig. 13).

## RESULTS AND DISCUSSION

### STRESS STATE

The stress state in the original design scenario (loads and boundary conditions) is determined by means of the von Mises stress. Stress concentration is similar for both specimens; however, in the region of interest where the crack is located, the stress value is larger (approximately 1%) in specimen 1 (Fig. 14).

The fatigue safety factor (FSF) is defined as a contour plot of the factor of safety with respect to a fatigue failure at a given design life (standard value of  $1 \cdot 10^9$  cycles) [29, 30]. Fig 15 depicts the direct influence of the geometric variable defining longitudinal spacing on the determination of the FSF distribution for specimen 2.

The influence on the determination of the FSF value also results in a modification of the weight; the weight variable is determined for each combination formed by both specimens and longitudinal spacing values (Table 3).

Tab. 3. Weight comparison (in kg) for each combination of specimens and longitudinal spacing values

		Specimen 1	Specimen 2
Spacing (mm)	400	1.97	2.06
	500	2.65	2.74
	600	3.32	3.41

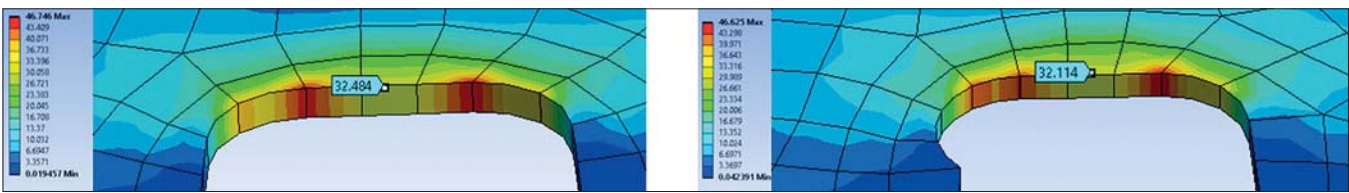


Fig. 14. Comparison between the von Mises stress (MPa) between both specimens in the region of interest

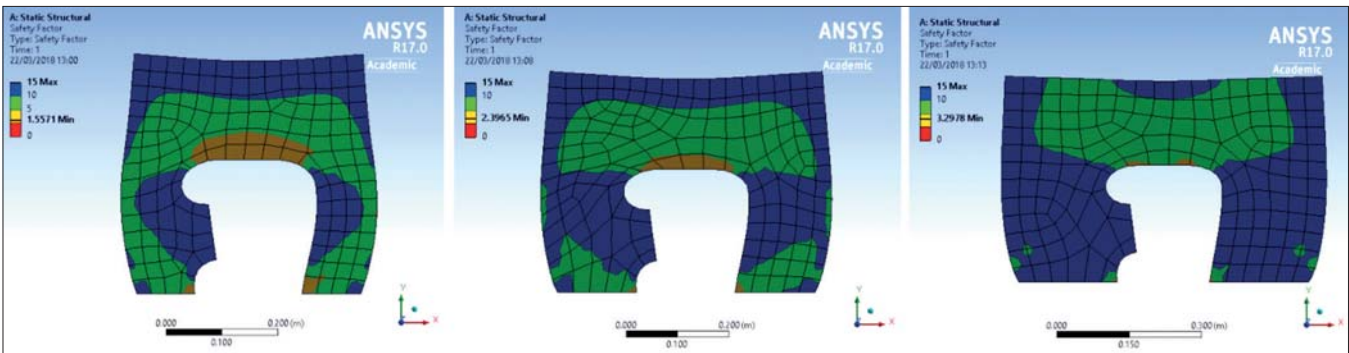


Fig. 15. Evolution of the FSF in specimen 2 for the different values of longitudinal spacing (400, 500, and 600 mm, respectively)

Fig. 16 shows the comparison of the behavior of the weight variable and the value of the minimum FSF under modifications of the longitudinal spacing for specimen 2.

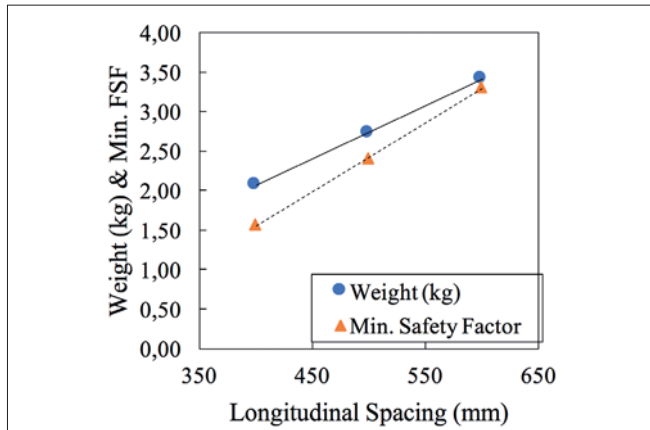


Fig. 16. Comparison of the evolution of the data concerning the weight and the minimum FSF in specimen 2 caused by modifications of the longitudinal spacing

Since the sub model is located in a transverse web whose dimensions are constant because the main particulars of the vessel do not change, the state of loads acting on the specimens maintains its initial value in the process of varying the thickness and longitudinal spacing. For the range of longitudinal spacing values, both variables have a linear trend with a sensitivity of min FSF larger than weight (approximately 22%). To mitigate the loss of fatigue life, in terms of the minimum FSF, caused by the reduction of the longitudinal spacing (without the need for additional reinforcement elements), it is necessary to increase the thickness value, and the relationship between both variables (thickness and longitudinal spacing) is established to obtain the same minimum FSF value. An iterative process is conducted wherein it is necessary to fix an initial thickness (20 mm) and initial spacing (600 mm), and to make the extrapolation of the results more reliable for introducing two intermediate points (550 mm and 450 mm) that correspond to two new longitudinal spacing values. The initial combination of 600 mm longitudinal spacing and 20 mm thickness provides the design fatigue life and, in the range of longitudinal spacing values (400-600 mm), the stiffener and its cut-out (specimen 1 and specimen 2) keep their dimensions unchanged. The necessary increase in thickness is computed to reduce the effect of the decrease in longitudinal spacing and provide the same fatigue life as the initial situation for the same loading history (Table 4).

Tab. 4. Thickness and longitudinal spacing for the same fatigue life (FSF) values

Spacing (mm)	Specimen 1	Specimen 2
	Thickness (mm)	
600	20	20
550	21.8	21.8
500	23.2	23.2
450	26.8	26.6
400	30.5	30.2

There is an inverse relationship between the thickness and longitudinal spacing in the behavior between both variables, and this is determined via statistical treatment through a quadratic local regression model (Table 5 and Fig. 17). For both specimens, the local quadratic, linear, and logarithmic regression models have a correlation coefficient ( $R^2$ ) of 0.99, 0.95, and 0.97, respectively, so the local quadratic regression model is chosen as a better fit than the linear and logarithmic regression model by 3.66 and 1.74%, respectively. For the same decrease in the longitudinal spacing (25%), it is necessary to increase the thickness by 25.4% in specimen 1, while an increase of 24.8% is required for specimen 2.

Tab. 5. Quadratic regression coefficients for specimen 1 and 2 ( $t = as^2 + bs + c$ )

	a	b	c
Specimen 1	0.0002	-0.2234	92.46
Specimen 2		-0.2104	88.76

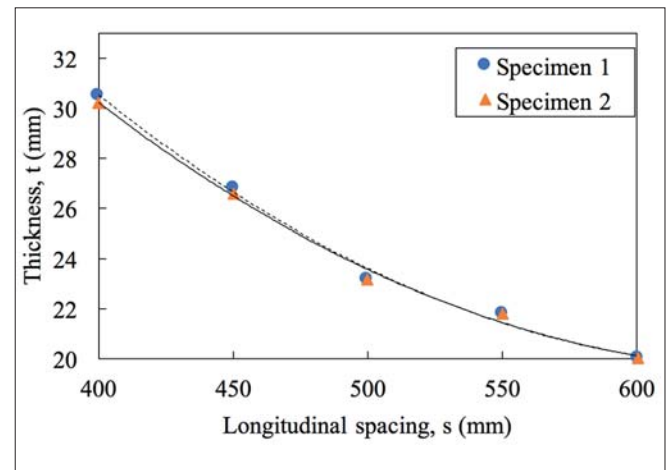


Fig. 17. Relationship between thickness and longitudinal spacing variables using local quadratic regression model for both specimens

## FATIGUE SENSITIVITY CURVES

To consider the possible scenarios that generate load conditions that differ from the original conditions, fatigue sensitivity curves are calculated to provide a valuable tool for designing the structures. Fatigue sensitivity curves are defined as the graphs obtained by joining the points representing the available life for different values of the stress range expressed in terms of the loading history scale factor. The influence of scale factor on the increase and decrease of the stress range based on the initial load in the fatigue life is analyzed and investigated. For each combination between specimens and longitudinal spacing values, 25 possible equidistant variations of the stress ranges are considered, starting from the initial value (scale factor equals one) and extending to  $\pm 50\%$  with respect to the initial value, which includes a total of 150 numerical tests. Fatigue sensitivity curves are superimposed for each case of the three longitudinal spacing values and specimen 1 from the establishment of a standard design life of 1,000,000 cycles (Fig. 18).

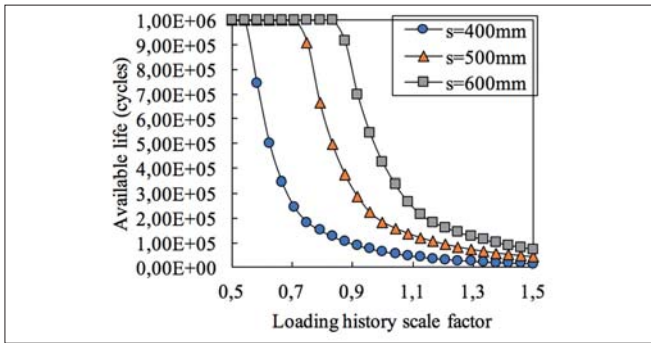


Fig. 18. Fatigue sensitivity curves for specimen 1

The union of all points of the fatigue sensitivity curves propose a possible extrapolation of the results by approximating the point cloud of each sub model tested via a common hyperbola. The sensitivity in terms of the modification of fatigue life tends to be inversely proportional to the scale factor used regardless of the value of the longitudinal spacing, with a very strong decrease in the fatigue life whose values tend to be adjusted as the scale factor increases. Fig. 18 shows the evolution of the fatigue life of specimen 1 for three possible values of the longitudinal spacing as the initial stress range in terms of loading history scale factor is changed. A common pattern is observed in the structural behavior regardless of the value of the longitudinal spacing. The decrease in fatigue life as a consequence of increasing the stress range is more pronounced at lower values of longitudinal spacing and at higher values of stress range (with respect to its design value). The number of fatigue life cycles tends to adjust for the different values of longitudinal stiffening.

### BIAXIALITY INDICATION

Biaxiality indication (BI) is defined as the smaller principal stress divided by the larger principal stress, with the principal stress divided by the principal stress nearest zero being ignored [31]. A biaxiality of 0 corresponds to uniaxial stress, a value of  $-1$  corresponds to pure shear, and a value of 1 corresponds to a pure biaxial state (Fig. 19).

The biaxial stress state of specimen 1 shows a clear increasing trend; however, the value has a convex shape for the rest of the options, and it reaches the maximum for the 500 mm spacing. For the pure shear state, the biaxial stress state trend is decreasing with concave and convex forms, where there is no considerable difference between all sub models and the low

spacing values are quite dispersed, while there is a difference between the sub models at high spacing values. Furthermore, there are only two options where it is slightly increasing but almost imperceptible, and that is for specimen 2 (Fig. 20).

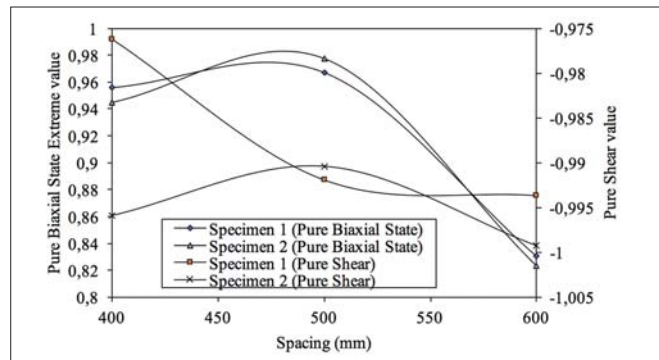


Fig. 20. Pure biaxial state and pure shear for both specimens

The relationship between BI and minimum FSF concepts is established; the zone of low values of the FSF corresponds with a uniaxial stress state, and the next zone, in the order of importance, is the cut-out vertical surroundings where the pure shear stress state predominates. Finally, in the load side and low values of longitudinal spacing governs the pure biaxial stress state.

### CRACK GROWTH

From experimental tests, the crack growth process is obtained by characterizing the crack length and the number of load cycles applied, and a quadratic regression model is established from nine ( $n = 9$ ) measurements (Fig. 21).

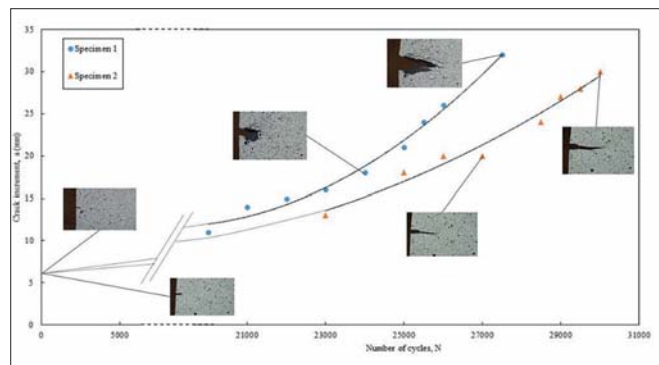


Fig. 21. Evolution of crack length (a) for the number of cycles for both specimens

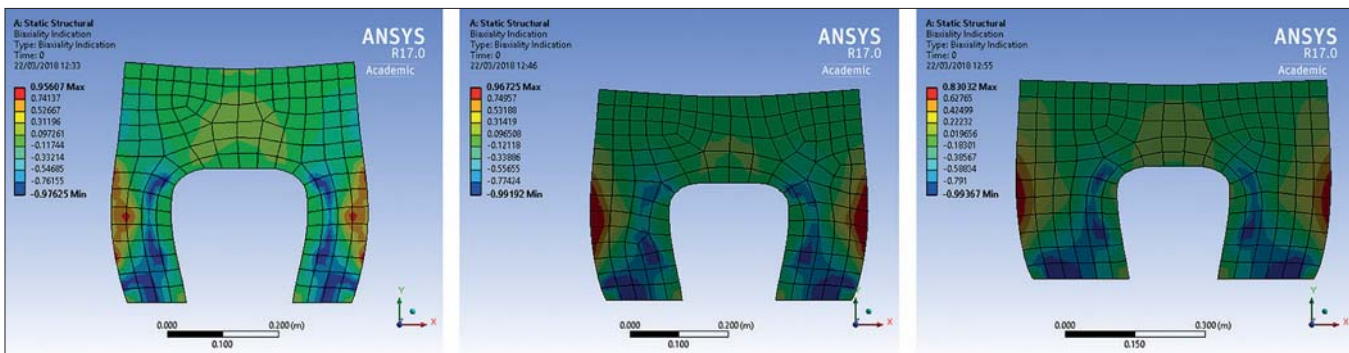


Fig. 19. Distribution of biaxiality indication for specimen 1 and each of the values of the longitudinal spacing (400, 500, and 600 mm)

The procedure comprises crack tip advances by the fatigue following the Paris law [32],

$$\frac{da}{dN} \approx \frac{\Delta a}{\Delta N} = \frac{a_i - a_{i-1}}{N_i - N_{i-1}} = C \Delta K^m \quad (8)$$

where  $C$  and  $m$  represent constants that are dependent on the load and boundary conditions and  $\Delta K$  denotes the range of the stress intensity factor given by

$$\Delta K_i = (K_{\max} - K_{\min}) = (\sigma_{\max} - \sigma_{\min}) \cdot Y(a_{m,i}) \cdot \sqrt{\pi \cdot a_{m,i}}$$

with  $a_m = \frac{a_i + a_{i-1}}{2}$  (9)

where  $Y(a_{m,i})$  denotes a dimensionless geometric factor that updates its value with each crack length in the fracture process depending on specimen geometry, actual crack length  $a_{m,i}$ , and nominal stress  $\sigma$  [33]. Two random increments of the crack size evolution record are studied to obtain the two constants that define the Paris Law, and a system of two equations with two unknowns is acquired from the determination of the maximum and minimum stress level (using the load history and geometry of the specimen) and the crack length associated to that increment. The resolution leads to the expression

$$\frac{da}{dN} = (2.94 \cdot 10^{-8}) \Delta K^{22} \quad (10)$$

The graphical output is represented in a log-log diagram (Fig. 22).

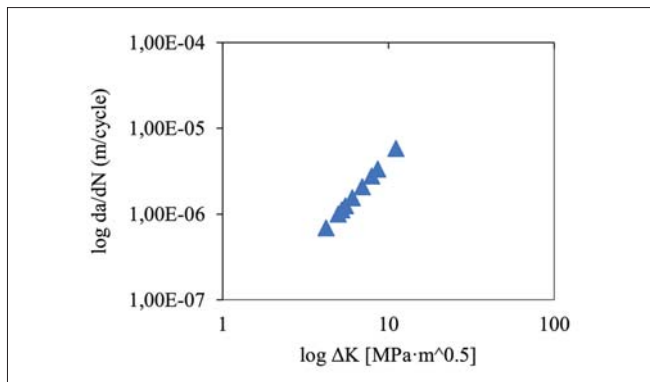


Fig. 22. Relationship between crack propagation rate and stress intensity factor range

The values of the constants that define the crack growth rate from the Paris law are appropriate according to the literature [34]. An analysis of variance (ANOVA) is performed to check the accuracy of the proposed results using a linear regression model (Table 6).

Tab. 6. Analysis of variance (ANOVA)

Concept	Degrees of freedom	Sum of squares	Mean squares
Sum of Squares Regression (SSR)	1	$2.06 \cdot 10^{-11}$	$2.067 \cdot 10^{-11}$
Sum of Squares Error (SSE)	n-2	$5.61 \cdot 10^{-13}$	$8.02 \cdot 10^{-14}$
Sum of Squares Total (SST)	n-1	$2.12 \cdot 10^{-11}$	-

The difference between the measured value and the set value using the regression model (SSE) is obtained from the residuals plot (Fig. 23) from the regression line (with their respective standard error;  $3.24 \cdot 10^{-7}$  for the y-intercept and  $4.61 \cdot 10^{-8}$  for the slope). The statistical model obtains a standard error of the regression model of  $2.83 \cdot 10^{-7}$ , a correlation coefficient ( $R^2$ ) of 0.97, and an F-factor of 257.63.

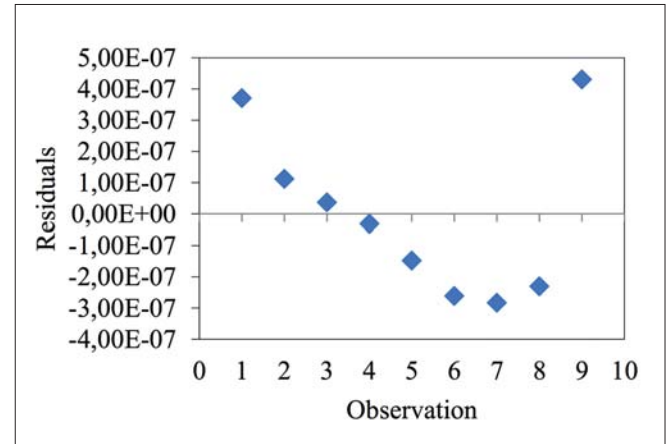


Fig. 23. Residuals plot

## STRESS INTENSITY FACTOR

The stress intensity factor (SIF) is used as the controlling parameter for evaluating the critical state of a crack and for determining the design criteria and structural behavior. Fig. 24 shows the relationship between the crack length and the SIF value for each tested specimen from a numerical approach.

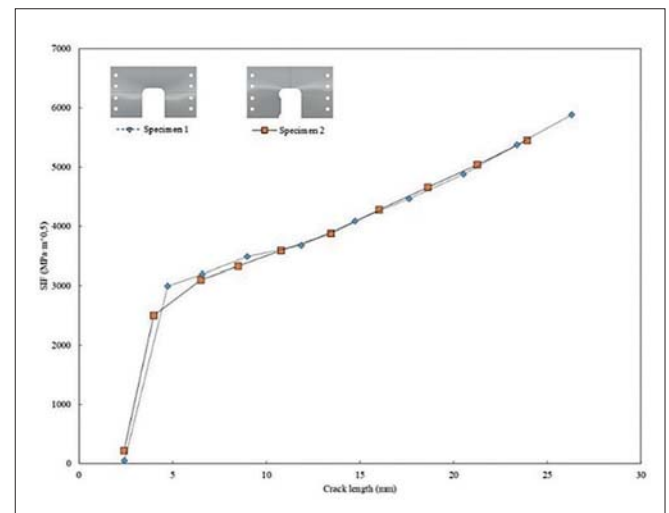


Fig. 24. Evolution of the maximum value of the stress intensity factor in both specimens in the crack growth process

The distribution of the SIF on the crack front is characterized by the non-uniformity of SIF during the crack growth process, regardless of the specimen geometry. Fig. 25 reports the non-uniform value of the SIF for two crack lengths in specimen 1.

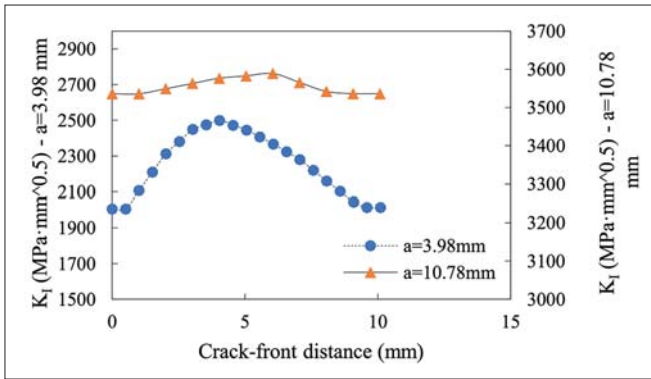


Fig. 25. Stress intensity factor variation on the crack-front in specimen 1

Fig. 26 shows the same previous case from the point of view of the structural assessment.

From the obtained results, the SIF distribution at the crack front cannot be used as a design parameter due to the non-uniformity of the stress intensity factor along the crack front for each of the tested specimens. However, it can be used in terms of the maximum value because it follows a linear trend along the crack growth process (Fig. 26) that can be extrapolated by a linear regression model and used in the design as a merit value. Table 7 shows the coefficients of the linear regression model for each of the specimens and the correlation coefficient ( $R^2$ ) from the data represented in Fig. 24.

Tab. 7. Linear regression model ( $SIF = m \cdot a + n$ ) for each specimen on the behavior at the maximum SIF value under crack growth (a)

	m	n	$R^2$	Mean error (%)
Specimen 1	145.33	2238.1	0.9861	1.39
Specimen 2	119.8	2217.1	0.9929	0.71

## CONCLUSIONS

This study reported an experimental procedure for determining the mechanical behavior and fatigue design of a typical marine structure based on different geometries of specimens, obtaining the best of them in structural terms, and

determining the degree of influence and relationship between the variables that define the study model and the boundary conditions present. Based on the results, it can be concluded that specimen 2 has a slight improvement over specimen 1 and that the decision to modify the longitudinal spacing variable has a significant influence on the determination of fatigue life. This fact was determined by a larger material arrangement, and the decision to increase the FSF with the cost of the weight increase was justified from a structural behavior point of view because the tendency to increase the FSF was greater than that of the weight at equal modifications of the longitudinal spacing.

A quadratic relationship was observed between the variables thickness and longitudinal stiffener spacing that allows for the extrapolation of the fatigue life behavior of the specimens in the presence of modifications in any of its variables. The hyperbolic character that correlated the fatigue life variable with the variation of the stress range of the loading history was obtained independently of the value of the variable that defined the longitudinal spacing. The constants of the Paris law were determined (which are validated according to the statistical values that support the proposed regression model) and consequently, the structural behavior of this type of structure is obtained. These results can be extrapolated to other ships with similar geometric structural details.

Obtaining the SIF in the crack front in the crack propagation procedure leads to two conclusions: the SIF exhibits an increasing linear trend as the crack front advances regardless of the specimen tested, and there is no relationship of similarity and extrapolation of the SIF value between both specimens and between different crack lengths within the crack growth process of the same specimen. The magnitude of KI varies along the crack front, and this variation depends on the specimen thickness and boundary conditions.

## REFERENCES

1. W. Fricke, A. Von Lileienfeld-Toal, and H. Paetzoldt, "Fatigue strength investigations of welded details of stiffened plate

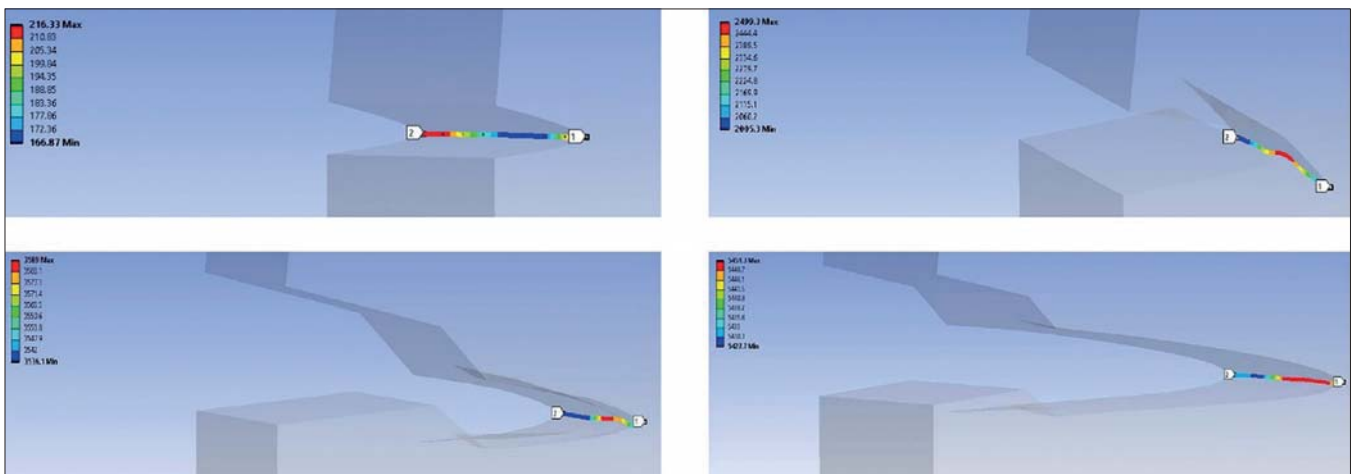


Fig. 26. Time evolution of the stress intensity factor on the crack front in specimen 1

- structures in steel ships,” *International Journal of Fatigue*, vol. 34(1), pp. 17–26, 2012. doi: 10.1016/j.ijfatigue.2011.01.021.
2. J. Kuniala, “Fatigue Analysis of 3-Dimensional Ship Structural Detail,” Aalto University School of Engineering. Thesis for the degree of Master of Science in Technology, 2016.
  3. W. Fricke, “Fatigue analysis of welded joints: state of development,” *Marine Structures*, vol. 16(3), pp. 185–200, 2003. doi: 10.1016/S0951-8339(02)00075-8.
  4. W. Fricke, O. Doerk, and C. Weissenbord, “Comparison of different calculation methods for structural stresses at welded joints,” *International Journal of Fatigue*, vol. 25(5), pp. 359–369, 2003. doi: 10.1016/S0142-1123(02)00167-6.
  5. W. Fricke and H. Paetzold, “Full-scale fatigue tests of ship structures to validate the S-N approaches for fatigue strength assessment,” *Marine Structures*, vol. 23(1), pp. 115–130, 2010. doi: 10.1016/j.marstruc.2010.01.004.
  6. I. Lotsberg, “Fatigue design of plated structures using finite element analysis,” *Ships and Offshore Structures*, vol. 1(1), pp. 45–54, 2006. doi: 10.1533/saos.2005.0006.
  7. W. Fricke, “Recent developments and future challenges in fatigue strength assessment of welded joints,” *Proc Inst Mech Eng C J Mech Eng Sci.*, vol. 229(7), pp. 1224–1239, 2014. doi: 10.1177/0954406214550015.
  8. K. Tran Nguyen, Y. Garbatov, and C. Guedes Soares, “Fatigue damage assessment of corroded oil tanker details based on global and local stress approaches,” *International Journal of Fatigue*, vol. 43, pp. 197–206, 2012. doi: 10.1016/j.ijfatigue.2012.04.004.
  9. M. Aygül, “Fatigue Analysis of Welded Structures Using the Finite Element Method,” Thesis for the Degree of Licentiate of Engineering. Chalmers University of Technology, 2012.
  10. I. Poutiainen, P. Tanskanen, and G. Marquis, “Finite element methods for structural hot spot stress determination - a comparison of procedures,” *International Journal of Fatigue*, vol. 26(11), pp. 1147–1157, 2004. doi: 10.1016/j.ijfatigue.2004.04.003.
  11. Z. Wang, “Fatigue Behavior and Failure Assessment of Plate Connections in Ship Shaped Structures,” PhD thesis. National University of Singapore, 2008.
  12. H. M. Westergaard, “Bearing Pressures and Cracks,” *Journal of Applied mechanics*, vol. 6, pp. A49–53, 1939.
  13. G. R. Irwin, “Analysis of stresses and strains near the end of a crack traversing a plate,” *Journal of Applied mechanics*, vol. 24, pp. 361–364, 1957.
  14. M. L. Williams, “On the Stress Distribution at the Base of a Stationary Crack,” *Journal of Applied mechanics*, vol. 24(1), pp. 109–114, 1956.
  15. F. Erdogan and G. C. Sih, “On the crack extension in plates under plane loading and transverse shear,” *Journal of basic Engineering*, vol. 85(4), pp. 519–527, 1963. doi: 10.1115/1.3656897.
  16. M. Hussain, S. Pu, and J. Underwood, “Strain energy release rate for a crack under combined mode I and mode II,” *Proceedings of the 1973 National Symposium on Fracture Mechanics, Part II* (ASTM International), pp. 2–28, 1974. doi: 10.1520/STP33130S.
  17. M. Chafi and A. Boulenouar, “A Numerical Modelling of Mixed Mode Crack Initiation and Growth in Functionally Graded Materials,” *Materials Research*, vol. 22(3), pp. e20180701, 2019. doi: 10.1590/1980-5373-mr-2018-0701
  18. A. Carpinteri, “Stress-singularity and generalized fracture toughness at the vertex of re-entrant corners,” *Engineering Fracture Mechanics*, vol. 26(1), pp. 143–155, 1987. doi: 10.1016/0013-7944(87)90086-5.
  19. M. Strandberg, “Fracture at V-notches with contained plasticity,” *Engineering Fracture Mechanics*, vol. 69(3), pp. 403–415, 2002. doi: 10.1016/S0013-7944(01)00079-0.
  20. J. D. Carroll, W. Abuzaid, J. Lambros, and H. Sehitoglu, “High resolution digital image correlation measurements of strain accumulation in fatigue crack growth,” *International Journal of Fatigue*, vol. 57, pp. 140–150, 2013. <https://doi.org/10.1016/j.ijfatigue.2012.06.010>.
  21. J. Blaber, B. Adair, and A. Antoniou, “NCorr: Open-Source 2D Digital Image Correlation Matlab Software,” *Experimental Mechanics*, vol. 55, pp. 1105–1122, 2015. doi: 10.1007/s11340-015-0009-1.
  22. R. Branco, F. V. Antunes, J. A. Martins Ferreira, and J. M. Silva, “Determination of Paris law constants with a reverse engineering technique,” *Engineering Failure Analysis*, vol. 16, pp. 631–638, 2009. doi: 10.1016/j.engfailanal.2008.02.004.
  23. I. Galic, I. Cular, V. Kresimir, and Z. Tonkovic, “Comparison of SIF solutions obtained by XFEM and conventional FEM or cracks in complex geometries like valve body,” *Procedia Structural Integrity*, vol. 13, pp. 2109–2113, 2018. doi: 10.1016/j.prostr.2018.12.200.
  24. N. Möes, J. Dolbow, and T. Belytschko, “A finite element method for crack growth without remeshing,” *International Journal for Numerical Methods in Engineering*, vol. 46, pp. 131–150, 1999. doi:10.1002/(sici)1097-0207(19990910)46:1%3c131::aid-nme726%3e3.0.co;2-j.

25. F. Zhou, J. Molinari, and Y. Li, "Three-dimensional numerical simulations of dynamic fracture in silicon carbide reinforced aluminium," *Engineering Fracture Mechanics*, vol. 71, pp. 1357–1378, 2004. doi: [https://doi.org/10.1016/S0013-7944\(03\)00168-1](https://doi.org/10.1016/S0013-7944(03)00168-1).
26. A. O. Ayhan, "Three-dimensional fracture analysis using tetrahedral enriched elements and fully unstructured mesh," *International Journal of Solids and Structures*, vol. 48, pp. 492–505, 2011. doi: <https://doi.org/10.1016/j.ijsolstr.2010.10.012>.
27. W. Huang, Y. Garbatov, and C. Guedes Soares, "Fatigue reliability assessment of a complex welded structure subjected to multiple cracks," *Engineering Structures*, vol. 56, pp. 868–879, 2013. doi: <https://doi.org/10.1016/j.engstruct.2013.06.011>
28. T. Ulleland and M. Svensson, "Stress Concentration Factors in Side Shells Longitudinals Connected to Transverse Webframes," *Proceedings of the Eleventh International Offshore and Polar Engineering Conference*, 2001.
29. M. S. Vidhya and K. V. M. Christina, "Fatigue Life, Fatigue Damage, Fatigue Factor of Safety, Fatigue Sensitivity, Biaxiality Indication and Equivalent Stress of a Radial Connecting Rod," *International Research Journal of Engineering and Technology*, vol. 7(9), pp. 1499–1502, 2020.
30. H. R. Wasmi, M. Q. Abdullah, and O. A. Jassim, "Testing and Estimation Fatigue Life of a Flange Connection used in Power Plant by ANSYS," *International Journal of Current Engineering and Technology*, vol. 6(4), pp. 1302–1306, 2006.
31. A. Bhanage and K. Padmanabhan, "Design for fatigue and simulation of glass fibre/epoxy composite automobile leaf spring," *ARPN Journal of Engineering and Applied Sciences*, vol. 9(3), pp. 196, 2014.
32. P. C. Paris and F. Erdogan, "A critical analysis of crack propagation laws," *Journal of Basic Engineering*, vol. 85 (4), pp. 528–534, 1963. doi: 10.1115/1.3656900.
33. N. Perez, *Fracture Mechanics*. Springer US, 2004.
34. M. Mlikota, S. Staib, S. Schmauder, and Z. Bozic, "Numerical determination of Paris law constants for carbon steel using a two-scale model," *Journal of Physics: Conference Series*, vol. 843, pp. 012042, 2017. doi: 10.1088/1742-6596/843/1/012042.

## CONTACT WITH THE AUTHORS

**Arturo Silva-Campillo**  
e-mail: [a.silva@upm.es](mailto:a.silva@upm.es)

Universidad Politécnica de Madrid  
Avenida de la Memoria  
28040 Madrid  
**SPAIN**

**Juan Carlos Suárez-Bermejo**  
e-mail: [juancarlos.suarez@upm.es](mailto:juancarlos.suarez@upm.es)

Universidad Politécnica de Madrid  
Avenida de la Memoria  
28040 Madrid  
**SPAIN**

**Miguel Ángel Herreros-Sierra**  
e-mail: [miguelangel.herreros@upm.es](mailto:miguelangel.herreros@upm.es)

Universidad Politécnica de Madrid  
Avenida de la Memoria  
28040 Madrid  
**SPAIN**

## JOINTS OF STEEL SANDWICH STRUCTURES

Janusz Kozak

Gdańsk University of Technology, Poland

\* Corresponding author: [kozak@pg.edu.pl](mailto:kozak@pg.edu.pl) (J. Kozak)

### ABSTRACT

*Steel sandwich structures are perceived as alternatives to single-skin welded structures in the shipbuilding industry due its advantages like significant reduction of mass in relation to typical single skin structure. However, beside problems with their strength properties itself, applications in real structures requires of solving the problem of joining, both for connection sandwich to sandwich as well as sandwiches to single-shell structures. Proper design of joints is connected with some factors like lack of attempt to interior of panel, introduction of additional parts and welds with completely different stiffness. In the paper the results of laboratory fatigue tests of selected joints as well as numerical calculation of stressed for different kind of joints of sandwich structures are presented. As result of calculations optimisation of geometry for selected joints is performed.*

**Keywords:** steel sandwich; joints; strength; laboratory test

### INTRODUCTION

Modern ship represents complex engineering object consists of wide spectrum of materials and requires often sophisticated manufacturing technologies. Among modern materials can be mentioned: composites [1], [2] or with elastic memory [3]. Such materials are often used in yacht [4] or floating objects like ramps [5]. In the same time new joining techniques like underwater welding [6], [7] has been introduced and these have also had an impact on the shipbuilding industry.

One example is laser welding techniques, which have slowly started to prove their potential as alternative methods of joining. Such capabilities give the chance of changing the configuration of a typical ship skin structure into a “steel sandwich” representing two shells connected by an internal system of thin stiffeners (webs). A typical representative of such a structural part is a steel or aluminium panel manufactured from two shell plates of 3–4 mm in thickness, internally supported by a one directional system of stiffeners of ~40 mm in depth, with all components connected by laser welding, as shown in Fig. 1a.

The introduction of internal stiffeners makes possible to create required strength characteristics of panel. Examples of the possible forms for stiffeners are shown in Fig. 1b.

One of the barriers for overcoming the application of such panels in ship structures is joining, for both one panel to another and a panel to a classical single-skin structure. The joining problem arises from both the closing of internal space of the panel and from the disproportion of thicknesses of shell plating. Such a problem generates the necessity for new designs of such joints [8, 9].

### METHODS FOR JOINING OF PANEL STRUCTURES

Among the methods for the joining of panel structures, one can distinguish mechanical (bolts, riveting and kneading), thermal (welding) or chemical (bonding) methods. Bonded joints have significant advantages, such as a lack of stresses and deformation due to cold junctions in comparison to welding

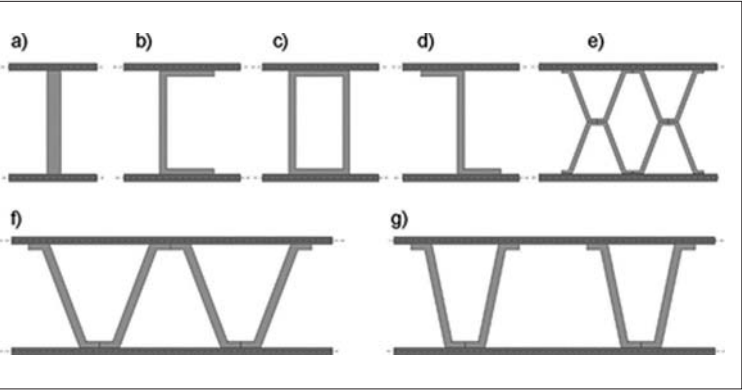


Fig. 1. a) Panel type I-core and b) potential configuration of stiffeners

processes. A significant disadvantage of these joints is their low resistance at higher temperature. Impact and vibration load resistance are also subjects of study [10].

Problems regarding the joining of metals by bonding have been the subject of several research projects. One of the proposed solutions is using intermediate elements fixed by bonding by: epoxy resin, polyurethane or cellular concrete. Examples of such proposals are presented in Fig. 2 [11].

For the above-mentioned reasons, welding remains a fundamental method for joining. The geometry of joints can be done by some approaches; for instance, by dedicated

prefabricated joining elements like square tubes, angle bars or directly by tabled joints [12]. One can find some other solutions, as presented in Fig. 3. Most simply direct butt joint of faces of skin is not applicable due to technological reasons – butt weld of shell plating thickness of 2.5 mm not guarantee proper quality of weld as well as stiffness and strength parameters.

An angular connection can be done using a similar method, as illustrated in Fig. 4.

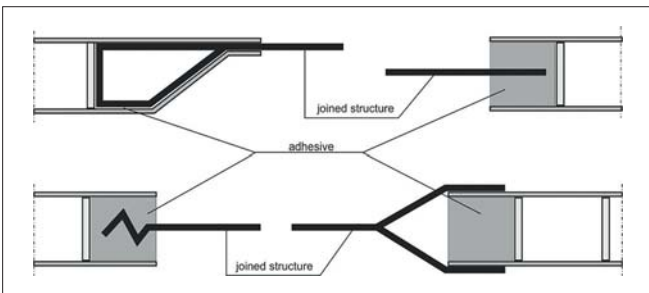


Fig. 2. Selected proposals for bonded joints [11]

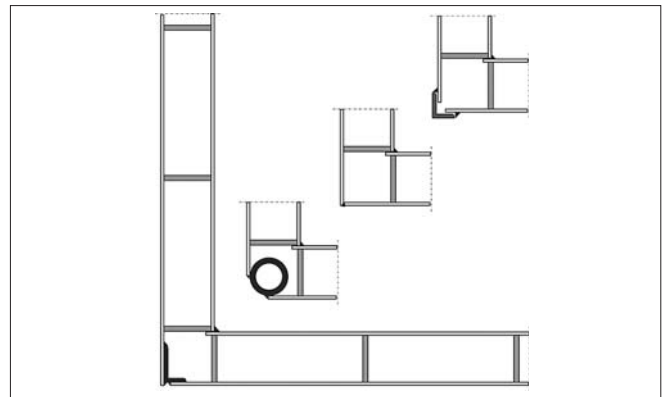


Fig. 4. Examples for panel-panel angular connection

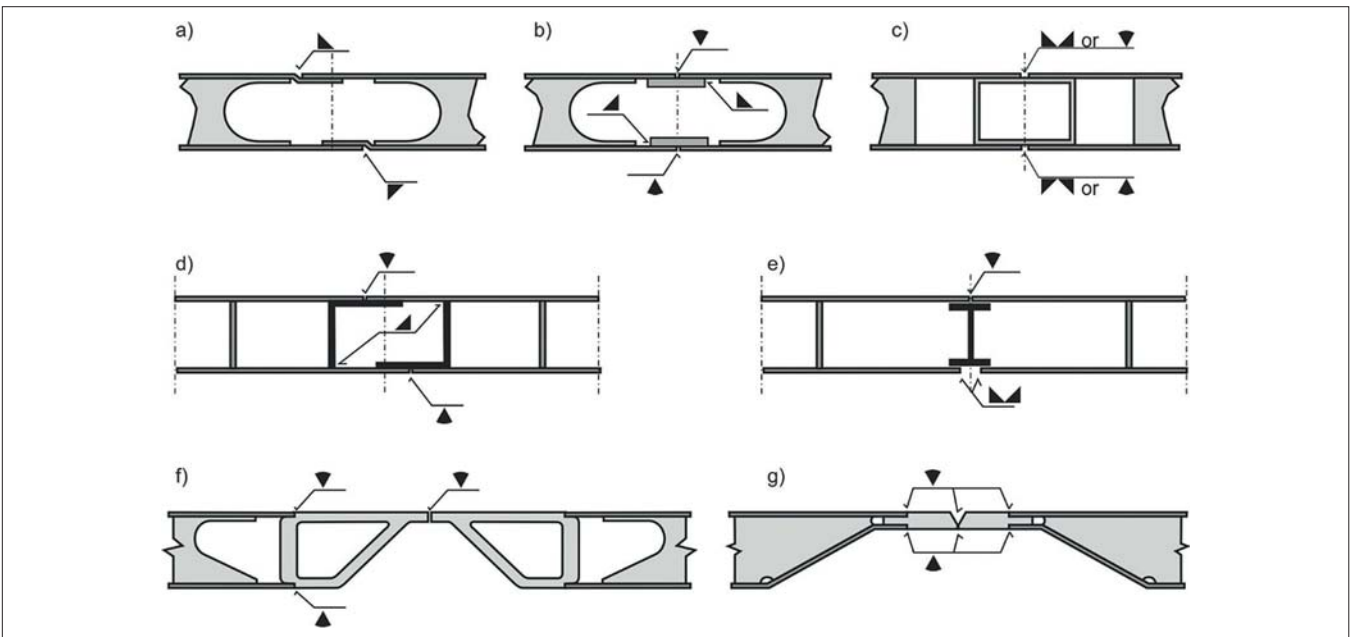


Fig. 3. Examples of butt welded panel-panel joints: a) without additional parts; b) by flat bar; c) by square tube; d), e) by rolled profile; f), g) with reduction of thickness

## LABORATORY TEST OF NATURAL SCALE SANDWICH-SANDWICH JOINTS

Due to problems with the theoretical modelling of strength properties of sandwich panels, especially regarding their fatigue [13], [14], laboratory tests of natural scale structures are still the most credible source of information [15].

Two variants of joints were subjected to testing: by flat bar with a thickness of 2.5 mm (Fig. 3b) and by square tube with dimensions of 40×40×3 mm (Fig. 3c). For comparison, the same geometry of panel without joint was tested on a specimen width of 200 mm. All specimen were made from panels of plates thickness 2.5 mm, stiffened by flat bars 40×4 mm 120 mm spanned. Figure 5 shows the specimen ready for testing and model on the test stand is shown in Fig. 6. Application of load via actuator 250 kN was controlled by Instron Labtronic 8800 system.



Fig. 5. Model of joint during preparation

All models were tested under sinusoidal load with a stress ratio  $R = 0$ .



Fig. 6. Model during test

An example of destruction is presented in Fig. 7. Analysis of the process of failure shows that both types of joint fatigue crack initiates in the middle part of joint, in fusion line of one of joining weld and propagates in the joining element to the edge of specimen, towards the weld.

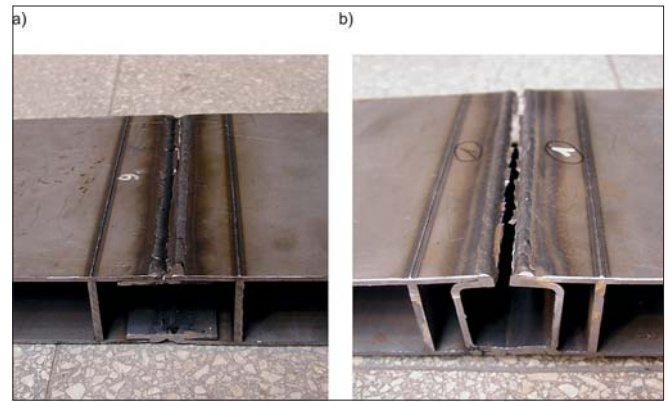


Fig. 7. Example of destruction: a) joint by flat bar; b) joint by square tube

A summary of the test results is presented in Fig. 8.

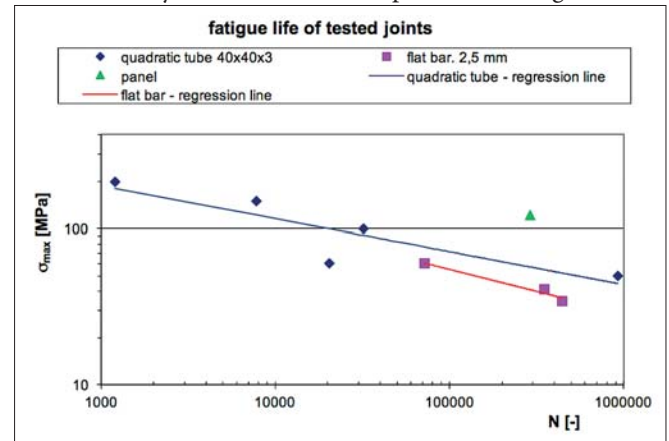


Fig. 8. Fatigue test results for selected joints

The analysis of the presented results shows that the fatigue life of the joint by flat bar is lower than for the square tube; however, the results for both joints present lower durability than the pure panel itself. The qualitative results are presented in Fig. 9.

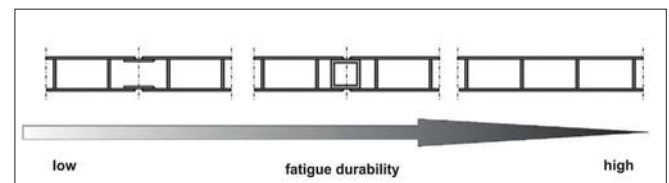


Fig. 9. Quantitative presentation of fatigue life of tested joints

## PARAMETRIC STUDY OF GEOMETRY FOR SELECTED JOINTS

As discussed, there are some problems with the theoretical modelling of the strength properties of sandwich panels. The specific geometry and material structure of the laser-welded joints require very careful modelling of the geometry of the laser weld, material zones around it, as well as some phenomena occurring under load. The laser weld while loading passes

three operation stages [15, 16]: rotation of the joined elements; contact of the plating with the stiffener; common displacement of the plating and the stiffener in the same direction. In order to reflect the nature of rotation, relevantly defined “contact regions” must be introduced at selected stiffener edges.

As presented above, the fatigue life of the tested joints presents significant diversification. Such a wide spectrum of results suggests the need for an individual approach to a given configuration, load-boundary condition and due to the complex geometry, this optimisation must be multi-parametric. One possibility for such an optimisation is acquisition of knowledge on properties of particular solution of joint like stress to weight ratio in the form of a catalogue based upon parametrised numerical solutions. Part of such an approach is presented below for selected geometries of butt panel-panel joints. Calculations are carried out for the geometries presented in Fig. 10.

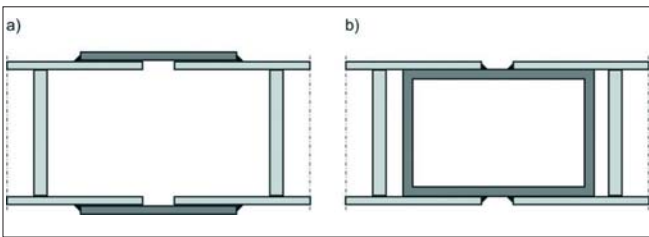


Fig. 10. Variants of geometry of analysed joints: a) cover plate; b) quadratic tube [17]

The model was made using ~15000 elements with applied double symmetry (minimum length element side of 0.1 mm) with both tension and compression loads. For modelling PLANE 183 element form ANSYS library have been used. The numerical model with its boundary and load conditions is presented in Fig. 11a [17].

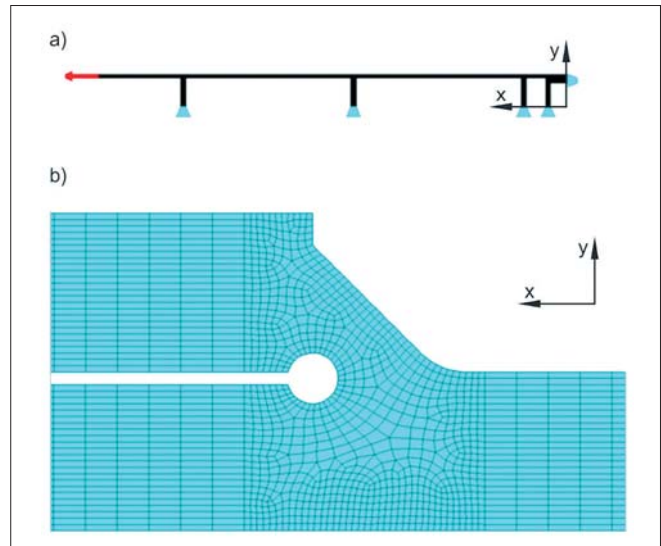


Fig. 11. Model of joint by square tube: a) boundary and load conditions; b) mesh [17]

To model the real behaviour of a laser welded joint, a circular concentrator was introduced to avoid singularity in some region of the joint [14]. The details of the model with the concentrator are presented in Fig. 11b.

The shell plating thickness, the height of the stiffeners and the density of the core material are treated as independent variables, while the geometry of the joint was linked to one, characteristic size and this parameter was treated also as a dependent variable.

The applied parametric variables are presented for both cases in Fig. 12. The height of the stiffener was constant at  $h_w = 40$  mm, the stiffener distance was 120 mm and the shell plate thickness was also constant at  $t_f = 2.5$  mm.

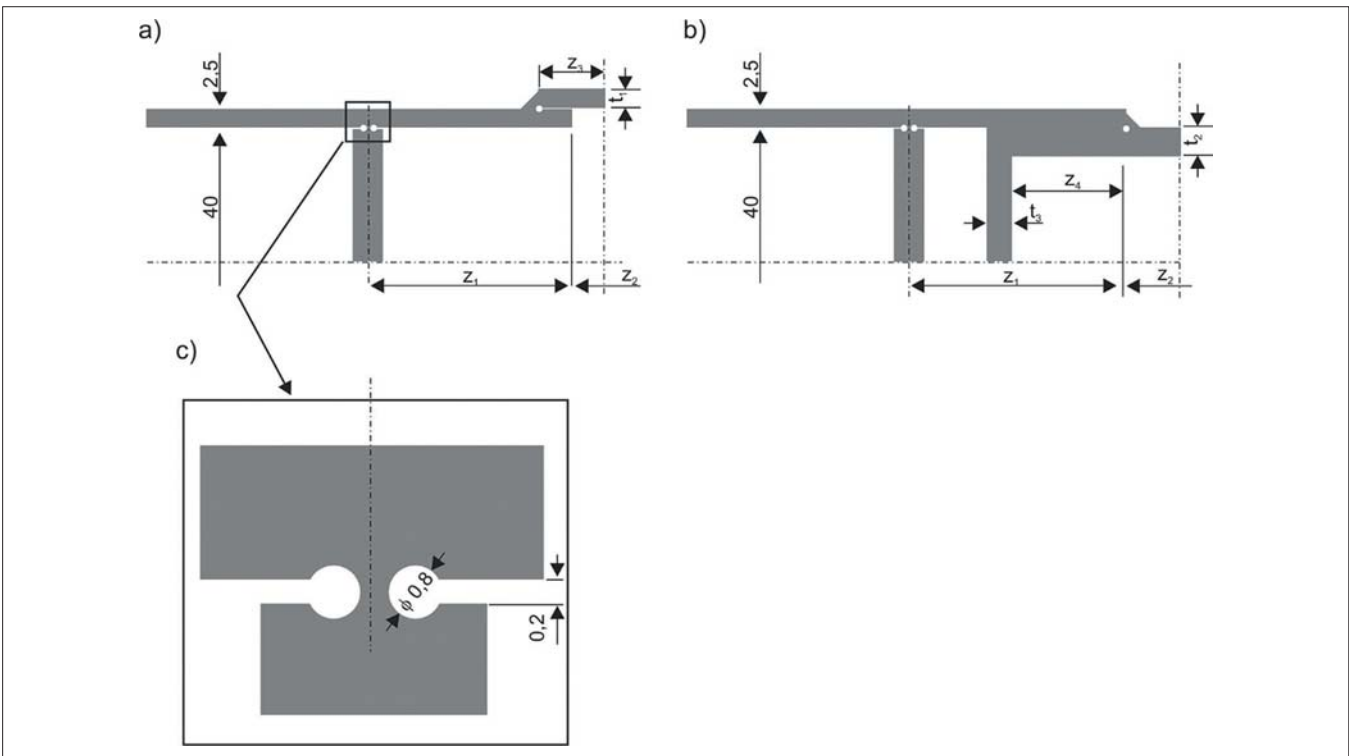


Fig. 12. Geometry and variables assumed for calculation of joints: a) by cover plate; b) by quadratic tube; c) model of connection between shell and stiffener

## MODEL OF JOINT BY COVER PLATE

The applied variation range of parameters describing the geometry during the parametrisation process of the model is presented in Fig. 13.

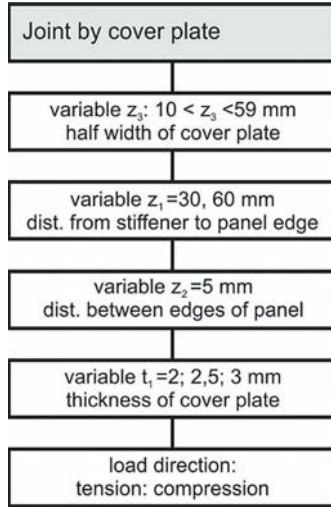


Fig. 13. Range of variation of parameters describing geometry

For the sake of comparison, calculations for different geometries and uniformisation of stresses were made by introducing of a geometric concentration factor  $k_g$ , defined as:

$$k_g = \frac{\sigma_{\max, \text{red.}}}{\sigma_{\text{nom}}},$$

where:

$\sigma_{\max, \text{red.}}$  – maximal reduced stresses of Huber-Mises;

$\sigma_{\text{nom}}$  – nominal stresses,  $\sigma_{\text{nom}} = \frac{P}{A}$ ;

$P$  – load;

$A$  – cross section of model area.

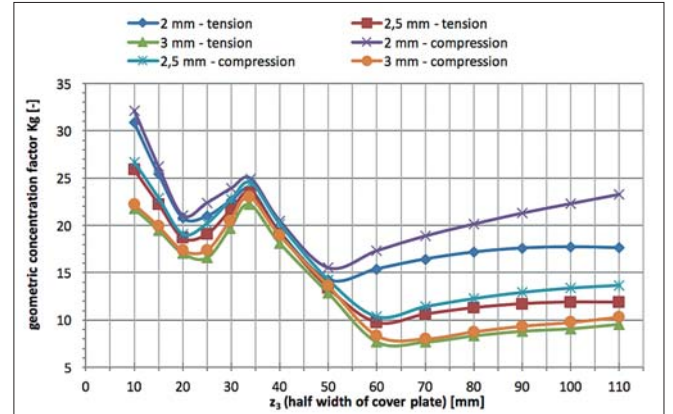


Fig. 13 Geometric concentration factor  $k_g$  for joint of panels by cover plate for  $z_1 = 30$  mm

Figure 13 shows the geometric concentration factor  $k_g$  for joint of panels by cover plate for  $z_1 = 30$  mm.

Due to the wide range of parameters applied for clarity of presentations, three-dimensional diagrams are presented below, where the vertical axis represents the geometric concentration factor  $k_g$  and each configuration of parameters is represented by one point in the diagram. For better visualisation of the results, smoothed surfaces using the distance-weighted smallest square method with Statistica were made.

Figure 14 shows the variation of geometric concentration factor  $k_g$  for the cover plate joint for two distances of panel edge from the first stiffener axis (see variable  $z_1$  in Fig. 12) for  $z_1 = 30$  mm in Fig. 14a and for  $z_1 = 60$  mm in Fig. 14b.

Analysis of Fig. 14 shows that it is possible to find local minimum of  $k_g$  both for thickness and for the width of the cover plate.

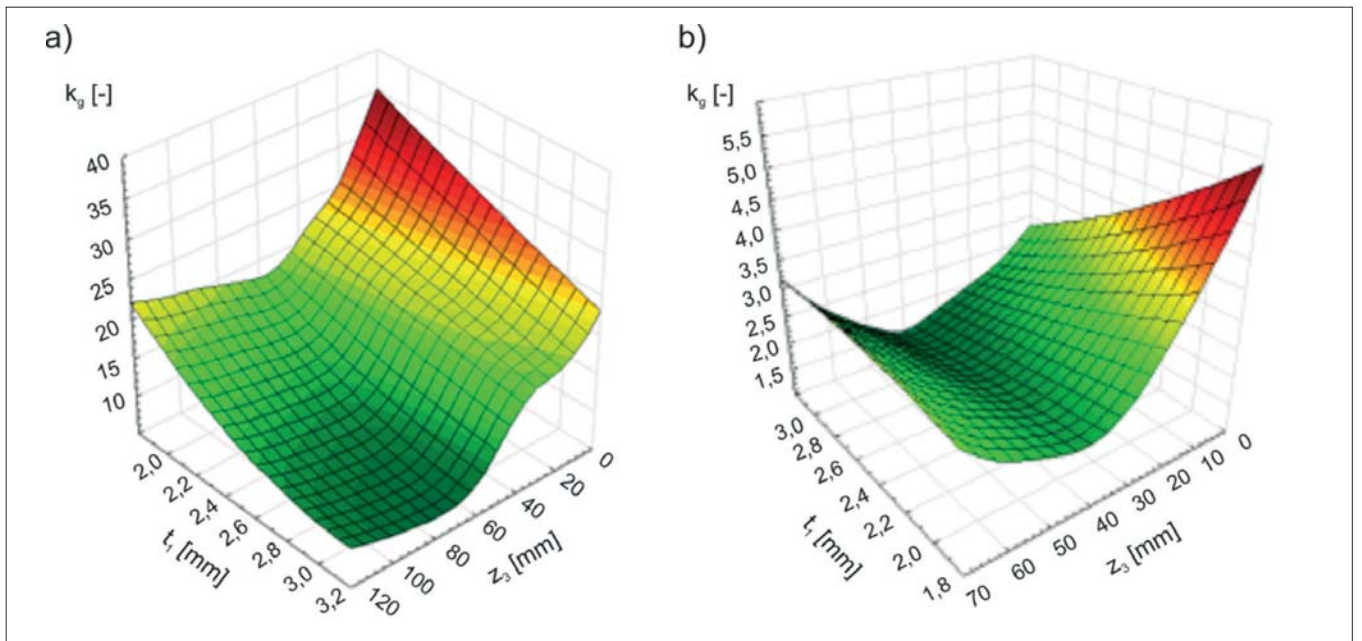


Fig. 14. Variation of geometric concentration factor  $k_g$  for cover plate joint for two values of distance of panel edge from first stiffener axis (see variable  $z_1$  in Fig. 12): a)  $z_1 = 30$  mm; b)  $z_1 = 60$  mm

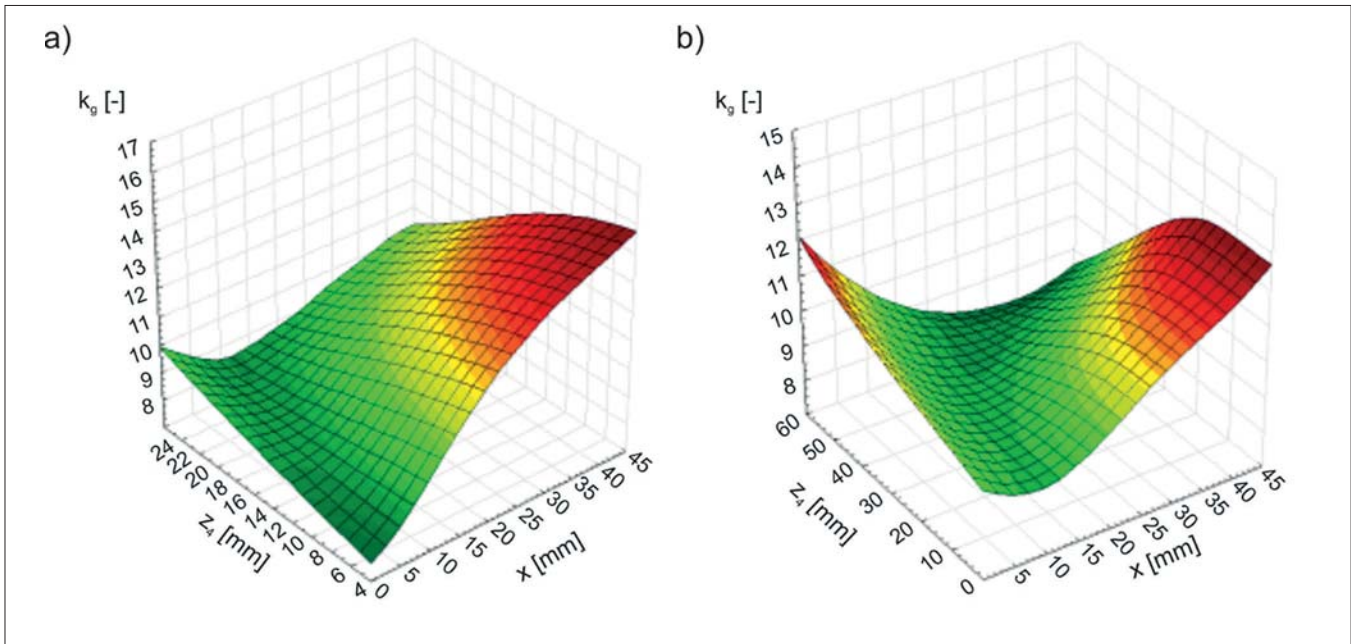


Fig. 15. Variation of geometric concentration factor  $k_g$  for quadratic tube joint for two values of distance of panel edge from first stiffener axis (see variable  $z_1$  in Fig. 12b): a)  $z_1 = 30$  mm; b)  $z_1 = 60$  mm, where:  $z_1$  - distance of panel edge from first stiffener axis (mm) (Fig. 12b);  $z_4$  - insertion of tube into panel (mm) (Fig. 12b);  $x$  - coordinate of location of point of stress concentration (mm)

## MODEL OF JOINT BY QUADRATIC TUBE

Following the approach presented for the cover plate joint, the same calculations were made for the joint by quadratic tube. Figure 15 shows the variation of geometric concentration factor  $k_g$  for the quadratic tube joint as a function of insertion of tube into the panel (see variable  $z_4$  in Fig. 12b), as well as the distance from the centre line of joint  $x$  for two values of distance of panel edge from the first stiffener axis (see variable  $z_1$  in Fig. 12b): for  $z_1 = 30$  mm in Fig. 15a and for  $z_1 = 60$  mm in Fig. 15b.

Similarly to the cover plate joint, one can distinguish a clear minimum of  $k_g$ , suggesting the existence of the optimal geometry of such a joint. By comparing the minimum of  $k_g$  for both presented geometries, one can find that the concentration coefficient  $k_g$  for the joint with the quadratic tube is significantly lower towards the joint by cover plate.

Figure 16 shows a comparison of the geometric concentration factor  $k_g$  for both joints with different characteristics as a function of relative mass of the joint.

Beside of very low mass of joint to mass of panel ratio one is possible to observe some systematic relationship between geometric concentration factor and this very ratio for profile applied connection. For each type of geometry there is almost linear characteristic of such relation. But for cover plate connection there is region of geometrical parameters, where such relationship reverse its inclination and significant reduction of geometrical concentration factor is observed. It suggest to search optimal geometry on the left side of minimum of such distribution.

Such a parameter set is designed to give direct data to support the optimisation process of the joint geometry.

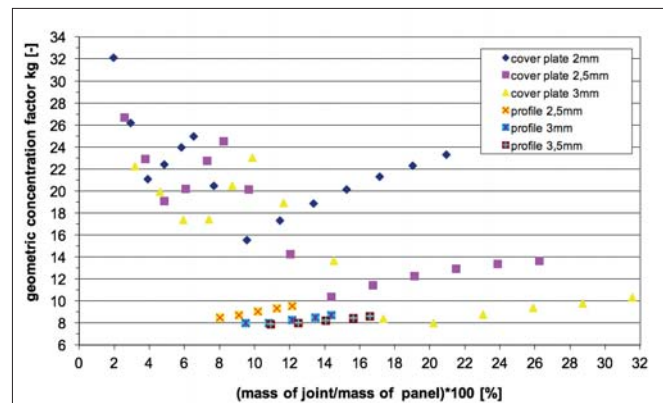


Fig. 16 Comparison of geometric concentration factor  $k_g$  for both joints with  $z_1 = 30$  mm  $z_2 = 10$  mm as a function of relative mass of joint, where: For joint by cover plate half width of cover plate (parameter  $z_3$  Fig. 12a) from left to right

- for cover plate thickness 2 and 2.5 mm: respectively 10, 15, 20, 25, 30, 34, 40, 50, 60, 70, 80, 90, 100 and 110 (mm);

- for cover plate thickness 3 mm: respectively 10, 15, 20, 25, 29, 33, 40, 50, 60, 70, 80, 90, 100 and 110 (mm).

For joint by quadratic tube insertion of profile into panel (parameter  $z_4$  Fig. 12b) from left to right:

- for thickness of profile 2.5 mm: respectively 5, 10, 15, 20 and 24 (mm);

- for thickness of profile 3 mm: respectively 5, 10, 15, 20 and 23.5 (mm);

- for thickness of profile 3.5 mm: respectively 5, 10, 15, 20 and 23 (mm).

## CONCLUSIONS

Steel sandwich structures are new promising structural materials. However, the problem of joining them with themselves and with neighbouring single-skin structures does limit their future possible applications. Such joints must present good strength properties together with relative low mass. Of course, the assembly of structures using such joints must be easy and possible to perform for typical manufacturing

conditions and equipment. Such needs require an optimisation process to be performed to reach a balance between the strength and weight.

- In the paper quantitative results from laboratory tests of sandwich-sandwich joints regarding fatigue properties are presented. The analysis of the results obtained shows that the fatigue life of the joint by flat bar is lower than for the square tube for given properties of geometry of joint.
- The parametrical process for numerical searching of influence of geometry on maximum stresses to mass ratio is presented. Methodology applied give supporting tool for searching of optimal geometry of joint. Obtained results shows possibility for performing optimisation process due to fact that there is possible to found parameters of geometry which presents minimum of stress concentration factor.

## REFERENCES

1. X. Li, Z. Zhu, Y. Li, and Z. Hu, 'Design and Mechanical Analysis of a Composite T-Type Connection Structure for Marine Structures', Polish Marit. Res., vol. 27, no. 2, 2020, doi: 10.2478/pomr-2020-0036.
2. N. N. Yang, T. Y. Zhao, J. G. Gu, and Z. P. Chen, 'Damage and Fracture Analysis of Bolted Joints of Composite Materials Based on Peridynamic Theory', Polish Marit. Res., vol. 26, no. 2, 2019, doi: 10.2478/pomr-2019-0022.
3. L. Matuszewski, 'Application of shape memory alloys in pipeline couplings for shipbuilding', Polish Marit. Res., vol. 27, no. 3, 2020, doi: 10.2478/pomr-2020-0049.
4. T. Niksa-Rynkiewicz, M. Landowski, and P. Szalewski, 'Application of apriori algorithm in the lamination process in yacht production', Polish Marit. Res., vol. 27, no. 3, 2020, doi: 10.2478/pomr-2020-0047.
5. T. Ferenc and T. Mikulski, 'Validation Process for Computational Model of Full-Scale Segment for Design of Composite Footbridge', Polish Marit. Res., vol. 27, no. 2, 2020, doi: 10.2478/pomr-2020-0037.
6. T. Urbański, A. Banaszek, and W. Jurczak, 'Prediction of Welding-Induced Distortion of Fixed Plate Edge Using Design of Experiment Approach', Polish Marit. Res., vol. 27, no. 1, 2020, doi: 10.2478/pomr-2020-0014.
7. K. Sun, Y. Hu, Y. Shi, and B. Liao, 'Microstructure Evolution and Mechanical Properties of Underwater Dry Welded Metal of High Strength Steel Q690E under Different Water Depths', Polish Marit. Res., vol. 27, no. 4, 2020, doi: 10.2478/pomr-2020-0071.
8. B. Metschkow and T. Graczyk, 'Laser welded joints in shipbuilding', Marine Technology II, WIT Press, 1999, p. 171–182.
9. F. Roland: Laser Welding in Shipbuilding – Chances and Obstacles. Kimm, Korea: Proceedings of the 8th Symposium on Laser Materials, 1997, p. 237–252.
10. BONDSHIP: Code part BONDSHIP guidelines\_tcm4-178376.pdf. <https://www.scribd.com/document/246094980/Code-Part-BONDSHIP-Guidelines> [attemp: 12nd February 2021].
11. M. Hentinen, M. Hildebrand, M. Visuri: Adhesively bonded joints between FRP sandwich and metal. VTT Tiedotteita – Meddelanden. Research Notes 1862. Technical Research Centre of Finland Espoo, 1979.
12. R. Pyszek: Strength assessment of a version of joint of sandwich panels. Polish Maritime Research, ISSN 1233-2585, Nr S1/2006.
13. P. Gallo, M. Guglielmo, J. Romanoff, and H. Remes, 'Influence of crack tip plasticity on fatigue behaviour of laser stake-welded T-joints made of thin plates', Int. J. Mech. Sci., vol. 136, 2018, doi: 10.1016/j.ijmecsci.2017.12.011.
14. K. Niklas and J. Kozak, 'Influence of the notch rounding radius on estimating the elastic notch stress concentration factor in a laser welded tee joint', in Materials Science Forum, 2012, vol. 726, doi: 10.4028/www.scientific.net/MSF.726.100.
15. J. Kozak, 'Selected problems on application of steel sandwich panels to marine structures', Polish Marit. Res., vol. 16, no. 4, 2009, doi: 10.2478/v10012-008-0050-4.
16. D. Boroński J. Kozak: Research on deformations of laser-welded joint of a steel sandwich structure model. Polish Marit. Res., vol. 2, no. 11, 2004.
17. K. Niklas, 'Search for optimum geometry of selected steel sandwich panel joints', Polish Marit. Res., vol. 15, no. 2, 2008, doi: 10.2478/v10012-007-0061-6.

## CONTACT WITH THE AUTHOR

**Janusz Kozak**  
*e-mail: kozak@pg.gda.pl*

Gdańsk University of Technology  
Narutowicza 11/12  
80-233 Gdańsk  
**POLAND**